A Measurement of the Triple Gauge Boson Couplings and W Boson Polarisation in W-Pair Production at LEP2

Jonathan P. Couchman

University College London

Submitted to the University of London
in fulfilment of the requirements
for the award of the degree of
Doctor of Philosophy.
October 2000.

Abstract

Measurements of the trilinear gauge boson vertex coupling (TGC) parameters and the W polarisation of W^+W^- boson pairs produced in e^+e^- collisions are presented. The data were recorded by the OPAL experiment at LEP during 1998, where a total integrated luminosity of 183 pb^{-1} was obtained at a centre-of-mass energy of 189 GeV. Only events where one W boson decays into a quark and an anti-quark, and the other W decays into a lepton and a neutrino are used. The selected data sample comprises of 1075 events.

All the measurements are performed through a spin density matrix analysis of the W boson decay products. In addition to this, an analysis of the W production angle is performed to further constrain the measured trilinear gauge boson coupling parameters.

The sets of TGC parameters measured are $\Delta\kappa_\gamma$-λ-Δg_1^z and $\tilde{\kappa}_z$-$\tilde{\lambda}_z$-g_4^z. The first set are all CP-conserving, where as the second set are all CP-violating. Both sets of parameters may have anomalous values without violating the $SU(2)_L \times U(1)_Y$ gauge symmetry of the electroweak Lagrangian. The mea-

sured values of the CP-conserving parameters are:

$$\begin{aligned} \Delta\kappa_\gamma &= -0.235^{+0.282}_{-0.232} \\ \lambda &= -0.082^{+0.102}_{-0.095} \\ \Delta g_1^z &= -0.038^{+0.102}_{-0.095} \end{aligned}$$

and for the CP-violating parameters the following are obtained:

$$\begin{aligned} \tilde{\kappa}_z &= -0.184^{+0.091}_{-0.065} \\ \tilde{\lambda}_z &= -0.136^{+0.161}_{-0.194} \\ g_4^z &= +0.070^{+0.263}_{-0.255} \end{aligned}$$

All errors include both statistical and systematic uncertainties.

In addition to the measurement of the TGC parameters, the SDM analysis is used to directly measure the W bosons polarisation states. The W boson may have either longitudinal or transverse polarisation. The fraction of W bosons produced with longitudinal polarisation is found to be $\sigma_{\mathrm{L}}/\sigma_{\mathrm{total}} = (21.9 \pm 3.4 \pm 1.6)\%$, where the first error is statistical and the second systematic.

The joint W-pair production fractions were found to be; $\sigma_{\mathrm{TT}}/\sigma_{\mathrm{total}} = (76.8 \pm 9.0 \pm 3.2)\%$, $\sigma_{\mathrm{LL}}/\sigma_{\mathrm{total}} = (20.6 \pm 7.2 \pm 1.8)\%$ and $\sigma_{\mathrm{TL}}/\sigma_{\mathrm{total}} = (2.6 \pm 14.7 \pm 3.8)\%$.

All results are consistent with Standard Model expectations.

Acknowledgements

I would like to thank the following people for their invaluable help with my research; Gideon Bella, Stephen Betts, Dave Charlton, Peter Clarke, Paul Dervan, Georgios Gounaris, David Miller, Jenny Thomas and Helge Voss.

In addition, I would like to thank the following people for making my time of research such fun; Jacqueline Fryer, Matthew Balme, Claire Gwenlan, Eileen Heaphy, Chris Smith, Mark Sutton and everyone in the UCL HEP group and OPAL collaboration that I haven't mentioned yet.

Finally I would like to express my gratitude to PPARC for funding my research.

Cheers everyone!

Contents

1 The Standard Model **18**

1.1 The Fundamental Particles 19

1.1.1 The Fermions 19

1.1.2 Bosons: The Force-carrying Particles 21

1.2 Spin, Helicity and Polarisation 24

1.3 The Electroweak Theory 25

2 The LEP Accelerator and OPAL Detector **27**

2.1 The LEP Accelerator 27

2.2 The OPAL Detector 31

2.2.1 Central Tracking Detector 32

2.2.2 The OPAL Magnet 37

2.2.3 The Time-Of-Flight Detector 37

2.2.4 Electromagnetic Calorimeter (ECAL) 38

2.2.5 Hadronic Calorimeter (HCAL) 40

2.2.6 Muon Chambers 42

2.2.7 Forward Detector (FD) 43

2.2.8 The Silicon-Tungsten Calorimeter (SW) 44

2.2.9 The OPAL Trigger 44

2.2.10 Data Acquisition 45

3 Trilinear Gauge Boson Couplings and W-Pair Production. 46

3.1 The TGC Lagrangian 47

3.2 TGCs and W Pair Production at LEP 54

3.2.1 Polarisation of the W-Pair System 56

3.3 W Boson Decays 66

3.4 Polarisation Properties 70

3.4.1 The Two-Particle Joint Spin Density Matrix 70

3.4.2 The Single W Spin Density Matrix 74

4 Application to Data Events 81

4.1 Calculating the SDM Elements 81

4.2 Calculating the Polarised Cross-Sections 88

4.3 Considerations for Real Events 88

4.4 Events with $q\bar{q}\ell\bar{\nu}_\ell$ Final States 93

5 Selection of Data 96

5.1 Background Events 96

5.1.1 Neutral Current Four-Fermion Production 96

5.1.2 The $Z^0/\gamma \to q\bar{q}$ Background 98

5.1.3 The Two-Photon Background 99

5.2 Monte Carlo Generators 100

5.2.1 Four-Fermion Monte Carlo Generators 100

5.2.2 WW Monte Carlo Generators 103

5.2.3 Background Generators 105

5.2.4 Jet Fragmentation 105

5.2.5 Monte Carlo Samples Used 105

5.3 Detector Simulation 108

5.4 Data Selection and Reconstruction 109

5.4.1 Selection of $q\bar{q}\ell\bar{\nu}_\ell$ Events 109
5.4.2 Event Reconstruction 124
5.4.3 189 GeV Data Sample 126

6 Extracting the TGCs **132**
6.1 The χ^2 Fit to the Single W SDM Elements 132
6.1.1 Overcoming Problems of Detector Effects. 136
6.1.2 Systematic Checks of the SDM Fit Method 143
6.2 The χ^2 Fit to the $\cos\theta_W$ Distribution 146
6.2.1 Systematic Checks of the $\cos\theta_W$ Fit Method 146
6.3 The Combined Fit 147
6.4 Fit to Many Subsamples 150

7 TGCs from 189 GeV Data **163**
7.1 Fit to Single W SDM Elements 163
7.2 Fit to the Normalised $\cos\theta_W$ Distribution 167
7.3 The Combined Fit 168
7.4 Including Systematics 173

8 Method to Measure Polarised Cross-sections **180**
8.1 Correcting for Detector Effects 180
8.2 Correction for Background 192

9 Measurements of Polarised Cross-sections from Data **199**
9.1 Individual W Polarised Cross-Sections 199
9.2 W-Pair Polarised Cross-Sections 202

10 Evaluation of Systematic Uncertainties **205**
10.1 Uncertainties in Electroweak Modelling 206

10.2 Jet Fragmentation 206
10.3 Jet Reconstruction 208
10.4 Background 212
10.5 Detector Simulation and Lepton Response 213
10.6 Overall Systematic Uncertainty 216

11 Conclusions **220**
11.1 Tests of CP-Invariance 221
11.2 Measurement of TGCs 222
11.3 Measurement of W Polarisation 225

A Summations to Calculate SDM Elements **227**
A.1 Summation to Calculate Single W SDM Elements 227
A.2 Summation to Calculate Two-Particle Joint W SDM Elements 228

B Stability of the χ^2 fit **243**

List of Figures

1.1 The muon decay process 20
1.2 Schematic of jet formation via quark, anti-quark separation . . 24

2.1 Diagram of the accelerators at CERN. 30
2.2 Schematic representation of the OPAL detector 33
2.3 Detailed schematic of the OPAL cross-section 34

3.1 The trilinear gauge vertex 47
3.2 The two W-pair production processes which contain the trilinear gauge vertex 55
3.3 The t-channel single W production process which contains the trilinear gauge vertex 55
3.4 The t-channel W-pair production process 56
3.5 W-pair production cross-section as a function of centre-of-mass energy for the Standard Model 61
3.6 W-pair production cross-section as a function of centre-of-mass energy for a non-Standard Model case 62
3.7 The differential cross-section of W production at 189 GeV with CP-conserving anomalous couplings implemented 64
3.8 The differential cross-section of W production at 189 GeV with CP-violating anomalous couplings implemented 65

3.9 Production and decay angles of W bosons 68
3.10 Analytical prediction of the two-particle joint Spin Density Matrix elements 71
3.11 Single W Spin Density Matrix elements. 76
3.12 The analytical predictions for the individual W polarised differential cross-sections. 77
3.13 Analytical prediction for the imaginary parts of the single W Spin Density Matrix elements. 80

4.1 Angular distributions calculated from Standard Model Monte Carlo 82
4.2 Single W SDM elements calculated from Standard Model Monte Carlo 85
4.3 Two-particle joint W SDM elements calculated from Standard Model Monte Carlo 87
4.4 Polarised differential cross-sections calculated from Standard Model Monte Carlo. 89
4.5 CC03 Diagrams 94
4.6 CC10 Diagrams 94
4.7 CC20 Diagrams 95

5.1 NC24 Diagrams 97
5.2 NC48 Diagrams 98
5.3 $Z^0/\gamma \to q\bar{q}$ processes 99
5.4 2-photon process 99
5.5 Interfering QCD background 101
5.6 Outline of the organisation of the GOPAL program. 108
5.7 $\cos\theta_W$ distributions for all and selected events only 123

5.8 True and reconstructed angular distributions for selected events 128
5.9 The angular distributions of the selected data events at 189 GeV 129

6.1 Single W SDM elements extracted from fully detector simulated Monte Carlo 137
6.2 Comparison of reweighted Monte Carlo to generated Monte Carlo 140
6.3 Comparison of the SDM elements extracted from reweighted Monte Carlo to those extracted from generated Monte Carlo . 142
6.4 Bias plots of the CP-conserving TGCs fit using the WVCXME reweighting scheme 153
6.5 Bias plots of the CP-conserving TGCs fit using the BILGOU reweighting scheme 154
6.6 Bias plots of the CP-violating TGCs fit using the BILGOU reweighting scheme 155
6.7 Pull distributions for Standard Model Monte Carlo for the combined fit to the CP-conserving couplings using the BILGOU reweighting scheme 158
6.8 Pull distributions for Standard Model Monte Carlo for the combined fit to the CP-conserving couplings using the WVCXME reweighting scheme 159
6.9 Pull distributions for Standard Model Monte Carlo for the $\cos\theta_{\mathrm{W}}$fit to the CP-conserving couplings 160
6.10 Pull distributions for Standard Model Monte Carlo for the combined fit to the CP-violating couplings 161
6.11 Pull distributions for Standard Model Monte Carlo for the $\cos\theta_{\mathrm{W}}$fit to the CP-violating couplings 162

7.1 Single W SDM elements extracted from 189 GeV data 165
7.2 Normalised $\cos\theta_{\mathrm{W}}$ disribution extracted from the 189 GeV data 167
7.3 χ^2 plots of the fit of the CP-conserving couplings using the WVCXME reweighting scheme. 170
7.4 χ^2 plots of the fit of the CP-conserving couplings using the BILGOU reweighting scheme. 171
7.5 χ^2 plots of the fit of the CP-violating couplings using the BILGOU reweighting scheme. 172
7.6 χ^2 plots of the fit of the CP-conserving couplings, including systematic uncertainties, using the WVCXME reweighting scheme 176
7.7 χ^2 plots of the fit of the CP-conserving couplings, including systematic uncertainties, using the BILGOU reweighting scheme. 177
7.8 χ^2 plots of the fit of the CP-violating couplings, including systematic uncertainties, using the BILGOU reweighting scheme 178

8.1 Resolution of angular variables 184
8.2 Distribution of correction factors for $-0.25 < \cos\theta_{\mathrm{W}} < +0.0$ . . 185
8.3 Distribution of correction factors for $0.75 < \cos\theta_{\mathrm{W}} < 1.0$ 186
8.4 Corrected single SDM elements from PYTHIA Monte Carlo . 187
8.5 Corrected differential cross-sections calculated from PYTHIA Monte Carlo 189
8.6 The fraction of each polarisation state from Monte Carlo . . . 190
8.7 Polarised cross-sections from Monte Carlo sub-sample. 191
8.8 Comparison of true and measured fractions of longitudinal W bosons from Monte Carlo sub-samples. 193

8.9 Comparison of true and measured fractions of each polarisation state from Monte Carlo sub-samples. 194
8.10 Measured fractions of polarised cross-sections from Monte Carlo sub-samples 195
8.11 Contribution to the polarised cross-sections from background events 197
8.12 Effect of background on normalised polarised differential cross-sections. 198

9.1 Individual W differential polarised cross-sections extracted from 189 GeV data 200
9.2 W-pair polarised cross-sections extracted from 189 GeV data . 204

10.1 Single W SDM elements for generator modelling studies 207
10.2 Single W SDM elements for hadronisation studies 209

11.1 Model independent test of CP and CPT-violation 223
11.2 Plots of the final χ^2 fits for all TGCs 226

B.1 Bias plots of the CP-conserving TGCs fit using the BILGOU reweighting scheme 245
B.2 Bias plots of the CP-violating TGCs fit using the BILGOU reweighting scheme 246
B.3 Pull distributions for Standard Model Monte Carlo for the combined fit to the CP-conserving couplings using the BILGOU reweighting scheme 247
B.4 Pull distributions for Standard Model Monte Carlo for the combined fit to the CP-violating couplings 248
B.5 Plots of the final χ^2 fits for all TGCs 250

B.6 Plots of the final χ^2 fits for all TGCs 251

List of Tables

1.1 The basic properties and quantum numbers of the fermions . . 22

3.1 Properties of the 14 TGC parameters 51
3.2 Helicity amplitudes for the W-pair production process. 60
3.3 Effects of anomalous couplings on the W-pair polarisation. . . 63
3.4 Fraction of W-pairs with each polarisation state 66
3.5 SDM elements related through CP-invariance 73

5.1 Monte Carlo runs used in the analysis 107
5.2 Variables used in the lepton candidate likelihood determination 115
5.3 Variables used in the likelihood selection 118
5.4 Variables used in the tau lepton candidate likelihood determination 120
5.5 Variables used in the relative likelihood selection of $W^+W^- \to q\bar{q}\tau\bar{\nu}_\tau$ events 122
5.6 The performance of the selection of CC03 $q\bar{q}\ell\bar{\nu}_\ell$ signal events . 123
5.7 The expected and observed number of events 124
5.8 The expected and observed number of events after kinematic fits have been performed 127
5.9 Cuts applied in the tau event preselection 130
5.10 The expected background cross-sections selected at 189 GeV . 131

6.1 Correlations between single W SDM elements extracted from Standard Model Monte Carlo 136
6.2 Correlations between single W SDM elements extracted from non-Standard Model Monte Carlo 138
6.3 Bias fits to the single W SDM elements for CP-conserving anomalous couplings 144
6.4 Bias fits to the single W SDM elements for CP-violating anomalous couplings 145
6.5 Bias fits to the single $\cos\theta_{\mathrm{W}}$ distribution for CP-conserving anomalous couplings 148
6.6 Bias fits to the $\cos\theta_{\mathrm{W}}$ distribution for CP-violating anomalous couplings 149
6.7 Bias fits of CP-conserving anomalous couplings using the combined fit 151
6.8 Bias fits of CP-violating anomalous couplings using the combined fit 152
6.9 The expected statistical errors of the TGC parameter fits . . . 157

7.1 Correlations between single W SDM elements extracted from 189 GeV data 164
7.2 The absolute values of the χ^2 minimum for the fit to each coupling 173
7.3 Measured values of all trilinear gauge coupling parameters from the 189 GeV data using the BILGOU reweighting scheme 179

8.1 Fractional polarised cross-sections calculated from signal and signal plus background Monte Carlo. 196

9.1 Fraction of longitudinally polarised W bosons. 201

9.2 Fractions of W-pairs of each polarisation state. 203

10.1 Systematic uncertainties due to generator modelling 208
10.2 Systematic uncertainties due to hadronisation modelling . . . 210
10.3 Systematic uncertainties due to jet reconstruction 211
10.4 Systematic uncertainties due to background modelling 213
10.5 Systematic uncertainties due to lepton identification as a function of the lepton polar angle 214
10.6 Systematic uncertainties due to lepton identification as a function of the lepton energy 215
10.7 Systematic uncertainties due to charge/momentum lepton uncertainty 217
10.8 Total systematic uncertainty on SDM observables and $\cos\theta_{\mathrm{W}}$ distribution 218
10.9 Systematic uncertainties on the fractional polarised cross-sections 219

B.1 Measured values of all trilinear gauge coupling parameters from the 189 GeV data using the BILGOU reweighting scheme 249

Chapter 1

The Standard Model

The most widely accepted theory that describes interactions at their most fundamental level is the Standard Model. This theory has so far stood up to to all the tests that have been applied to it at the highest possible energies reachable today. It is, however, a far from complete theory and is only a low energy approximation.

A scientists goal should always be to question the theories and test them to see how accurately they represent the true data. One of the main aims of particle physics has been exactly this, to test the Standard Model. In this thesis some previously unexplored areas of the Standard Model are investigated, along with some areas that are not well constrained and the results are compared directly to those predicted by the Standard Model.

Firstly, in this chapter a few of the basic ideas of the Standard Model are described to give an overview of the theory that is being tested.

1.1 The Fundamental Particles

The Standard Model can be described in terms of the interactions of a few fundamental particles. These particles are separated into two distinct groups, the "matter" particles called fermions, and the "force-carrying" particles called bosons. The two groups of particles differ in their intrinsic angular momentum. The fermions have half-integer spin and the bosons have integer spin[1]. A description of the two types of particles is given below.

1.1.1 The Fermions

The fermions can be subdivided into two groups, those that can interact via the strong force, and those that cannot. The first group are called the quarks and the second the leptons. Both groups contain six particles and six anti-particles which are separated into three generations.

The Leptons

The six leptons are, generation one; electron (e^-) and electron-neutrino (ν_e). Generation two; muon (μ^-) and muon-neutrino (ν_μ). Generation three; tau (τ^-) and tau-neutrino (ν_τ). The corresponding anti-particles, positron, anti-muon and anti-tau, have the same mass as the particles and the opposite quantum numbers.

The fermions have half-integral spin so they may exist in two helicity states. However, the neutrinos only exist in left-handed states and anti-neutrinos in right-handed. For this to be possible, the neutrinos must be massless[2] and this is how they are described within the Standard Model.

[1] The spins are taken in units of $\hbar$.

[2] There is now strong evidence from the Super-Kamiokande experiment that the neutrinos may not be massless[1, 2, 3, 4]. Thus they must exist in both helicity states.

The mass of the leptons increases with generation, the electron is the lightest (~ 0.51 MeV) and tau the heaviest (~ 1.78 GeV).

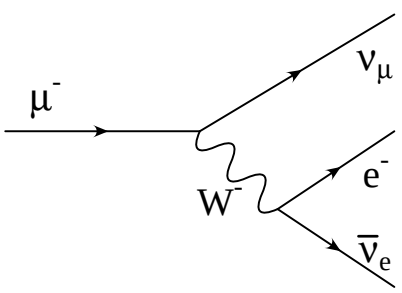

Figure 1.1: *The muon decay process.*

The massive leptons have charge -1.9×10^{-19} Coulombs, but this is often denoted in terms of the positron charge, e, thus they are said to have charge -1 and the massive anti-leptons to have charge +1. The neutrinos have zero charge. The massive leptons in higher generations may decay into those from lower generations, for example, the dominant muon decay channel is $\mu^- \rightarrow \mathrm{e}^-\bar{\nu}_\mathrm{e}\nu_\mu$, as shown in figure 1.1. The main tau decay channels are shown below. (1.3) is known as the one prong hadronic decay and (1.4) is known as the three prong hadronic decay.

$$\tau^- \rightarrow \mu^-\bar{\nu}_\mu\nu_\tau \quad (1.1)$$

$$\tau^- \rightarrow \mathrm{e}^-\bar{\nu}_\mathrm{e}\nu_\tau \quad (1.2)$$

$$\tau^- \rightarrow \pi^- n\pi^0\nu_\tau \quad (1.3)$$

$$\tau^- \rightarrow \pi^-\pi^-\pi^+\nu_\tau \quad (1.4)$$

The Quarks

All quarks have mass and this increases with generation. Each generation contains two quarks with fractional charge, one with $\frac{2}{3}$e and the other $-\frac{1}{3}$e. The quarks are called; up, down, strange, charm, bottom and top. All these quarks also have an anti-particle of the same mass, but opposite quantum

numbers. The up quark is the lightest quark with a mass of 1.5 - 5 MeV, whereas the top quark is the heaviest, with a mass up to 100,000 times greater than the up quark at about 170 GeV. For a full description of the quark, as well as the lepton properties see [5].

Quarks are never observed in isolation. They are always found in bound states with other quarks. The composites of quarks are called hadrons. Quarks have the quantum number of colour and may take one of three *colour charges*, red, blue or green (or the corresponding anti-red, anti-blue and anti-green for the anti-particles). The bound states of quarks must be *colourless* objects, and so hadrons can come in two types, fermionic baryons comprised of three quarks or three anti-quarks, one of each colour, and bosonic mesons comprised of a quark and an anti-quark, one with colour and the other with the anti of this colour. Both baryons and mesons will always have integer charge. The most well known baryons are the proton, which is a uud bound state, and the neutron, which is a udd bound state.

A summary of the properties and basic quantum numbers of all the fermions is shown in table 1.1.

1.1.2 Bosons: The Force-carrying Particles

Within the Standard Model all interactions of fermions are mediated by the exchange of a gauge boson. So all the forces may be described by the interaction of fermions and bosons. Each force has it's own gauge bosons associated with it.

- The electromagnetic force is mediated by a single boson called the photon (γ). This boson is massless and chargeless. It couples to the

Fermion	Gen.	Flavour	Mass (MeV)	Charge (Q)	$(t_3)_L$	Colour Charge
Leptons	1	e	0.51	-1	$-\frac{1}{2}$	0
		ν_e	0	0	$+\frac{1}{2}$	0
	2	μ	105.7	-1	$-\frac{1}{2}$	0
		ν_μ	0	0	$+\frac{1}{2}$	0
	3	τ	1777	-1	$-\frac{1}{2}$	0
		ν_τ	0	0	$+\frac{1}{2}$	0
Quarks	1	u	1.5-5	$+\frac{2}{3}$	$+\frac{1}{2}$	R,G,B
		d	17-27	$-\frac{1}{3}$	$-\frac{1}{2}$	R,G,B
	2	s	60-170	$+\frac{2}{3}$	$+\frac{1}{2}$	R,G,B
		c	1100-1400	$-\frac{1}{3}$	$-\frac{1}{2}$	R,G,B
	3	b	4100-4400	$+\frac{2}{3}$	$+\frac{1}{2}$	R,G,B
		t	173800	$-\frac{1}{3}$	$-\frac{1}{2}$	R,G,B

Table 1.1: *The properties and basic quantum numbers of the fermions.* t_3 *is the weak isospin of the particle, which is the quantum number for the weak force. The quantum numbers for the corresponding anti-particles are obtained by taking the negative of the numbers given in the table.*

charge of other particles, so only charged particles feel the effect of the electromagnetic force.

- The weak force has three mediating bosons. There is the chargeless Z^0 which has a mass of 91.2 GeV and a width of 2.5 GeV [5, 6]. Then there are the two charged bosons $W^\pm$ which each have a mass of 80.45 GeV [7, 8] and a width of 2.0 GeV [8].

  The W bosons couple to the weak isospin of particles (t_3). Only left

handed fermions and right handed anti-fermions have non-zero weak isospin. W bosons themselves also have non-zero weak isospin so can couple to each other.

The Z^0 boson couples to a combination of both weak isospin and charge, as shown in equation 1.5. It has zero weak isospin itself.

$$C_{Z^0} = \frac{(t_3 - \sin\theta_w \mathrm{Q})}{\sin\theta_w \cos\theta_w} \tag{1.5}$$

In equation 1.5, θ_w is known as the Weinberg or weak mixing angle and is related to the masses of the Z^0 and $W^{\pm}$ as follows:

$$\cos\theta_w = \frac{M_W}{M_Z} \simeq 0.87679 \tag{1.6}$$

The weak force is the only force that couples to all the fermions. When a W boson interacts with a fermion it will always change the flavour of the fermion. There are no flavour changing neutral weak interactions.

A property of the weak force is that its bosons can couple to each other in certain combinations and also the photon. The coupling of a W^+ and a W^- boson to a photon or Z^0 boson is known as a Trilinear or Triple Gauge Coupling (TGC) and this process is the basis for this thesis.

- The Strong Force has eight mediating bosons called gluons. These are massless and chargeless and couple to the colour charge of particles. Of the fermions only quarks have non-zero colour charge. Gluons are the only bosons that have non-zero colour charge and can couple to other gluons.

The strong force is unlike the other two forces in that its strength actually increases with distance. This is the reason that no unbound quarks are seen. All quarks are bound as colourless baryons or mesons as discussed earlier.

A consequence of this property is that if two bound quarks are separated the potential energy between them increases until it reaches a level where two new quarks will form. Although each of these is a colour singlet, they effectively combine with the original object to form colourless objects. Continued separation will cause further quark pairs to form. Figure 1.2 shows a simple schematic of this process. If this separation occurs at high energy, the newly formed quark anti-quark pairs are seen as jets of particles. As the quarks in each jet form hadrons, this process is known as hadronisation.

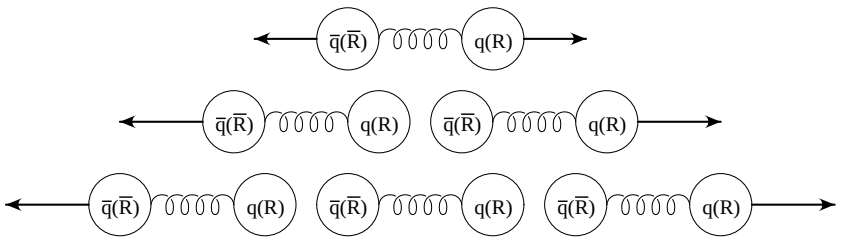

Figure 1.2: *Production of quark anti-quark pairs when a single pair are separated.*

1.2 Spin, Helicity and Polarisation

The intrinsic angular momentum of a particle is known as its spin. The fermions all have spin half, whereas the bosons have spin one. The component

of the spin in the direction of motion of a particle is called helicity. This means that the fermions can have helicity $\pm\frac{1}{2}$.

Massless particles may exist in just one helicity state. Neutrinos only exist in negative helicity states, known as left handed states, and anti-neutrinos in positive helicity, right handed states.

The $W^{\pm}$ and Z^0 bosons have spin 1 so may have helicity ± 1 or zero. As the photon and gluon are massless, they cannot exist in a helicity zero state. However, virtual photons and gluons do have mass, so they may have the zero helicity states

Particles with helicity ± 1 are said to be transversely polarised and those with zero helicity are longitudinally polarised.

1.3 The Electroweak Theory

All the forces described above are formulated in the Standard Model as gauge symmetric quantum field theories. The strong force is described by quantum chromodynamics (QCD), whereas the electromagnetic and weak forces are both described by the electroweak theory.

Any system can be described by its Lagrangian. The Lagrangian contains creation and annihilation operators that act at a particular position in space, and thus they are field operators, hence the name "quantum field theory."

The theory contains fermionic fields representing the fermions and when local symmetry is imposed, gauge fields arise that form the interaction terms with the fermionic fields. These gauge fields are then identified as the gauge bosons discussed earlier.

The Electroweak theory is an $SU(2)_L \times U(1)_Y$ gauge symmetric field theory. It has four gauge fields, three associated with weak isospin, these being

the $\mathbf{W}^{\mu}$ fields. The subscript on the $\mathrm{SU}(2)_L$ indicates that these fields only couple to left-handed fermions. There is then the B^{μ} field that couples to the weak hypercharge (Y) of particles. All fermions have non-zero weak hypercharge.

The four fields cannot be directly associated with the four gauge bosons discussed earlier, for a start they represent massless particles. These fields may be connected to the massive gauge bosons via the Higgs mechanism [9]. This causes the gauge fields to mix. The $W^{+\mu}$ and $W^{-\mu}$ fields gain mass from the vacuum expectation value. These two fields can then be directly related with the W^{+} and W^{-} bosons. The $W^{0\mu}$ and B^{μ} fields mix to form two new fields, the Z^{μ} and A^{μ} fields, that can be identified as the Z^{0} and γ bosons respectively. The form of the mixed fields is shown below.

$$Z^{\mu} = \cos\theta_w W^{0\mu} - \sin\theta_w B^{\mu} \tag{1.7}$$

$$A^{\mu} = \sin\theta_w W^{0\mu} + \cos\theta_w B^{\mu} \tag{1.8}$$

Chapter 2

The LEP Accelerator and OPAL Detector

This thesis uses data collected by the OPAL detector, which is one of the four detectors situated on the LEP accelerator ring. This chapter will give a brief description of both the LEP accelerator and the OPAL detector.

2.1 The LEP Accelerator

The Large Electron-Positron storage ring (LEP) collider [10] is based at CERN (*La Centre Européene pour la Recherche Nucléaire*) beneath the border between Switzerland and France, near Geneva. It is the largest synchrotron accelerator in the world, with the main ring tunnel having a circumference of 26.67 km. Although studies and plans for LEP machines started as early as 1976, the first fill wasn't until 13th July 1989, with actual physics runs starting a month later, on the 13th August.

As the name suggests, LEP was designed to bring extremely high energy electrons and positrons into collision with one another. Initially, the energies

of the positron and electron beams were such that the centre of mass energy ($\sqrt{s}$) at the point of collision was 91 GeV, the rest mass of the Z^0 boson, thereby opening a whole new world of investigation into the neutral current interactions in the electroweak force. LEP was a huge success, with over 900,000 Z^0 bosons being produced in the first year alone. LEP ran at this energy until 1995. Then the machine was upgraded [11, 12], so that it could run at above the $W^{\pm}$ pair threshold, allowing the investigation of the charged current sector of the electroweak force [13]. However, unlike for the Z^0 boson, where it is most profitable to have collisions close to the Z^0 boson mass, the higher the energy, the better for $W^{\pm}$ bosons as its production cross-section increases with energy, up to a centre-of-mass energy of approximately 200 GeV. So each year the centre-of-mass energy was increased.

The complete LEP collider does not consist of just the very large LEP ring, although this is easily the greatest engineering feat of the project. There are a number of other, smaller, older, CERN accelerators around which the particles are accelerated, before injection into the main ring. Figure 2.1 shows the lay out of the complete system. The electrons are produced by thermionic emission, these are then accelerated along an electron linear collider, the Lep Injector Linac (LIL). Some of the electrons are collided with a tungsten target to produce the positrons, the remaining electrons, along with the positrons, are then passed into the Electron Positron Accumulator ring (EPA), where they are stored and accumulated before injection. The particles are then passed into the Proton Synchrotron (PS) where they are initially accelerated to a few GeV. They are then transfered to the Super Proton Synchrotron (SPS) where further acceleration takes place and finally they are injected into the LEP ring.

The LEP ring is 26.67 km in circumference and lies between 40 and 150

m below the surface. The plane of the ring is inclined by 1.4%. This is purely due to engineering reasons, ensuring that no shaft had to be deeper than 150 m, but also that the underground caverns and tunnel would be located in solid rock. The LEP ring consists of eight arcs and four straight sections. The arcs contain magnetic cells to guide the beams around the ring. Each magnetic cell is comprised of a defocusing quadrupole, a vertical orbit corrector, a group of six bending dipoles, a focusing sextuplet, a focusing quadrupole, a horizontal orbit corrector, a second group of six bending dipoles, and finally a defocusing sextuple. The total length of a cell being 79.11 m and each arc contains 31 of these cells. Acceleration of the beams occurs in the straight sections. Also on these straight sections are the four experiments, OPAL, ALEPH, DELPHI and L3, where the beams are brought into collision.

The energy and number of particles in a bunch is limited by the synchrotron radiation, causing an upper limit on both current and energy. The ring is designed with the maximum radius of curvature to minimise the energy loss through synchrotron radiation. The main loss of particles is through beam-gas interactions, so a high vacuum has to be maintained in the tunnel. Without beams the pressure in the tunnel is 10^{-12} Torr, and with beams circulating this is degraded to 10^{-9} Torr. The main problem with maintaining this vacuum is out-gassing caused by synchrotron radiation interacting with the beam pipe walls. Synchrotron radiation can also cause heating of the vacuum chambers, and so the chamber walls are made of aluminium which is cooled by surrounding water channels.

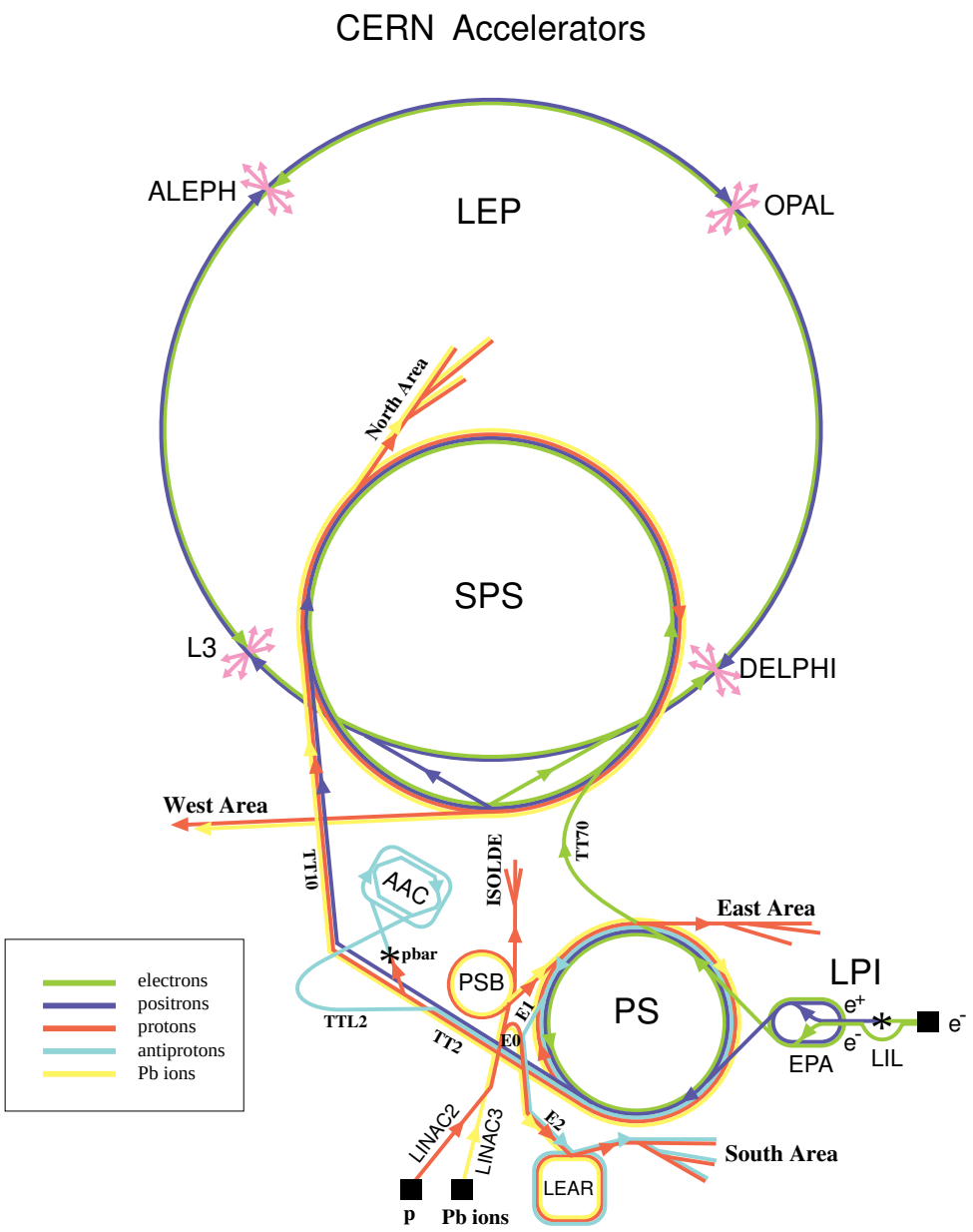

LEP: Large Electron Positron collider
SPS: Super Proton Synchrotron
AAC: Antiproton Accumulator Complex
ISOLDE: Isotope Separator OnLine DEvice
PSB: Proton Synchrotron Booster
PS: Proton Synchrotron
LPI: Lep Pre-Injector
EPA: Electron Positron Accumulator
LIL: Lep Injector Linac
LINAC: LINear ACcelerator
LEAR: Low Energy Antiproton Ring

Rudolf LEY, PS Division, CERN, 02.09.96

Figure 2.1: *Diagram representing all the accelerators at CERN and how they are used in unison to produce a final high energy circulating ring around LEP.*

2.2 The OPAL Detector

Like the other three LEP detectors the OPAL (Omni Purpose Apparatus for Lep) detector is a symmetric barrel detector. It was designed to give good measurement of both particle momenta and energy and in some cases even particle species. It roughly consists of a long central cylinder, called the barrel, and two flat endcaps at either end of the barrel to give the widest possible coverage of the solid angle.

A diagram of the OPAL detector is shown in figure 2.2. Indicated on the diagram is the OPAL co-ordinate system. The electrons and positrons travel along the beam pipe and are bought into collision within the detector. The z-axis is parallel to the beam pipe and positive in the direction of the electrons' momentum. The x-axis indicated in figure 2.2 is taken as positive in the direction pointing towards the centre of the LEP ring.

The main features of the OPAL detector are shown in figure 2.2, and they can concisely be described as follows:

• A central detector, consisting of vertex and tracking subdetectors and surrounded by a solenoid. The central detector provides measurements of the particle's direction and momentum and their identification by dE/dx as well as reconstruction of primary and secondary vertices at and near the interaction region. The solenoid causes bending of the charged particles in the tracking chamber.

• An electromagnetic calorimeter to provide identification of photons and electrons and to measure their energy.

• A hadronic calorimeter to measure hadronic energy. This is implemented by measuring the total absorption using instrumentation which incorporates the magnetic yoke.

• A Muon detector to identify muons by measurement of their position

and direction within and behind the hadron calorimeter.

• A forward detector, situated in the very forward direction, and used to measure the received LEP luminosity at OPAL using Bhabha scattering events.

A representation of the cross-section of the OPAL detector can be seen in figure 2.3. A detailed description of each OPAL subdetector is beyond the bounds of this thesis, however, a brief overview of each subdetector is given for completeness. A complete and detailed description of the OPAL detector and all its constituent parts can be found in [14].

2.2.1 Central Tracking Detector

Within the central detectors of OPAL tracking of charged particles is performed. Listed in order of increasing radius, this job is undertaken by, the silicon microvertex detector (SI), the central vertex detector (CV), the central jet chamber (CJ) and the central Z chambers (CZ). The configuration of these subdetectors is shown on figure 2.3.

Silicon Microvertex Subdetector (SI)

The SI detector [15] is designed to give accurate measurement and detailed information on the primary vertices of interaction between the electron and positron particles in the beam. It is designed so that it can also measure the positions of any secondary vertices resulting from the decays of particles that could have been produced in the primary interaction, such as τ-leptons and heavy flavour hadrons. The SI consists of two cylinders of silicon ladders. The inner cylinder has a radius of 61 mm, consisting of 11 ladders and the outer a radius of 75 mm, consisting of 14 ladders. Each ladder has two back-to-back single sided sets of silicon wafers, one giving co-ordinates in the r-ϕ

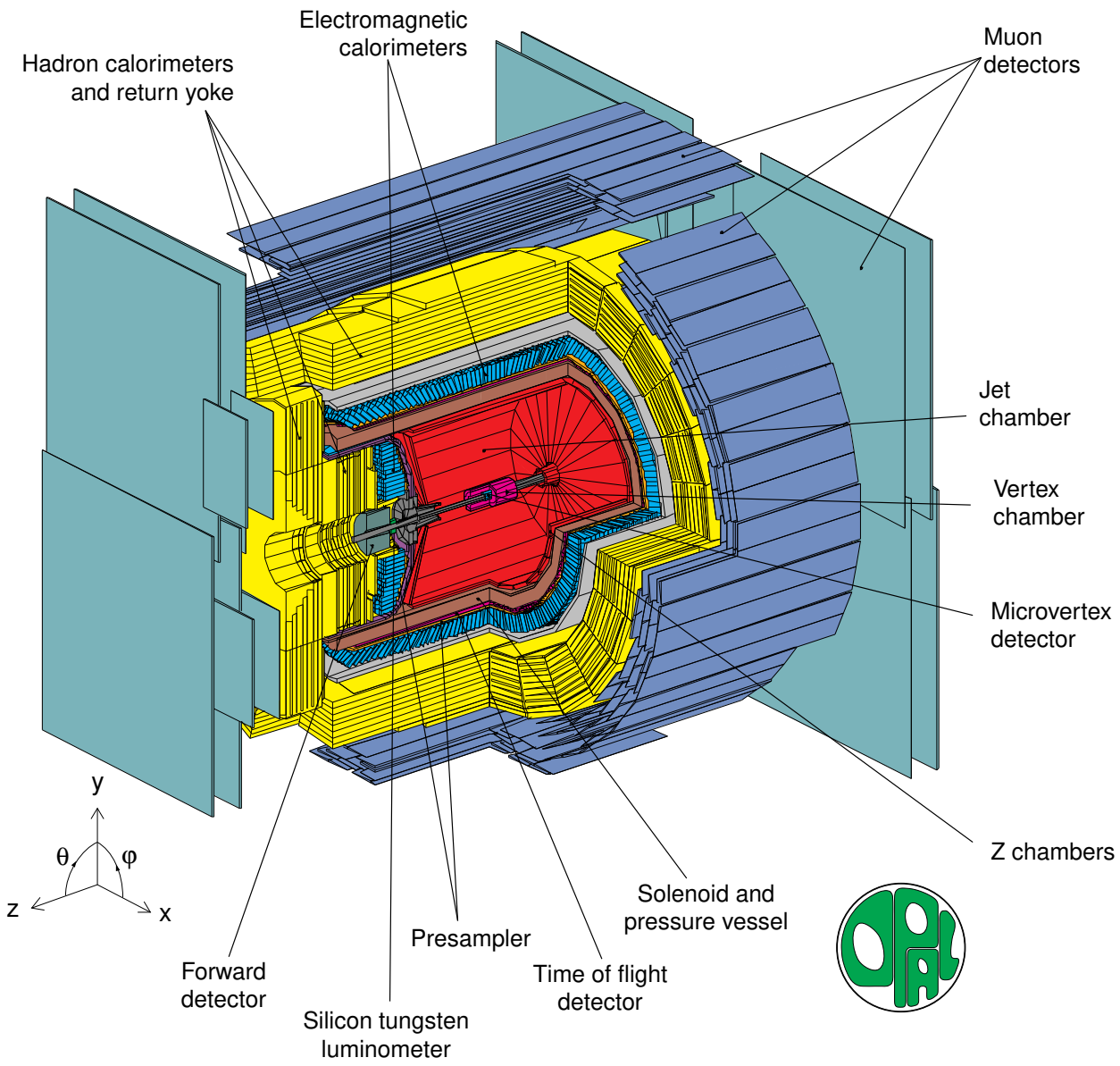

Figure 2.2: *A schematic representation of the OPAL detector.*

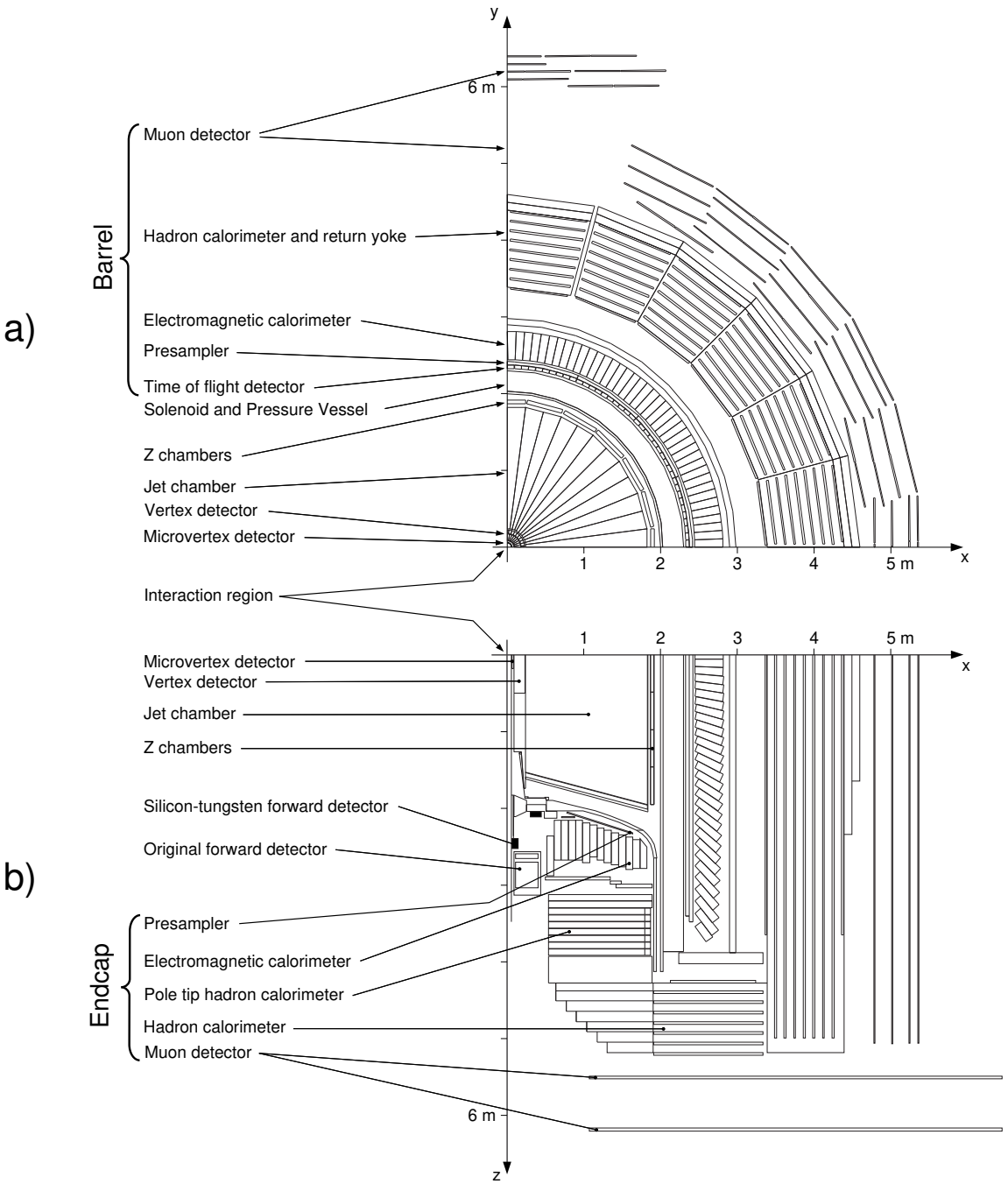

Figure 2.3: *A detailed schematic of the OPAL cross-section.*

plane and the other along the z-axis.

To measure the path of charged particles the strips have a voltage bias across them. When a charged particle passes through them charge from ionisation in the silicon is collected on the read-out strips. By combining information from all the strips on both layers, the path of the particle travelling through the silicon can be reconstructed.

Central Vertex Chamber (CV)

The central vertex tracking drift chamber [16] is situated inside the central jet chamber and is 1 m long. Its main job is to measure the vertex positions of decay particles and improve the momentum resolution for charged particles. It consists of two layers of drift chambers. The inner layer containing 36 cells of axial wires and the outer layer 36 stereo cells. The outer cells contain read-out wires that are inclined at an angle of approximately 4° to the inner, axial wires. The inner layer lies between radii 103 mm to 162 mm, and the outer layer between radii 188 mm and 213 mm.

The CV chamber, like all the central tracking drift chambers, is filled with 88.2% argon, 9.8% methane and 2.0% isobutane at a pressure of 4 bar. When a charged particle passes through this chamber it ionises the gas, this is detected in the sense wires. The inner axial cells provide measurements in the $r - \phi$ plane with resolution of 50 μm. Combining information from the inner and outer cells gives a resolution of about 700 μm on the position in the z-plane.

Central Jet Chamber (CJ)

The job of the Central Jet chamber [17, 18] is to improve the measurement of the trajectory of the charged particles. It also has an important role in

helping in particle identification by measuring the specific energy loss, dE/dx. The curvature of the track of the charged particle in the magnetic field as it passes through CJ can be measured, thus making it possible to calculate the momentum of the tracked particle.

The chamber is 4 m long, with an inner radius of 0.245 m and an outer radius of 1.85 m. The chamber is divided around the ϕ direction into 24 segments of equal size. Each segment contains 159 anode sense wires running parallel with the beam direction along the z-axis. The wires are arranged in radial planes.

Between a polar angle of $43^\circ < \theta < 137^\circ$, 159 points on the track are measured. For 98% of the 4π solid angle at least 20 points are measured on every track. The $r - \phi$ position of the hits is given by the radial position of the relevant wire and the drift time. A resolution of 135 μm is achieved. The z-position is given by the time difference between signals at either end of the wire, a resolution of 6 cm is possible in the z-direction.

Central Z Chamber (CZ)

The Central Z subdetector [19] surrounds CJ and makes precise measurements of the Z position of a particle's track as it exits CJ. CZ is made up of 24 chambers each of which is 4 m long, 500 mm wide and 59 mm thick. Each chamber is divided into 8 cells along the z-direction, each cell contains 6 sense wires lying perpendicular to the z-direction.

CZ covers a polar angle range of $44^\circ < \theta < 136^\circ$. Its resolution is 300 μm in z and 1.5 cm in $r - \phi$.

2.2.2 The OPAL Magnet

The OPAL magnet consists of a water cooled solenoid and an iron yoke to provide flux return. The solenoid and pressure vessel surround the central tracking chambers and the iron yoke is incorporated into the hadron calorimeter.

The purpose of the magnet is to cause charged particles to move in a helical path, therefore aiding measurement of particle momentum within CJ. The solenoid provides a field of 0.435 T within the central tracking region and is uniform to within 0.5%.

2.2.3 The Time-Of-Flight Detector

The time-of-flight system measures the transit time of particles travelling from the interaction region, which helps in charged particle identification. Its main job is, however, to aid in the rejection of cosmic ray events and generate trigger signals. It is divided into two parts, the time-of-flight barrel (TB) and the tile endcaps (TE)

Time-Of-Flight Barrel (TB)

TB is situated at a radius of 2.36 m, surrounding the solenoid. It is made up of 160 scintillation counters, which are trapezoidal in shape. Each one is 6.84 m in length, 45 mm in depth and ranges between 89 mm and 91 mm in width. The tiles form a layer that covers a solid angle range of $|\cos\theta| < 0.82$. The time resolution of TB is approximately 300 ps and the difference in time between the signal arriving at each end of the counter is used to make a z-position measurement.

Tile Endcaps (TE)

The tile endcaps [20] were installed into OPAL in 1996, and perform the same function in the endcap region as TB does in the barrel region. TE consists of 10 mm thick scintillating plastic tiles. Embedded in the tiles are wavelength shifting optical fibres. It has a timing precision of about 3 ns and covers the region close to the beam pipe. It is an essential detector in both exotic particle searches and two photon studies. An extension of TE, the Minimal Ionising Particle (MIP) plug was installed in 1997, and gives coverage of the polar angular region down to 43 mrad from the beam pipe.

2.2.4 Electromagnetic Calorimeter (ECAL)

The electromagnetic calorimeter is designed to give the most precise and important measurement of particles' energies. It can measure energies between a few tens of MeV up to 100 GeV. It measures the energies and positions of electrons, positrons and photons, and helps to discriminate between electrons and hadrons. ECAL is divided into a barrel region and two endcap regions and gives a coverage of 98% of the solid angle. Each region consists of a presampler in front of a lead-glass calorimeter.

Electromagnetic Presamplers (PB & PE)

Most electromagnetic showers are initiated before reaching ECAL as there are approximately two radiation lengths between the interaction region and the calorimeter, because of this there is a presampler [21] incorporated into the ECAL. The presamplers help in energy resolution of the shower and discrimination between particles.

The barrel presampler is a 6.623 m long cylinder of radius 2.388 m situated

between the time-of-flight barrel and the barrel electromagnetic calorimeter. It consists of 16 chambers containing two layers of streamer mode drift tubes with sense wires parallel to the beam axis. The barrel presampler covers a polar angle range of $|\cos\theta| < 0.81$. The two endcap presamplers (PE) are situated between the time-of-flight endcap (TE) and the endcap electromagnetic calorimeters. Each PE is divided into 16 overlapping wedges and gives full azimuthal angle coverage and a polar angle coverage of $0.86 < |\cos\theta| < 0.95$.

Electromagnetic Calorimeters (EB & EE)

The electromagnetic calorimeter is separated into three sections, a barrel section and two endcap regions. The barrel section is a cylindrical array of 9440 lead-glass blocks. These blocks are pointed towards the interaction region, but slightly tilted away from the exact interaction point. This orientation serves to prevent neutral particles being lost in the gaps between blocks whilst also trying to prevent most particles traversing more than one block. Each block is 37 cm deep, which is 24.6 radiation lengths, and has an approximate surface area of 10 $\times$ 10 cm. The blocks have a density of 5.54 gcm^{-3} and are situated at a radius of 2.455 m from the interaction point.

The subdetector works on the principle that relativistic particles travelling through the blocks will emit Čerenkov radiation which can be collected by photomultiplyer tubes at the end of the blocks. EB covers a polar angle range of $|\cos\theta| < 0.82$ and has a spatial resolution for a particle of, say 6 GeV, of approximately 11 mm. The energy resolution of EB in units of GeV is:

$$\frac{\sigma_E}{E} \simeq 0.2\% + \frac{6.3\%}{\sqrt{E}} \tag{2.1}$$

The endcap electromagnetic calorimeters [22] cover a polar angle range

of $0.83 < |\cos\theta| < 0.95$. Each of the two EEs consists of 1132 lead-glass scintillator blocks. These blocks differ slightly from those in EB in that they have a smaller density, 4.06 gcm^{-3}. The blocks vary in length from 380 to 520 mm, so that they will fit around the dome shape of the pressure bell at either end of the detector. Particles traversing the blocks are presented with a minimum of 20.5 radiation lengths. The energy resolution is approximately 1% in the energy region 3-50 GeV.

2.2.5 Hadronic Calorimeter (HCAL)

The hadronic calorimeter [23, 24, 25], like the electromagnetic calorimeter, has a barrel region and two endcap regions covering roughly the same regions as the ECAL, however, HCAL also has a hadron poletip calorimeter which covers regions were the momentum resolution of the central detectors is poor. HCAL uses the iron return yoke of the OPAL magnet as passive absorbing material. Layers of the iron are sandwiched by planes of detectors.

Due to the large amount of material between HCAL and the interaction point, most hadronic showers are likely to have initiated long before reaching HCAL, this means that the hadronic energy measurement is made by adding the energy deposited in HCAL with that deposited in ECAL. The energy resolution for all parts of HCAL are similar, although there is more variation with energy for the poletip calorimeter. The resolutions, depending on the energy measured are;

$$\frac{\sigma_E}{E} \simeq \frac{100\%}{\sqrt{E}} \quad \text{for} E < 15\text{GeV} \tag{2.2}$$

$$\frac{\sigma_E}{E} \simeq \frac{140\%}{\sqrt{E}} \quad \text{for} E < 50\text{GeV} \tag{2.3}$$

Barrel Hadronic Calorimeter (HB)

The barrel hadronic calorimeter has an inner radius of 3.39 m and outer radius 4.39 m, and is cylindrical in shape. There are eight layers of 100 mm thick iron and these are separated by nine layers of detector. The detectors consist of limited streamer mode tubes with wires parallel to the beam axis. The tubes are filled with 75% isobutane and 25% argon. The iron layers are separated by 25 mm.

Endcap Hadronic Calorimeter (HE)

The endcap hadronic calorimeters are situated at either end of the OPAL detector. They work on very similar principles to the HB. There are seven layers of 100 mm thick iron and eight layers of detector. These detector layers are of the same design as for HB. The iron layers are separated by 35 mm.

Poletip Hadronic Calorimeter (HP)

The poletip hadronic calorimeters are of slightly different design to HB and HE. They lie behind the endcap electromagnetic calorimeters and give coverage of the polar region $0.91 < |\cos\theta| < 0.99$. They are made of ten layers of detector separated by nine layers of 80 mm thick iron. The gaps between the iron are just 10 mm. Unlike the other parts of HCAL, the detectors in HP are multi-wire chambers operating in high gain mode. They contain 55% CO_2 and 45% n-pentane.

2.2.6 Muon Chambers

The muon chambers, like many of the other detectors, are split into a barrel region and an endcap region. They give coverage of 93% of the solid angle, and are designed to detect muons. Muons are highly penetrating and will pass through the ECAL and HCAL. Hadrons also usually pass through ECAL, but almost never through HCAL to reach the muon chambers. The probability of a pion reaching the muon chambers is less than 0.1%, so misidentification within the muon chambers is highly unlikely.

Muon Barrel (MB)

The muon barrel [26] consists of 110 drift chambers arranged so that there are 44 chambers on either side of the OPAL detector, twelve chambers below and ten above. The side chambers are 10 m long, the top 6 m long and the bottom chambers 8.4 m long. All the chambers are 1.2 m wide and 900 mm deep. Four layers of chambers give polar angle coverage of $|\cos\theta| < 0.68$, but due to structural support, only one layer gives coverage up to $|\cos\theta| < 0.72$. The cells consist of two chambers containing 90% argon and 10% ethane. They have a z-position resolution of 2 mm and a ϕ-position resolution of 1.5 mm.

Muon Endcaps (ME)

The muon endcaps [27] cover a polar range of about $0.67 < |\cos\theta| < 0.985$ either side of the detector. Each consists of eight quadrant chambers, which are 6 m $\times$ 6 m in size, and four patch chambers, 3 m $\times$ 2.5 m in size. The chambers are filled with 75% argon and 25% isobutane and consist of two layers of limited streamer tubes. All the streamer tubes are aligned perpendicular to the beam axis. One layer has the wires in the tubes aligned

vertically and the other horizontally. The spatial resolution is ~ 2 mm.

2.2.7 Forward Detector (FD)

The forward detectors [28, 29] are situated at either end of the detector to measure very low angle particles. The FDs are in fact made up of four separate subdetectors; the main calorimeter (FK), the forward tube chambers (FB), the γ-catcher (FE) and the far forward luminosity monitor (FF). Their principle purpose ss to measure the luminosity OPAL received by identifying Bhabha events, for which the cross-section is well known.

The main calorimeter is made up of 16 azimuthal segments of lead-scintillator sandwich. Each segment has a presampler of 4 radiation lengths thickness and a main calorimeter of 20 radiation lengths. The azimuthal angular resolution is 2° and the energy resolution of FK in units of GeV is:

$$\frac{\sigma_E}{E} \simeq \frac{18\%}{\sqrt{E}} \tag{2.4}$$

The polar angle resolution ranges from 4° at the inner edge, to 10° at the outer edge. The tube chambers (FB) consist of three planes of proportional tubes, two of which are mutually perpendicular and the third at 45° to these. Information from FB is combined with that from FK to provide a more precise position measurement. Resolutions of 2 mrad can be achieved in the polar angle and a spatial resolution of 3 mm is possible.

Filling the gaps between the electromagnetic endcap and the forward calorimeter are the gamma catchers (FE). They are small annular 7 radiation length lead-scintillator calorimeters. They have an electromagnetic energy resolution of about 20%.

The far forward monitors (FF) are used to measure positions and energies of showers from electrons and positrons in the 5-10 mrad region, close to the

horizontal plane. They are also used to measure OPAL trigger rates during data taking. They consist of 20 radiation length lead-scintillator calorimeters and are stationed ±7.85 m from the interaction point.

2.2.8 The Silicon-Tungsten Calorimeter (SW)

The silicon-tungsten calorimeters [30] are situated either side of OPAL, 2.389 m in the z direction from the interaction point. They were installed in 1993 to give an improvement on the luminosity measurement. They are sampling calorimeters and consist of 19 layers of sampling silicon separated by 18 layers of tungsten. Each calorimeter is divided azimuthally into 16 wedges and can achieve a spatial resolution in r of $\sim$10 μm and an energy resolution in units of GeV of:

$$\frac{\sigma_E}{E} \simeq \frac{28\%}{\sqrt{E}} \tag{2.5}$$

2.2.9 The OPAL Trigger

As the electrons and positrons circulate around the LEP ring the OPAL detectors must be ready to detect events when they occur. The electrons and positrons circulate in several bunches which cross at a frequency of about 45 kHz. The OPAL detector is synchronised to become active when the bunches cross at its central point.

A large number of different events occur when the bunches cross, however many of them are of no interest for physics. The OPAL trigger system [31, 32] decides whether the detector should read out the event or if the subdetectors should be reset and the event ignored. The trigger has two types of signal to decide whether the event is interesting. The $\theta - \phi$ signals are made by dividing the 4π solid angle into 144 overlapping bins, 6 in θ and 24 in ϕ. The

trigger signals sent by detectors are matched to this spatial binning and then a decision can be made on the event. The second signals are stand alone signals, each subdetector has an energy and/or track count threshold, and if this threshold is breached then the event is read out.

The trigger system consists of a pre-trigger and trigger. Both combine stand alone and $\theta - \phi$ signals, however, since 1994, when LEP changed from $8 + 8$ bunch mode to $4 + 4$ bunch mode, the pre-trigger was no longer used, although it was still kept in place to minimise change. The time taken for a negative decision by the trigger is about 14.5 μs and it takes about 4.5 μs to reset the subdetectors. The trigger system reduces the 45 kHz frequency of bunch crossing to an event rate of about 10 - 15 Hz.

2.2.10 Data Acquisition

Once an event has been selected as interesting by the trigger, information about the event is read out by all the subdetectors individually. This isn't, however, the end of the story. Once the event is read out, the information from each subdetector is combined and passed into the filter [33], at which point, typically 15-35% of the selected events are rejected. Selected events are then passed to ROPE (Reconstruction of OPal Events) [34], which reconstructs the individual events using calibration constants from individual subdetectors. Information about reconstructed events is written to an optical disk as a Data Summary Table (DST). This DST is then stored on tape and disk so that it can be used in analysis.

Chapter 3

Trilinear Gauge Boson Couplings and W-Pair Production.

Within the Standard Model, the vector bosons not only couple with fermions, but they can also couple to each other in certain combinations. The coupling of three gauge bosons is known as a trilinear gauge boson interaction [35, 36]. These occur when two oppositely charged W bosons couple to a photon or Z^0 boson, as shown in figure 3.1. These are the only two possible TGC interactions in the electroweak sector. Gluons may couple with each other in many combinations.

The coupling of four gauge bosons in the electroweak sector is also possible [37, 38, 39]. There are four possible combinations within the Standard Model. The coupling of Four W bosons ($W^+W^-W^+W^-$), the coupling of two W bosons and two Z^0 bosons ($W^+W^-Z^0Z^0$), the coupling of two W bosons and two photons ($W^+W^-\gamma\gamma$), and the coupling of two W bosons a Z^0 boson and a photon ($W^+W^-Z^0\gamma$). Measurements of the quartic couplings have

been made at OPAL [40].

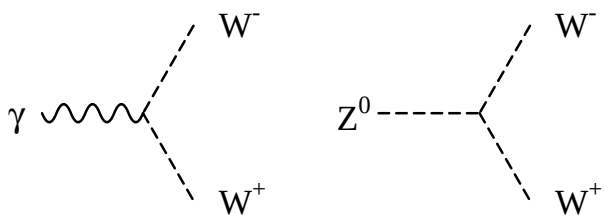

Figure 3.1: *The self coupling of three gauge bosons, known as the Trilinear Gauge Vertex.*

This thesis is only concerned with the trilinear gauge coupling of the Z^0 and γ bosons to $W^{\pm}$ bosons. In this chapter the theoretical description of the trilinear gauge coupling will be discussed. It will then be shown that the main processes at LEP containing this coupling are W-pair production processes. Accordingly all possible W-pair production processes are then discussed. This will include the identification of the role that the spin of the W bosons take in this process and the Spin Density Matrix (SDM) will be introduced. Throughout, some theoretical predictions on what observations could be made through Standard Model and non-Standard Model interactions are given.

3.1 The TGC Lagrangian

Any system is described fully by its Lagrangian. The general couplings of two charged vector bosons with a neutral vector boson can be described by the effective Lagrangian given in equation 3.1 [35, 36, 41, 42]. Where e is the positron charge and θ_w is the weak mixing angle of the Standard Model.

The Lagrangian contains 14 separate terms and each term has a coupling

parameter, indicated in red. The coupling parameters are known as the Trilinear Gauge Couplings, or TGCs. Many of the terms in the Lagrangian (3.1) would give cross sections which diverge with the energy scale, $\sqrt{s}$. This would lead to unitarity violation. As this is not possible, there then would have to be *new physics* interactions occurring to counter the effect. Thus, within the Standard Model, the values of the coupling parameters which violate unitarity are zero.

$$
\begin{aligned}
\mathcal{L}_{\mathrm{TGC}} &= ie g_1^\gamma (A_\mu(\partial_\mu W_{-\nu} - \partial_\nu W_{-\mu})W_\nu^+ - A_\mu(\partial^\mu W^{+\nu} - \partial^\nu W^{+\mu})W_\nu^-) \\
&+ ie\kappa_\gamma(\partial_\mu A_\nu - \partial_\nu A_\mu)W^{+\mu}W^{-\nu} \\
&+ ie\cot\theta_w g_1^Z (Z_\mu(\partial_\mu W_{-\nu} - \partial_\nu W_{-\mu})W_\nu^+ - Z_\mu(\partial^\mu W^{+\nu} - \partial^\nu W^{+\mu})W_\nu^-) \\
&+ ie\cot\theta_w\kappa_Z(\partial_\mu Z_\nu - \partial_\nu Z_\mu)W^{+\mu}W^{-\nu} \\
&+ ie\frac{\lambda_\gamma}{M_W^2}((\partial_\mu A_\rho - \partial_\rho A_\mu)(\partial^\rho W^{+\nu} - \partial_\nu W^{+\rho})(\partial_\nu W^{-\mu} - \partial_\mu W^{-\nu})) \\
&+ ie\cot\theta_w\frac{\lambda_Z}{M_W^2}((\partial_\mu Z_\rho - \partial_\rho Z_\mu)(\partial^\rho W^{+\nu} - \partial_\nu W^{+\rho})(\partial_\nu W^{-\mu} - \partial_\mu W^{-\nu})) \\
&- eg_4^\gamma W_\nu^+ W_\mu^-(\partial^\mu A^\nu + \partial^\nu A^\mu) \\
&- e\cot\theta_w g_4^Z W_\nu^+ W_\mu^-(\partial^\mu Z^\nu + \partial^\nu Z^\mu) \\
&+ eg_5^\gamma\epsilon_{\mu\nu\rho\sigma}((\partial^\rho W^{-\mu})W^{+\nu} - (\partial^\rho W^{+\nu})W^{-\mu})A^\sigma \\
&+ e\cot\theta_w g_5^Z\epsilon_{\mu\nu\rho\sigma}((\partial^\rho W^{-\mu})W^{+\nu} - (\partial^\rho W^{+\nu})W^{-\mu})Z^\sigma \\
&+ ie\tilde{\kappa}_\gamma W_\nu^+ W_\mu^-\frac{1}{2}\epsilon^{\mu\nu\rho\sigma}(\partial_\rho A_\sigma - \partial_\sigma A_\rho) \\
&+ ie\frac{\tilde{\lambda}_\gamma}{M_W^2}((\partial^\mu W_{+\nu} - \partial^\nu W_{+\mu})(\partial_\rho W_{-\mu} - \partial_\mu W^{-\rho})\frac{1}{2}\epsilon^{\nu\rho\sigma\ell}(\partial_\sigma A_\ell - \partial_\ell A_\sigma) \\
&+ ie\cot\theta_w\tilde{\kappa}_Z W_\nu^+ W_\mu^-\frac{1}{2}\epsilon^{\mu\nu\rho\sigma}(\partial_\rho Z_\sigma - \partial_\sigma Z_\rho) \\
&+ ie\cot\theta_w\frac{\tilde{\lambda}_Z}{M_W^2}((\partial^\mu W_{+\nu} - \partial^\nu W_{+\mu})(\partial_\rho W_{-\mu} - \partial_\mu W^{-\rho})\frac{1}{2}\epsilon^{\nu\rho\sigma\ell}(\partial_\sigma Z_\ell - \partial_\ell Z_\sigma)
\end{aligned}
\tag{3.1}
$$

The Standard Model values of the TGC parameters κ_γ, κ_z, g_1^γ and g_1^z are one, all other parameters are set to zero. This leaves the Lagrangian

shown in equation 3.2, which describes the trilinear gauge boson interaction within the Standard Model. Table 3.1 shows the properties of all the 14 TGC parameters.

$$\begin{aligned}
\mathcal{L}_{\mathrm{TGC}} &= ie(A_\mu(\partial_\mu W_{-\nu} - \partial_\nu W_{-\mu})W^+_\nu - A_\mu(\partial^\mu W^{+\nu} - \partial^\nu W^{+\mu})W^-_\nu) \\
&+ ie(\partial_\mu A_\nu - \partial_\nu A_\mu)W^{+\mu}W^{-\nu} \\
&+ ie\cot\theta_w(Z_\mu(\partial_\mu W_{-\nu} - \partial_\nu W_{-\mu})W^+_\nu - Z_\mu(\partial^\mu W^{+\nu} - \partial^\nu W^{+\mu})W^-_\nu) \\
&+ ie\cot\theta_w(\partial_\mu Z_\nu - \partial_\nu Z_\mu)W^{+\mu}W^{-\nu} \qquad (3.2)
\end{aligned}$$

The first six couplings of the Lagrangian, equation 3.1, respect the discrete parity (P) and charge (C) symmetries. The first term of the Lagrangian is for a photon coupling to two W bosons. It is called the *minimal* coupling term. The value of the g_1^γ determines the charge of the positive W boson, $\mathcal{C}_W$, in units of the positron charge, e, and therefore has a value of one, equation 3.3.

$$\mathcal{C}_W = e g_1^\gamma \qquad (3.3)$$

The second photon TGC, κ_γ is called the *anomalous* magnetic moment of the W [43, 44]. κ_γ and λ_γ are related to the magnetic dipole moment of the W^+, μ_W [45, 46], as in equation 3.4.

$$\mu_W = \frac{e}{2M_W}(1 + \kappa_\gamma + \lambda_\gamma) \qquad (3.4)$$

Both these two photon TGCs, κ_γ and λ_γ, are also related to the electric quadrupole moment of the W^+, Q_W, as in equation 3.5.

$$Q_W = -\frac{e}{M_W}(\kappa_\gamma - \lambda_\gamma) \qquad (3.5)$$

Of the remaining eight couplings, g_5^γ and g_5^z, violate both C and P symmetry, but respect combined CP-invariance. The other six couplings all violate CP. g_4^γ and g_4^z[1] violate charge conjugation symmetry. However, if g_4^γ or g_5^γ are non-vanishing at $q^2 = 0$, the photon part of the Lagrangian, equation 3.1, will not be electromagnetically gauge invariant [41].

The remaining four couplings $\tilde{\kappa}_\gamma$, $\tilde{\kappa}_z$, $\tilde{\lambda}_\gamma$ and $\tilde{\lambda}_z$ all violate parity. The photon P and CP-violating couplings, $\tilde{\kappa}_\gamma$ and $\tilde{\lambda}_\gamma$, are related to the electric dipole moment of the W^+, d_W, as in equation 3.6.

$$d_W = \frac{e}{2M_W}(\tilde{\kappa}_\gamma + \tilde{\lambda}_\gamma) \tag{3.6}$$

$\tilde{\kappa}_\gamma$ and $\tilde{\lambda}_\gamma$ are also related to the magnetic quadrupole moment, $\tilde{Q}_W$, of the W^+as follows:

$$\tilde{Q}_W = -\frac{e}{M_W}(\tilde{\kappa}_\gamma - \tilde{\lambda}_\gamma) \tag{3.7}$$

The Lagrangian given in equation 3.1 only contains the lowest dimension operators, up to dimension six. As the strength of the coupling is generally suppressed by factors like $(\sqrt{s}/\Lambda_{NP})^{d-4}$ [12], where Λ_{NP} is the scale of new physics and d is the dimension of the operator, neglecting operators of dimension higher than six is a valid assumption at LEP energies[2].

A further consequence of higher dimensional operators would be to render the photon part of the effective Lagrangian gauge invariant, even in the presence of non-vanishing, C-violating photon couplings, g_4^γ and g_5^γ [35].

[1] The coupling parameterisation given here is taken from [35]. It should be noted that the equivalent parameter to g_4^z in [36] would be $-\hat{\hat{\kappa}}_Z$.

[2] It should be noted that if the scale of new physics is less than 1 TeV, or if there is no light Higgs, then terms with higher dimensions cannot be neglected [47].

Coupling	Dim.	SM Value	C-Conserving	P-Conserving	CP-Conserving
g_1^γ, g_1^z	4	1	$\surd$	$\surd$	$\surd$
κ_γ, κ_z	4	1	$\surd$	$\surd$	$\surd$
λ_γ, λ_z	6	0	$\surd$	$\surd$	$\surd$
g_4^γ, g_4^z	6	0	$\times$	$\surd$	$\times$
g_5^γ, g_5^z	6	0	$\times$	$\times$	$\surd$
$\tilde{\kappa}_\gamma$, $\tilde{\kappa}_z$	4	0	$\surd$	$\times$	$\times$
$\tilde{\lambda}_\gamma$, $\tilde{\lambda}_z$	4	0	$\surd$	$\times$	$\times$

Table 3.1: *Properties of the 14 TGC parameters. Dim. is the dimension of the operator needed to induce each coupling.*

Constraining the Number of Parameters

Considering terms with operators up to dimension six gives the 14 TGCs in equation 3.1. However, further constraints can be made to the theory, by taking into consideration physical effects seen in other experimental data. Precise measurements made at LEP-1 on the Z^0 resonance [48, 49, 50, 51] support embedding any anomalous terms in an $SU(2)_L \times U(1)_Y$ gauge invariant structure [36].

By enforcing $SU(2)_L \times U(1)_Y$ gauge invariance and considering only operators up to dimension six [52], the TGC *New Physics* (NP) Lagrangian can be expressed in terms of the unmixed fields, the W^3B base [36, 42], as in equation 3.8.

$$\begin{aligned} \mathcal{L}_{TGC} &= g' \frac{\alpha_{B\phi}}{M_W^2} \mathcal{O}_{B\phi} + g \frac{\alpha_{W\phi}}{M_W^2} \mathcal{O}_{W\phi} + g \frac{\alpha_W}{M_W^2} \mathcal{O}_W \\ &+ \frac{gg'}{2} \frac{\tilde{\alpha}_{BW}}{M_W^2} \tilde{\mathcal{O}}_{BW} + g \frac{\tilde{\alpha}_W}{M_W^2} \tilde{\mathcal{O}}_W \end{aligned} \tag{3.8}$$

Where $e = g \sin\theta_w = g' \cos\theta_w$. The $\mathcal{O}$ are the operators capable of induc-

ing the TGC NP couplings. The explicit form of the CP-conserving operators are given by equation 3.9 and the CP-violating are given by equation 3.10

$$\begin{aligned} \mathcal{O}_{B\phi} &= iB^{\mu\nu}(D_\mu\Phi)^\dagger(D_\nu\Phi) \\ \mathcal{O}_{W\phi} &= i(D_\mu\Phi)^\dagger\boldsymbol{\tau}\cdot\mathbf{W}^{\mu\nu}(D_\nu\Phi) \\ \mathcal{O}_W &= \frac{1}{3!}(\mathbf{W}^\mu{}_\rho\times\mathbf{W}^\rho{}_\nu)\cdot\mathbf{W}^\nu{}_\mu \end{aligned} \tag{3.9}$$

$$\begin{aligned} \tilde{\mathcal{O}}_{BW} &= \Phi^\dagger\frac{\boldsymbol{\tau}}{2}\cdot\tilde{\mathbf{W}}^{\mu\nu}\Phi B_{\mu\nu} \\ \tilde{\mathcal{O}}_W &= \frac{1}{3!}(\mathbf{W}^\mu{}_\rho\times\mathbf{W}^\rho{}_\nu)\cdot\tilde{\mathbf{W}}^\nu{}_\mu \end{aligned} \tag{3.10}$$

where

$$\tilde{B}^{\mu\nu}=\frac{1}{2}\epsilon^{\mu\nu\rho\sigma}B_{\rho\sigma}\ ,\ \tilde{\mathbf{W}}^{\mu\nu}=\frac{1}{2}\epsilon^{\mu\nu\rho\sigma}\mathbf{W}_{\rho\sigma} \tag{3.11}$$

the $\boldsymbol{\tau}$ are the Pauli matrices, which represent the generators of the SU(2) group and Φ is the Higgs doublet. $B_{\mu\nu}$ is the $\mathrm{U}(1)_Y$ gauge field strength, $\mathbf{W}_{\mu\nu}$ is the $\mathrm{SU}(2)_L$ gauge field strength and D_μ is the $\mathrm{SU}(2)_L\times\mathrm{U}(1)_Y$ covariant derivative. All of these are given below, (3.12), (3.13) and (3.14).

$$B_{\mu\nu} = \partial_\mu B_\nu-\partial_\nu B_\mu \tag{3.12}$$

$$\mathbf{W}_{\mu\nu} = \partial_\mu\mathbf{W}_\nu-\partial_\nu\mathbf{W}_\mu-g\mathbf{W}_\mu\times\mathbf{W}_\nu \tag{3.13}$$

$$D_\mu = \partial_\mu+ig\frac{\boldsymbol{\tau}}{2}\cdot\mathbf{W}_\mu+ig'YB_\mu \tag{3.14}$$

In the covariant derivative, Y is the hypercharge of the field upon which D_μ is acting. The α_i parameters in equation 3.8 can then be written in terms of the TGC parameters given in equation 3.1:

$$\begin{aligned} \alpha_{W\phi} &= \cos^2\theta_w \Delta g_1^z \\ \alpha_{B\phi} &= \Delta\kappa_\gamma - \Delta g_1^z \cos^2\theta_w \\ \alpha_W &= \lambda \\ \tilde{\alpha}_{BW} &= \tilde{\kappa}_\gamma \\ \tilde{\alpha}_W &= \tilde{\lambda}_\gamma \end{aligned} \tag{3.15}$$

with the constraints:

$$\begin{aligned} \Delta\kappa_z &= \Delta g_1^z - \tan^2\theta_w \Delta\kappa_\gamma \\ \lambda &= \lambda_\gamma = \lambda_z \\ \tilde{\kappa}_z &= -\tan^2\theta_w \tilde{\kappa}_\gamma \\ \tilde{\lambda}_z &= \tilde{\lambda}_\gamma \end{aligned} \tag{3.16}$$

Where the Δ indicates the deviation from their Standard Model value, so $\Delta g_1^z = g_1^z - 1$ and $\Delta\kappa_\gamma = \kappa_\gamma - 1$.

Not all 14 TGC parameters from equation 3.1 were included in this $\mathrm{SU}(2)_L \times \mathrm{U}(1)_Y$ gauge invariant constraint. The couplings that violate charge conjugation symmetry, g_4^γ, g_5^γ and the analogous Z couplings, have been ignored. This is because, as mentioned earlier, without the intervention of higher order operators, if the photon couplings were non-vanishing at $q^2 = 0$ they would violate electromagnetic gauge invariance. However, similar constraints through $\mathrm{SU}(2)_L \times \mathrm{U}(1)_Y$ gauge symmetry can be put on the charge conjugation violating parameters [53, 54], for example, the constraint on g_4^γ and g_4^z is shown in equation 3.17.

$$g_4^z = g_4^\gamma \tag{3.17}$$

We have considered both CP-conserving and CP-violating anomalous couplings within the Lagrangian, and embedded them in a $SU(2)_L \times U(1)_Y$ gauge invariant structure. However, there is very good experimental evidence from the measurement of the neutron electric dipole moment [55, 56], against the existence of a CP-violating electromagnetic interaction. Also, bounds on the W Boson electric dipole moment [57], which is related to the CP-violating photon TGCs, equation 3.6, would suggest that the existence of an anomalous CP-violating photon TGC is unlikely. However, these measurements do not constrain the C-violating coupling, g_4^γ, as highly as they do the P-violating couplings [58]. LEP1 data also suggests that $SU(2)_L \times U(1)_Y$ symmetry holds to very high precision.

All this would then suggest that the possibility of a CP-violating TGC as highly unlikely and thus the 14 TGC parameter set can be reduced to just three parameters; $\Delta\kappa_\gamma$, Δg_1^z and λ. However, few direct limits have been placed on the CP-violating couplings. Values for all the CP-violating TGCs have been reported by the ALEPH collaboration [59, 60], and for $\tilde{\kappa}_z$ and $\tilde{\lambda}_z$ by the DELPHI collaboration [63]. Values of $\tilde{\kappa}_\gamma$ and $\tilde{\lambda}_\gamma$ have been reported by D0 collaboration from the process $p\bar{p} \to \ell\nu\gamma + X$ [61, 62]. All these sets of results do not constrain the couplings to $SU(2)_L \times U(1)_Y$ gauge invariance.

The set of couplings measured in this thesis will all require the $SU(2)_L \times U(1)_Y$ gauge symmetry constraints, but will not be constrained to CP-invariance, and so are as follows; $\Delta\kappa_\gamma$, Δg_1^z, λ, $\tilde{\kappa}_z$, $\tilde{\lambda}_z$ and g_4^z.

3.2 TGCs and W Pair Production at LEP

LEP is an electron-positron collider which has run above the W-pair production threshold since 1996. The coupling of three gauge bosons, as

shown in figure 3.1, is possible at LEP through the annihilation of the leptons into a photon or Z^0 which then decays into two W bosons (figure 3.2). There is also a third possible process with the triple gauge vertex, the t-channel process shown in figure 3.3. The first two TGC processes produce pairs of W bosons, however, the t-channel produces only one and so is, accordingly, known as the single W channel or process.

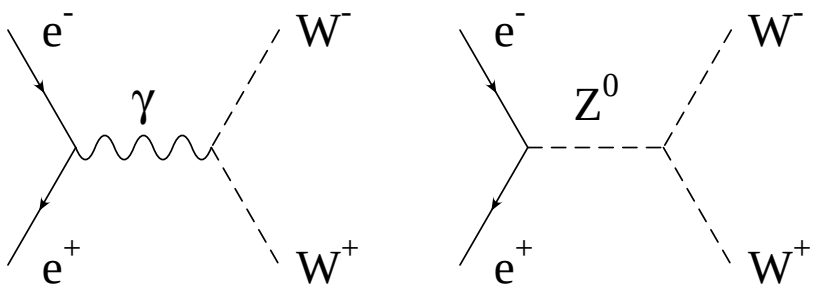

Figure 3.2: *The two W-pair production processes which contain the trilinear gauge vertex.*

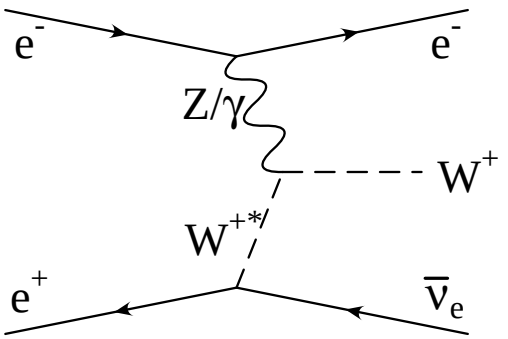

Figure 3.3: *The t-channel single W production process which contains the trilinear gauge vertex.*

There is a third channel that produces an identical final state of a pair of W bosons as the TGC W-pair production channel, but does not include the

TGC vertex. This is known as the neutrino exchange, or t-channel W-pair production channel and is shown in figure 3.4. Although the single W production has fairly different characteristics to the TGC W-pair production, and so can be separated from W-pair events, the t-channel W-pair production has very similar characteristics, therefore all three W-pair production processes have to be considered together.

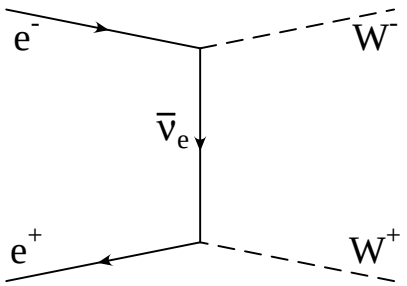

Figure 3.4: *The t-channel W-pair production process. This is the only W-pair production process at LEP that does not contain the trilinear gauge vertex.*

3.2.1 Polarisation of the W-Pair System

W bosons can have helicity ± 1 or 0. A W boson with helicity ± 1 is said to be transversely polarised and one with zero helicity is longitudinally polarised. This means that there are four possible final polarised states of the W boson pair; transverse-transverse (TT), longitudinal-longitudinal (LL), transverse-longitudinal (TL) and longitudinal-transverse (TL).

Of the final helicity combinations, all may be produced by both the s-channel and t-channel processes, except the final state where the W bosons have opposite helicity ± 1 and ∓ 1. These two final helicity states have angular momentum $J=2$ and are only accessible through the t-channel neutrino

exchange process.

It is possible to write the helicity amplitude for $e^+e^- \to W^+W^-$ in terms of the t-channel neutrino exchange process and the s-channel TGC processes, including all 14 couplings parameters. For a final helicity state $\tau\tau'$, where τ is the helicity of the W^- and τ' that of the W^+, and with initial helicity of the electron $\lambda = \pm\frac{1}{2}$, (In the limit of massless leptons, the helicity of the positron is $\lambda' = -\lambda$), the helicity amplitude is given as:

$$\begin{aligned} F_{\lambda\tau\tau'} = \; & - \frac{e^2\lambda}{2} s[C^{(\nu)}(\lambda,t) M^{(\nu)}_{\lambda\tau\tau'}(s, cos\theta_{\mathrm{W}}) \\ & + \sum_{i=1}^{7} \left(C_i^{(\gamma)}(\lambda,s) + C_i^{(\mathrm{Z})}(\lambda,s) \right) M_{i,\lambda\tau\tau'}(s, \cos\theta_{\mathrm{W}})] \end{aligned} \tag{3.18}$$

s is the square of the centre-of-mass energy and θ_W is the angle between the electron direction and the W^- direction in the centre of mass frame, known as the W production angle. t is the four-momentum transfer and is given by,

$$t = M_W^2 - \frac{1}{2} s(1 - \beta \cos\theta_{\mathrm{W}}) \tag{3.19}$$

where,

$$\beta = (1 - 4M_{\mathrm{W}}^2/s)^{\frac{1}{2}} \tag{3.20}$$

Equation 3.18 for the helicity amplitude consists of three parts. The first, denoted by superscript ν is for W-pair production through neutrino exchange. The second and third are for W-pair production through photon and Z^0 decays, and are denoted by superscript γ and Z respectively. The TGC parts are each summed over the seven possible couplings given in the Lagrangian, equation 3.1. The Cs are the terms which carry the dependence

on the coupling value and hence there are seven each for the photon and Z^0 TGCs. The Ms give the helicity composition and W production angle for each of the different coupling terms, note that these are the same for the photon and Z^0 TGC for each respective i.

The explicit expressions for each of the Cs and Ms can be calculated from the Feynman diagrams and written in terms of the couplings given in equation 3.1 [36, 41, 65]. They are shown in table 3.2, where in the Z^0 propagator, D_Z is approximated at $s > 4M_W^2$ to be:

$$D_Z \simeq s - M_Z^2 \tag{3.21}$$

and

$$a = \frac{-1 + 4\sin^2\theta_w}{4\sin\theta_w\cos\theta_w},\ b = \frac{-1}{4\sin\theta_w\cos\theta_w} \tag{3.22}$$

The first column of table 3.2 gives the Cs given in equation 3.18[3]. The first row is for the neutrino exchange process. Due to the standard V−A constraint, the first term in this row will be zero when the electron spin $\lambda = +\frac{1}{2}$.

To calculate the total amplitude for a certain helicity combination you must multiply each term in the first column with the corresponding term in the column denoted with the required helicity. Each product must be summed together, then the final sum multiplied with the term at the top of the corresponding column. For helicity combinations with $\tau' = 0$ and $\tau = \pm 1$, the last column can be used with $\tau \to \tau'$, $\tau' \to \tau$ and $\epsilon \to -\epsilon$.

So, for example, the Standard Model amplitude, $F^{\lambda}_{\tau\tau'}$, for a pair of W

[3]It should be noted that each term in column one does not directly relate to a single coupling in equation 3.1. This is because the terms in table 3.2 were derived in [41], who use a slightly different parameter set.

bosons with spin $\tau = \tau' = +1$, with the initial electron spin $\lambda = -\frac{1}{2}$, would be:

$$\begin{aligned} F^{\frac{1}{2}}_{+1,+1} &= \frac{e^2 s}{2} \sin\theta_{\mathrm{W}} \left[(\frac{-2}{4t \sin^2\theta_w})(\cos\theta_{\mathrm{W}} - \beta) \right. \\ &+ \left. (\frac{-2}{s} + \frac{2\cot\theta_w}{D_Z}(a+b))(-\beta) \right] \end{aligned} \tag{3.23}$$

The equivalent term for an initial electron spin of $\lambda = +\frac{1}{2}$ is as in equation 3.24. Notice how the terms due to the neutrino exchange are now absent due to the fact that right handed neutrinos cannot be produced.

$$F^{-\frac{1}{2}}_{+1,+1} = \frac{-e^2 s}{2} \sin\theta_{\mathrm{W}} \left[(\frac{-2}{s} + \frac{2\cot\theta_w}{D_Z}(a-b))(-\beta) \right] \tag{3.24}$$

Another important thing to note from table 3.2 is the column for W boson helicities $\tau = -\tau' = \pm 1$, this shows explicitly that these combinations can only be produced via the neutrino exchange process.

The W-pair production differential cross-section due to both the neutrino exchange and the TGC channels can be written in terms of the helicity amplitudes:

$$\frac{d\sigma(\mathrm{e^+e^-} \to \mathrm{W^+W^-})}{d\cos\theta_{\mathrm{W}}} = \frac{|\vec{P}|}{16\pi s\sqrt{s}} \sum_{\lambda\tau\tau'} \left| F^{\lambda}_{\tau\tau'} \right|^2 \ , \tag{3.25}$$

where the $\mathrm{W}^{\pm}$ centre-of-mass momentum $|\vec{P}| = \sqrt{s/4 - M^2_{\mathrm{W}}}$.

As well as the total cross-section, predictions about the polarised cross-sections can also be made, for example, the production of pairs of transverse W bosons σ_{TT}. Figure 3.5 shows how the total cross-section and the total polarised cross-sections behave as a function of centre-of-mass energy, $\sqrt{s}$. The range is from the threshold of W-pair production, through the energy range of LEP-2 (162-202 GeV), and beyond.

	$\tau=\tau'=\pm1$	$\tau=-\tau'=\pm1$	$\tau=\tau'=0$	$\tau=0,\tau'=\pm1,\epsilon=+1$
	$\frac{-e^2s\lambda}{2}\sin\theta_W$	$\frac{-e^2s\lambda}{2}\sin\theta_W$	$\frac{-e^2s\lambda}{2}\sin\theta_W$	$\frac{-e^2s\lambda}{2\sqrt{2}}(\tau'\cos\theta_W-2\lambda)$
$\frac{2\lambda-1}{4t\sin^2\theta_w}$	$\cos\theta_W-\beta$	$-\cos\theta_W-2\tau\lambda$	$\frac{s}{2M_W^2}[\cos\theta_W-\beta(1+\frac{2M_W^2}{s})]$	$\frac{\sqrt{s}[\cos\theta_W(1+\beta^2)-2\beta]}{2M_W}-\frac{2M_W\tau'\sin^2\theta_W}{\sqrt{s}(\tau'\cos\theta_W-2\lambda)}$
$\frac{-2(1+\Delta g_1^\gamma)}{s}+\frac{2\cot\theta_w(1+\Delta g_1^Z)}{D_Z}(a-2b\lambda)$	$-\beta$	0	$-\beta(1+\frac{s}{2M_W^2})$	$-\beta\frac{\sqrt{s}}{M_W}$
$\frac{-\Delta\kappa_\gamma}{s}+\frac{\cot\theta_w(\Delta\kappa_Z-\Delta g_1^Z)(a-2b\lambda)}{D_Z}$	0	0	$-\beta\frac{s}{M_W^2}$	$-\beta\frac{\sqrt{s}}{M_W}$
$\frac{-\lambda_\gamma}{s}+\frac{\cot\theta_w\Delta\lambda_Z(a-2b\lambda)}{D_Z}$	$-\beta\frac{s}{M_W^2}$	0	0	$-\beta\frac{\sqrt{s}}{M_W}$
$\frac{g_5^\gamma}{s}-\frac{\cot\theta_w g_5^Z(a-2b\lambda)}{D_Z}$	0	0	0	$\beta^2\tau'(\frac{\sqrt{s}}{M_W})^3$
$\frac{ig_4^\gamma}{s}-\frac{i\cot\theta_w g_4^Z(a-2b\lambda)}{D_Z}$	0	0	0	$-\beta^2\epsilon\frac{\sqrt{s}}{M_W}$
$\frac{-i\tilde{\kappa}_\gamma-\tilde{\lambda}_\gamma}{s}+\frac{i\cot\theta_w(\tilde{\kappa}_Z-\tilde{\lambda}_Z)(a-2b\lambda)}{D_Z}$	2τ	0	0	$\tau'\epsilon\frac{\sqrt{s}}{M_W}$
$\frac{i\tilde{\lambda}_\gamma}{2s}-\frac{i\cot\theta_w\tilde{\lambda}_Z(a-2b\lambda)}{2D_Z}$	$2\tau\beta^2\frac{s}{M_W^2}$	0	0	0

Table 3.2: *The elements needed to construct the helicity amplitudes for the W-pair production process.*

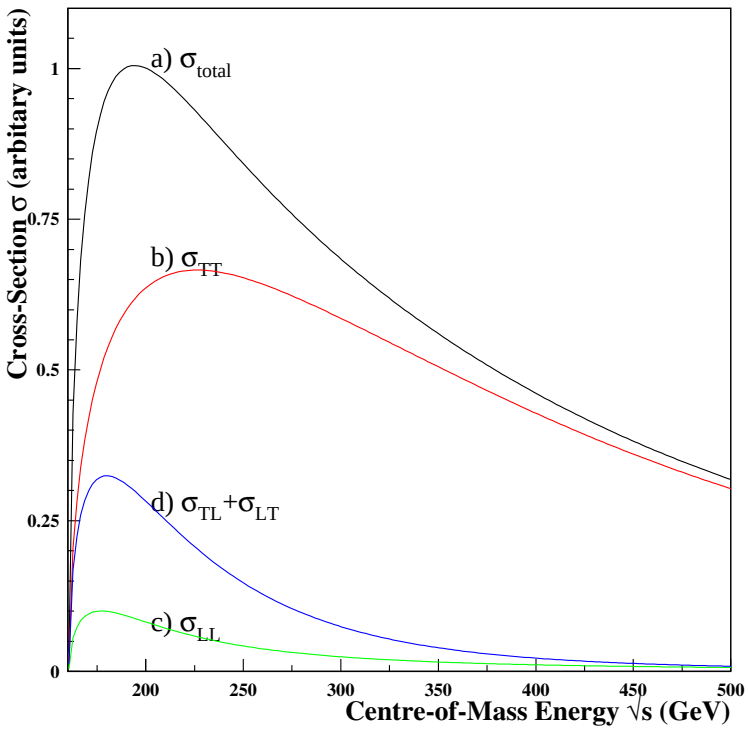

Figure 3.5: *The Standard Model total production cross-section for W pairs as a function of centre-of-mass energy. Also shown is the total cross-section for the production of W-pairs with different polarisation states. Transverse-transverse (TT), longitudinal-longitudinal (LL) and transverse-longitudinal (TL+LT).*

It can be seen that the total cross-section and each for the different polarisation states rise rapidly from the threshold value, however, they all peak at different values of $\sqrt{s}$, with the total cross-section for W-pair production peaking at about 200 GeV. From table 3.2, it can be shown that the cross-section for transverse-longitudinal (TL) W-pairs is always equal to that of longitudinal-transverse (LT) W-pairs, even in the presence of anomalous couplings.

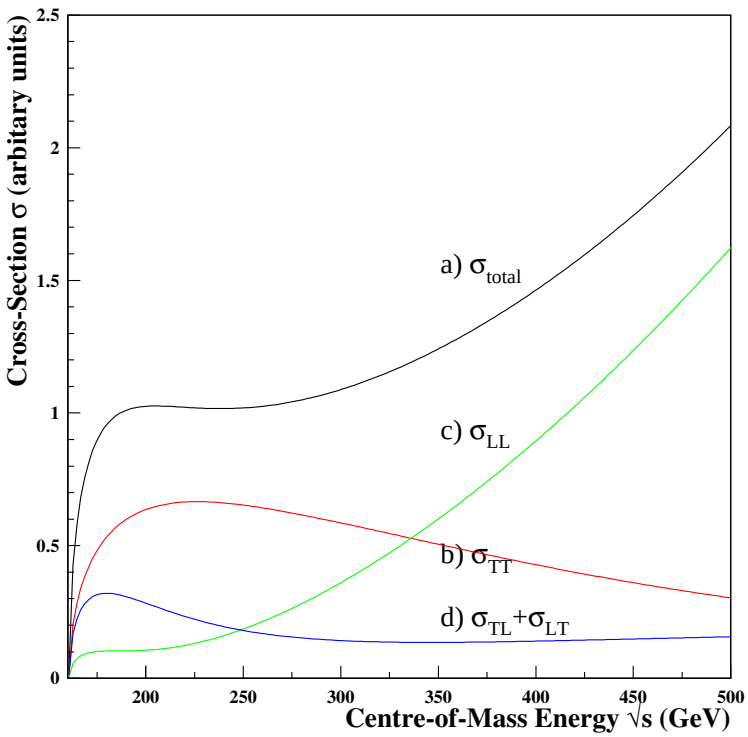

Figure 3.6: *The total production cross-section for W pair production as a function of centre-of-mass energy in the presence of the anomalous TGC* $\Delta\kappa_\gamma$*=+1. Also shown is the total cross-section for the production of W-pairs with different polarisation states.*

Figure 3.6 shows the total cross-sections as a function of centre-of-mass energy in the presence of an anomalous coupling of $\Delta\kappa_\gamma$=+1. The cross-section *blows-up* with energy, which would violate unitarity unless some non-Standard Model process occurs at some higher energy value, Λ_{NP}. With a non-zero value of $\Delta\kappa_\gamma$, as the centre-of-mass energy increases the W-pairs produced become almost entirely longitudinally polarised, so the dominant polarisation state becomes LL. With the presence of any of the anomalous couplings, as $\sqrt{s}$ is increased, the polarisation of the W-pairs becomes dominated by just one of the polarisation states. Some of the polarisation states are completely insensitive to certain anomalous couplings. Table 3.3 shows which polarisation states are sensitive to which anomalous couplings and which state dominates when $\sqrt{s}$ becomes large.

Coupling	Δg_1^z	$\Delta\kappa_\gamma$	λ	g_5^z	g_4^z	$\tilde{\kappa}_z$	$\tilde{\lambda}_z$
TT	$\surd$	$\times$	$\surd_D$	$\times$	$\times$	$\surd$	$\surd_D$
LL	$\surd_D$	$\surd_D$	$\times$	$\times$	$\times$	$\times$	$\times$
TL	$\surd$	$\surd$	$\surd$	$\surd_D$	$\surd_D$	$\surd_D$	$\times$

Table 3.3: *Table showing which final helicity states are sensitive to each anomalous coupling. A tick indicates that the final state is sensitive to the corresponding coupling. The subscript D indicates which helicity state becomes dominant at very high energy in the presence of the corresponding anomalous coupling.*

Plots of the differential cross-section of W-pair production as a function of the W production angle have been made at centre-of-mass energy 189 GeV, as this corresponds to the data sample considered in this thesis. Figure 3.7 shows the total differential cross-sections and polarised differential

cross-sections for the Standard Model and anomalous C and P-conserving couplings. The anomalous couplings have been set at values ±1.

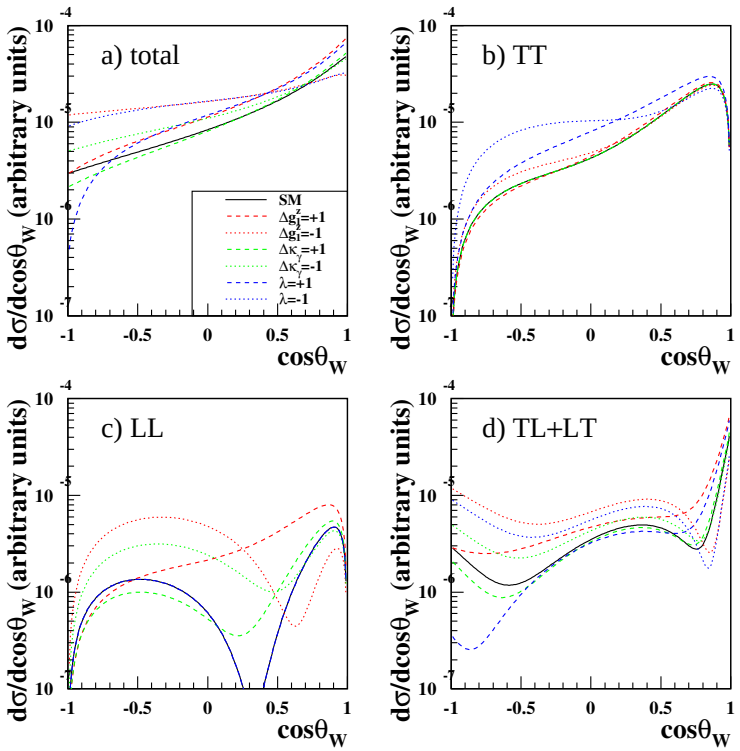

Figure 3.7: *The differential cross-section of W-pair production as a function of the* W^- *production angle,* $\cos\theta_W$*, at 189 GeV. Shown is the case for the Standard Model and also with various CP-conserving anomalous couplings implemented.*

Figure 3.8 shows the total differential cross-sections and polarised differential cross-sections for the Standard Model and anomalous CP-violating couplings. The anomalous couplings have been set at values ±1.

Figures 3.7 and 3.8 show explicitly the observations made in table 3.3, which were derived by looking at table 3.2. It immediately can be seen that

the LL differential cross-section is insensitive to λ and all the CP-violating couplings. TT is insensitive to $\Delta\kappa_\gamma$ and g_4^z. For the CP-violating couplings the negative coupling has an identical effect as the positive coupling.

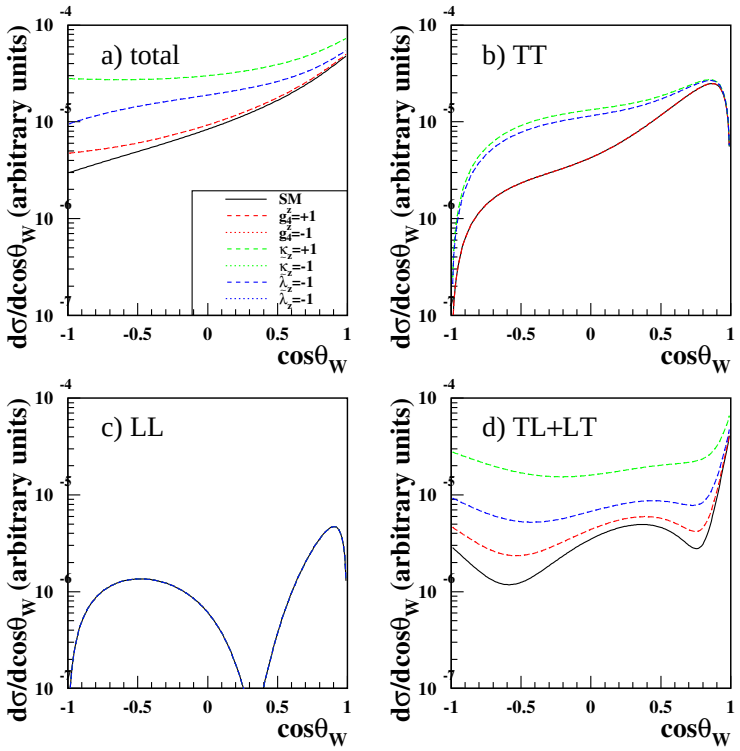

Figure 3.8: *The differential cross-section of W-pair production as a function of the* W^- *production angle,* $\cos\theta_W$*, at 189 GeV. Shown is the case for the Standard Model and also with various CP-violating anomalous couplings implemented.*

By integrating over $\cos\theta_W$, the fraction of TT, LL and TL+LT W-pairs can be calculated. This has been done for figures 3.7 and 3.8 and the results are displayed in table 3.4. Also shown in this table is the proportion of each helicity state at a much higher energy than LEP-2 has run at. This is to

indicate once again which helicity state dominates the total cross-section.

Coupling	189 GeV			1 TeV		
	TT	LL	LT+TL	TT	LL	LT+TL
SM	0.593	0.094	0.313	0.975	0.007	0.019
$\Delta g_1^z = +1$	0.448	0.165	0.385	0.008	0.901	0.091
$\Delta g_1^z = -1$	0.426	0.181	0.393	0.008	0.901	0.091
$\Delta\kappa_\gamma = +1$	0.589	0.103	0.308	0.010	0.966	0.024
$\Delta\kappa_\gamma = -1$	0.516	0.152	0.332	0.010	0.965	0.026
$\lambda = +1$	0.653	0.071	0.276	0.988	0.000	0.012
$\lambda = -1$	0.609	0.067	0.334	0.987	0.000	0.013
$g_4^z = \pm 1$	0.542	0.085	0.372	0.149	0.003	0.848
$\tilde{\kappa}_z = \pm 1$	0.383	0.033	0.584	0.045	0.001	0.954
$\tilde{\lambda}_z = \pm 1$	0.567	0.054	0.379	0.987	0.000	0.013

Table 3.4: *The fraction of W-pairs with each polarisation state for the Standard Model, and with various anomalous couplings implemented. The first column is at* $\sqrt{s} = 189$ *GeV and the second is at* $\sqrt{s} = 1$ *TeV.*

3.3 W Boson Decays

As W bosons are massive vector bosons they only have a very short lifetime. This means that within the OPAL detector the W-bosons are never directly observed, only their decay products are measured. W bosons decay into two fermions. A W^-can decay into a lepton and anti-neutrino or a quark anti-quark pair. The branching ratios for each of these decays have been measured at OPAL from the W-pair production process [66], and is found to agree well with theoretical predictions [12] for the Standard Model and the

world average [5]. The branching ratios calculated from all data collected at OPAL, assuming lepton universality to calculate the $q\bar{q}$ branching ratio, is given below. In each case the first error is statistical and the second systematic.

$$\begin{aligned}
\mathrm{Br}(W \to e\bar{\nu}_e) &= 0.1046 \pm 0.0042 \pm 0.0014, \\
\mathrm{Br}(W \to \mu\bar{\nu}_\mu) &= 0.1050 \pm 0.0041 \pm 0.0012, \\
\mathrm{Br}(W \to \tau\bar{\nu}_\tau) &= 0.1075 \pm 0.0052 \pm 0.0021, \\
\mathrm{Br}(W \to q\bar{q}) &= 0.6832 \pm 0.0061 \pm 0.0028.
\end{aligned}$$

With each W boson being able to decay into a lepton and neutrino or two quarks, this means that there are effectively three possible final states; Two leptons and two neutrinos, $\ell\bar{\nu}_\ell\bar{\ell}\nu_\ell$, known as the leptonic channel. Two quarks and two anti-quarks, $q\bar{q}q\bar{q}$, known as the hadronic channel. Finally there is a final state of a lepton, a neutrino, a quark and an anti-quark, $\ell\bar{\nu}_\ell q\bar{q}$, known as the semi-leptonic channel. The branching ratios for these three channels given in [12] are, 45.6%, 10.5% and 43.9% respectively.

As the decay of W bosons into fermions has been well studied and understood and is believed to proceed via the standard V−A coupling, it is possible to predict the angular distribution of the decay fermions if the helicity of the W boson is known. The dependence of the angular distribution of the fermions, in the W boson rest frame, on the helicity of the W boson are given by the so called D-functions [36]. The explicit form of these D-functions is given in equation 3.26, where $D_{\tau'\tau}(\theta^*, \phi^*) = D^*_{\tau\tau'}(\theta^*, \phi^*)$.

$$
\begin{aligned}
D_{++} &= \frac{1}{2}(1+\cos^2\theta^*) - \cos\theta^* \\
D_{--} &= \frac{1}{2}(1+\cos^2\theta^*) + \cos\theta^* \\
D_{00} &= \sin^2\theta^* \\
D_{+-} &= \frac{1}{2}\sin^2\theta^* \mathrm{e}^{+2i\phi^*} \\
D_{+0} &= +\frac{1}{2}\sqrt{2}\sin\theta^*(\cos\theta^* - 1)\mathrm{e}^{+i\phi^*} \\
D_{-0} &= -\frac{1}{2}\sqrt{2}\sin\theta^*(\cos\theta^* - 1)\mathrm{e}^{-i\phi^*}
\end{aligned}
\tag{3.26}
$$

In the above equations θ^* is the polar angle of the decay fermion in the W rest frame and ϕ^* is the azimuthal angle of the decay fermion in the W rest frame, as illustrated in figure 3.9.

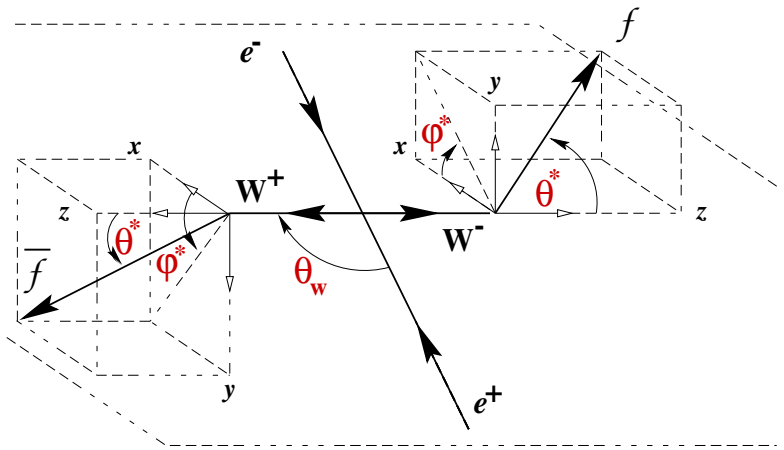

Figure 3.9: *Production and decay angles of W bosons.*

Knowing how the decay fermions couple to the W bosons of different helicity and also how the W bosons are produced in the W-pair through the helicity amplitudes, (3.18), an analytical expression for the differential cross-section of the process $\mathrm{e}^+\mathrm{e}^- \to \mathrm{W}^+\mathrm{W}^- \to f_1\bar{f}_2 f_3 \bar{f}_4$ may be written,

(3.27). Where θ_{f_1} and ϕ_{f_1} are the W^- decay angles analogous to θ^* and ϕ^* respectively. $\theta_{\bar{f}_4}$ and $\phi_{\bar{f}_4}$ are the W^+ decay angles analogous to θ^* and ϕ^* respectively. $\mathrm{Br}(X \to a\bar{b})$ denotes the branching ratio for that process.

$$\begin{aligned}
&\frac{d\sigma(e^+e^- \to W^+W^- \to f_1\bar{f}_2 f_3 \bar{f}_4)}{d\cos\theta_W d\cos\theta_{f_1} d\phi_{f_1} d\cos\theta_{\bar{f}_4} d\phi_{\bar{f}_4}} = \\
&\mathrm{Br}(W^- \to f_1\bar{f}_2)\mathrm{Br}(W^+ \to f_3\bar{f}_4)\frac{|\vec{P}|}{16\pi s\sqrt{s}}\left(\frac{3}{8\pi}\right)^2 \\
\times &\sum_{\lambda\tau_1\tau'_1\tau_2\tau'_2} \left[F^{\lambda}_{\tau_1\tau_2}(s,\cos\theta_W)\right]\left[F^{\lambda}_{\tau'_1\tau'_2}(s,\cos\theta_W)\right]^* \\
\times &\; D_{\tau_1\tau'_1}(\theta_{f_1},\phi_{f_1}) D_{\tau_2\tau'_2}(\pi-\theta_{\bar{f}_4},\phi_{\bar{f}_4}+\pi)
\end{aligned} \tag{3.27}$$

This equation is the differential cross-section in terms of the W^- production angle, $\cos\theta_W$, the production angles of the particle from the W^- decay in the W^- rest frame, θ_{f_1}, ϕ_{f_1}, and the production angles of the anti-particle from the W^+ decay in the W^+ rest frame, $\theta_{\bar{f}_4}$, $\phi_{\bar{f}_4}$. Thus it is known as the 5-fold differential cross-section.

With a final state of four fermions all the possible final helicity states interfere with one another, so it is no longer meaningful to speak of TT, LL or TL final helicity states. The subscripts on the D-functions, shown in equation 3.26, do not indicate the spins of the two separate W bosons, but rather are both for a single W boson. In the 5-fold differential cross-section the helicity amplitude is multiplied by the complex conjugate of another helicity amplitude which has different subscripts. The τ_1 and τ'_1 both refer to the W^- and so it can be seen that the first D-function relates to the W^-, and intuitively the second D-function must relate to the W^+. As the sum runs over all four τs this immediately implies there must now be 81 terms for each λ helicity in the sum, rather than the nine seen in equation 3.25.

Upon integration of the D-functions over the W decay angles the following

is obtained:

$$\int_{-1}^{+1}\int_{0}^{2\pi} D_{\tau\tau'}(\theta_f\phi_f)d\cos\theta_f d\phi_f = 2\pi\frac{4}{3}\delta_{\tau\tau'} \tag{3.28}$$

Integrating the 5-fold differential cross-section over both the W^- and W^+ decay angles will thus retrieve the W-pair production cross-section as given in equation 3.25.

3.4 Polarisation Properties

3.4.1 The Two-Particle Joint Spin Density Matrix

The polarisation properties of the $W^\pm$ bosons in the W-pair are completely described by the two-particle joint spin density matrix (SDM) [36, 41], whose elements are given by:

$$\rho_{\tau_1\tau'_1\tau_2\tau'_2}(s,\cos\theta_W) \equiv \frac{\sum_\lambda \left(F^\lambda_{\tau_1\tau_2}(s,\cos\theta_W)\right)\left(F^\lambda_{\tau'_1\tau'_2}(s,\cos\theta_W)\right)^*}{\sum_{\lambda\tau_1\tau_2}\left|F^\lambda_{\tau_1\tau_2}(s,\cos\theta_W)\right|^2} \tag{3.29}$$

The diagonal elements of the two-particle joint spin density matrix, which have $\tau_1 = \tau'_1$ and $\tau_2 = \tau'_2$ sum up to unity, i.e. the matrix has normalisation:

$$\sum_{\tau_1\tau_2}\rho_{\tau_1\tau_1\tau_2\tau_2}(s,\cos\theta_W) = 1 \tag{3.30}$$

This normalisation occurs because the diagonal elements are effectively the probability of producing a pair of W bosons with helicity state $\tau_1\tau_2$. The off-diagonal elements are complex, but the diagonal elements are always purely real. The matrix elements are functions of both the centre-of-mass energy squared, s, and the W production angle, $\cos\theta_W$. Examples of the

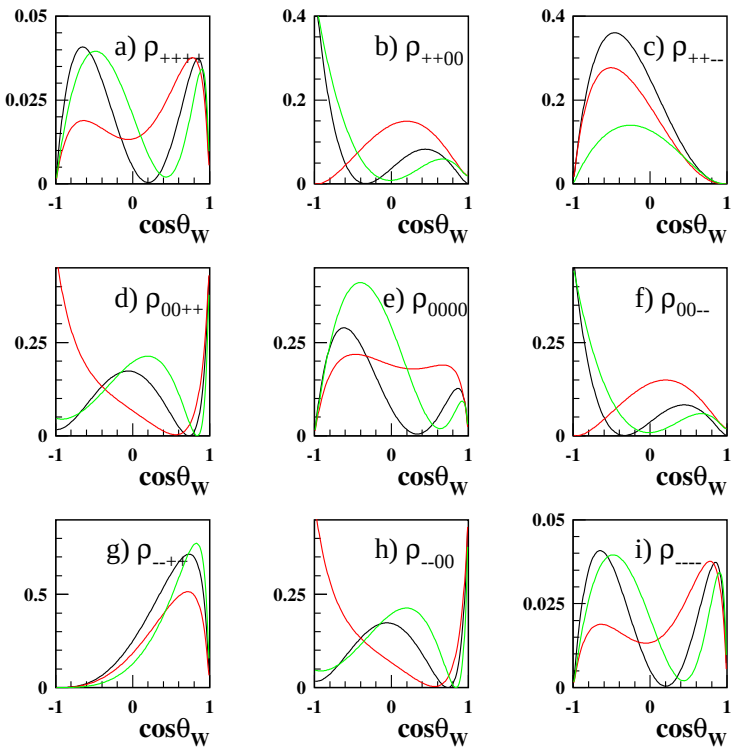

Figure 3.10: *Examples of the diagonal elements of the two-particle joint W Spin Density Matrix. The black line is the Standard Model case and the red (green) line is for an anomalous coupling of* $\Delta g_1^z = +1$ *(*-1*).*

analytical predictions for the diagonal elements as a function of $\cos\theta_{\mathrm{W}}$ can be seen in figure 3.10.

The two-particle joint density matrix is Hermitian and contains 81 elements. This means that, due to the normalisation given in equation 3.30, 80 of the elements are independent. However, if the W-pair production interaction is said to be CP-invariant, the helicity amplitudes fulfill the following relation:

$$F^{\lambda}_{\tau_1\tau_2}(s,\cos\theta_{\mathrm{W}}) = F^{\lambda}_{-\tau_2-\tau_1}(s,\cos\theta_{\mathrm{W}}) \tag{3.31}$$

A consequence of enforcing CP-invariance upon the reaction is to reduce the number of independent elements in the density matrix from 80 to 35. This is demonstrated in table 3.5, where the combinations of helicity amplitudes, and thus the SDM elements, that are equivalent due to CP-invariance are grouped into 36 sets.

As the two-particle joint density matrix contains all the information about the polarisation of the W bosons, the 5-fold differential cross-section given in equation 3.27 can now be written in terms of the joint density matrix, equation 3.32.

$$\begin{aligned}
&\frac{d\sigma(\mathrm{e^+e^-}\to\mathrm{W^+W^-}\to f_1\bar{f}_2 f_3\bar{f}_4)}{d\cos\theta_{\mathrm{W}}\, d\cos\theta_{f_1}\, d\phi_{f_1}\, d\cos\theta_{\bar{f}_4}\, d\phi_{\bar{f}_4}} \\
= \;& \frac{d\sigma(\mathrm{e^+e^-}\to\mathrm{W^+W^-})}{d\cos\theta_{\mathrm{W}}}\left(\frac{3}{8\pi}\right)^2 \\
\times \;& \sum_{\lambda\tau_1\tau'_1\tau_2\tau'_2} \rho_{\tau_1\tau'_1\tau_2\tau'_2}(s,\cos\theta_{\mathrm{W}}) D_{\tau_1\tau'_1}(\theta_{f_1},\phi_{f_1}) D_{\tau_2\tau'_2}(\pi-\theta_{\bar{f}_4},\phi_{\bar{f}_4}+\pi)
\end{aligned} \tag{3.32}$$

The density matrix contains the probability of producing W-pairs of certain helicity states so the differential polarised cross-sections for producing final states of two transversely polarised W bosons (TT), two longitudinally polarised W bosons (LL), a transversely polarised $\mathrm{W^-}$ boson with a longitudinally polarised polarised $\mathrm{W^+}$ boson (TL) and a transversely polarised $\mathrm{W^-}$ boson with a longitudinally polarised polarised $\mathrm{W^+}$ boson (LT) can be written in terms of the elements in the joint density matrix [41], as shown in equation 3.33.

SET	AMPLITUDE COMBINATIONS	SDM ELEMENTS	NO.
1	$F_{++}F^*_{++}$, $F_{--}F^*_{++}$, $F_{--}F^*_{--}$, $F_{++}F^*_{--}$	ρ_{++++}, ρ_{--+-}, ρ_{----}, ρ_{+-+-}	4
2	$F_{++}F^*_{+0}$, $F_{--}F^*_{+0}$, $F_{--}F^*_{0-}$, $F_{++}F^*_{0-}$	ρ_{+++0}, ρ_{--+0}, ρ_{0---}, ρ_{+0+-}	4
3	$F_{++}F^*_{+-}$, $F_{--}F^*_{+-}$	ρ_{+++-}, ρ_{-+--}	2
4	$F_{++}F^*_{0+}$, $F_{--}F^*_{0+}$, $F_{--}F^*_{-0}$, $F_{++}F^*_{-0}$	ρ_{+0++}, ρ_{-0-+}, ρ_{---0}, ρ_{+-+0}	4
5	$F_{++}F^*_{00}$, $F_{--}F^*_{00}$	ρ_{+0+0}, ρ_{-0-0}	2
6	$F_{++}F^*_{-+}$, $F_{--}F^*_{-+}$	ρ_{+-++}, ρ_{---+}	2
7	$F_{+0}F^*_{++}$, $F_{0-}F^*_{++}$, $F_{0-}F^*_{--}$, $F_{+0}F^*_{--}$	ρ_{++0+}, ρ_{0+-+}, ρ_{0---}, ρ_{+-0-}	4
8	$F_{+0}F^*_{+0}$, $F_{0-}F^*_{+0}$, $F_{0-}F^*_{0-}$, $F_{+0}F^*_{0-}$	ρ_{++00}, ρ_{0+-0}, ρ_{00--}, ρ_{+00-}	4
9	$F_{+0}F^*_{+-}$, $F_{0-}F^*_{+-}$	ρ_{++0-}, ρ_{0+--}	2
10	$F_{+0}F^*_{0+}$, $F_{0-}F^*_{0+}$, $F_{0-}F^*_{-0}$, $F_{+0}F^*_{-0}$	ρ_{+00+}, ρ_{00-+}, ρ_{0--0}, ρ_{+-00}	4
11	$F_{+0}F^*_{00}$, $F_{0-}F^*_{00}$	ρ_{+000}, ρ_{00-0}	2
12	$F_{+0}F^*_{-+}$, $F_{0-}F^*_{-+}$	ρ_{+-0+}, ρ_{0--+}	2
13	$F_{+-}F^*_{++}$, $F_{+-}F^*_{--}$	ρ_{++-+}, ρ_{+---}	2
14	$F_{+-}F^*_{+0}$, $F_{+-}F^*_{0-}$	ρ_{++-0}, ρ_{+0--}	2
15	$F_{+-}F^*_{+-}$	ρ_{++--}	1
16	$F_{+-}F^*_{0+}$, $F_{+-}F^*_{-0}$	ρ_{+0-+}, ρ_{+--0}	2
17	$F_{+-}F^*_{00}$	ρ_{+0-0}	1
18	$F_{+-}F^*_{-+}$	ρ_{+--+}	1
19	$F_{0+}F^*_{++}$, $F_{-0}F^*_{++}$, $F_{-0}F^*_{--}$, $F_{0+}F^*_{--}$	ρ_{0+++}, ρ_{-+0+}, ρ_{--0-}, ρ_{0-+-}	4
20	$F_{0+}F^*_{+0}$, $F_{-0}F^*_{+0}$, $F_{-0}F^*_{0-}$, $F_{0+}F^*_{0-}$	ρ_{0++0}, ρ_{-+00}, ρ_{-00-}, ρ_{00+-}	4
21	$F_{0+}F^*_{+-}$, $F_{-0}F^*_{+-}$	ρ_{0++-}, ρ_{-+0-}	2
22	$F_{0+}F^*_{0+}$, $F_{-0}F^*_{0+}$, $F_{-0}F^*_{-0}$, $F_{0+}F^*_{-0}$	ρ_{00++}, ρ_{-00+}, ρ_{--00}, ρ_{0-+0}	4
23	$F_{0+}F^*_{00}$, $F_{-0}F^*_{00}$	ρ_{00+0}, ρ_{-000}	2
24	$F_{0+}F^*_{-+}$, $F_{-0}F^*_{-+}$	ρ_{0-++}, ρ_{--0+}	2
25	$F_{00}F^*_{++}$, $F_{00}F^*_{--}$	ρ_{0+0+}, ρ_{0-0-}	2
26	$F_{00}F^*_{+0}$, $F_{00}F^*_{0-}$	ρ_{0+00}, ρ_{000-}	2
27	$F_{00}F^*_{+-}$	ρ_{0+0-}	1
28	$F_{00}F^*_{0+}$, $F_{00}F^*_{-0}$	ρ_{000+}, ρ_{0-00}	2
29	$F_{00}F^*_{00}$	ρ_{0000}	1
30	$F_{00}F^*_{-+}$	ρ_{0-0+}	1
31	$F_{-+}F^*_{++}$, $F_{-+}F^*_{--}$	ρ_{-+++}, ρ_{--+-}	2
32	$F_{-+}F^*_{+0}$, $F_{-+}F^*_{0-}$	ρ_{-++0}, ρ_{-0+-}	2
33	$F_{-+}F^*_{+-}$	ρ_{-++-}	1
34	$F_{-+}F^*_{0+}$, $F_{-+}F^*_{-0}$	ρ_{-0++}, ρ_{--+0}	2
35	$F_{-+}F^*_{00}$	ρ_{-0+0}	1
36	$F_{-+}F^*_{-+}$	ρ_{--++}	1
		TOTAL	81

Table 3.5: *The helicity amplitudes and thus the Spin Density Matrix elements that are related under CP-invariance. The helicity amplitude combinations in each set are equivalent to each other under CP-invariance. The SDM elements are those that correspond to each helicity amplitude combination. CP-invariance thus means that there are only 35 independent SDM elements.*

$$\begin{aligned}
\frac{d\sigma_{\mathrm{TT}}}{d\cos\theta_{\mathrm{W}}} = \frac{d\sigma(\mathrm{e^+e^-} \to \mathrm{W_T^-W_T^+})}{d\cos\theta_{\mathrm{W}}} &= \frac{d\sigma}{d\cos\theta_{\mathrm{W}}}\left(\rho_{++++} + \rho_{++--} + \rho_{--++} + \rho_{----}\right) \\
\frac{d\sigma_{\mathrm{LL}}}{d\cos\theta_{\mathrm{W}}} = \frac{d\sigma(\mathrm{e^+e^-} \to \mathrm{W_L^-W_L^+})}{d\cos\theta_{\mathrm{W}}} &= \frac{d\sigma}{d\cos\theta_{\mathrm{W}}}\left(\rho_{0000}\right) \\
\frac{d\sigma_{\mathrm{TL}}}{d\cos\theta_{\mathrm{W}}} = \frac{d\sigma(\mathrm{e^+e^-} \to \mathrm{W_T^-W_L^+})}{d\cos\theta_{\mathrm{W}}} &= \frac{d\sigma}{d\cos\theta_{\mathrm{W}}}\left(\rho_{++00} + \rho_{--00}\right) \\
\frac{d\sigma_{\mathrm{LT}}}{d\cos\theta_{\mathrm{W}}} = \frac{d\sigma(\mathrm{e^+e^-} \to \mathrm{W_L^-W_T^+})}{d\cos\theta_{\mathrm{W}}} &= \frac{d\sigma}{d\cos\theta_{\mathrm{W}}}\left(\rho_{00++} + \rho_{00--}\right)
\end{aligned} \tag{3.33}$$

From figure 3.10 it can be seen that $\rho_{++00} + \rho_{--00} = \rho_{00++} + \rho_{00--}$, even in the presence of anomalous couplings[4], so it intuitively follows that, as was stated earlier,

$$\frac{d\sigma_{\mathrm{TL}}}{d\cos\theta_{\mathrm{W}}} = \frac{d\sigma_{\mathrm{LT}}}{d\cos\theta_{\mathrm{W}}} \tag{3.34}$$

3.4.2 The Single W Spin Density Matrix

If only one of the W bosons in the W-pair is considered then the differential cross-section can then be written in terms of the single W Spin Density Matrix (SDM) [36, 41]. For example, if only the $\mathrm{W^-}$boson is considered,

$$\begin{aligned}
&\frac{d\sigma(\mathrm{e^+e^-} \to \mathrm{W^+W^-} \to \mathrm{W^+} + f_1\bar{f}_2)}{d\cos\theta_{\mathrm{W}} d\cos\theta_{f_1} d\phi_{f_1}} \\
&= \frac{d\sigma(\mathrm{e^+e^-} \to \mathrm{W^+W^-})}{d\cos\theta_{\mathrm{W}}}\left(\frac{3}{8\pi}\right)\sum_{\tau_1\tau'_1}\rho^{W^-}_{\tau_1\tau'_1}(s,\cos\theta_{\mathrm{W}})D_{\tau_1\tau'_1}(\theta_{f_1}\phi_{f_1})
\end{aligned} \tag{3.35}$$

Equation 3.35 is known as the 3-fold differential cross-section. The single W SDM completely describes the polarisation properties of one of the W bosons when the helicity of the other W boson has been effectively summed

[4]This holds true even if the anomalous coupling is CP-violating.

over. So the single W SDM is related to the two-particle joint density matrix as follows,

$$\rho^{W^-}_{\tau_1\tau'_1}(s,\cos\theta_{\rm W}) \equiv \sum_{\tau_2} \rho_{\tau_1\tau'_1\tau_2\tau_2}(s,\cos\theta_{\rm W}) \tag{3.36}$$

Like the two-particle joint SDM, the single W SDM has purely real diagonal elements and complex off-diagonal elements. The single W SDM contains nine elements, the diagonal elements of which are the probability of producing a W boson of helicity τ_1, and so are normalised to unity,

$$\sum_{\tau_1} \rho^{W^-}_{\tau_1\tau_1}(s,\cos\theta_{\rm W}) = 1 \tag{3.37}$$

Examples of some of the real parts of the single W SDM elements can be seen in figure 3.11. The individual W polarised cross-sections, which are the differential cross-sections for producing a transversely (T) or longitudinally (L) W boson in the pair, where the other W boson can take any polarisation, can be written in terms of the single W SDMs. So for the polarisation of the $\rm W^-$ we have,

$$\begin{aligned}
\frac{d\sigma_{\rm T}}{d\cos\theta_{\rm W}} = \frac{d\sigma(\rm e^+e^- \to W^+W^-_T)}{d\cos\theta_{\rm W}} &= \frac{d\sigma}{d\cos\theta_{\rm W}}(\rho^{W^-}_{++} + \rho^{W^-}_{--}) \\
\frac{d\sigma_{\rm L}}{d\cos\theta_{\rm W}} = \frac{d\sigma(\rm e^+e^- \to W^+W^-_L)}{d\cos\theta_{\rm W}} &= \frac{d\sigma}{d\cos\theta_{\rm W}}(\rho^{W^-}_{00})
\end{aligned} \tag{3.38}$$

Examples of the individual W polarised cross-sections can be seen in figure 3.12. Shown, are the cross-sections for the Standard Model as well as those with various anomalous couplings implemented.

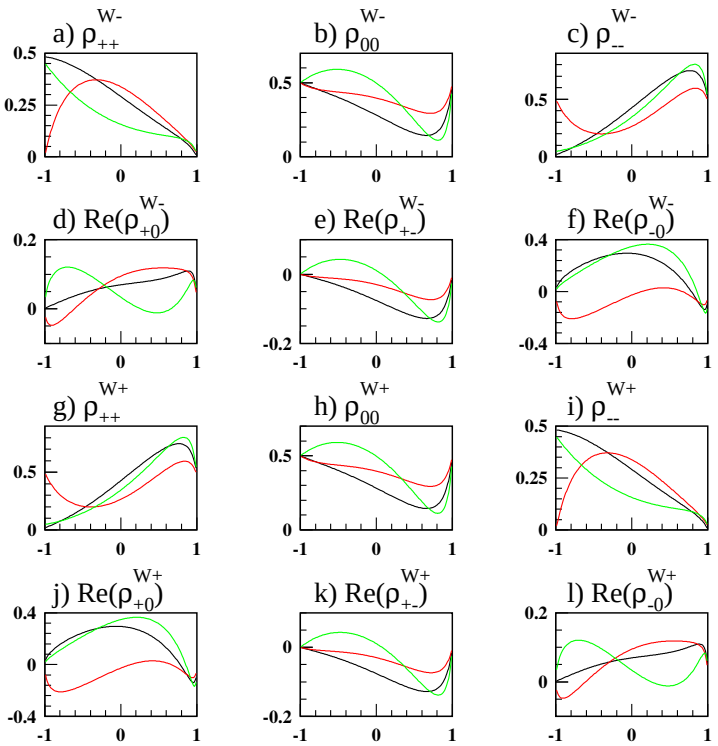

Figure 3.11: *The real parts of the single W spin density matrix elements. The black line is the Standard Model case and the red (green) line is with an anomalous coupling of* $\Delta g_1^z = +1\ (-1)$.

CPT and CP-Invariance

At tree level, for the helicity amplitudes, CPT-invariance implies [67] that,

$$F^{\lambda}_{\tau_1\tau_2}(s, \cos\theta_{\rm W}) = \left(F^{\lambda}_{-\tau_2-\tau_1}(s, \cos\theta_{\rm W})\right)^* \tag{3.39}$$

The consequences of this for the single W SDM elements are:

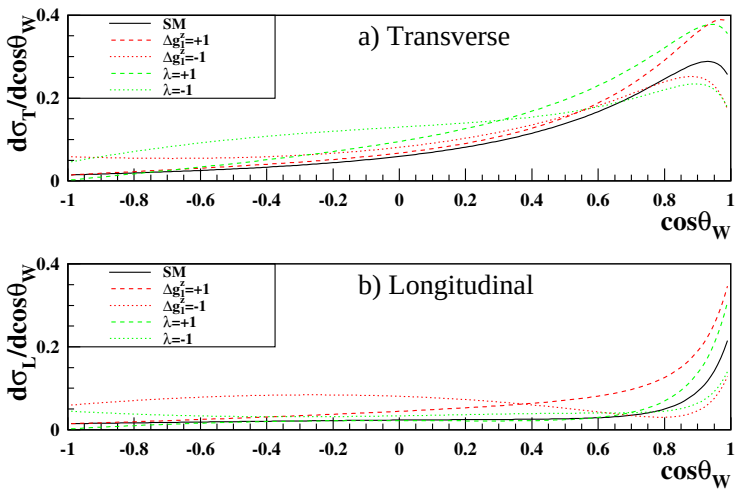

Figure 3.12: *The analytical predictions of the individual W polarised differential cross-sections for the production of transverse and longitudinal W bosons. Examples of the Standard Model as well as some non-Standard Model cases are shown.*

$$\rho^{W^-}_{\tau\tau'}(s, \cos\theta_{\mathrm{W}}) = \left(\rho^{W^+}_{-\tau-\tau'}(s, \cos\theta_{\mathrm{W}})\right)^* \tag{3.40}$$

The off-diagonal elements of the single W SDM are complex in nature, so if equation 3.40 is broken down into the real and imaginary parts, the following two relations are obtained:

$$Re\left(\rho^{W^-}_{\tau\tau'}(s, \cos\theta_{\mathrm{W}})\right) - Re\left(\rho^{W^+}_{-\tau-\tau'}(s, \cos\theta_{\mathrm{W}})\right) = 0 \tag{3.41}$$

$$Im\left(\rho^{W^-}_{\tau\tau'}(s, \cos\theta_{\mathrm{W}})\right) + Im\left(\rho^{W^+}_{-\tau-\tau'}(s, \cos\theta_{\mathrm{W}})\right) = 0 \tag{3.42}$$

The behaviour of the real parts for the single W^- and single W^+ SDM elements can be seen in figure 3.11 and thus equation 3.41 is confirmed, even in the presence of anomalous couplings.

As mentioned earlier, at tree level, for a CP-invariant reaction, the helicity amplitudes fulfill the following relation:

$$F^{\lambda}_{\tau_1\tau_2}(s,\cos\theta_{\mathrm{W}}) = F^{\lambda}_{-\tau_2-\tau_1}(s,\cos\theta_{\mathrm{W}}) \tag{3.43}$$

Thus the single W SDM elements for the W^- would then be related to those for the W^+ as follows:

$$\rho^{W^-}_{\tau\tau'}(s,\cos\theta_{\mathrm{W}}) = \rho^{W^+}_{-\tau-\tau'}(s,\cos\theta_{\mathrm{W}}) \tag{3.44}$$

Like equation 3.40, equation 3.44 has some important implications. Splitting the single W SDM elements into their real and imaginary parts once again, for the real parts equation 3.44 reproduces equation 3.41 which was brought about by CPT-invariance. However, for the imaginary parts the following is now true,

$$Im\left(\rho^{W^-}_{\tau\tau'}(s,\cos\theta_{\mathrm{W}})\right) - Im\left(\rho^{W^+}_{-\tau-\tau'}(s,\cos\theta_{\mathrm{W}})\right) = 0 \tag{3.45}$$

Combining equations 3.40 and 3.44 brings about a simple, but extremely important conclusion. At tree level in a CP-invariant interaction, the imaginary parts of all SDM elements are zero. Any deviation in the imaginary parts could only occur in the presence of CP-violation. Thus, this means that equation 3.45 gives a sensitive test of tree level CP-violation within weak bosonic self interactions. As CP and CPT-invariance give the same relations for the real parts of the SDM elements, then the real parts do not provide for sensitive tests of CP-invariance.

In the presence of CP-violation at tree level, the magnitude by which equation 3.45 differs from zero is given by:

$$
\begin{aligned}
& Im\left(\rho^{W^-}_{\tau\tau'}(s,\cos\theta_{\mathrm{W}})\right) - Im\left(\rho^{W^+}_{-\tau'-\tau}(s,\cos\theta_{\mathrm{W}})\right) \\
&= 2Im\left(\rho^{W^-}_{\tau\tau'}(s,\cos\theta_{\mathrm{W}})\right) \\
&= -2Im\left(\rho^{W^+}_{-\tau-\tau'}(s,\cos\theta_{\mathrm{W}})\right)
\end{aligned}
\tag{3.46}
$$

Figure 3.13 shows the imaginary parts of the off-diagonal elements of the single W SDM. It can immediately be seen that in the absence of CP-violation all these elements are zero. The plots with CP-violating couplings implemented verify the nature of the elements described by equation 3.46. Figure 3.13 also demonstrates that a matrix element with a positive CP-violating coupling implemented, is equal to the negative of the same matrix element with a negative CP-violating coupling implemented. With the real parts of the SDM elements there is no difference seen between a negative and positive CP-violating coupling of equal magnitude.

These relationships will break down in the face of effects beyond tree-level. The presence of loop effects, both CP-conserving and CP-violating will always cause the imaginary parts of the SDM elements to deviate from zero [67]. However, these deviations, unlike tree level CP-violation, cause both the W^- and W^+ elements to deviate from zero in the same way. So suitable combinations of SDM elements can be formed in which deviations due to loop effects cancel, these are shown in equation 3.47. Any deviation from these equations could only be due to tree level CP-violation and so give a genuine and sensitive test of CP-violation [36, 67].

$$
\begin{aligned}
Im(\rho^{W^-}_{+-}) &- Im(\rho^{W^+}_{-+}) = 0 \\
Im(\rho^{W^-}_{+0}) &- Im(\rho^{W^+}_{-0}) = 0 \\
Im(\rho^{W^-}_{-0}) &- Im(\rho^{W^+}_{+0}) = 0
\end{aligned}
\tag{3.47}
$$

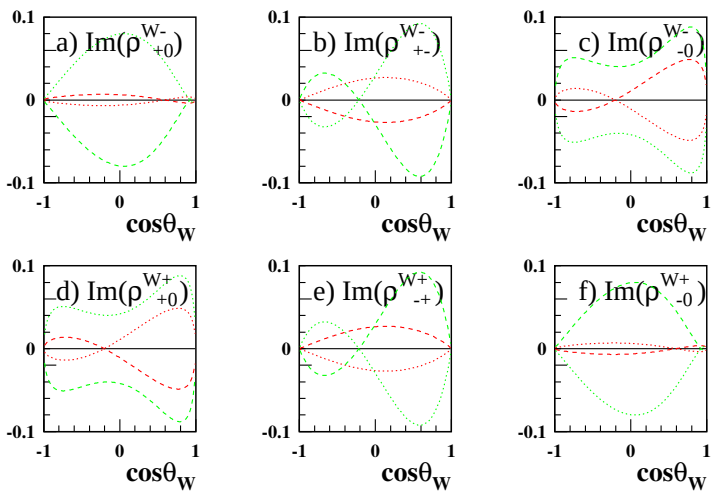

Figure 3.13: *Examples of the imaginary parts of the off-diagonal single W SDM elements. The solid black line is the Standard Model case. The red lines are for CP-violating anomalous coupling $\tilde{\kappa}_z$ and the green line is for CP-violating anomalous coupling $\tilde{\lambda}_z$. The dotted (dashed) line indicates a coupling of +1 (−1).*

Conversely, combinations of matrix elements may be formed to test for loop effects in which effects due to CP-violation cancel. These are derived from equation 3.42 and are shown explicitly in equation 3.48. Any deviations from these could only be an indication of effects beyond tree-level or the presence of CPT-violation.

$$\begin{aligned} Im(\rho^{W^-}_{+-}) &+ Im(\rho^{W^+}_{-+}) = 0 \\ Im(\rho^{W^-}_{+0}) &+ Im(\rho^{W^+}_{-0}) = 0 \\ Im(\rho^{W^-}_{-0}) &+ Im(\rho^{W^+}_{+0}) = 0 \end{aligned} \tag{3.48}$$

Chapter 4

Application to Data Events

In this chapter the experimental realisation of the theoretical properties of the W-pair production process are discussed. A method for extracting the SDM elements from the angular distributions of the W decay products will be presented. Then the possible final states available through W-pair production are identified and the characteristics of each discussed. It will be shown that the $W^+W^- \to q\bar{q}\ell\bar{\nu}_\ell$ channel represents the channel with the clearest access to the SDM elements and polarised cross-sections and so accordingly is chosen as the signal process.

4.1 Calculating the SDM Elements

The W-pair production process is characterised by a final state of four fermions. It was shown in equation 3.27 that the cross-section for the process $e^+e^- \to W^+W^- \to f_1\bar{f}_2 f_3\bar{f}_4$ may be written in terms of five angles, the production angle of the W^- boson, the polar and azimuthal angles of the W^- decay fermion in the W^- rest frame, $\cos\theta_{f_1}$, ϕ_{f_1} and the polar and azimuthal angles of the W^+ decay anti-fermion in the W^+ rest frame, $\cos\theta_{\bar{f}_4}$,

$\phi_{\bar{f}_4}$.

Monte Carlo generators can be used to generate pseudo-data events for the process $e^+e^- \to W^+W^- \to f_1\bar{f}_2 f_3 \bar{f}_4$. Figure 4.1 shows the Standard Model prediction of the distributions of the five angles in W-pair production and decay calculated from events generated by the EXCALIBUR Monte Carlo generator.

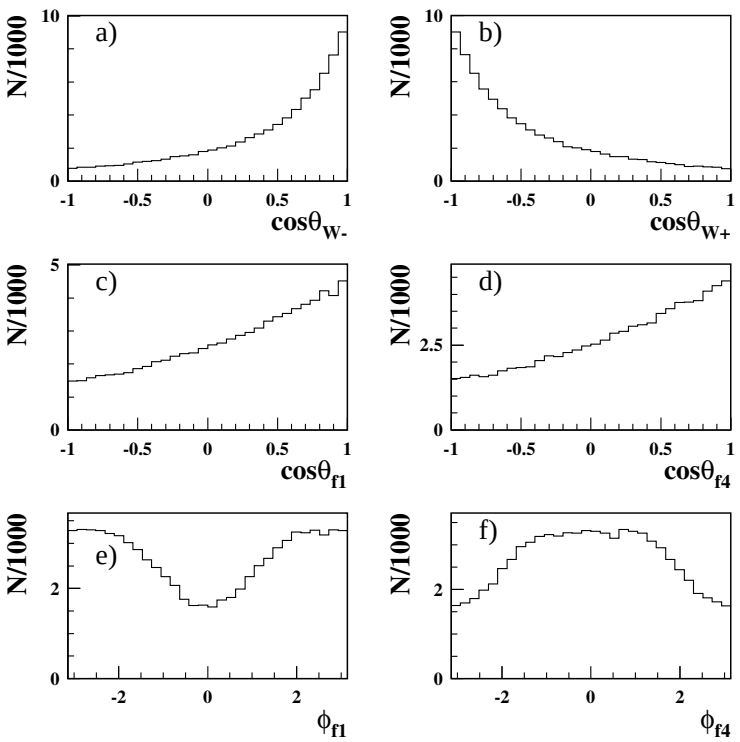

Figure 4.1: *The angular distributions from Monte Carlo generated W-pair events. a) the* W^- *production angle. b)* W^+ *production angle. c) & e) the polar and azimuthal angular distributions of the* W^- *decay fermion in the* W^- *rest frame. d) & f) the polar and azimuthal angular distributions of the* W^+ *decay anti-fermion in the* W^+ *rest frame.*

The equation describing the 5-fold differential cross-section in terms of these angles contains the helicity amplitudes and the D-functions that described how the decay fermions couple to the W bosons through the standard V−A coupling. This coupling, and hence the angular distribution of the fermions depends on the helicity of the W bosons.

Measuring the angular distribution of the W decay products then gives an effective way of measuring the W bosons' helicities. The D-functions, given in equation 3.26, can be inverted, so that rather than giving the angular distribution for a certain helicity, it will give the helicities for a certain angular distribution. A set of so-called projection operators [41] can thus be formed from the D-functions. When these operators are applied to the angular distributions of the decay fermions, they effectively *project out* information about the helicities of the W bosons. The projection operators are given the form of $\Lambda^{W^\pm}_{\tau\tau'}$, where the τ and τ' relate to the interfering spins of individual W bosons, and the $W^\pm$ indicates that there is a different set of operators for the W^+ boson and W^- boson. The full set of projection operators can be seen in equation 4.1, where $\Lambda_{\tau\tau'} = \Lambda^*_{\tau'\tau}$.

$$\begin{aligned}
\Lambda^{W^-}_{\pm\pm} = \Lambda^{W^+}_{\mp\mp} &= \frac{1}{2}(5\cos^2\theta_f \mp 2\cos\theta_f - 1) \\
\Lambda^{W^-}_{00} = \Lambda^{W^+}_{00} &= 2 - 5\cos^2\theta_f \\
\Lambda^{W^-}_{+-} = \Lambda^{W^+}_{+-} &= 2\mathrm{e}^{-2i\phi_f} \\
\Lambda^{W^-}_{\pm 0} = -\left(\Lambda^{W^+}_{\mp 0}\right)^* &= \frac{-8}{3\pi\sqrt{2}}(1 \mp 4\cos\theta_f)\mathrm{e}^{\mp i\phi_f}
\end{aligned} \tag{4.1}$$

The single W SDM elements that describe the helicity properties of one of the W bosons can now be calculated using these projection operators. The unnormalised single W density matrix elements can be extracted from the 3-fold angular distribution of the W^- decay fermion (or W^+ decay anti-

fermion), by integrating with the appropriate projection operators, for example:

$$\frac{d\sigma(\mathrm{e^+e^-}\to\mathrm{W^+W^-})}{d\cos\theta_\mathrm{W}}\rho^{\mathrm{W}^\pm}_{\tau\tau'} \tag{4.2}$$
$$=\frac{1}{\mathrm{Br}(\mathrm{W}^\pm\to f\bar{f})}\int\frac{d\sigma(\mathrm{e^+e^-}\to\mathrm{W}^\pm f\bar{f})}{d\cos\theta_\mathrm{W}d\cos\theta_f d\phi_f}\Lambda^{W^\pm}_{\tau\tau'}(\theta_f,\phi_f)d\cos\theta_f d\phi_f$$

Each projection operator projects out information about one of the W bosons in the W-pair. So, by integrating over combinations of the W^- and W^+ projection operators, all 81 of the unnormalised two-particle joint SDMs can be calculated, equation 4.3.

$$\frac{d\sigma(\mathrm{e^+e^-}\to\mathrm{W^+W^-})}{d\cos\theta_\mathrm{W}}\rho_{\tau_1\tau_1'\tau_2\tau_2'} \tag{4.3}$$
$$=\frac{1}{\mathrm{Br}(\mathrm{W^-}\to f_1\bar{f}_2)\mathrm{Br}(\mathrm{W^+}\to f_3\bar{f}_4)}\int\frac{d\sigma(\mathrm{e^+e^-}\to\mathrm{W^+W^-}\to f_1\bar{f}_2 f_3\bar{f}_4)}{d\cos\theta_\mathrm{W}d\cos\theta_{f_1}d\phi_{f_1}d\cos\theta_{\bar{f}_4}d\phi_{\bar{f}_4}}$$

$$\times\Lambda^{W^-}_{\tau_1\tau_1'}(\theta_{f_1},\phi_{f_1})\Lambda^{W^+}_{\tau_2\tau_2'}(\theta_{\bar{f}_4},\phi_{\bar{f}_4})d\cos\theta_{f_1}d\phi_{f_1}d\cos\theta_{\bar{f}_4}d\phi_{\bar{f}_4}$$

If the full angular distributions of the decay fermion from the W^- and the decay anti-fermion from the W^+ are known, all the SDM elements can be calculated. If the set of data are binned into bins of $\cos\theta_\mathrm{W}$, then experimentally equation 4.2 can be realised as a discrete summation over events, as in equation 4.4, where k is the bin of $\cos\theta_\mathrm{W}$, and N_k is the number of events in that bin.

$$\rho^{W^\pm}_{\tau\tau'}(k)=\frac{1}{N_k}\sum_{i=1}^{N_k}\Lambda^{W^\pm}_{\tau\tau'}(\cos\theta_f,\phi_f)_i \tag{4.4}$$

The summations needed for each of the single W^- SDM elements are shown appendix A.1. Performing these summations on the Monte Carlo

data whose angular distributions are shown in figure 4.1 will give the single W^- SDM elements for this set of data. These SDM elements are shown in figure 4.2. Overlaid are the analytical predictions for the Standard Model calculated from equation 3.29.

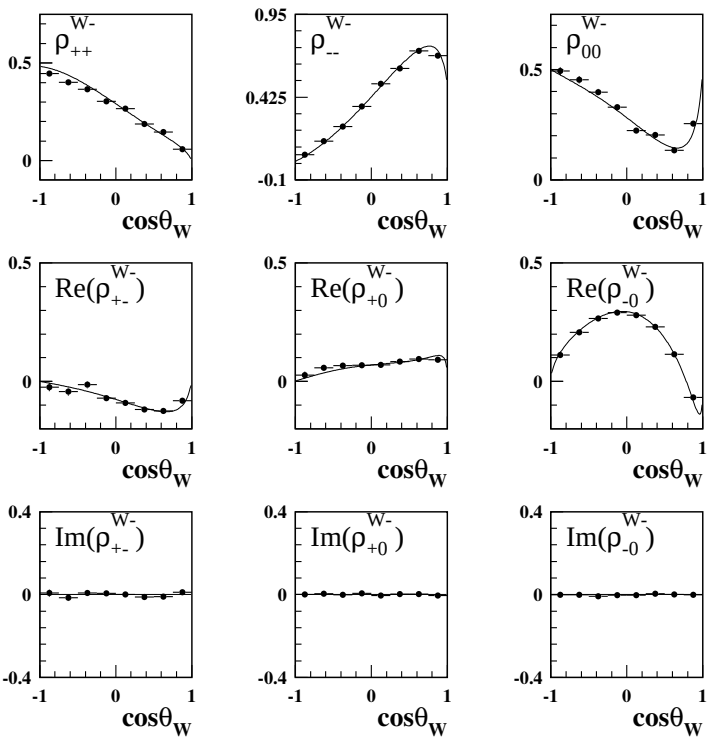

Figure 4.2: *The single* W^- *SDM elements calculated from a Standard Model EXCALIBUR Monte Carlo sample by application of the projection operators given in appendix A.1. Overlaid are the analytical predictions for the Standard Model.*

When calculating these SDM elements CPT-invariance can be assumed, so that information from the W^- and W^+ decay can be combined. CPT-invariance means $\rho^{W^-}_{\tau_1\tau_2} = (\rho^{W^+}_{-\tau_1-\tau_2})^*$. Therefore, the summation to calculate

each single W^- SDM element may now be written as a summation over the $W^- \to f_1\bar{f}_2$ decays, plus a summation over the $W^+ \to f_3\bar{f}_4$ decays with the appropriate CPT transform applied to the projection operator.

The equation needed to calculate the single W^- SDM elements when both the W^- decay fermion and the W^+ decay anti-fermion are measured in every event is shown in equation 4.5.

$$\rho^{W^-}_{\tau\tau'}(k) = \frac{1}{2N_k}\left[\sum_{i=1}^{N_k}\Lambda^{W^-}_{\tau\tau'}(\cos\theta_{f_1},\phi_{f_1})_i + \sum_{i=1}^{N_k}\left(\Lambda^{W^+}_{-\tau-\tau'}(\cos\theta_{\bar{f}_4},\phi_{\bar{f}_4})_i\right)^*\right] \quad (4.5)$$

If only one of the W bosons is measured in each event, the measurements from the W^+ and W^- can still be combined to form just the single W^- SDM elements as shown in equation 4.6. In this equation $N_k^{W^+}$ are the number of events with the $W^+ \to f\bar{f}$ decay measured in bin k of $\cos\theta_W$, and $N_k^{W^-}$ are the number of events with the $W^- \to f\bar{f}$ decay measured in bin k of $\cos\theta_W$. Thus $N_k^{W^+} + N_k^{W^-} = N_k$.

$$\rho^{W^-}_{\tau\tau'}(k) = \frac{1}{N_k}\left[\sum_{i=1}^{N_k^{W^-}}\Lambda^{W^-}_{\tau\tau'}(\cos\theta_{f_1},\phi_{f_1})_i + \sum_{i=1}^{N_k^{W^+}}\left(\Lambda^{W^+}_{-\tau-\tau'}(\cos\theta_{\bar{f}_4},\phi_{\bar{f}_4})_i\right)^*\right] \quad (4.6)$$

For the two-particle joint SDM elements both the decay fermion from the W^- and the anti-fermion of the W^+ in the W-pair event need to be measured. Experimentally, equation 4.3 can also be written in bins of $\cos\theta_W$ as a discrete summation over events, as shown in equation 4.7.

$$\rho_{\tau_1\tau_1'\tau_2\tau_2'}(k) = \frac{1}{N_k}\sum_{i=1}^{N_k}\Lambda_{\tau_1\tau_1'}(\cos\theta_{f_1},\phi_{f_1})_i\Lambda_{\tau_2\tau_2'}(\cos\theta_{\bar{f}_4},\phi_{\bar{f}_4})_i \quad (4.7)$$

The complete set of summations of operators giving all the two-particle joint SDM elements are given in appendix A.2. Taking, for example, the

operators for the diagonal elements ($\tau_1 = \tau'_1, \tau_2 = \tau'_2$) of the two-particle joint SDM and performing the summations on the Monte Carlo data, the two-particle SDM elements shown in figure 4.3 are obtained. Overlaid are the analytical predictions for the Standard Model calculated from equation 3.29.

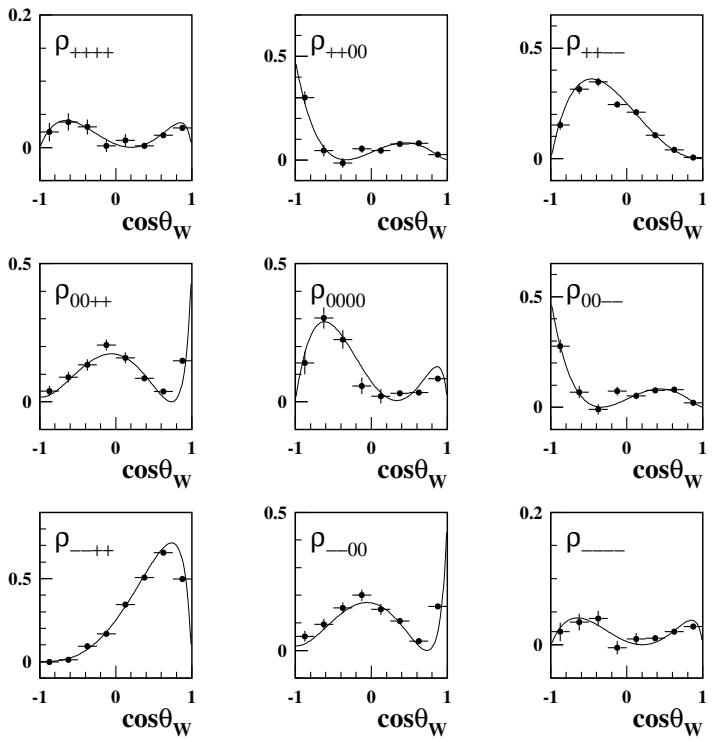

Figure 4.3: *The diagonal elements of the two-particle joint W SDM calculated from a Standard Model EXCALIBUR Monte Carlo sample by application of the projection operators given in appendix A.2. Overlaid are the analytical predictions for the Standard Model.*

4.2 Calculating the Polarised Cross-Sections

Having calculated both the single W and the two-particle joint SDM elements for the Monte Carlo, it is then possible to calculate the polarised differential cross-sections using equations 3.33 and 3.38 given earlier. The individual W ($d\sigma_L/d\cos\theta_W$, $d\sigma_T/d\cos\theta_W$) and the correlated W-pair ($d\sigma_{TT}/d\cos\theta_W$, $d\sigma_{LL}/d\cos\theta_W$, $d\sigma_{TL}/d\cos\theta_W$) polarised differential cross-sections for the Monte Carlo data are shown in figure 4.4. Overlaid are the analytical predictions for the Standard Model calculated from equation 3.25.

4.3 Considerations for Real Events

When looking at the Monte Carlo data samples, it was assumed that the angular distributions of all four of the decay fermions are well known and that each individual fermion is perfectly identified. This is not the case with real data. There are three possible decay channels of the W-pair. The leptonic (4.8), the hadronic (4.9) and the semi-leptonic (4.10). Each of these posses their own distinct signatures.

$$e^-e^+ \rightarrow W^-W^+ \rightarrow \ell^-\bar{\nu}_{\ell^-}\ell^+\nu_{\ell^+} \tag{4.8}$$

$$e^-e^+ \rightarrow W^-W^+ \rightarrow q\bar{q}q\bar{q} \tag{4.9}$$

$$e^-e^+ \rightarrow W^-W^+ \rightarrow \ell\bar{\nu}_\ell q\bar{q} \tag{4.10}$$

Each final fermion type has its own difficulties associated with it when trying to measure them. A brief description of these are given below. A full discussion on event selection and reconstruction is given in chapter 5.

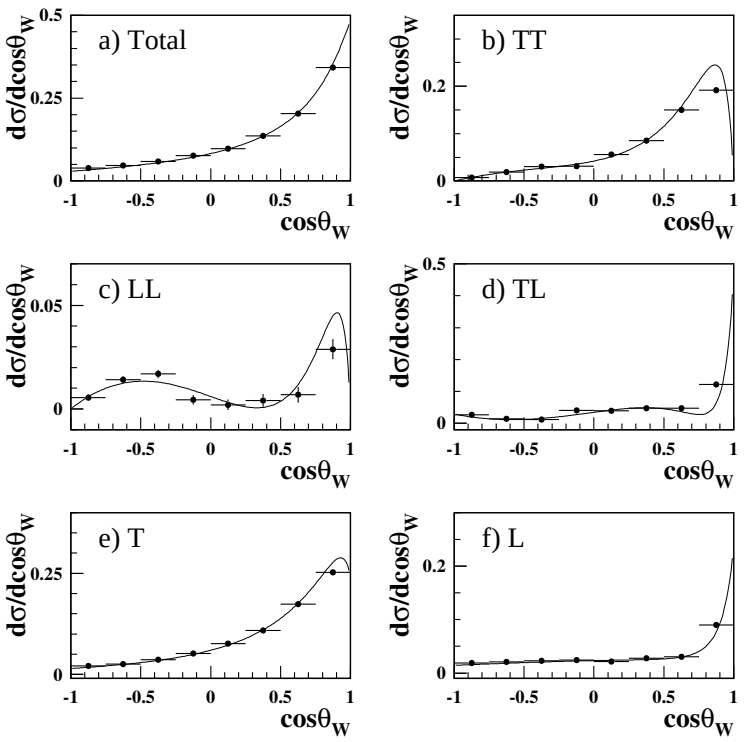

Figure 4.4: *The differential cross-sections for different W boson helicity states calculated from Standard Model Monte Carlo. a) is the total differential cross-section. b) is for the production of two transversely polarised W bosons. c) is for the production of two longitudinally polarised W bosons. d) is for the production of a longitudinal and a transverse W boson. e) and f) are for the production of at least one transverse and one longitudinal W boson in the pair respectively. Overlaid on all the plots is the analytical prediction for the Standard Model.*

- The massless neutrino cannot be detected and passes straight through without leaving any signal.

- The hadrons produce jets of hadronic particles, making identification of charge, and therefore differentiating between fermion and anti-fermion very difficult indeed.

- If the lepton is a τ it will decay before it is detected. It can decay into a lighter lepton and neutrinos or into hadronic particles. In all cases reconstruction of direction will be made difficult.

These differences in the way each fermion behaves then mean that each decay channel has its own set of difficulties associated with it when trying to reconstruct the W production and decay angles.

- The fully leptonic decay is measured as two leptons. So, although the lepton and anti-lepton are identified, the fact that not all the momentum is measured immediately complicates things. There will always be a two fold ambiguity within the calculation of the W production angle. All the missing momentum is assumed to be that of the two neutrinos. If there is any Initial State Radiation, the assumed four-momentum of the neutrinos will actually be that of the neutrinos plus the ISR photon. The production four-momentum of the W boson will then be calculated incorrectly and so leads to incorrect calculation of the the decay angles in the W rest frame. The problem will be further enhanced if one or both of the leptons are taus.

- The fully hadronic decay produces four jets of particles. All the the momentum components of the four jets will be measured, but there is still a three-fold problem. Firstly, each hadron has to be assigned to the correct jet. This can be done by, for example, using the Durham $k_\perp$ algorithm [68, 69, 70, 71] to force each selected event into four jets. Once this has been done the correct di-jet combination has to be identified,

i.e. the two jets from each W boson have to be paired together. This is possible by using a likelihood algorithm [72]. Both these processes are not 100% efficient. The charge of each jet is unknown, making it very difficult to distinguish between the particle and anti-particle from each W boson and even the W^+ and W^-. The charge can be inferred by a jet charge technique [73]. This technique only has limited success for calculating the charge of the di-jet pairs to identify the W^+ and W^-, but is almost useless when it comes to differentiating between the fractionally charged jets from the particle and anti-particle.

- The semi-leptonic decay is signified by two jets of particles and a lepton. Calculation of the W production angle can be performed as all the momentum from the hadronically decaying W boson can be measured. The problem of jet pairing only arises if there is a τ lepton present and even in this case it is far reduced from the problem seen in the fully hadronic channel. ISR can still cause problems as once again all the missing momentum is assigned to the neutrino. Identification of the W^- and W^+ bosons is given by the lepton charge. There is still an ambiguity in assigning the correct particles to each of the two jets from the hadronically decaying W boson. Identification of which jet represents the fermion and which the anti-fermion is also very difficult.

The semi-leptonic channel presents the fewest ambiguities when calculating the five decay angles of the event, so is chosen as the signal process. The polar and azimuthal angle of either the decay fermion or anti-fermion in the W rest frame can be calculated for each event. Thus the single W SDM elements can be calculated from the semi-leptonic decay events. For the $W\rightarrow q\bar{q}$ in the W-pair the fermion and anti-fermion cannot be distinguished, thus all the single W SDM elements cannot be calculated from these.

Certain projection operators (or combinations thereof) used to calculate the SDM elements are invariant under the transform $\theta_f \to \pi - \theta_f$, $\phi_f \to \phi_f + \pi$. This transform is equivalent to the interchange of the fermion and anti-fermion from one of the W bosons. Thus, these projection operators can be used on the hadronically decaying W boson with the choice of fermion being arbitrary. The projection operators that are invariant under this interchange include the following:

$$\begin{aligned} \Lambda^{W^\pm}_{++} + \Lambda^{W^\pm}_{--} &= 5\cos^2\theta_f - 1 \\ \Lambda^{W^\pm}_{00} &= 2 - 5\cos^2\theta_f \end{aligned} \tag{4.11}$$

Therefore ρ_{00} and $\rho_{++}+\rho_{--}$ can still be extracted from the hadronically decaying W boson. The combinations of SDM elements needed to calculate the W-pair polarised cross-sections only require the combinations shown in equation 4.11, so may also be extracted from the semi-leptonic events, as shown in equations 4.12-4.15. Both the individual W and W-pair polarised cross-sections can then be calculated from the semi-leptonic decay events.

$$\begin{aligned} \sigma_{\mathrm{TT}} &\propto \rho_{++++} + \rho_{----} + \rho_{++--} + \rho_{--++} \\ &\propto \Lambda^{W^-}_{++}\Lambda^{W^+}_{++} + \Lambda^{W^-}_{--}\Lambda^{W^+}_{--} + \Lambda^{W^-}_{++}\Lambda^{W^+}_{--} + \Lambda^{W^-}_{--}\Lambda^{W^+}_{++} \\ &\propto (\Lambda^{W^-}_{++} + \Lambda^{W^-}_{--})(\Lambda^{W^+}_{++} + \Lambda^{W^+}_{--}) \end{aligned} \tag{4.12}$$

$$\begin{aligned} \sigma_{\mathrm{LL}} &\propto \rho_{0000} \\ &\propto \Lambda^{W^-}_{00}\Lambda^{W^+}_{00} \end{aligned} \tag{4.13}$$

$$\begin{aligned}\sigma_{\mathrm{TL}} &\propto \rho_{++00} + \rho_{--00} \\ &\propto \Lambda^{W^-}_{++}\Lambda^{W^+}_{00} + \Lambda^{W^-}_{--}\Lambda^{W^+}_{00} \\ &\propto (\Lambda^{W^-}_{++} + \Lambda^{W^-}_{--})\Lambda^{W^+}_{00} \end{aligned} \tag{4.14}$$

$$\begin{aligned}\sigma_{\mathrm{LT}} &\propto \rho_{00++} + \rho_{00--} \\ &\propto \Lambda^{W^-}_{00}\Lambda^{W^+}_{++} + \Lambda^{W^-}_{00}\Lambda^{W^+}_{--} \\ &\propto \Lambda^{W^-}_{00}(\Lambda^{W^+}_{++} + \Lambda^{W^+}_{--}) \end{aligned} \tag{4.15}$$

4.4 Events with $\mathrm{q\bar{q}}\ell\bar{\nu}_\ell$ Final States

So far, the signal processes $\mathrm{e^-e^+} \rightarrow \mathrm{W^-W^+} \rightarrow \mathrm{q\bar{q}}\ell\bar{\nu}_\ell$ have been considered. At OPAL these are not the only processes that produce a final state of $\mathrm{q\bar{q}}\ell\bar{\nu}_\ell$. For example, the TGC process, seen in figure 3.3, which does not have a intermediate state of two W bosons, can also produce a final state of $\mathrm{q\bar{q}}\ell\bar{\nu}_\ell$. There are many more processes which produce the same final state which do not contain the TGC vertex or an intermediate state of two W bosons [74]. It is impossible to separate out these events in the data so they are considered as part of the signal.

The processes producing a final state of $\mathrm{q\bar{q}}\ell\bar{\nu}_\ell$ are called the Charged Current (CC) processes. They can be split into three sub-sets; CC03, which are the W-pair signal events shown figure 4.5. CC10, which are the processes capable of producing a final state with the lepton being an electron, a muon or a tau, this set includes the CC03 diagrams. The extra diagrams needed to complete this set are shown in figure 4.6. Finally there is the CC20 group which is all processes which produce a final state of an electron, an anti-neutrino and a quark anti-quark pair. This set includes the ten diagrams

from the CC10 set plus ten more diagrams that have a final state which can have only an electron or a positron as the lepton in the final state, shown in figure 4.7.

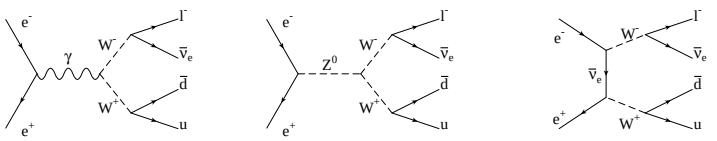

Figure 4.5: *CC03 diagrams.*

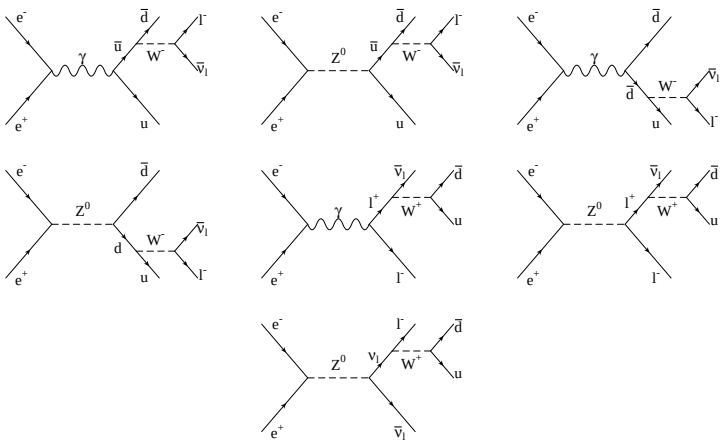

Figure 4.6: *This set of diagrams plus the CC03 set form the group known as CC10 diagrams.*

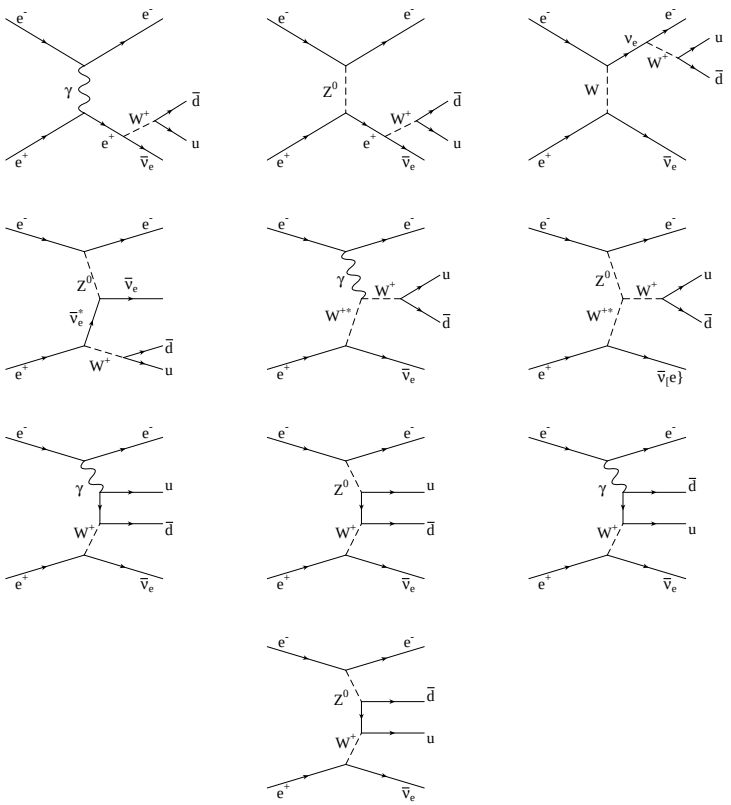

Figure 4.7: *This set of diagrams plus the CC10 set form the group known as CC20 diagrams.*

Chapter 5

Selection of Data

In this chapter the event selection procedures are described. The selection is designed to enhance the signal over background processes. The background processes fall into two categories, (i) the irreducible background from events leading to the same final state as the signal. These were described in the last chapter. (ii) background processes which lead to a similar, but not identical final state which can be mis-identified as signal events. These processes are described below. Also described in this chapter are the Monte Carlo generators used in the analysis.

5.1 Background Events

5.1.1 Neutral Current Four-Fermion Production

In addition to the charged current four-fermion processes already discussed, there is another class of four-fermion final state events called the neutral current (NC) processes. Unlike the charged current processes they do not contain a W boson, so rather than a final state of $q\bar{q}\ell\bar{\nu}_\ell$, these events contain two quarks and two charged leptons, $q\bar{q}\ell^+\ell^-$. With a final state such

as this, if one of the charged leptons is not detected by the OPAL detector, the event will appear to have a final state of $q\bar{q}\ell\bar{\nu}_\ell$.

There are 24 neutral current processes which can produce a final state with either electrons, muons or taus in it. These are called the NC24 diagrams. The diagrams for these processes are shown in figure 5.1.

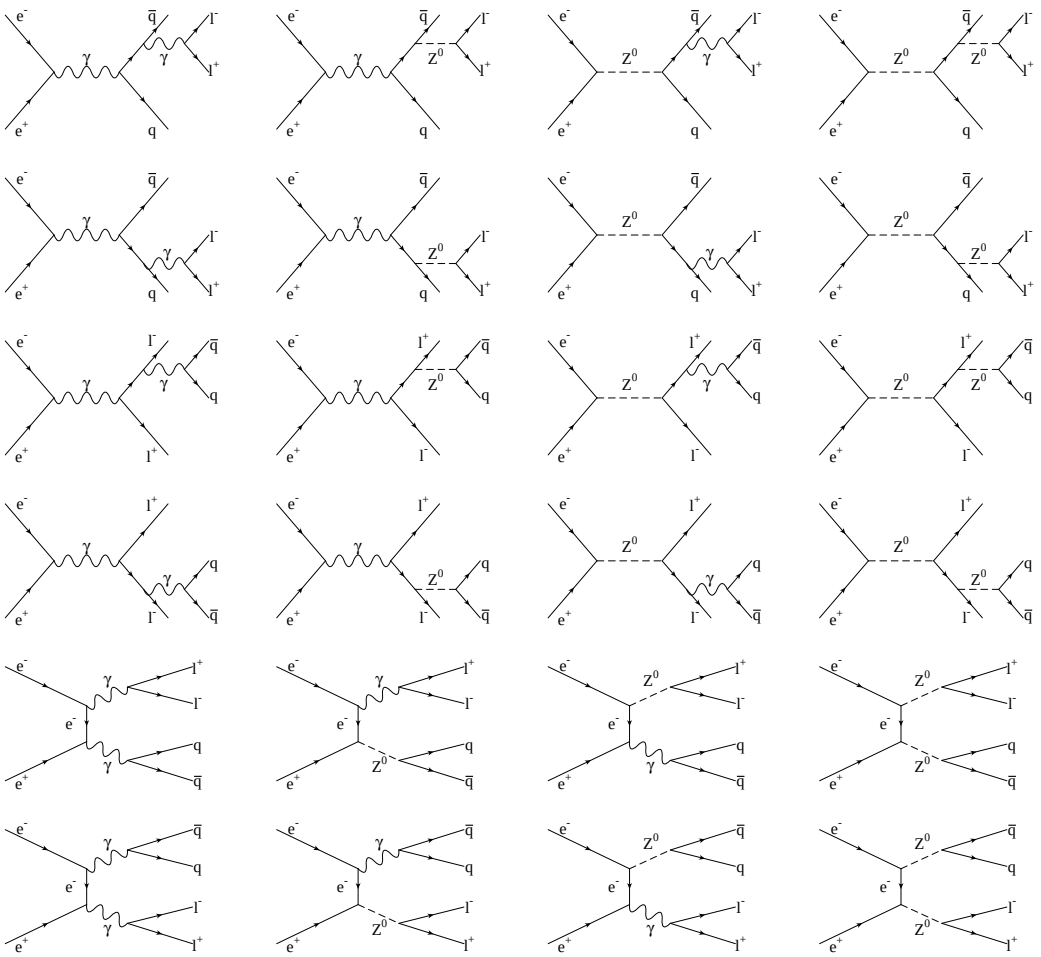

Figure 5.1: *NC24 diagrams.*

There are a further 24 neutral current processes that can only produce a final state with the charged leptons being an electron and a positron. The

diagrams representing these events are shown in figure 5.2. When combined with the NC24 events, this group is called the NC48 set.

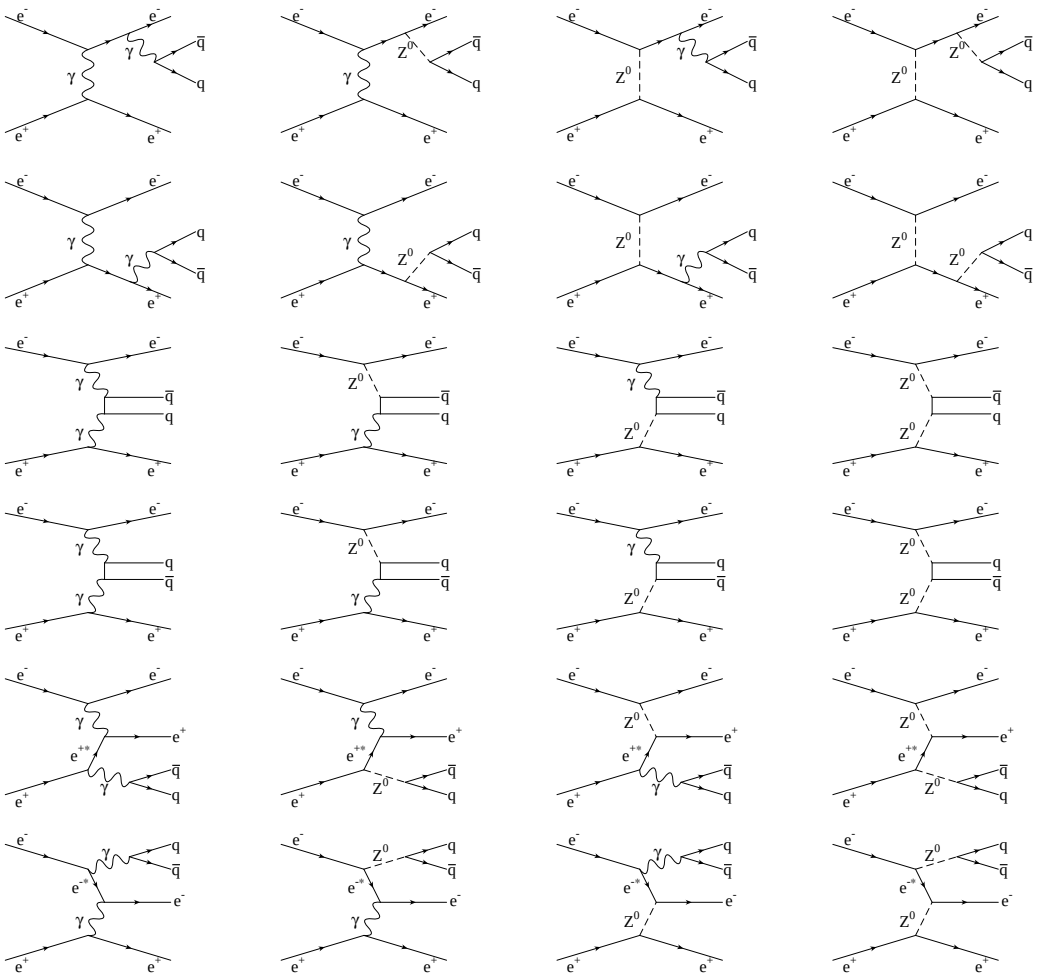

Figure 5.2: *Along with the NC24 diagrams, these make up the NC48 diagrams.*

5.1.2 The $Z^0/\gamma \to q\bar{q}$ Background

The $Z^0/\gamma \to q\bar{q}$ processes are shown in figure 5.3. The final states produced by this process are generally unlike the signal process. However, if the

initial state photon converts into an electron-positron pair and one of the leptons is *lost* down the beam pipe, the event could resemble a signal process. Furthermore, the photon is often radiated with an energy that means the Z^0 is on-shell. This would mean that the jets would be boosted and also have a similar invariant mass to a W boson. As the $Z^0/\gamma \rightarrow q\bar{q}$ process has a cross-section 13 times higher than that of the signal process it is a major contribution to the accepted background processes.

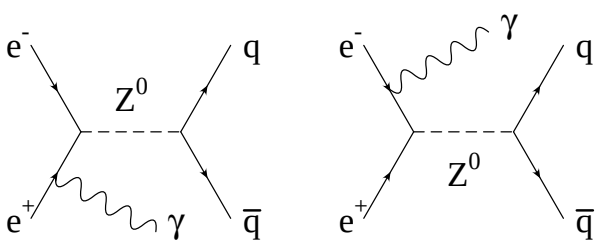

Figure 5.3: *The $Z^0/\gamma \rightarrow q\bar{q}$ background processes.*

5.1.3 The Two-Photon Background

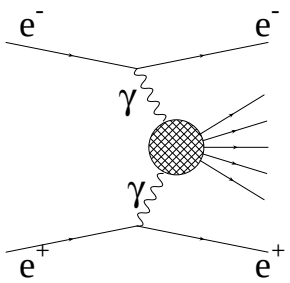

Figure 5.4: *The two-photon background processes.*

The two-photon process is shown in figure 5.4. The final state of this process does not really resemble the signal process, but the cross-section is extremely high, over a 1000 times greater than the signal processes cross-section, this means that some events may be accepted as signal events. There are two photon events where both beam leptons are lost down the beam pipe, these are called untagged events and will not contribute to the background. However, there are events where one

of the beam leptons is detected, these are called tagged events. These may contribute to the background as the lepton may resemble that from a $W^+W^- \to q\bar{q}e\bar{\nu}_e$ event. Even with these events, the chances of it being accepted in the selection is extremely low, so the two-photon process is not as large a contributor to the background as the $Z^0/\gamma \to q\bar{q}$ process.

5.2 Monte Carlo Generators

To mimic the actual events seen within the OPAL detector a number of Monte Carlo generators are employed throughout this analysis. These generators produce the final state four-vectors of all the particles within the event. Not only are there generators that produce four-fermions seen from the W-pair process, but there are also those which produce four-fermion final states through all the processes discussed in this and the last chapter. Generators are also used to simulate the other background events, such as $Z^0/\gamma \to q\bar{q}$. Many of these generators do not only produce the final particles calculated from the leading order Feynman diagrams, but they also include such effects as Initial State Radiation (ISR), Final State Radiation (FSR) and Coulomb corrections. In this section the different types of Monte Carlo generators used are discussed.

5.2.1 Four-Fermion Monte Carlo Generators

The four-fermion generators can produce all four-fermion final states, $q\bar{q}q\bar{q}$, $q\bar{q}\ell\bar{\nu}_\ell$ and $\ell^+\nu_\ell\ell'^-\bar{\nu}_{\ell'}$ through all possible processes including $e^+e^- \to W^+W^- \to f_1\bar{f}_2f_3\bar{f}_4$, as well as the other CC20 and NC48 processes. All the generators vary in a number of ways, not only in how they model the basic process, but also in what extra processes are added such as Coulomb

corrections. A brief description of all the four-fermion generators used in the analysis is given below.

EXCALIBUR

EXCALIBUR [75] is the most widely used generator. It contains not only the Standard Model matrix elements, but also the option to *switch on* a number of the anomalous couplings seen in the general Lagrangian, equation 3.1. The couplings that can be varied are; g_1^z, κ_γ, κ_z, λ_γ, λ_z, and g_5^z. They may be set at any value. It is not possible to implement the CP-violating couplings.

EXCALIBUR generates four-fermion final states through all possible electroweak four-fermion processes [74]. However, the QED two-photon diagram is omitted from the OPAL version because this process is not well understood and is better modelled by dedicated two-photon generators. This means that the interference terms of this process with the other NC48 diagrams are neglected. This is thought to be a small effect, especially compared to the uncertainty associated with the two-photon process itself.

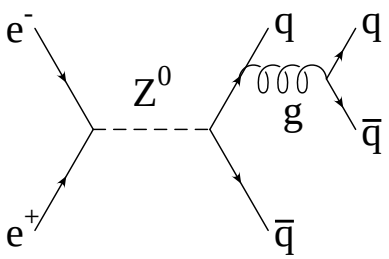

Figure 5.5: *The interfering QCD background.*

All fermions are assumed to be massless when they are generated. The generator also includes the width of the $W^{\pm}$ and Z^0 bosons. QED initial state corrections are implemented using a structure function formalism [76]. Interfering QCD backgrounds [77] are also possible. An example of these diagrams are as in figure 5.5. These interfering backgrounds are only relevant for the $q\bar{q}q\bar{q}$ channel and in the OPAL version

of EXCALIBUR they are not implemented. This is to avoid double-counting because they are also contained in the standard PYTHIA quark pair production Monte Carlo that is used as the background generator for the $q\bar{q}q\bar{q}$ channel. EXCALIBUR has a Coulomb correction [78] for the CC03 WW production. This correction accounts for the fact that if the two W bosons are travelling slowly with respect to each other, the pure Coulomb attraction between them is not negligible, and it changes the W boson momentum distribution. This effect is particularly important at the W-pair production threshold of 161 GeV.

A naive QCD correction is also implemented in EXCALIBUR. This is because, in addition to the four-fermion production that EXCALIBUR models, there is also four-fermion plus one-gluon production which enhances the WW production cross-section. The correction is applied naively to all final-states with $W\rightarrow q\bar{q}$ decays and it boosts the cross-section by $(1 + \alpha_s(M_W)/\pi)$ for each $W\rightarrow q\bar{q}$ decay. It should be noted that the $W\rightarrow q\bar{q}g$ topology is simulated in the events by the parton-shower part of the event generation, so multiplying the cross-section by this correction is a reasonable thing to do.

The naive QCD correction in principle should be applied to all diagrams with a vector boson $V\rightarrow q\bar{q}$ decay. However to achieve this $\alpha_s(Q^2)$ has to be evaluated at the correct (vector boson mass) scale Q^2. This is extremely involved, so the naive QCD correction is only applied to the WW diagrams, where Q is well defined (M_W).

ERATO

ERATO [54], like EXCALIBUR, can generate all four-fermion final states through all possible electroweak four-fermion processes. Once again fermions are assumed massless. It contains QED initial-state corrections and the

Coulomb correction. It also has radiative corrections related to the width of the unstable Z^0 and $W^{\pm}$ bosons.

The main difference from the EXCALIBUR generator is that any of the anomalous couplings seen in the general Lagrangian, equation 3.1, may be varied. These include the CP-violating couplings. All the couplings may be set to any value. It is possible to produce weighted events using ERATO aswell. This means that one set of events can be generated along with many sets of weights, each of which can weight the sample of events to a sample with any anomalous coupling.

grc4f

grc4f [79], like the other four-fermion generators, can generate all four-fermion final states through all possible electroweak four-fermion processes. However, it's structure is slightly different. It is based on the GRACE [80] system which automatically generates the matrix element in terms of the helicity amplitude. This means that the fermion masses are treated as non-zero. It contains the gauge boson widths and Coulomb corrections between the two intermediate W bosons. It also has initial state corrections, these are implemented in two ways. One is based on the electron structure function formalism, as for the other four-fermion generators, but it also uses a parton shower algorithm. All the C and P-conserving anomalous couplings may be *switched on* and set to any value. The CP-violating couplings may not be implemented.

5.2.2 WW Monte Carlo Generators

The WW generators share many features of the four-fermion generators, but they only contain the three CC03 diagrams. This means that only four

fermion final states via the process $e^+e^- \to W^+W^- \to f_1\bar{f}_2 f_3\bar{f}_4$ are calculated and so the interference between all possible final four-fermion processes are not included. It should be noted that all the four-fermion generators already discussed may also be used to generate just the CC03 events. Below is a brief description of the WW generators used in the analysis.

KORALW

KORALW [81, 82] generates $q\bar{q}q\bar{q}$, $q\bar{q}\ell\bar{\nu}_\ell$ and $\ell^+\nu_\ell\ell'^-\bar{\nu}_{\ell'}$ final states through the process $e^+e^- \to W^+W^- \to f_1\bar{f}_2 f_3\bar{f}_4$. The latest version of KORALW can generate four-fermion final states from all possible four-fermion processes, like the other four-fermion generators. However, that version was not used in this analysis. KORALW contains initial state QED corrections [83]. It contains gauge boson widths and a Coulomb correction. It also has a naive QCD correction. Any of the 14 anomalous couplings given by the standard Lagrangian, equation 3.1, may be *switched on*.

PYTHIA and HERWIG

PYTHIA [84] and HERWIG [85] are general purpose Monte Carlo generators for multi-particle production in high energy physics. They can both generate the four-fermion final states via the $e^+e^- \to W^+W^- \to f_1\bar{f}_2 f_3\bar{f}_4$ process. Being general purpose generators that can produce events for proton-proton and electron-proton colliders as well as electron-positron colliders, they do not contain the detailed modelling of all the specific corrections that are contained in the dedicated four-fermion generators. Both generators only generate events with Standard Model couplings.

5.2.3 Background Generators

A number of different Monte Carlo generators are used to produce simulation of the possible background events. For the $Z^0/\gamma \to q\bar{q}$ events both PYTHIA and HERWIG are used. The two-photon events are much less well understood than the other processes and there are a number of different generators available, each of which model the processes slightly differently. Of the dedicated two-photon generators the PHOJET [86, 87] generator is used to model some of the processes. In addition to PHOJET, the HERWIG and PYTHIA generators are also used to simulate some events. A combination of the three is used to produce the final sample of two-photon events.

5.2.4 Jet Fragmentation

The Monte Carlo generators produce the final four vectors of all the particles in the main process. However the quarks and τ leptons fragment into showers of particles. To model this process and also Final State Radiation (FSR), hadronisation programs are employed. There are two main fragmentation schemes used at OPAL; JETSET [84] which is the fragmentation scheme from PYTHIA, and the HERWIG fragmentation scheme. Both these hadronisation programs have been tuned using data measured at OPAL [88, 89] to give the best representation of true fragmentation.

5.2.5 Monte Carlo Samples Used

Table 5.1 shows all the fully detector simulated Monte Carlo samples used in this analysis. In addition to these, a number of generator level samples of EXCALIBUR, ERATO and KORALW were used that had not been subjected to detector simulation. A key to some of the important points in

table 5.1 is given below

† contains $e^+e^- \to \ell\ell\ell\ell$ where $\ell = \mu, \tau, \nu_e, \nu_\mu$ and ν_τ. Events not included are eeff (f=e,μ,τ,q) and 4-ν.

‡ contains final states $\ell\nu q\bar{q}$, $\ell\ell q\bar{q}$ and $\nu\nu q\bar{q}$.

⋆ contains all possible four quark final states.

∗ TGC indicates the sample contains events sensitive to TGCs only.

◁ non-TGC indicates the sample contains events insensitive to TGCs only.

⊕ $q\bar{q}\tau\nu_\tau$ final states only.

◇ events supplied with weights to make sample Standard Model or with various anomalous couplings present.

Run No.	Generator	type	No. events	Model	Frag. scheme
8027	PYTHIA	CC03	100000	Standard	JETSET
8099	HERWIG	CC03	100000	Standard	HERWIG/JETSET
8626	KORALW	CC03	200000	Standard	JETSET
9865	GRC4F	CC03	246570	Standard	JETSET
9866	GRC4F	CC03	246570	Standard	HERWIG
8263	EXCALIBUR	CC03	200000	Standard	JETSET
8264	EXCALIBUR	CC03	100000	$\Delta\kappa_\gamma = +1$	JETSET
8265	EXCALIBUR	CC03	100000	$\Delta\kappa_\gamma = -1$	JETSET
8266	EXCALIBUR	CC03	100000	$\Delta g_1^z = +1$	JETSET
8267	EXCALIBUR	CC03	100000	$\Delta g_1^z = -1$	JETSET
8268	EXCALIBUR	CC03	100000	$\lambda = +1$	JETSET
8269	EXCALIBUR	CC03	100000	$\lambda = +1$	JETSET
7844	GRC4F	4-fermion (llll)†	15855	Standard	JETSET
8055	GRC4F	4-fermion (llqq)‡	43396	Standard	JETSET
7846	GRC4F	4-fermion (qqqq)*	42088	Standard	JETSET
8100	EXCALIBUR	4-fermion (TGC)*	460000	Standard	JETSET
8101	EXCALIBUR	4-fermion (non-TGC)$^\triangleleft$	52300	Standard	JETSET
9103	EXCALIBUR	4-fermion (qqtv)$^\oplus$	61000	Standard	JETSET
8251	EXCALIBUR	4-fermion (TGC)	100000	$\Delta\kappa_\gamma = +2$	JETSET
8105	EXCALIBUR	4-fermion (TGC)	100000	$\Delta\kappa_\gamma = +1$	JETSET
8252	EXCALIBUR	4-fermion (TGC)	100000	$\Delta\kappa_\gamma = +0.5$	JETSET
8253	EXCALIBUR	4-fermion (TGC)	100000	$\Delta\kappa_\gamma = -0.5$	JETSET
8106	EXCALIBUR	4-fermion (TGC)	100000	$\Delta\kappa_\gamma = -1$	JETSET
8254	EXCALIBUR	4-fermion (TGC)	100000	$\Delta\kappa_\gamma = -2$	JETSET
8255	EXCALIBUR	4-fermion (TGC)	100000	$\Delta g_1^z = +2$	JETSET
8107	EXCALIBUR	4-fermion (TGC)	100000	$\Delta g_1^z = +1$	JETSET
8256	EXCALIBUR	4-fermion (TGC)	100000	$\Delta g_1^z = +0.5$	JETSET
8257	EXCALIBUR	4-fermion (TGC)	100000	$\Delta g_1^z = -0.5$	JETSET
8108	EXCALIBUR	4-fermion (TGC)	100000	$\Delta g_1^z = -1$	JETSET
8258	EXCALIBUR	4-fermion (TGC)	100000	$\Delta g_1^z = -2$	JETSET
8259	EXCALIBUR	4-fermion (TGC)	100000	$\lambda = +2$	JETSET
8109	EXCALIBUR	4-fermion (TGC)	100000	$\lambda = +1$	JETSET
8260	EXCALIBUR	4-fermion (TGC)	100000	$\lambda = +0.5$	JETSET
8261	EXCALIBUR	4-fermion (TGC)	100000	$\lambda = -0.5$	JETSET
8110	EXCALIBUR	4-fermion (TGC)	100000	$\lambda = -1$	JETSET
8262	EXCALIBUR	4-fermion (TGC)	100000	$\lambda = -2$	JETSET
9019	ERATO	4-fermion (TGC)	200000	Standard$^\diamond$	JETSET
5078	PYTHIA	quark-pairs	500000	Standard	JETSET
5080	HERWIG	quark-pairs	100000	Standard	JETSET
1045	PYTHIA	2-photon	200000	Standard	JETSET
1049	HERWIG	2-photon	150000	Standard	HERWIG
1055	PYTHIA	2-photon	5000	Standard	JETSET
1042	PHOJET	2-photon	999999	Standard	JETSET

Table 5.1: *The fully detector simulated Monte Carlo samples used in this analysis.*

5.3 Detector Simulation

Detector simulation is accomplished by passing the four-vectors of all the particles produced by the Monte Carlo generator into a computer simulation of the OPAL detector.

This is done by the GOPAL [90] Monte Carlo program. This is based on the CERN GEANT [91] simulation package. The event generator produces four-vector files for the particles. These are passed to GOPAL which simulates the detector response, all the default constants for each of the OPAL subdetectors are also passed into GOPAL. The output of GOPAL is a copy of the constants used and the simulated "raw data." These can then be passed into the ROPE program in the same way as the "real data" from the OPAL detector. DSTs can be produced and analysed in the same way for the Monte Carlo as is done for the data.

A schematic for this process is shown in figure 5.6.

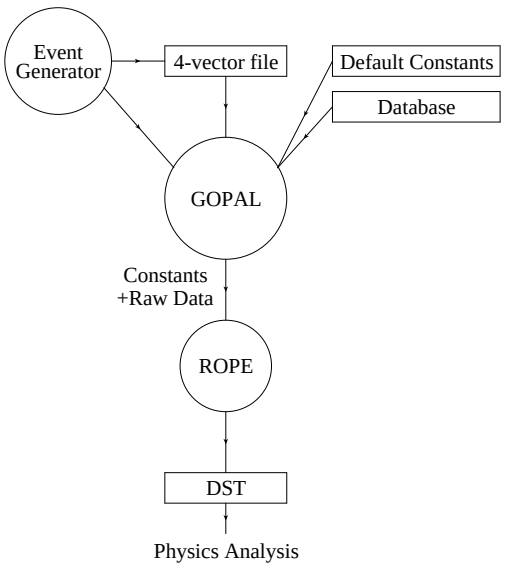

Figure 5.6: *Outline of the organisation of the GOPAL program.*

5.4 Data Selection and Reconstruction

The selection and reconstruction of $q\bar{q}\ell\bar{\nu}_\ell$ events consists of two basic phases. Firstly the selection of $q\bar{q}\ell\bar{\nu}_\ell$ events is made using the WW package [92], a set of routines developed by OPAL and designed for the study of W-pair events. This selection is the same as used by OPAL to measure the total W-pair production cross-section [66] and therefore does not require completely reconstructed events.

For the measurement of TGCs and the study of W decays, the tracks in the event need to be more cleanly reconstructed. The second phase of selection and reconstruction involves taking the events selected by the previous process and performing kinematic fits on them, this then rejects any poorly reconstructed events. This process is achieved using the WV package [93], which is a set of routines designed to complement the WW package.

5.4.1 Selection of $q\bar{q}\ell\bar{\nu}_\ell$ Events

This selection of events is based on that used by OPAL at the lower centre-of-mass energies of 172 GeV and 183 GeV, described in detail in [94, 95]. Due to the higher energy, a number of the cuts have slightly changed, but the basic structure remains the same.

Firstly, it should be noted that only events that fail the $\ell^+\nu_\ell\ell'^-\bar{\nu}_{\ell'}$ selection [66] are considered as possible $q\bar{q}\ell\bar{\nu}_\ell$ events. Also the full $q\bar{q}\tau\bar{\nu}_\tau$ selection is only applied to events that have already failed the $q\bar{q}e\bar{\nu}_e$ and $q\bar{q}\mu\bar{\nu}_\mu$ selection.

The selection of the $q\bar{q}e\bar{\nu}_e$ and $q\bar{q}\mu\bar{\nu}_\mu$ events proceeds in four stages:

- Identification of the candidate lepton.
- Preselection.

- Relative likelihood selection.
- Event Categorisation.

This selection will select some $q\bar{q}\tau\bar{\nu}_\tau$ events as $q\bar{q}e\bar{\nu}_e$ or $q\bar{q}\mu\bar{\nu}_\mu$ events. These are separated out in the event categorisation section. Below, each of these stages is described in detail. Any events not selected as $q\bar{q}e\bar{\nu}_e$ and $q\bar{q}\mu\bar{\nu}_\mu$ are then passed through the $q\bar{q}\tau\bar{\nu}_\tau$ selection, which is discussed later in this section.

For the preselection and likelihood selection a number of variables are used, before going on to discuss how these processes proceed, these variables are defined below:

- d_0 $r-\phi$ impact parameter.
- z_0 z impact parameter.
- $P(\ell)$, the lepton identification probability for the candidate lepton track. For example P(e) is the electron identification probability and $P(\mu)$ is the muon identification probability.
- E_{lepton}, the energy of the lepton candidate. For the electron this is calculated using the electromagnetic calorimeter energy. For the muons the track momentum is used.
- p_{lepton}, the momentum of the lepton track. For the three prong tau decay it is the sum of the momenta of the three tracks.
- I_{200}, the sum of the lepton candidate track momentum and ECAL cluster energy within a 200 mrad cone about the candidate track (excluding clusters associated with the candidate track).
- E/p, the ratio of the energy of the associated ECAL clusters to the track momentum.

- $\Delta\phi_{\mathrm{EC/CT}}$, difference between the ϕ measurement from the track and from the associated ECAL cluster.
- $\frac{\mathrm{dE}}{\mathrm{dx}}$, the energy loss of the particle in the tracking chamber.
- $\mathrm{X_{GCONV}}$, the output of the IDGCON conversion finder which checks if the track is compatible with an electron or positron originating from a gamma conversion.
- $\mathrm{N_{blk}^{90}}$, the number of blocks containing 90% of the ECAL cluster energy.
- $\mathrm{N_{HC2}}$, the number of layers with hits in the first two layers of an associated hadron calorimeter cluster.
- $\mathrm{N_{HCAL}}$, the number of HCAL layers hit in an associated HCAL cluster.
- $\mathrm{N_{muon}}$, the number of muon hits associated with track.
- $\mathrm{X_{hits/layer}}$, the number of hits in the hadron calorimeter divided by the number of layers with hits.
- $\cos\theta_{\mathrm{lpmis}}$, the cosine of the angle between the lepton track and the missing momentum vector.
- $\sqrt{s'}$, the reconstructed invariant mass s'.
- $\mathrm{R_{vis}}$, the visible energy of the event scaled by $\sqrt{s}$.
- $\mathrm{N_{CT}}$, the number of tracks in the central tracking chamber which passed the WW quality cuts.
- $\mathrm{N_{CT}^{MIN}}$, the minimum number of tracks in a jet when the event (including the lepton candidate) is forced into three jets.
- $\mathrm{N_{EC}}$, the number of electromagnetic calorimeter clusters.

- R_{shw}, the total ECAL energy scaled to $\sqrt{s}$.
- E_{FD}, the energy in the calorimeter of the low angle detectors.
- E_{γ}, the energy of the highest energy isolated photon.
- $|\vec{p}|$, the scalar momentum of the lepton.
- $P(s')$, the probability from a kinematic fit which estimates the reconstructed invariant mass of the event, $\sqrt{s'}$.
- $\cos\theta_{mis}$, the cosine of the angle the missing momentum vector makes with the beam axis.
- $\sum P_t$, the transverse momentum of the event relative to the beam axis, calculated using tracks, ECAL clusters and HCAL clusters.
- $N_{CT}^{lepton-jet}$, the number of tracks in the jet containing the lepton when the event (including lepton candidate) is forced into three jets.
- E_{τ}, the sum of the candidate track momentum and energies of the ECAL clusters within a 200 mrad cone about the candidate track (not including clusters associated with the candidate track).
- I_{200}^{CT}, the sum of the track momentum of all the tracks within a 200 mrad isolation cone.
- $I_{200-500}$, the sum of the track momentum and ECAL energy of all the tracks and ECAL clusters within a 200-500 mrad isolation annulus around the candidate track.
- $\cos\theta_{\ell\vec{p}}$, the cosine of the angle between the track momentum and the missing momentum vector.

- M_τ, the invariant mass calculated from the track momentum and energies of ECAL clusters within a 200 mrad cone about the candidate track.
- $\cos\theta_\ell$, cosine of the polar angle of the lepton candidate.
- E_{qq}, energy of the jet-jet system.
- y_{23}, the y-cut value for the transition between two and three jets.
- $\cos\theta_{\ell,(\mathrm{jet})}$, cosine between the lepton and the nearest jet axis.

Identification of Lepton Candidates

For every event two lepton candidates are selected. The track in the event which is most consistent with being an electron and the track most consistent with being a muon from the decay of a W boson into a lepton ($W \to \ell\bar{\nu}_\ell$) are taken as the lepton candidates. Some events will obviously not contain a lepton, but a track will still be assigned as a lepton however improbable. This procedure does not require explicit lepton identification and is designed to maximise efficiency. For each track in an event which passes the WW112 track quality requirements, a likelihood function is used to give the probability that the track selected arose from a $W \to e\bar{\nu}_e$ P(e), or from a $W \to \mu\bar{\nu}_\mu$ decay, P(μ). The WW112 track quality requirements are:

- Momentum < 100 GeV.
- Transverse momentum > 150 MeV.
- $d_0 < 2$ cm.
- $z_0 < 25$ cm.

- χ^2 per degree of freedom, in both $r-\phi$ and z, less than 100.
- At least half the maximum possible number of CJ hits for a track at the measured value of $\cos\theta$ with an absolute minimum of 20 hits.
- Tracks crossing the anode plane, $7.9^o < q.\phi_{\rm CJ} < 10.5^o$, are required to be well measured, $\sigma_p/p < 0.5$. Where q is the measured charge of the track and $\phi_{\rm CJ}$ is the local azimuthal angle of the track within the CJ sector.

The variables used in the likelihood function can be split into two groups. Firstly those that represent the probability of the track being due to a lepton, namely the energy loss of the track through the tracking chamber and the number of hits in the hadron calorimeter. The second group are variables that represent the probability that the track came from the decay of a W boson, such as the energy deposited in the electromagnetic calorimeter. Table 5.2 lists all the variables used in the likelihood calculation.

For each variable a probability is calculated from comparison with a reference histogram. There is a reference histogram for each flavour of lepton, these are derived from large samples of Monte Carlo events. To calculate the overall probability for each track, the probabilities for each variable are multiplied together. The track with the highest P(e) is taken as the candidate electron in the $\rm W^+W^- \to q\bar{q}e\bar{\nu}_e$ selection and the track with the highest P(μ) is taken as the candidate muon in the $\rm W^+W^- \to q\bar{q}\mu\bar{\nu}_\mu$ selection. At this stage no events are rejected, so every event will have one electron and one muon candidate.

The use of this many variables ensures that the identification of the lepton candidate is extremely efficient. Studies using Monte Carlo show that for

Variable	$W \to e\bar{\nu}_e$	$W \to \mu\bar{\nu}_\mu$
p_{lepton}		$\surd$
E_{lepton}	$\surd$	$\surd$
I_{200}	$\surd$	$\surd$
E/p	$\surd$	
$\Delta\phi_{EC/CT}$	$\surd$	
dE/dx	$\surd$	
X_{GCONV}	$\surd$	
N^{90}_{blk}	$\surd$	
N_{HC2}	$\surd$	
N_{HCAL}		$\surd$
N_{MUON}		$\surd$
$X_{\text{hits/layer}}$		$\surd$

Table 5.2: *Variables used to calculate the likelihood of the electron and muon lepton candidate.*

events where the lepton track passes the WW track quality cuts, the following efficiencies are possible. In 98.1% of the $W^+W^- \to q\bar{q}e\bar{\nu}_e$ events the correct track is identified as the lepton and in 99.1% of the $W^+W^- \to q\bar{q}\mu\bar{\nu}_\mu$ events the correct track is identified as the lepton.

Preselection

The preselection cuts are applied to remove background events that are obviously not $W^+W^- \to q\bar{q}\ell\bar{\nu}_\ell$ events, such as the two-photon events. It also removes a significant fraction of the $Z^0/\gamma \to q\bar{q}$ events.

A number of cuts are applied to both the $W^+W^- \to q\bar{q}e\bar{\nu}_e$ and $W^+W^- \to q\bar{q}\mu\bar{\nu}_\mu$ selections, these are:

- $E_{lepton} > 10$ GeV
- $\cos\theta_{lpmis} < 0.9$
- $P(e), P(\mu) > 10^{-9}$
- $0.3 < R_{vis} < 1.2$
- $N_{CT} > 5$
- $R_{shw} > 0.1$
- $N_{EC} > 7$
- $E_{FD} < (\sqrt{s} - M_{Z^0} - 10\text{GeV})$
- $E_{\gamma} < (\sqrt{s} - M_{Z^0} - 10\text{GeV})$

In addition to these, the reconstructed s' is required to be greater than 60 GeV^2 for the $W \to e\bar{\nu}_e$ and greater than 90 GeV for the $W \to \mu\bar{\nu}_\mu$.

Further cuts are applied to the $W^+W^- \to q\bar{q}e\bar{\nu}_e$ selection designed to reduce the backgrounds from two-photon events, which can resemble $W^+W^- \to q\bar{q}e\bar{\nu}_e$ events and also further reduce the backgrounds from radiative $Z^0/\gamma \to q\bar{q}$ events where the initial state photon converts into an electron-positron pair and one of the leptons is lost down the beam pipe. The cuts designed to reduce these backgrounds are:

- If E_{lepton} is within 12 GeV of $(\sqrt{s} - M_{Z^0})$ then the following are applied:
  - $\to$ Event is rejected if the track of the lepton candidate and an oppositely charged track appear to have originated from the conversion of a photon.
  - $\to$ $5 < \frac{dE}{dx} < 15$ keVcm^{-1}.

→ If $\frac{dE}{dx}$ is not well measured the event is rejected.

→ If the electron candidates within 32°of the beam-pipe then $|\vec{p}| > 10$ GeV.

- If the lepton candidate appears to have come from the conversion of a photon and the kinematic fit converged, then $P(\sqrt{s}) < 0.01$.

- $|\cos\theta_{mis}| < 0.975$. This cut is designed to reject events where a lepton passing down the beam pipe is mistaken as the missing momentum of a neutrino.

Relative Likelihood Selection

For events that have passed the initial preselection, a likelihood is given to them that they are a $W^+W^- \to q\bar{q}e\bar{\nu}_e$ event ($L^{q\bar{q}e\nu}$) or a $W^+W^- \to q\bar{q}\mu\bar{\nu}_\mu$ event ($L^{q\bar{q}\mu\nu}$). A number of variables are looked at to calculate this likelihood. These variables are shown in table 5.3.

A probability is calculated for each variable by comparing the observed value with expected distributions obtained from Monte Carlo events. The likelihood $L^{q\bar{q}\ell\nu}$ is calculated as the product of these probabilities. Using the same approach a likelihood is also calculated for the event being a background $Z^0/\gamma \to q\bar{q}$ event ($L^{q\bar{q}}$). A relative likelihood is then calculated for the event. For example, the relative likelihood that the event is a $W^+W^- \to q\bar{q}e\bar{\nu}_e$ would be:

$$\mathcal{L}^{q\bar{q}e\nu} = \frac{L^{q\bar{q}e\nu}}{L^{q\bar{q}e\nu} + f \times L^{q\bar{q}}} \tag{5.1}$$

Where f is the expected ratio of preselected background to signal cross-sections calculated from Monte Carlo. Events with $\mathcal{L}^{q\bar{q}e\nu} > 0.5$ are selected as

Variable	$W^+W^- \to q\bar{q}e\bar{\nu}_e$	$W^+W^- \to q\bar{q}\mu\bar{\nu}_\mu$
E_{lepton}	$\surd$	$\surd$
I_{200}	$\surd$	$\surd$
$P(\ell)$	$\surd$	$\surd$
$\cos\theta_{mis}$	$\surd$	$\surd$
R_{vis}	$\surd$	$\surd$
$\sum PT$	$\surd$	$\surd$
$\cos\theta_{lpmis}$	$\surd$	$\surd$
$P(s')$		$\surd$
$N_{CT}^{lepton-jet}$		$\surd$
$\sqrt{s'}$	$\surd$	$\surd$

Table 5.3: *Variables used to calculate the relative likelihood selection of the* $W^+W^- \to q\bar{q}e\bar{\nu}_e$ *and* $W^+W^- \to q\bar{q}\mu\bar{\nu}_\mu$ *events.*

$W^+W^- \to q\bar{q}e\bar{\nu}_e$ events and those with $\mathcal{L}^{q\bar{q}\mu\nu} > 0.5$ are selected as $W^+W^- \to q\bar{q}\mu\bar{\nu}_\mu$ events. Events can be selected as both of these. The combination of preselection and likelihood selection rejects over 99.5% of the $Z^0/\gamma \to q\bar{q}$ background and is approximately 90% efficient for $W^+W^- \to q\bar{q}e\bar{\nu}_e$ and $W^+W^- \to q\bar{q}\mu\bar{\nu}_\mu$ events.

Event Categorisation

The preselection and likelihood selection are optimised to separate the $W^+W^- \to q\bar{q}e\bar{\nu}_e$ and $W^+W^- \to q\bar{q}\mu\bar{\nu}_\mu$ events from the background $Z^0/\gamma \to q\bar{q}$ events. As a result of the relative likelihood selection, events are classified as $W^+W^- \to q\bar{q}e\bar{\nu}_e$ or $W^+W^- \to q\bar{q}\mu\bar{\nu}_\mu$ events, or as both. For the ambiguous events, a relative likelihood is constructed to discriminate between the two possible cases, so all events can only be put in just one category.

However, approximately 30% of the events will actually be $W^+W^- \to q\bar{q}\tau\bar{\nu}_\tau$ events. So all events passing the $W^+W^- \to q\bar{q}e\bar{\nu}_e$ selection are reclassified as $W^+W^- \to q\bar{q}e\bar{\nu}_e$ or $W^+W^- \to q\bar{q}\tau\bar{\nu}_\tau$ events. A similar procedure is undertaken for the events passing the $W^+W^- \to q\bar{q}\mu\bar{\nu}_\mu$ selection.

New relative likelihoods are calculated. The predominant $W^+W^- \to q\bar{q}\tau\bar{\nu}_\tau$ events that are selected as $W^+W^- \to q\bar{q}e\bar{\nu}_e$ events are where the tau lepton decays into an electron, $W^+W^- \to q\bar{q}\tau\bar{\nu}_\tau \to q\bar{q}e\bar{\nu}_e\nu_\tau\bar{\nu}_\tau$, or a one prong hadronic state, $W^+W^- \to q\bar{q}\tau\bar{\nu}_\tau \to q\bar{q}\pi^\pm n\pi^0\nu_\tau\bar{\nu}_\tau$. Likelihoods are calculated for the event being from each of these two processes using the same variables as before. Relative likelihoods are then formed to discriminate between the $W^+W^- \to q\bar{q}e\bar{\nu}_e$ and $W^+W^- \to q\bar{q}\tau\bar{\nu}_\tau$ events. An example of the relative likelihood between $W^+W^- \to q\bar{q}e\bar{\nu}_e$ and $W^+W^- \to q\bar{q}\tau\bar{\nu}_\tau \to q\bar{q}e\bar{\nu}_e\nu_\tau\bar{\nu}_\tau$ is shown below:

$$\mathcal{L}^{q\bar{q}e\bar{\nu}_e\nu_\tau\bar{\nu}_\tau} = \frac{L^{q\bar{q}e\bar{\nu}_e\nu_\tau\bar{\nu}_\tau}}{L^{q\bar{q}e\bar{\nu}_e\nu_\tau\bar{\nu}_\tau} + L^{q\bar{q}e\nu}} \tag{5.2}$$

If any of these relative likelihoods are greater than 0.5 the event is categorised as a $W^+W^- \to q\bar{q}\tau\bar{\nu}_\tau$ event. A similar procedure is applied to the $W^+W^- \to q\bar{q}\mu\bar{\nu}_\mu$ events to separate out the $W^+W^- \to q\bar{q}\tau\bar{\nu}_\tau \to q\bar{q}\mu\bar{\nu}_\mu\nu_\tau\bar{\nu}_\tau$ and $W^+W^- \to q\bar{q}\tau\bar{\nu}_\tau \to q\bar{q}\pi^\pm n\pi^0\nu_\tau\bar{\nu}_\tau$ events from them.

Selection of $W^+W^- \to q\bar{q}\tau\bar{\nu}_\tau$ Events

The only events so far categorised as $W^+W^- \to q\bar{q}\tau\bar{\nu}_\tau$ events are those that passed either the $W^+W^- \to q\bar{q}e\bar{\nu}_e$ or $W^+W^- \to q\bar{q}\mu\bar{\nu}_\mu$ selection. These amount to only about 30% of the total number of $W^+W^- \to q\bar{q}\tau\bar{\nu}_\tau$ events. All events that failed both the $W^+W^- \to q\bar{q}e\bar{\nu}_e$ and $W^+W^- \to q\bar{q}\mu\bar{\nu}_\mu$ selection are now subjected to the $W^+W^- \to q\bar{q}\tau\bar{\nu}_\tau$ selection. The selection is designed to be sensitive to the four main tau decay channels, namely the

electron, the muon, the hadronic one prong and the hadronic three prong, $W^+W^- \to q\bar{q}\tau\bar{\nu}_\tau \to q\bar{q}\pi^\pm\pi^\pm\pi^\mp\nu_\tau\bar{\nu}_\tau$.

Variable	$\tau \to$ e	$\tau \to \mu$	$\tau \to$ 1h	$\tau \to$ 3h
p_{lepton}		$\surd$		$\surd$
E_{lepton}	$\surd$	$\surd$		
E_τ			$\surd$	
I_{200}	$\surd$	$\surd$		
I^{CT}_{200}			$\surd$	$\surd$
$I_{200-500}$			$\surd$	$\surd$
E/p	$\surd$			
$\Delta\phi_{EC/CT}$	$\surd$			
dE/dx	$\surd$			
X_{GCONV}	$\surd$			
N^{90}_{blk}	$\surd$			
N_{HC2}	$\surd$			
N_{HCAL}		$\surd$		
N_{MUON}		$\surd$		
$X_{\mathrm{hits/layer}}$		$\surd$		
$\cos\theta_{\ell\vec{p}}$			$\surd$	
$N^{\mathrm{lepton-jet}}_{\mathrm{CT}}$			$\surd$	$\surd$
M_τ			$\surd$	$\surd$

Table 5.4: *Variables used to calculate the likelihood of the tau lepton candidate in the four tau decay channels.*

The selection proceeds as for the $W^+W^- \to q\bar{q}e\bar{\nu}_e$ and $W^+W^- \to q\bar{q}\mu\bar{\nu}_\mu$ channels. The identification of the lepton candidate is replaced by the identification of the track most consistent with being from each of the four possible

tau decay channels. For the three prong tau decay the combination of three tracks most consistent with being from this process is identified. The variables used in this process are shown in table 5.4. The efficiency of this identification is less than that for the electrons and muons, but still a respectable 79.5% of events are expected to have the correct track(s) identified as the tau.

Now preselection is applied. A list of all the cuts applied in the preselection for each τ decay channel is shown in table 5.9.

The likelihood selection applied uses the same variables as for the other leptons, but with the addition of more information about the tracks. An event is selected as coming from a certain channel if the relative likelihood is greater than 0.75. Once again, events passing more than one $W^+W^- \rightarrow q\bar{q}\tau\bar{\nu}_\tau$ likelihood selection are subjected to a new likelihood selection using a subset of variables to ensure it enters into the final data set only once. A list of all the variables used in the likelihood selection can be found in table 5.5.

Performance of Selection

The performance of the selection on CC03 Monte Carlo signal events is shown in table 5.6. The overall selection efficiency of the signal events is estimated to be $(87.7 \pm 1.1)\%$.

Figure 5.7 shows the $\cos\theta_W$ distributions of all Monte Carlo events compared to that of selected events only from a sample of CC03 Monte Carlo.

Variable	$\tau \to$ e	$\tau \to \mu$	$\tau \to$ 1h	$\tau \to$ 3h
E_{lepton}	$\surd$	$\surd$	$\surd$	$\surd$
$\mathrm{PR}(\ell)$	$\surd$	$\surd$		$\surd$
I_{200}	$\surd$	$\surd$		$\surd$
I_{200}^{CT}			$\surd$	
$I_{200-500}$	$\surd$	$\surd$	$\surd$	
Y_{23}			$\surd$	$\surd$
$\cos\theta_{\mathrm{mis}}$	$\surd$	$\surd$	$\surd$	$\surd$
R_{vis}	$\surd$	$\surd$	$\surd$	$\surd$
R_{mis}			$\surd$	$\surd$
$\sum PT$	$\surd$	$\surd$	$\surd$	$\surd$
$\cos\theta_{\mathrm{lpmis}}$			$\surd$	$\surd$
$\mathrm{P}(\sqrt{s'})$			$\surd$	$\surd$
$\sqrt{s'}$	$\surd$	$\surd$	$\surd$	$\surd$
$\mathrm{N}_{\mathrm{CT}}^{\mathrm{min}}$	$\surd$	$\surd$	$\surd$	$\surd$
$\mathrm{N}_{\mathrm{CT}}^{\mathrm{lepton-jet}}$			$\surd$	
E_{qq}			$\surd$	
$\cos\theta_{\ell,(\mathrm{jet})}$	$\surd$	$\surd$	$\surd$	$\surd$

Table 5.5: *Variables used to calculate the relative likelihood of the* $\mathrm{W^+W^-} \to \mathrm{q\bar{q}}\tau\bar{\nu}_\tau$ *events. There is a different subset for each type of* τ *decay.*

The number of background events expected to be selected by this method calculated from Monte Carlo are shown in table 5.10. The expected selected cross-section is shown, along with the number of events this corresponds to in the 189 GeV data. Table 5.7 shows a summary of all these results, along with the actual number of events selected from the OPAL data. Good agreement is seen between the expected number of events and the selected number of

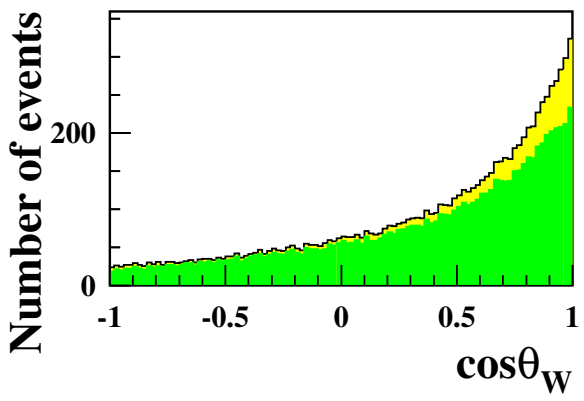

Figure 5.7: *The* $\cos\theta_{\mathrm{W}}$ *distributions calculated for a sample of CC03 Monte Carlo. The yellow histogram represents all events and the green histogram is for selected events only.*

events. The 1246 events actually selected consists of 389 $\mathrm{q\bar{q}e\bar{\nu}_e}$, 420 $\mathrm{q\bar{q}\mu\bar{\nu}_\mu}$ and 437 $\mathrm{q\bar{q}\tau\bar{\nu}_\tau}$.

selected as	$\mathrm{W^+W^-} \rightarrow \mathrm{q\bar{q}e\bar{\nu}_e}$	$\mathrm{W^+W^-} \rightarrow \mathrm{q\bar{q}\mu\bar{\nu}_\mu}$	$\mathrm{W^+W^-} \rightarrow \mathrm{q\bar{q}\tau\bar{\nu}_\tau}$
$\mathrm{q\bar{q}e\bar{\nu}_e}$	85.42 ± 0.84 %	0.12 ± 0.01 %	3.80 ± 0.50 %
$\mathrm{q\bar{q}\mu\bar{\nu}_\mu}$	0.15 ± 0.01 %	89.16 ± 0.80 %	4.30 ± 0.50 %
$\mathrm{q\bar{q}\tau\bar{\nu}_\tau}$	4.55 ± 0.50 %	4.41 ± 0.50 %	68.44 ± 1.44 %

Table 5.6: *The performance of the selection of events. Shown is the efficiency of selection each type of event. The first column indicates what the event was selected as and then the following columns indicate what percentage of each type of generated events was selected as the type indicated.*

Selected as	$W^+W^- \to q\bar{q}\ell\bar{\nu}_\ell$
Efficiency [%]	87.7 ± 1.1
Signal events	1173 ±28
4-fermion, TGC-dep.	24 ± 4
4-fermion, TGC-indep.	34 ± 3
$Z^0/\gamma \to f\bar{f}$	48 ± 5
Two-photon	3 ± 2
Total Background	111 ± 8
Total expected	1284 ± 29
Observed	1246

Table 5.7: *The expected number of events selected from each of the different processes. Also shown is the total number of observed events at 189 GeV.*

5.4.2 Event Reconstruction

So far, all the events that are likely to arise from W-pair production have been selected, however some of these may have very poorly measured elements and so the angular distribution of the particles cannot be well reconstructed. For the analysis of the W spins it is vital to have well reconstructed angles, so events without these need to be removed from the sample.

All events will have a track identified as the lepton. The electron direction is reconstructed by the tracking detectors and the energy is measured in the electromagnetic calorimeters. For the muons the momentum is measured using the tracking detectors. The case of the $W^+W^- \to q\bar{q}\tau\bar{\nu}_\tau$ event is slightly different, but this will either have one track or a narrow jet that is identified as the tau candidate. The energy of the τ candidate can only be derived from a kinematic fit.

Now, all the other tracks and calorimeter clusters can be said to have

come from the hadronically decaying W boson. These are grouped into two jets using the Durham $k_\perp$ algorithm [68, 69, 70, 71]. The total energy and momentum of each of the jets are calculated with the method described in [96].

To improve the quality of the measurement of the kinematical variables, a series of kinematically constrained fits are used:

A. Requiring a conservation of energy and momentum, neglecting ISR.

B. Constraining in addition the reconstructed masses of the two W bosons to be equal.

C. Constraining in addition each reconstructed W mass to the average value measured at the Tevatron, M_W=80.40 GeV/c^2 [97, 98].

For the $W^+W^- \to q\bar{q}e\bar{\nu}_e$ and $W^+W^- \to q\bar{q}\mu\bar{\nu}_\mu$ events kinematic fit A is performed. This fit uses five constraints, four from conservation of energy and momentum and one from the masslessness of the neutrino. This then gives one over-constraint and, hence is called the 1c fit. Events are accepted if this fit converges with a probability larger than 0.001. This requirement rejects about 2% of the signal events and 4% of the background.

To give further improvement in the angular observables a second kinematic fit can be applied to the events which passed the 1c fit. This fit, kinematic fit C, includes an additional contribution from the invariant mass of the charged lepton-neutrino system and another from the di-jet system. These two extra constraints, requiring the two W boson masses to be constrained by the average W boson mass measured at the Tevatron [97, 98], then means that there are three over-constraints and this is then accordingly known as the 3c fit. The correct mass distribution is a Breit-Wigner with the

central value at the Tevatron value. However, due to the difficulties of including the Breit-Wigner, the W mass distribution is treated as a Gaussian. In order to simulate the expected Briet-Wigner form, the variance of the Gaussian is updated at each iteration of the kinematic fit in such a way that the probabilities of observing the current fitted W mass are equal whether calculated using the Gaussian or the Briet-Wigner. Events are accepted if the 3c fit converges with a probability greater than 0.001. Around 4% of the events fail to do this, and for these the results from the 1c fit are reverted to.

For the $W^+W^- \to q\bar{q}\tau\bar{\nu}_\tau$ events kinematical fit B is applied. In addition to the 1c fit constraints, we have the extra constraint of the W bosons having equal mass. This results in one over constraint in the $W^+W^- \to q\bar{q}\tau\bar{\nu}_\tau$ events. This fit is required to converge with a probability greater than 0.025.

About 14% of the signal events are expected to fail this fit and so are rejected, however, about 41% of the selected background are also expected to fail this fit. The fit requirements also suppress those events which were correctly identified as $W^+W^- \to q\bar{q}\tau\bar{\nu}_\tau$ events, but where the τ decay products were identified incorrectly. The fraction of such events in the sample is reduced from 18% to 12%.

Figure 5.8 shows the distribution of kinematical variables of the selected events after the kinematical fits have been performed compared to the true distributions. Reasonable agreement is seen between the two.

5.4.3 189 GeV Data Sample

A summary of the composition of the expected data sample after selection and kinematical fits is shown in table 5.8.

After selection and reconstruction of the OPAL data events at 189 GeV, there were 1246 $W^+W^- \to q\bar{q}\ell\bar{\nu}_\ell$ events selected. After the kinematic fits

were applied this number reduced to 1075 events. Of these 1075 events, 368 were $q\bar{q}e\bar{\nu}_e$, 387 were $q\bar{q}\mu\bar{\nu}_\mu$ and 320 were $q\bar{q}\tau\bar{\nu}_\tau$. The angular distributions of these events can be seen in figure 5.9. Also shown on the plots are the expected distributions for the Standard Model as well as for some non-standard cases. The expected background contribution is indicated by the hatched histogram.

Selected as	$W^+W^- \to q\bar{q}\ell\bar{\nu}_\ell$
Efficiency [%]	78.7 ± 1.1
Signal events	1053 ±25
4-fermion, TGC-dep.	11 ± 3
4-fermion, TGC-indep.	16 ± 3
$Z^0/\gamma \to f\bar{f}$	27 ± 4
Two-photon	1 ± 1
Total Background	55 ± 6
Total expected	1108 ± 27
Observed	1075

Table 5.8: *The expected number of selected events from each of the different processes after the corresponding kinematic fits have been performed. Also shown is the number of actual events selected at 189 GeV.*

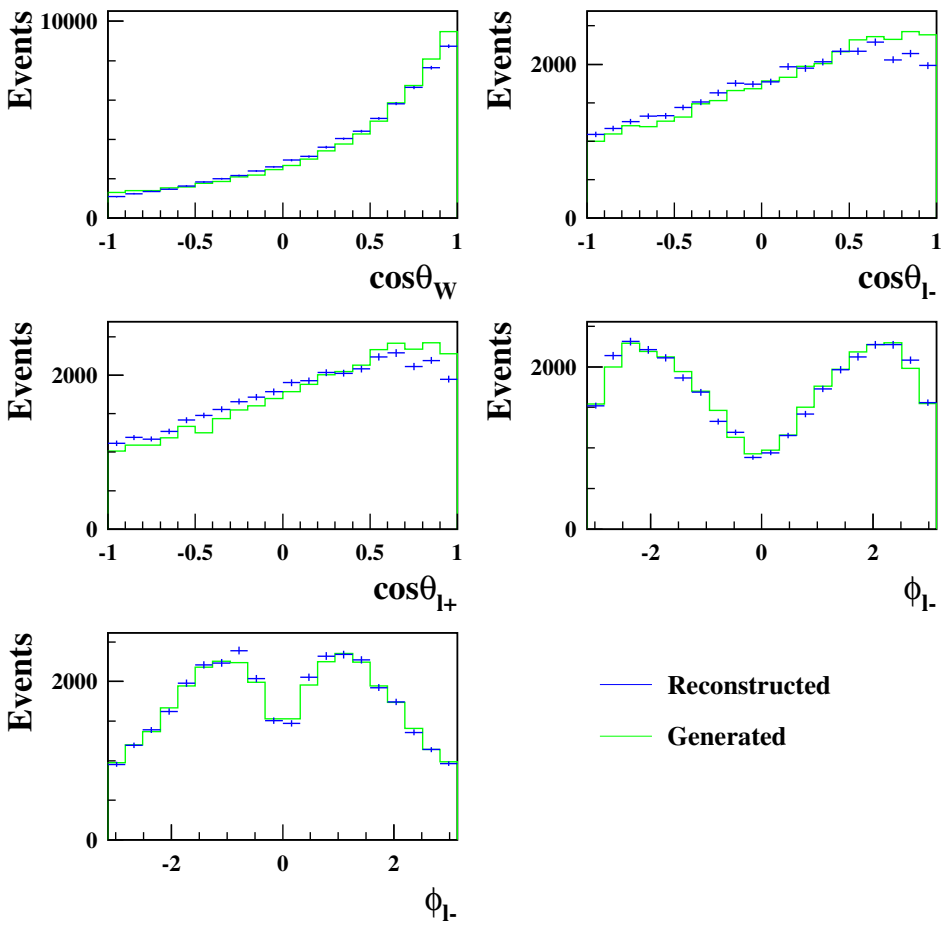

Figure 5.8: *The angular distributions for selected events only. The green histogram represents the true, generated angles. The blue points represent the reconstructed angles after the kinematic fits have been performed.*

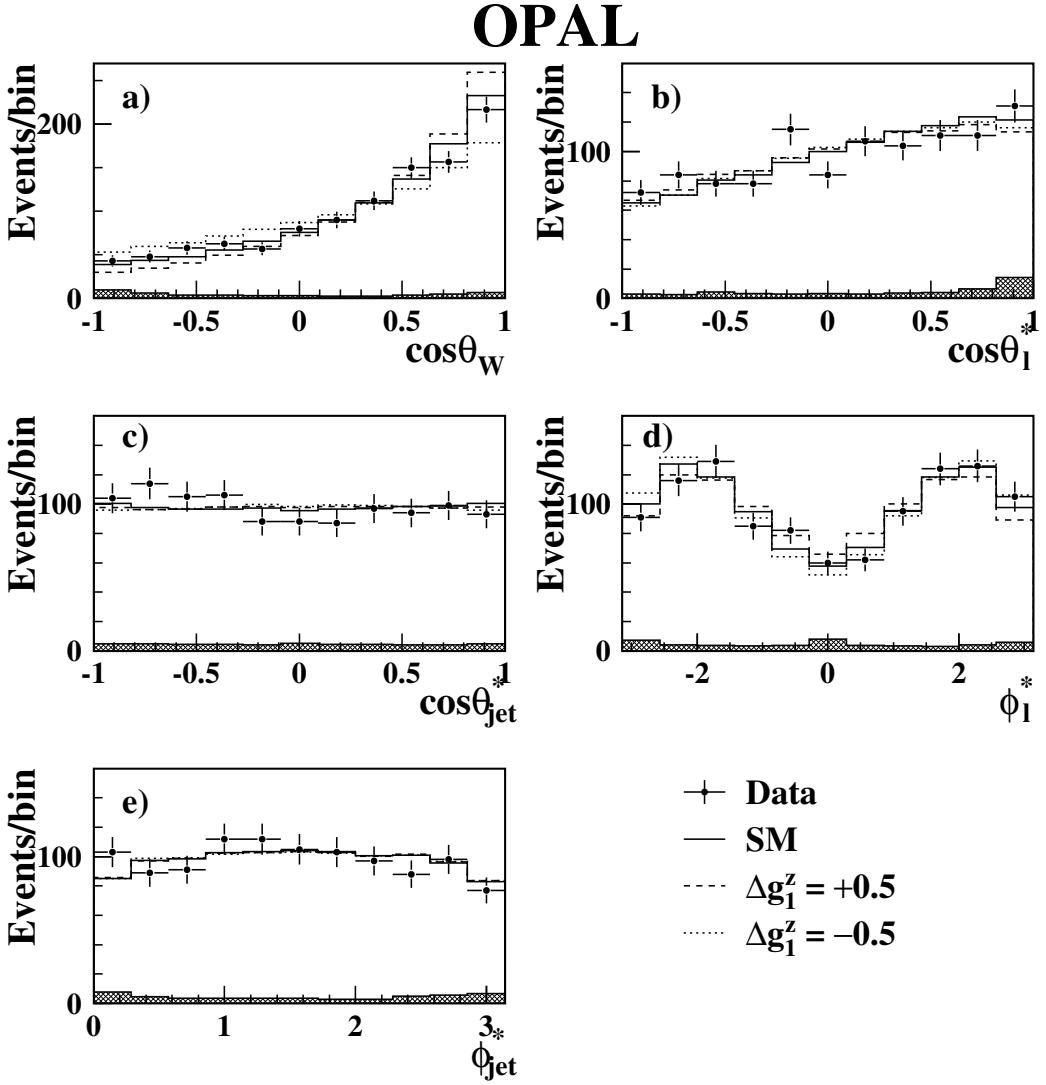

Figure 5.9: *Distributions of the kinematic variables* $\cos\theta_{\mathrm{W}}$, $\cos\theta_l^*$, $\cos\theta_{\mathrm{jet}}^*$, ϕ_l^* *and* ϕ_{jet}^*, *as obtained from the* $\mathrm{q\bar{q}}\ell\bar{\nu}_\ell$ *events. The points represent the data. The histograms show the expectation of the Standard Model and the cases* $\Delta g_1^z = \pm 0.5$. *The shaded histogram shows the non-*$\mathrm{q\bar{q}}\ell\bar{\nu}_\ell$ *background. In the case of the* W^+ *decaying to the lepton, the value of* ϕ_l^* *is shifted by* π *in order to overlay the* W^+ *and* W^- *distributions.*

Variable	$\tau \to$ e	$\tau \to \mu$	$\tau \to$ 1h	$\tau \to$ 3h
R_{shw}	>0.1	>0.1	>0.1	>0.1
R_{vis}	0.3> R_{vis} >0.8	0.3> R_{vis} >0.8	0.3> R_{vis} >1.0	0.3> R_{vis} >1.0
E_{lepton}	> 2 GeV	> 2 GeV	> 2.5 GeV	> 10 GeV
$P(\ell)$	$> 10^{-8}$	$> 10^{-6}$		
N_{CT}	> 5	> 5	> 5	> 5
N_{EC}	> 7	> 7	> 7	> 7
E_{FD}	$< (\sqrt{s} - M_{Z^0} - 10\text{GeV})$	$< (\sqrt{s} - M_{Z^0} - 10\text{GeV})$	$< (\sqrt{s} - M_{Z^0} - 10\text{GeV})$	$< (\sqrt{s} - M_{Z^0} - 10\text{GeV})$
E_γ	$< (\sqrt{s} - M_{Z^0} - 10\text{GeV})$	$< (\sqrt{s} - M_{Z^0} - 10\text{GeV})$	$< (\sqrt{s} - M_{Z^0} - 10\text{GeV})$	$< (\sqrt{s} - M_{Z^0} - 10\text{GeV})$
$\cos\theta_{ell\vec{p}}$			< 0.9	< 0.9
I_{200}	< 10 GeV	< 10 GeV		
I_{200}^{CT}				< 5 GeV
$\lvert\cos\theta_\ell\rvert$	< 0.95	< 0.95	< 0.95	< 0.95
$\lvert\cos\theta_{mis}$	< 0.95	< 0.95	< 0.95	< 0.95
E_{qq}	> 20 GeV	> 20 GeV	> 20 GeV	> 20 GeV
$\sqrt{s'}$			> 100 GeV	> 100 GeV
$\sqrt{s'}$	$< \sqrt{s} - 5\text{GeV}$	$< \sqrt{s} - 5\text{GeV}$	$< \sqrt{s} - 5\text{GeV}$	$< \sqrt{s} - 5\text{GeV}$

Table 5.9: *The cuts applied in the preselection for each τ decay channel.*

Background Process	Selected as					
	$W^+W^- \to q\bar{q}e\bar{\nu}_e$		$W^+W^- \to q\bar{q}\mu\bar{\nu}_\mu$		$W^+W^- \to q\bar{q}\tau\bar{\nu}_\tau$	
	cross-section (fb)	No. Events	Cross-section (fb)	No. Events	Cross-section (fb)	No. Events
$q\bar{q}q\bar{q}$	0 ± 1	0.0 ± 0.2	1 ± 1	0.2 ± 0.2	13 ± 3	2.4 ± 0.5
$q\bar{q}e\bar{\nu}_e$	54 ± 21	10.2 ± 3.8	2 ± 1	0.4 ± 0.2	74 ± 8	13.5 ± 1.5
$q\bar{q}\ell^+\ell^-$	2 ± 1	0.4 ± 0.2	28 ± 2	5.1 ± 0.4	46 ± 4	8.4 ± 0.7
$q\bar{q}e^+e^-$	30 ± 7	5.5 ± 1.3	0 ± 0	0 ± 0	48 ± 12	8.8 ± 2.2
$q\bar{q}\nu\nu$	0 ± 0	0 ± 0	0 ± 0	0 ± 0	32 ± 3	5.9 ± 0.5
$Z^0/\gamma \to q\bar{q}$	40 ± 8	7.3 ± 1.5	22 ± 4	4.0 ± 0.7	192 ± 29	35.1 ± 5.3
$Z^0/\gamma \to e^+e^-$	2 ± 1	0.4 ± 0.2	1 ± 1	0.2 ± 0.2	5 ± 1	0.9 ± 0.2
Two photon	7 ± 7	1.3 ± 1.3	1 ± 1	0.2 ± 0.2	7 ± 7	1.3 ± 1.3
Total	137 ± 24	25.1 ± 4.4	55 ± 6	10.1 ± 1.1	417 ± 34	76.3 ± 6.2

Table 5.10: *The expected cross-sections of the background processes that will be selected at 189 GeV. Also shown is the number of events this corresponds to for an accepted integrated luminosity of 183 pb^{-1}. For $q\bar{q}\ell^+\ell^-$ $\ell = \mu, tau$*

Chapter 6

Extracting the TGCs

In this chapter the most efficient way of extracting the values of the TGCs from the data using a SDM analysis will be discussed. It has already been shown that the semi-leptonically decaying W-pair events give the best opportunity for comprehensive analysis and so accordingly have been chosen as the signal process. Only the leptonically decaying W boson in the W-pairs gives access to all the individual elements of the single W SDM. For the TGC fits the only information used from the hadronically decaying W boson will be the W boson production angle. Both the single W SDM elements and the W boson production angle will be used to calculate the values of the TGCs.

6.1 The χ^2 Fit to the Single W SDM Elements

The approach used is to perform a χ^2 fit between the SDM elements measured in the data with the predictions made using fully simulated Monte Carlo with different TGC values.

The simple form of a χ^2 [99] is given by:

$$\chi^2 = \sum_{k=1}^{N} \left[\frac{y(x_k) - f(x_k; a)}{\sigma_k} \right]^2 \tag{6.1}$$

Here $y(x_k)$ is the measured value of an observable corresponding to a precise value of x_k, σ_k is the error on that value and $f(x_k; a)$ is the theoretical value corresponding to a precise value of x_k and is a function of the parameter that is being measured, a. The χ^2 is formed by the sum over all the measured values, k, of the observables.

In this context $y(x_k)$ is the measured value of the SDM element in bin k of $\cos\theta_{\mathrm{W}}$. The theoretical value of the SDM element in bin k, corresponding to $f(x_k; a)$, is a function of the TGC parameter being measured. The error, σ_k, is the standard deviation on the mean of the measured SDM element in bin k. The standard deviation on the mean is given by equation 6.2

$$\sigma_k = \sqrt{\frac{1}{N_k(N_k-1)} \sum_{i=1}^{N_k} \left(y(x_k)_i - y(x_k)\right)^2} \tag{6.2}$$

Where $y(x_k)_i$ is the measured value from event i and $y(x_k)$ is the mean value of all events. In effect, the projection operator $\Lambda_{\tau\tau'}$ applied to a single event gives the single measurement $y(x_k)_i$. The form of equation 6.2 to calculate the statistical error on each SDM element for each bin of $\cos\theta_{\mathrm{W}}$ is therefore given by equation 6.3.

$$\sigma^k_{\tau\tau'} = \sqrt{\frac{1}{N_k(N_k-1)} \sum_{i=i}^{N_k} (\Lambda_{\tau\tau'}(\theta^*_i; \phi^*_i)_k - \rho^{me}_{\tau\tau'}(k))^2} \tag{6.3}$$

$\Lambda_{\tau\tau'}(\theta^*_i; \phi^*_i)_k$ (i.e. $y(x_k)_i$) represents the projection operators given in equation 4.1 and $\rho^{me}_{\tau\tau'}(k)$ (i.e. $y(x_k)$) is the calculated SDM element. The χ^2 given in equation 6.1 is formed by the sum over all observables. Each SDM element is separated into N bins of $\cos\theta_{\mathrm{W}}$, so effectively represents N

observables. As there are nine SDM, it would also seem sensible to sum over all these, so the χ^2 would have the form shown in equation 6.4.

$$\chi^2 = \sum_{k=1}^{N} \sum_{\tau=-1}^{1} \sum_{\tau'=-1}^{1} \left[\frac{\rho^{me}_{\tau\tau'}(k) - \rho^{th}_{\tau\tau'}(k;a)}{\sigma_{\tau\tau'}(k)} \right]^2 \tag{6.4}$$

Due to the hermitian nature of the spin density matrix, $\rho_{\tau\tau'} = \rho^*_{\tau'\tau}$, not all the elements of the matrix are independent observables. In fact, only the diagonal elements (ρ_{++}, ρ_{--} and ρ_{00}) and three of the off-diagonal elements, ρ_{+-} ($=\rho^*_{-+}$), ρ_{+0} ($=\rho^*_{0+}$) and ρ_{-0} ($=\rho^*_{0-}$) need be included in the χ^2 fit.

The diagonal matrix elements are purely real and so represent three observables. However, as seen earlier, ρ_{+-}, ρ_{+0} and ρ_{-0} are complex, so have both real and imaginary parts. Each of these then effectively represents 2 observables, the coefficient of the real part and that of the imaginary. This then totals nine observables to which the χ^2 fit can be performed:

$$\begin{gathered} \rho_{++},\ \rho_{--},\ \rho_{00} \\ \mathrm{Re}(\rho_{+-}),\ \mathrm{Re}(\rho_{+0}),\ \mathrm{Re}(\rho_{-0}) \\ \mathrm{Im}(\rho_{+-}),\ \mathrm{Im}(\rho_{+0}),\ \mathrm{Im}(\rho_{-0}) \end{gathered} \tag{6.5}$$

The imaginary SDM observables are completely insensitive to the CP-conserving couplings and are therefore not used when fitting these couplings. When fitting the CP-violating couplings all nine observables are used.

The χ^2 given in equation 6.4 is a naive simplification that assumes each measured SDM element is completely uncorrelated from all the other SDM elements. All SDM elements in a $\cos\theta_{\mathrm{W}}$ bin are derived from the same data subset and are therefore correlated. The diagonal elements of the SDM are normalised to unity, so are highly correlated. Correlations between different bins of $\cos\theta_{\mathrm{W}}$ may be assumed to be negligible as they use different subsets

of the data sample. The correlation can be included in equation 6.4 by introducing a covariance matrix, as shown in equation 6.6[1].

$$\chi^2 = \sum_{k=1}^{N} \sum_{i=1}^{9} \sum_{j=1}^{9} \left[\left(\rho_i^{me}(k) - \rho_i^{th}(k;a)\right) \left(V_{ij}^{-1}(k)\right) \left(\rho_j^{me}(k) - \rho_j^{th}(k;a)\right) \right]^2 \tag{6.6}$$

In equation 6.6 the ρ_i and ρ_j represent the nine SDM observables indicated in equation 6.5. The covariance matrix, $V_{ij}(k)$, is given by:

$$V_{ij}(k) = \omega_{ij}(k)\sigma_i(k)\sigma_j(k) \tag{6.7}$$

Where $\omega_{ij}(k)$ is the correlation between SDM observable i and j in bin k of $\cos\theta_{\mathrm{W}}$. A statistical analysis can be applied to the data to directly calculate the covariance matrix:

$$V_{ij} = \frac{1}{N_k(N_k-1)} \left[\sum_{\epsilon=1}^{N_k} \left(\Lambda_i(\theta_\epsilon^*;\phi_\epsilon^*)_k - \rho_i^{me}(k)\right) \left(\Lambda_j(\theta_\epsilon^*;\phi_\epsilon^*)_k - \rho_j^{me}(k)\right) \right] \tag{6.8}$$

Table 6.1 shows the correlations between all the SDM observables in one bin of $\cos\theta_{\mathrm{W}}$, calculated from a SM sample of EXCALIBUR Monte Carlo data. The SDM elements were divided into eight equal bins in $\cos\theta_{\mathrm{W}}$. The results shown are for the first bin. The correlations for the other seven bins are of similar magnitude. It was found that the intra-bin correlations were negligible.

It was found that the correlations for non-Standard Model Monte Carlo were similar to those in table 6.1, although not identical. An example with Monte Carlo generated with an anomalous coupling of $\Delta g_1^z = -2$ is shown in table 6.2.

[1] The stability of forming χ^2s with highly correlated elements is discussed in appendix B.

	ρ_{++}	ρ_{--}	ρ_{00}	$\mathrm{Re}(\rho_{+-})$	$\mathrm{Re}(\rho_{+0})$	$\mathrm{Re}(\rho_{-0})$	$\mathrm{Im}(\rho_{+-})$	$\mathrm{Im}(\rho_{+0})$	$\mathrm{Im}(\rho_{-0})$
ρ_{++}	1.00	0.35	-0.89	-0.01	-0.10	0.02	0.02	0.00	0.01
ρ_{--}	0.35	1.00	-0.74	-0.02	-0.10	0.16	0.01	0.00	0.00
ρ_{00}	-0.89	-0.74	1.00	0.02	0.12	-0.09	-0.01	0.00	-0.01
$\mathrm{Re}(\rho_{+-})$	-0.01	-0.02	0.02	1.00	-0.11	0.17	0.00	0.01	0.00
$\mathrm{Re}(\rho_{+0})$	-0.10	-0.10	0.12	-0.11	1.00	-0.68	0.02	0.02	0.01
$\mathrm{Re}(\rho_{-0})$	0.02	0.16	-0.09	0.17	-0.68	1.00	0.00	-0.01	-0.01
$\mathrm{Im}(\rho_{+-})$	0.02	0.01	-0.01	0.00	0.02	0.00	1.00	0.00	-0.04
$\mathrm{Im}(\rho_{+0})$	0.00	0.00	0.00	0.01	0.02	-0.01	0.00	1.00	0.68
$\mathrm{Im}(\rho_{-0})$	0.01	0.00	-0.01	0.00	0.01	-0.01	-0.04	0.68	1.00

Table 6.1: *The correlations between the* $-1 < \cos\theta_{\mathrm{W}} < -0.875$ *bin of all the single W SDM observables used to calculate the TGCs. These values were calculated from a Standard Model four-fermion Monte Carlo sample.*

6.1.1 Overcoming Problems of Detector Effects.

The SDM elements extracted from the data will not represent the true SDM elements. The less than perfect angular resolution, the finite selection efficiency and the acceptance of the OPAL detector are just some of the factors that will have an effect on the SDM elements. The data sample is expected to contain some background events and these will also cause deviation from the true SDM elements. The problem is increased further when you include such effects as ISR and the finite W width. Figure 6.1 indicates the extent of the problem detector effects cause. It shows the SDM elements extracted from a sample of fully detector simulated Monte Carlo events containing all possible signal and background processes. They have been passed through the same selection and reconstruction as is used for the data. Overlaid is the theoretical prediction for the Standard Model calculated from the purely analytical expression of the process $\mathrm{e^+e^-} \rightarrow \mathrm{W^+W^-} \rightarrow f_1\bar{f}_2 f_3 \bar{f}_4$, equation 3.29.

The deviations due to the experimental effects are obvious in figure 6.1. The SDM elements extracted from the data cannot be directly compared

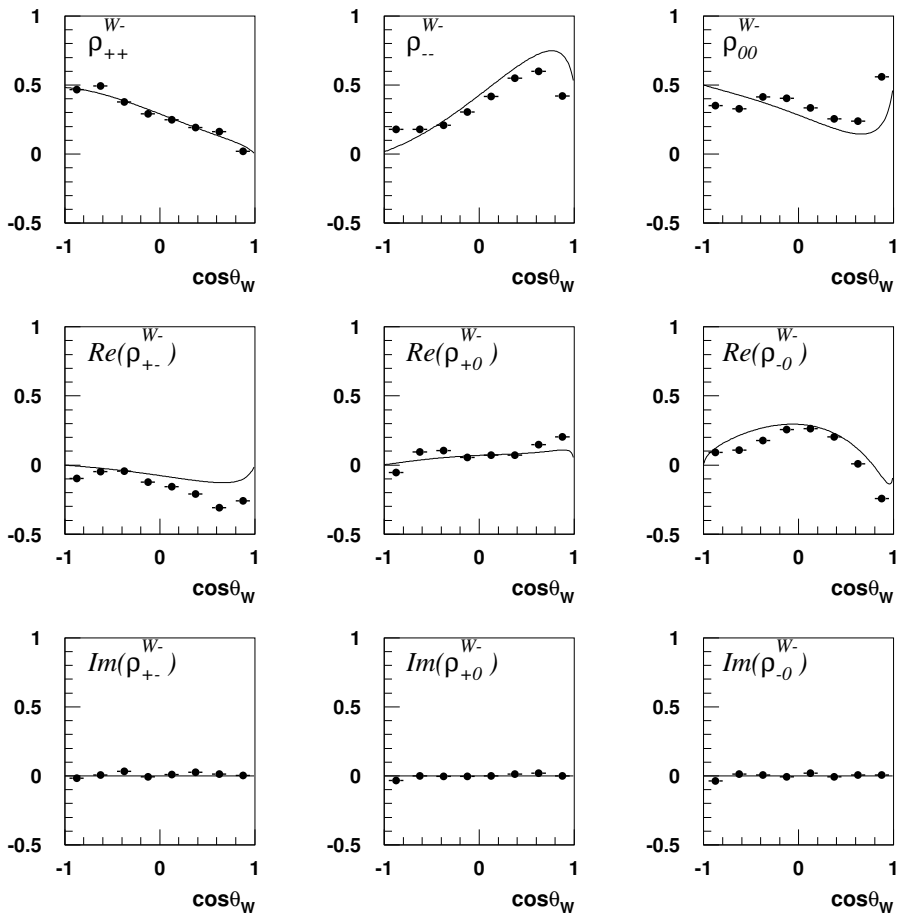

Figure 6.1: *The Single W SDM elements extracted from a fully detector simulated Standard Model Monte Carlo sample. The solid line is the theoretical prediction calculated from the analytical expression.*

	ρ_{++}	ρ_{--}	ρ_{00}	$\mathrm{Re}(\rho_{+-})$	$\mathrm{Re}(\rho_{+0})$	$\mathrm{Re}(\rho_{-0})$	$\mathrm{Im}(\rho_{+-})$	$\mathrm{Im}(\rho_{+0})$	$\mathrm{Im}(\rho_{-0})$
ρ_{++}	1.00	0.29	-0.86	-0.02	-0.08	-0.01	0.00	-0.03	-0.02
ρ_{--}	0.29	1.00	-0.73	-0.06	-0.04	0.11	0.03	-0.03	-0.04
ρ_{00}	-0.86	-0.73	1.00	0.05	0.08	-0.05	-0.02	0.04	0.04
$\mathrm{Re}(\rho_{+-})$	-0.02	-0.06	0.05	1.00	-0.13	0.17	0.07	0.00	0.00
$\mathrm{Re}(\rho_{+0})$	-0.08	-0.04	0.08	-0.13	1.00	-0.62	0.00	0.02	0.02
$\mathrm{Re}(\rho_{-0})$	-0.01	0.11	-0.05	0.17	-0.62	1.00	0.01	-0.02	-0.04
$\mathrm{Im}(\rho_{+-})$	0.00	0.03	-0.02	0.01	0.00	0.01	1.00	-0.03	-0.05
$\mathrm{Im}(\rho_{+0})$	-0.03	-0.03	0.04	0.00	0.02	-0.02	-0.03	1.00	0.64
$\mathrm{Im}(\rho_{-0})$	-0.02	-0.04	0.04	0.00	0.02	-0.04	-0.05	0.64	1.00

Table 6.2: *The correlations between the* $-1 < \cos\theta_{\mathrm{W}} < -0.875$ *bin of all the single W SDM observables used to calculate the TGCs. These values were calculated from a non-Standard Model four-fermion Monte Carlo sample with* $\Delta g_1^z = -2.0$.

with the theoretical predictions from the analytical formula, however they can be compared directly to SDM elements extracted from fully detector simulated Monte Carlo. The χ^2 curve is formed from the difference between SDM elements obtained from the data and from fully simulated Monte Carlo with different values of TGC.

A large number of samples of fully detector simulated Monte Carlo generated with a wide range of anomalous couplings are not available, so a different method is required to produce samples that can then be used in the χ^2 minimisation. A reweighting technique is employed to produce Monte Carlo samples with an arbitrary coupling. This method is discussed below.

Reweighting Monte Carlo

For any Monte Carlo event a probability for it occurring, i.e. it's normalised cross-section, can be calculated from the square of the amplitude for this event. The probability can be calculated of it being a Standard Model event or an event in the presence of an anomalous coupling. The ratio of these

two probabilities can be used to reweight a set of Standard Model events into a sample corresponding to the non-Standard Model anomalous coupling.

The WVCXME [100] program was developed from the EXCALIBUR four-fermion Monte Carlo generator. It uses the matrix elements from the generator program to calculate the amplitude squared. All it needs to know is the four-vectors of the four-fermions in the event and then it can calculate the amplitude squared for the Standard Model or with an anomalous coupling present. The generator includes all the features discussed in section 5.2.1. EXCALIBUR is a four-fermion generator, so WVCXME also takes into account the non-CC03 events that are sensitive to TGCs, and also the interference between the four-fermion final states.

An example of the relevant angles for the SDM analysis calculated from a fully detector simulated Standard Model four-fermion EXCALIBUR sample of Monte Carlo events, that have been reweighted to a sample with $\Delta\kappa_\gamma = -2.0$, is shown in figure 6.2. Also shown on the same figure are the angles calculated from a fully detector simulated sample of EXCALIBUR Monte Carlo events that were generated with a coupling of $\Delta\kappa_\gamma = -2.0$. The angles from the reweighted sample agree well with those from the sample generated with the anomalous coupling.

EXCALIBUR, and thus WVCXME, only contains the CP-conserving couplings, so this technique cannot be employed to produce samples of Monte Carlo with CP-violating couplings. However a similar reweighting technique can be used to make samples of Monte Carlo with CP-violating couplings using a different method to calculate the weights.

The analytical expression of the 5-fold differential cross-section for the CC03 events, given by equation 3.27, can be used to calculate weights for the W-pair events within a Monte Carlo sample. It does not contain any of

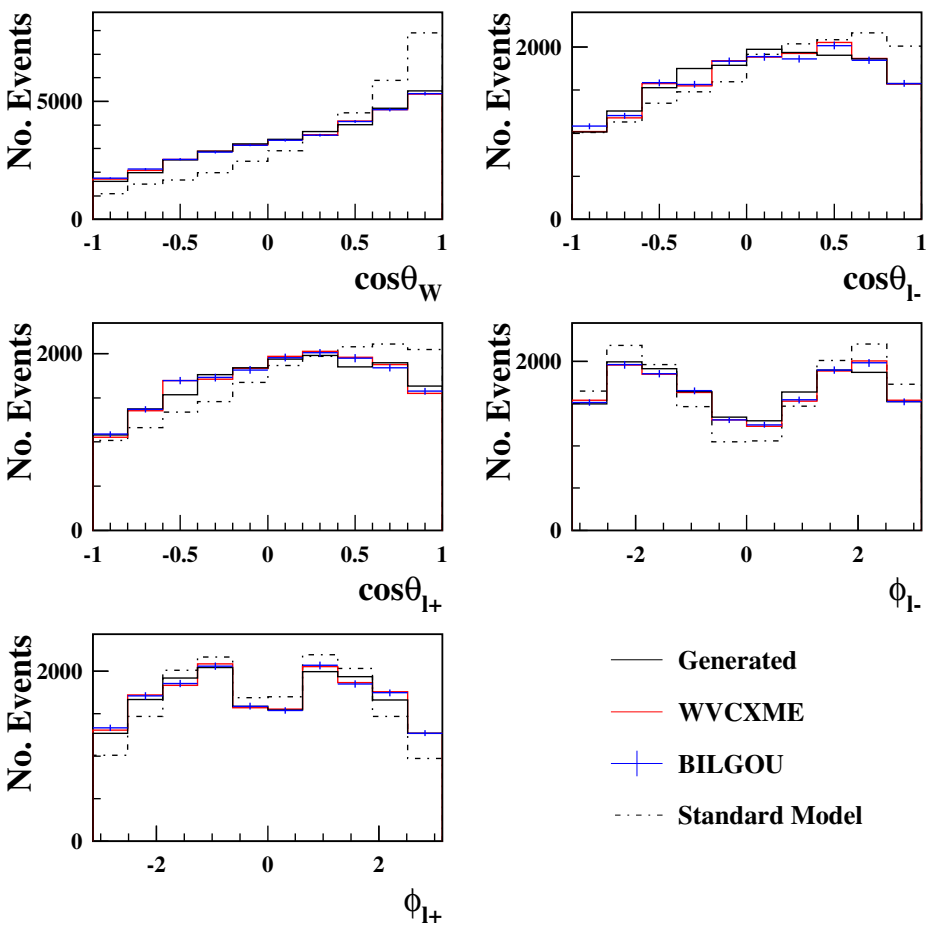

Figure 6.2: *Comparison of angular distributions from EXCALIBUR Monte Carlo generated with anomalous coupling* $\Delta\kappa_\gamma = -2.0$ *(green line) and a Standard Model sample reweighted to a coupling of* $\Delta\kappa_\gamma = -2.0$ *using WVCXME (red line) and BILGOU (blue points). Also shown is the distribution of angles from Standard Model Monte Carlo. This has been normalised to the other samples so the event shapes can be compared.*

the *add-ons* that WVCXME has, such as accounting for the finite W width, and it can only calculate weights for the CC03 events in the four-fermion sample. However, within these limitations, as it contains all 14 anomalous couplings, it can be used to calculate weights for CP-violating couplings.

ISR can be accounted for by using the generated four-vectors of the four-fermions to boost the input angles, used in calculating the weight, back into the true centre-of-mass frame. Using equation 3.27, the Standard Model cross-section for a Standard Model Monte Carlo event (SM) can be calculated and also the cross-section for an anomalous coupling (α) being present. The ratio of these two is then the equivalent weight, shown in equation 6.9. In equation 6.9 Ω represents the set of five angles; $\cos\theta_{\mathrm{W}}$, $\cos\theta_{f_1}$, $\cos\theta_{\bar{f}_4}$, ϕ_{f_1} and $\phi_{\bar{f}_4}$.

$$\mathrm{wgt} = \left(\frac{\mathrm{d}\sigma}{\mathrm{d}\Omega}\right)^{\alpha} \Bigg/ \left(\frac{\mathrm{d}\sigma}{\mathrm{d}\Omega}\right)^{SM} \tag{6.9}$$

As this method is based on analytical expressions from papers by Bilenkii and Gounaris, the reweighting scheme is known as the BILGOU reweighting scheme. The angular distributions for a Standard Model EXCALIBUR Monte Carlo sample, reweighted to an anomalous coupling of $\Delta\kappa_\gamma = -2.0$, using the BILGOU reweighting scheme are shown in figure 6.2. The distributions agree well with both those generated with a coupling of $\Delta\kappa_\gamma = -2.0$ and those reweighted using WVCXME.

The single W SDM elements extracted from a sample of fully detector simulated EXCALIBUR Monte Carlo generated with an anomalous coupling of $\Delta\kappa_\gamma = -2.0$ are shown in figure 6.3. Also shown are the SDM elements extracted from a Standard Model sample which has been reweighted using both methods of reweighting. Good agreement is seen in most cases.

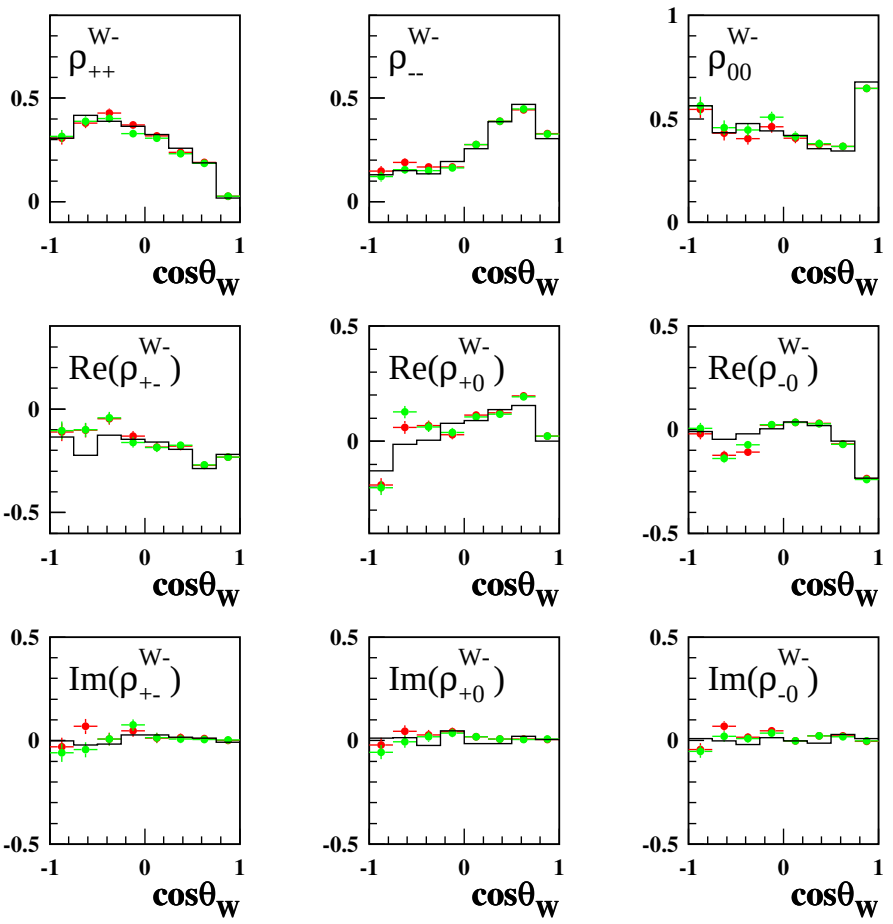

Figure 6.3: *Comparison of the SDM elements extracted from EXCALIBUR Monte Carlo, generated with anomalous coupling* $\Delta\kappa_\gamma = -2.0$ *(black line) and a Standard Model sample, reweighted to a coupling of* $\Delta\kappa_\gamma = -2.0$*, using WVCXME (red points) and BILGOU (green points).*

6.1.2 Systematic Checks of the SDM Fit Method

Reweighting methods are prone to introduce biases. Therefore, the possible scale of any biases has been measured by applying the χ^2 fit method to samples of fully simulated four-fermion Monte Carlo data that have been generated with non-Standard Model couplings.

For the CP-conserving couplings, fully simulated samples of four-fermion EXCALIBUR are available with anomalous couplings; $\Delta\kappa_\gamma$, Δg_1^z and λ, with values of of ± 2, ± 1 and $\pm\frac{1}{2}$. All these were generated with the $\mathrm{SU}(2)_L \times \mathrm{U}(1)_Y$ constraints on the couplings, equation 3.16. Fits were performed to all the samples using both reweighting techniques. Table 6.3 shows all the results and figures 6.4 and 6.5 show the bias plots. The values in table 6.3 show no bias towards the Standard Model for any particular coupling value. The differences between the measured and the generated values are all less than the statistical accuracy expected on the data sample shown in table 6.9. Both reweighting techniques give similar results.

For the CP-violating couplings only the BILGOU reweighting technique can be used. The ERATO generator was used to generate the Monte Carlo samples with CP-violating anomalous couplings. Standard Model EXCALIBUR is still used as the sample that is reweighted to calculate the coupling values. Samples of fully detector simulated ERATO with $\tilde{\kappa}_z$, $\tilde{\lambda}_z$ and g_4^z values from -1 to +1 in nine equal increments were available. Table 6.4 shows a sample of the fit results and figure 6.6 shows the bias plots for the samples with these couplings. All results are consistent within the generated coupling.

Coupling	Generated Value	Fitted Value	
		WVCXME	BILGOU
$\Delta\kappa_\gamma$	-2.0	$-2.00^{+0.04}_{-0.04}$	$-1.99^{+0.04}_{-0.04}$
$\Delta\kappa_\gamma$	-1.0	$-0.98^{+0.04}_{-0.04}$	$-0.98^{+0.04}_{-0.03}$
$\Delta\kappa_\gamma$	-0.5	$-0.44^{+0.04}_{-0.04}$	$-0.45^{+0.05}_{-0.04}$
$\Delta\kappa_\gamma$	0.0	$+0.02^{+0.05}_{-0.07}$	$-0.01^{+0.07}_{-0.07}$
$\Delta\kappa_\gamma$	$+0.5$	$+0.19^{+0.09}_{-0.09}$	$+0.35^{+0.15}_{-0.13}$
$\Delta\kappa_\gamma$	$+1.0$	$+0.87^{+0.05}_{-0.06}$	$+0.88^{+0.05}_{-0.06}$
$\Delta\kappa_\gamma$	$+2.0$	$+1.96^{+0.04}_{-0.04}$	$+1.87^{+0.05}_{-0.03}$
Δg_1^z	-2.0	$-1.99^{+0.05}_{-0.05}$	$-1.94^{+0.05}_{-0.05}$
Δg_1^z	-1.0	$-0.95^{+0.04}_{-0.04}$	$-0.93^{+0.04}_{-0.04}$
Δg_1^z	-0.5	$-0.49^{+0.04}_{-0.04}$	$-0.51^{+0.04}_{-0.04}$
Δg_1^z	0.0	$0.0^{+0.02}_{-0.02}$	$-0.02^{+0.03}_{-0.02}$
Δg_1^z	$+0.5$	$+0.45^{+0.03}_{-0.03}$	$+0.43^{+0.03}_{-0.03}$
Δg_1^z	$+1.0$	$+0.96^{+0.02}_{-0.02}$	$+0.96^{+0.02}_{-0.02}$
Δg_1^z	$+2.0$	$+1.97^{+0.06}_{-0.06}$	$+2.11^{+0.07}_{-0.07}$
λ	-2.0	$-1.90^{+0.07}_{-0.07}$	$-1.89^{+0.07}_{-0.07}$
λ	-1.0	$-0.86^{+0.05}_{-0.05}$	$-0.91^{+0.06}_{-0.06}$
λ	-0.5	$-0.42^{+0.05}_{-0.05}$	$-0.44^{+0.05}_{-0.05}$
λ	0.0	$+0.01^{+0.04}_{-0.02}$	$+0.02^{+0.03}_{-0.03}$
λ	$+0.5$	$+0.48^{+0.03}_{-0.03}$	$+0.49^{+0.03}_{-0.03}$
λ	$+1.0$	$+0.93^{+0.01}_{-0.01}$	$+1.03^{+0.02}_{-0.02}$
λ	$+2.0$	$+1.92^{+0.07}_{-0.07}$	$+1.93^{+0.07}_{-0.07}$

Table 6.3: *The bias fits to the single W SDM elements extracted from large Monte Carlo data samples generated with anomalous CP-conserving couplings. Both reweighting techniques were used. The errors shown are the statistical uncertainty on the fit to the large sample.*

Coupling	Generated Value	Fitted Value	
		WVCXME	BILGOU
$\tilde{\kappa}_z$	-1.00	-	$-1.04^{+0.05}_{-0.05}$
$\tilde{\kappa}_z$	-0.50	-	$-0.51^{+0.04}_{-0.04}$
$\tilde{\kappa}_z$	-0.25	-	$-0.29^{+0.03}_{-0.03}$
$\tilde{\kappa}_z$	0.0	-	$-0.01^{+0.03}_{-0.03}$
$\tilde{\kappa}_z$	$+0.25$	-	$+0.27^{+0.03}_{-0.03}$
$\tilde{\kappa}_z$	$+0.50$	-	$+0.50^{+0.03}_{-0.03}$
$\tilde{\kappa}_z$	$+1.00$	-	$+1.02^{+0.05}_{-0.05}$
$\tilde{\lambda}_z$	-1.00	-	$-0.93^{+0.06}_{-0.05}$
$\tilde{\lambda}_z$	-0.50	-	$-0.53^{+0.05}_{-0.05}$
$\tilde{\lambda}_z$	-0.25	-	$-0.29^{+0.04}_{-0.04}$
$\tilde{\lambda}_z$	0.0	-	$-0.02^{+0.03}_{-0.03}$
$\tilde{\lambda}_z$	$+0.25$	-	$+0.21^{+0.04}_{-0.04}$
$\tilde{\lambda}_z$	$+0.50$	-	$+0.46^{+0.05}_{-0.04}$
$\tilde{\lambda}_z$	$+1.00$	-	$+0.92^{+0.06}_{-0.06}$
g_4^z	-1.00	-	$-0.97^{+0.06}_{-0.06}$
g_4^z	-0.50	-	$-0.56^{+0.05}_{-0.05}$
g_4^z	-0.25	-	$-0.21^{+0.04}_{-0.04}$
g_4^z	0.0	-	$-0.02^{+0.04}_{-0.04}$
g_4^z	$+0.25$	-	$+0.21^{+0.04}_{-0.04}$
g_4^z	$+0.50$	-	$+0.53^{+0.05}_{-0.05}$
g_4^z	$+1.00$	-	$+1.02^{+0.06}_{-0.06}$

Table 6.4: *The bias fits to the single W SDM elements extracted from large Monte Carlo data samples generated with anomalous CP-violating couplings. The errors shown are the statistical uncertainty on fit to the large samples.*

6.2 The χ^2 Fit to the $\cos\theta_W$ Distribution

The single W SDM elements are normalised to the total number of events in each bin of $\cos\theta_W$. This means that single W SDM elements are effectively independent of the shape of the $\cos\theta_W$ distribution. The W production angle is sensitive to the TGCs. This means that there is an observable that has been measured, is completely uncorrelated to the single W SDM elements, and as yet has not been used in the TGC fit.

The W production angle, $\cos\theta_W$, can be binned into eight bins like the single W SDM elements and normalised to the total number of events. Then a χ^2 fit can be performed in a similar way as for the SDM elements. The reweighted Monte Carlo method can be used to calculate the theoretical distributions in the χ^2 minimisation. The form of the χ^2 would be as in equation 6.10, where N_{tot} is the total number of events and $\sigma_{N_k^{me}}$ is the error on the number of events measured in bin k of $\cos\theta_W$. The error is simply the square-root of the number of events in the bin.

$$\chi^2 = \sum_{k=1}^{N} \left[\left(\frac{N_k^{me}}{N_{tot}^{me}} - \frac{N_k^{th}}{N_{tot}^{th}} \right) \left(\frac{N_{tot}^{me}}{\sigma_{N_k^{me}}} \right) \right]^2 \tag{6.10}$$

6.2.1 Systematic Checks of the $\cos\theta_W$ Fit Method

To test the $\cos\theta_W$ fit method, fits are performed to the $\cos\theta_W$ distributions calculated from fully detector simulated Monte Carlo that has been generated with anomalous couplings. The results of these fits for the CP-conserving couplings can be seen in table 6.5 and the bias plots are shown in figures 6.4 and 6.5. The results for the CP-violating couplings can be seen in table 6.6 and the bias plots are shown in figure 6.6.

The fits of the CP-conserving couplings show no obvious bias towards the Standard Model or any other coupling. All fitted values are consistent with

the generated values. The measured value at $\Delta\kappa_\gamma = +1$ using the BILGOU reweighting scheme is less consistent with the generated value, but is still consistent within the expected statistical error on the data sample, given in table 6.9.

The fits of the CP-violating couplings show a slight bias towards lower couplings than the generated values. This is expected due to the slight systematic difference between the $\cos\theta_{\mathrm{W}}$ distribution extracted from the Standard Model ERATO sample and that calculated from the EXCALIBUR sample that is reweighted to perform the fit. The ERATO $\cos\theta_{\mathrm{W}}$ distribution is slightly steeper than the EXCALIBUR one for all CP-violating couplings. This systematic difference is accounted for in the systematic uncertainties described in chapter 10.

The $\cos\theta_{\mathrm{W}}$ distribution is much less sensitive to the CP-violating couplings than the CP-conserving ones. This is to be expected as the CP-violating couplings have a large effect on the imaginary observables and a much lesser effect on the real observables, such as cross-sections [41]. The CP-conserving couplings have a large effect on the real observables, but no effect on any of the imaginary observables.

6.3 The Combined Fit

The single W SDM elements and the $\cos\theta_{\mathrm{W}}$ distribution are completely uncorrelated. This means that the χ^2s for both fits can be added together. This fit will then include all the observables used in the SDM analysis.

Bias tests performed using this combined fit are shown in table 6.8 and 6.7 and the bias plots are shown in figure 6.4, 6.5 and 6.6. The combined fit

Coupling	Generated Value	Fitted Value	
		WVCXME	BILGOU
$\Delta\kappa_\gamma$	-2.0	$-1.90^{+0.04}_{-0.04}$	$-1.89^{+0.04}_{-0.04}$
$\Delta\kappa_\gamma$	-1.0	$-0.98^{+0.03}_{-0.03}$	$-0.95^{+0.03}_{-0.04}$
$\Delta\kappa_\gamma$	-0.5	$-0.46^{+0.04}_{-0.04}$	$-0.44^{+0.04}_{-0.04}$
$\Delta\kappa_\gamma$	0.0	$0.0^{+0.05}_{-0.05}$	$-0.02^{+0.06}_{-0.06}$
$\Delta\kappa_\gamma$	$+0.5$	$+0.55^{+0.20}_{-0.12}$	$+0.43^{+0.08}_{-0.08}$
$\Delta\kappa_\gamma$	$+1.0$	$+1.08^{+0.14}_{-0.23}$	$+0.49^{+0.10}_{-0.09}$
$\Delta\kappa_\gamma$	$+2.0$	$+1.96^{+0.04}_{-0.06}$	$+2.10^{+0.06}_{-0.06}$
Δg_1^z	-2.0	$-1.84^{+0.05}_{-0.05}$	$-1.82^{+0.05}_{-0.05}$
Δg_1^z	-1.0	$-0.97^{+0.02}_{-0.01}$	$-0.96^{+0.02}_{-0.02}$
Δg_1^z	-0.5	$-0.49^{+0.02}_{-0.02}$	$-0.49^{+0.01}_{-0.01}$
Δg_1^z	0.0	$0.0^{+0.02}_{-0.01}$	$-0.01^{+0.01}_{-0.02}$
Δg_1^z	$+0.5$	$+0.47^{+0.08}_{-0.05}$	$+0.41^{+0.05}_{-0.04}$
Δg_1^z	$+1.0$	$+0.95^{+0.04}_{-0.04}$	$+0.95^{+0.04}_{-0.04}$
Δg_1^z	$+2.0$	$+1.85^{+0.03}_{-0.03}$	$+1.84^{+0.03}_{-0.03}$
λ	-2.0	$-1.92^{+0.03}_{-0.03}$	$-1.91^{+0.03}_{-0.03}$
λ	-1.0	$-0.97^{+0.02}_{-0.02}$	$-0.98^{+0.02}_{-0.02}$
λ	-0.5	$-0.49^{+0.02}_{-0.02}$	$-0.49^{+0.02}_{-0.02}$
λ	0.0	$0.0^{+0.01}_{-0.01}$	$0.0^{+0.03}_{-0.03}$
λ	$+0.5$	$+0.48^{+0.05}_{-0.05}$	$+0.42^{+0.04}_{-0.04}$
λ	$+1.0$	$+0.96^{+0.04}_{-0.04}$	$+1.07^{+0.04}_{-0.04}$
λ	$+2.0$	$+1.92^{+0.04}_{-0.03}$	$+1.99^{+0.04}_{-0.04}$

Table 6.5: *The bias fits to the* $\cos\theta_{\rm W}$ *distribution extracted from large Monte Carlo data samples generated with anomalous CP-conserving couplings. Both reweighting techniques were used. The errors shown are the statistical uncertainty on fit to the large samples.*

Coupling	Generated Value	Fitted Value	
		WVCXME	BILGOU
$\tilde{\kappa}_z$	-1.00	-	$\pm 0.89^{+0.04}_{-0.04}$
$\tilde{\kappa}_z$	-0.50	-	$\pm 0.46^{+0.04}_{-0.04}$
$\tilde{\kappa}_z$	-0.25	-	$\pm 0.20^{+0.03}_{-0.03}$
$\tilde{\kappa}_z$	0.0	-	$0.0^{+0.03}_{-0.03}$
$\tilde{\kappa}_z$	$+0.25$	-	$\pm 0.20^{+0.03}_{-0.03}$
$\tilde{\kappa}_z$	$+0.50$	-	$\pm 0.46^{+0.04}_{-0.04}$
$\tilde{\kappa}_z$	$+1.00$	-	$\pm 0.89^{+0.04}_{-0.04}$
$\tilde{\lambda}_z$	-1.00	-	$\pm 0.93^{+0.03}_{-0.03}$
$\tilde{\lambda}_z$	-0.50	-	$\pm 0.44^{+0.03}_{-0.03}$
$\tilde{\lambda}_z$	-0.25	-	$\pm 0.15^{+0.05}_{-0.05}$
$\tilde{\lambda}_z$	0.0	-	$0.0^{+0.06}_{-0.06}$
$\tilde{\lambda}_z$	$+0.25$	-	$\pm 0.15^{+0.05}_{-0.05}$
$\tilde{\lambda}_z$	$+0.50$	-	$\pm 0.44^{+0.03}_{-0.03}$
$\tilde{\lambda}_z$	$+1.00$	-	$\pm 0.93^{+0.03}_{-0.03}$
g_4^z	-1.00	-	$\pm 0.89^{+0.11}_{-0.11}$
g_4^z	-0.50	-	$\pm 0.41^{+0.20}_{-0.20}$
g_4^z	-0.25	-	$\pm 0.13^{+0.15}_{-0.15}$
g_4^z	$+0.00$	-	$0.0^{+0.11}_{-0.11}$
g_4^z	$+0.25$	-	$\pm 0.13^{+0.15}_{-0.15}$
g_4^z	$+0.50$	-	$\pm 0.41^{+0.20}_{-0.20}$
g_4^z	$+1.00$	-	$\pm 0.89^{+0.11}_{-0.11}$

Table 6.6: *The bias fits to the* $\cos\theta_{\mathrm{W}}$ *distribution extracted from large Monte Carlo data samples generated with anomalous CP-violating couplings. The errors shown are the statistical uncertainty on fit to the large samples.*

gives a noticeable improvement on the fitted values compared to the SDM elements or $\cos\theta_{\mathrm{W}}$ distributions on their own.

6.4 Fit to Many Subsamples

Fitting to subsamples of Monte Carlo with the same statistics as the data sample will give a test of the reliability of the statistical error calculated for the fit. For the error to be reliable 67% of the fitted coupling values should lie within one standard deviation of the generated value. If this is true, then the distribution of $\frac{x-x_0}{\Delta x}$, where x is the fitted value of the coupling, x_0 is the generated value and Δx is the statistical error on x, should be a Gaussian with a width consistent with unity. These distributions are known as the pull distributions.

These tests were performed for all six couplings being measured, using both reweighting methods where applicable. Fits were not only made to Standard Model Monte Carlo but also samples with all the anomalous couplings used in the bias tests. A summary of the results is shown below.

Figure 6.7 shows the distributions of fitted values of the CP-conserving couplings. The fits were made to 139 Standard Model subsamples using the BILGOU reweighting scheme, and are for the combined fit result. The plots on the left just show the distributions and demonstrate that the fit is Gaussian and the mean is at the Standard Model value of the couplings. The width of this distribution can be taken as the expected statistical error on the measured value of the coupling. The plots on the right are the pull distributions. Figure 6.8 shows the distributions of the combined fit of the CP-conserving couplings, using the WVCXME reweighting scheme. For both

Coupling	Generated Value	Fitted Value	
		WVCXME	BILGOU
$\Delta\kappa_\gamma$	-2.0	$-1.95^{+0.03}_{-0.03}$	$-1.94^{+0.03}_{-0.02}$
$\Delta\kappa_\gamma$	-1.0	$-0.98^{+0.03}_{-0.03}$	$-0.96^{+0.03}_{-0.02}$
$\Delta\kappa_\gamma$	-0.5	$-0.45^{+0.03}_{-0.03}$	$-0.44^{+0.03}_{-0.03}$
$\Delta\kappa_\gamma$	0.0	$0.0^{+0.04}_{-0.03}$	$0.0^{+0.05}_{-0.04}$
$\Delta\kappa_\gamma$	$+0.5$	$+0.38^{+0.06}_{-0.07}$	$+0.40^{+0.06}_{-0.07}$
$\Delta\kappa_\gamma$	$+1.0$	$+0.87^{+0.06}_{-0.05}$	$+0.85^{+0.05}_{-0.07}$
$\Delta\kappa_\gamma$	$+2.0$	$+1.99^{+0.03}_{-0.03}$	$+1.97^{+0.03}_{-0.03}$
Δg_1^z	-2.0	$-1.93^{+0.03}_{-0.02}$	$-1.89^{+0.03}_{-0.03}$
Δg_1^z	-1.0	$-0.96^{+0.02}_{-0.02}$	$-0.95^{+0.02}_{-0.02}$
Δg_1^z	-0.5	$-0.49^{+0.01}_{-0.01}$	$-0.49^{+0.01}_{-0.01}$
Δg_1^z	0.0	$0.0^{+0.01}_{-0.01}$	$0.0^{+0.01}_{-0.01}$
Δg_1^z	$+0.5$	$+0.46^{+0.04}_{-0.04}$	$+0.42^{+0.03}_{-0.03}$
Δg_1^z	$+1.0$	$+0.95^{+0.03}_{-0.03}$	$+0.95^{+0.03}_{-0.03}$
Δg_1^z	$+2.0$	$+1.89^{+0.03}_{-0.03}$	$+1.89^{+0.03}_{-0.03}$
λ	-2.0	$-1.94^{+0.03}_{-0.03}$	$-1.89^{+0.02}_{-0.02}$
λ	-1.0	$-0.97^{+0.02}_{-0.02}$	$-0.97^{+0.02}_{-0.02}$
λ	-0.5	$-0.49^{+0.02}_{-0.02}$	$-0.49^{+0.02}_{-0.02}$
λ	0.0	$0.0^{+0.01}_{-0.01}$	$+0.00^{+0.02}_{-0.02}$
λ	$+0.5$	$+0.48^{+0.03}_{-0.03}$	$+0.46^{+0.02}_{-0.02}$
λ	$+1.0$	$+0.93^{+0.01}_{-0.01}$	$+1.03^{+0.02}_{-0.02}$
λ	$+2.0$	$+1.96^{+0.02}_{-0.02}$	$+1.98^{+0.02}_{-0.02}$

Table 6.7: *The bias fits to large Monte Carlo data samples generated with anomalous CP-conserving couplings using the combined fit. Both reweighting techniques were used. The errors shown are the statistical uncertainty on fit to the large samples.*

Coupling	Generated Value	Fitted Value	
		WVCXME	BILGOU
$\tilde{\kappa}_z$	-1.00	-	$-1.01^{+0.02}_{-0.02}$
$\tilde{\kappa}_z$	-0.50	-	$-0.50^{+0.02}_{-0.02}$
$\tilde{\kappa}_z$	-0.25	-	$-0.25^{+0.01}_{-0.01}$
$\tilde{\kappa}_z$	0.0	-	$-0.01^{+0.01}_{-0.01}$
$\tilde{\kappa}_z$	$+0.25$	-	$+0.24^{+0.01}_{-0.01}$
$\tilde{\kappa}_z$	$+0.50$	-	$+0.50^{+0.02}_{-0.02}$
$\tilde{\kappa}_z$	$+1.00$	-	$+1.00^{+0.02}_{-0.02}$
$\tilde{\lambda}_z$	-1.00	-	$-0.93^{+0.03}_{-0.03}$
$\tilde{\lambda}_z$	-0.50	-	$-0.46^{+0.02}_{-0.02}$
$\tilde{\lambda}_z$	-0.25	-	$-0.24^{+0.02}_{-0.02}$
$\tilde{\lambda}_z$	0.0	-	$0.0^{+0.02}_{-0.02}$
$\tilde{\lambda}_z$	$+0.25$	-	$+0.18^{+0.02}_{-0.02}$
$\tilde{\lambda}_z$	$+0.50$	-	$+0.44^{+0.03}_{-0.03}$
$\tilde{\lambda}_z$	$+1.00$	-	$+0.94^{+0.03}_{-0.03}$
g_4^z	-1.00	-	$-0.94^{+0.05}_{-0.05}$
g_4^z	-0.50	-	$-0.48^{+0.04}_{-0.04}$
g_4^z	-0.25	-	$-0.25^{+0.04}_{-0.05}$
g_4^z	0.0	-	$-0.01^{+0.04}_{-0.04}$
g_4^z	$+0.25$	-	$+0.26^{+0.04}_{-0.04}$
g_4^z	$+0.50$	-	$+0.49^{+0.04}_{-0.04}$
g_4^z	$+1.00$	-	$+0.94^{+0.04}_{-0.04}$

Table 6.8: *The bias fits to large Monte Carlo data samples generated with anomalous CP-violating couplings using the combined fit. The errors shown are the statistical uncertainty on fit to the large samples.*

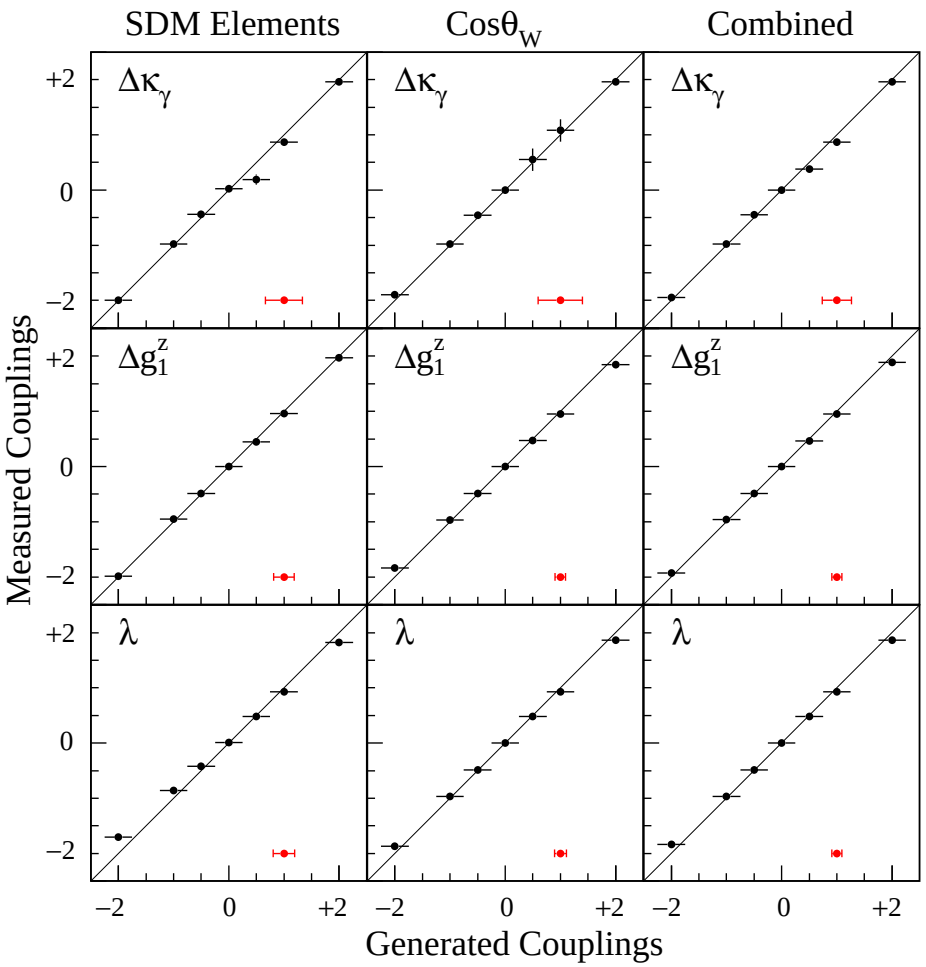

Figure 6.4: *Bias plots of the CP-conserving TGC fits using the WVCXME reweighting scheme. The first column is the fit to the SDM elements, the second column is the fit to the W production angle, and the third column is the combined fit. The solid line represents the perfect fit. The red points represent the expected statistical error on the data.*

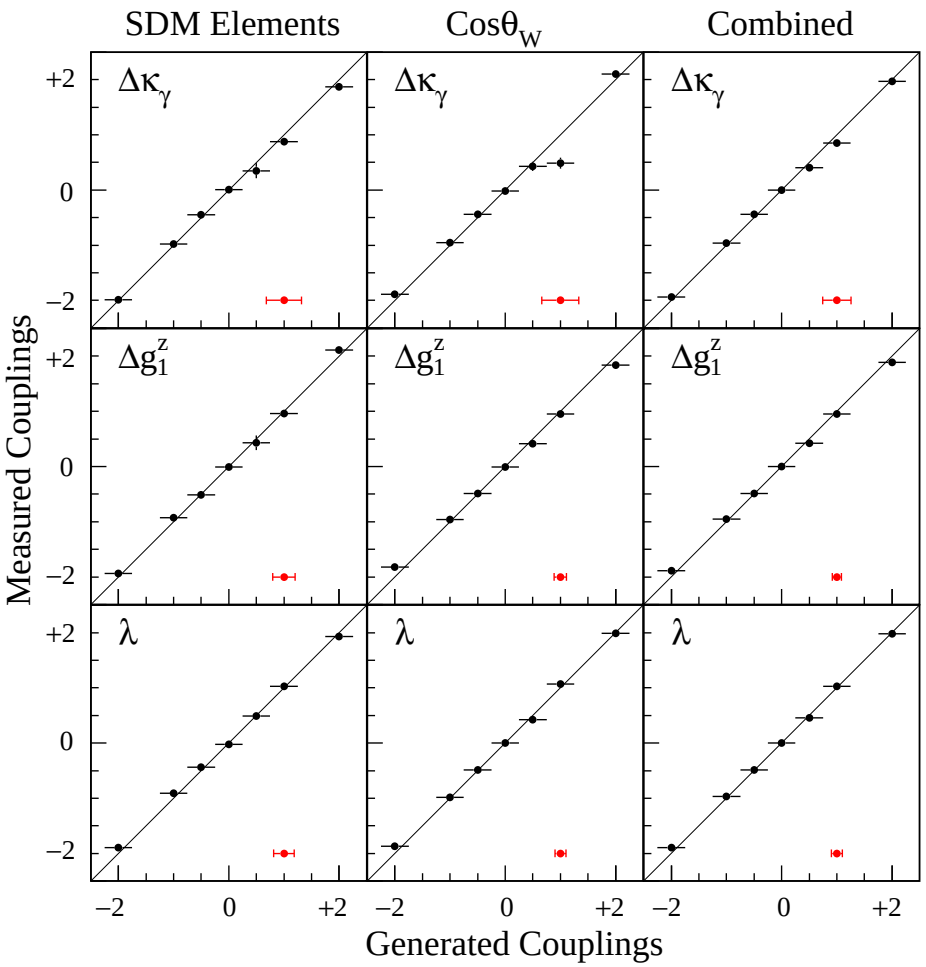

Figure 6.5: *Bias plots of the CP-conserving TGC fits using the BILGOU reweighting scheme. The first column is the fit to the SDM elements, the second column is the fit to the W production angle, and the third column is the combined fit. The solid line represents the perfect fit. The red points represent the expected statistical error on the data.*

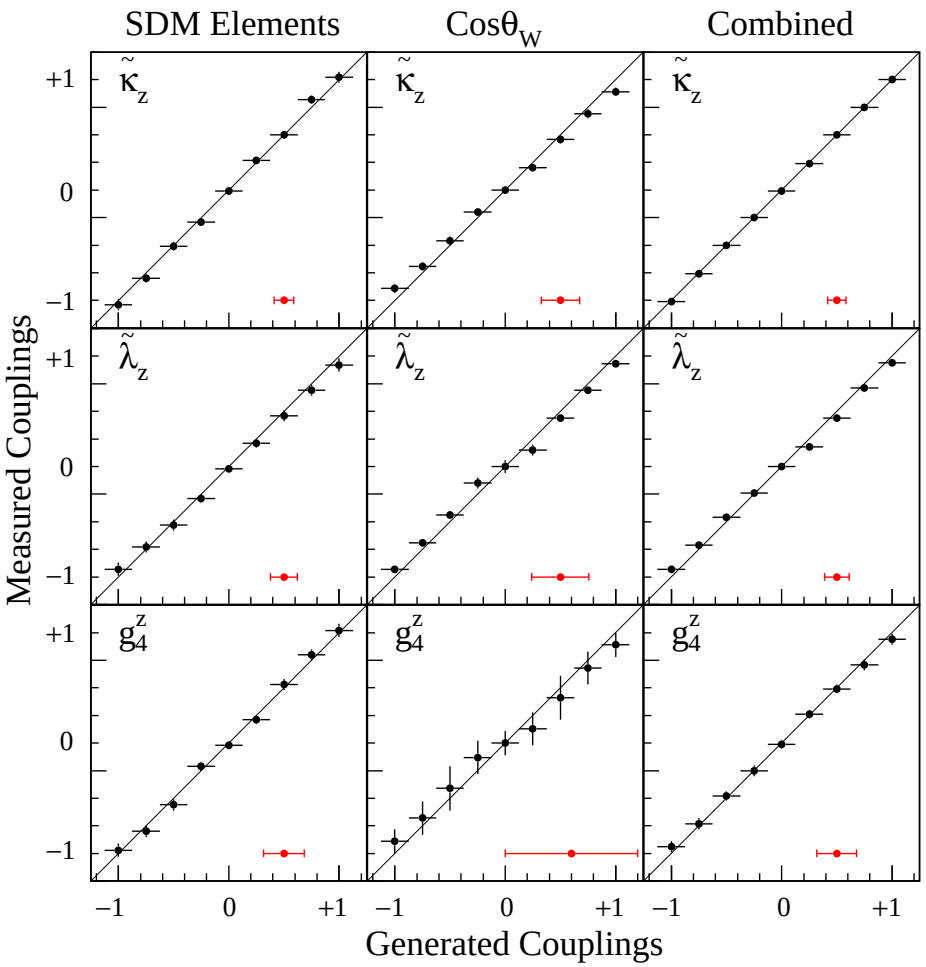

Figure 6.6: *Bias plots of the CP-violating TGC fits using the BILGOU reweighting scheme. The first column is the fit to the SDM elements, the second column is the fit to the W production angle, and the third column is the combined fit. The solid line represents the perfect fit. The red points represent the expected statistical error on the data.*

reweighting methods the width of the pull distributions is close to unity for all couplings.

For both reweighting schemes, the fits for $\Delta\kappa_\gamma$ show a number of results with a large deviation from the generated value of coupling. These generally take a value greater than $\Delta\kappa_\gamma$=+1. This is because the $\cos\theta_{\rm W}$ distribution for $\Delta\kappa_\gamma$=+2 is the same as that for the Standard Model. The plots of fits to just the $\cos\theta_{\rm W}$ distribution for the CP-conserving couplings, using the BILGOU reweighting scheme are shown in figure 6.9. For the fits to $\Delta\kappa_\gamma$ it is obvious that a large proportion of the samples are mistakenly fitted as $\Delta\kappa_\gamma$=+2. A similar effect is seen to a lesser extent in the Δg_1^z fits to $\cos\theta_{\rm W}$, where the $\cos\theta_{\rm W}$ distribution at about Δg_1^z=+1 is similar to that of the Standard Model.

Figure 6.10 shows the distributions of the fitted values of the CP-violating couplings for the combined fit using the BILGOU reweighting scheme. The distribution for $\tilde{\kappa}_z$ does not appear Gaussian, and there is a bias towards a coupling of zero. This is because any anomalous CP-violating coupling will cause a flattening in the $\cos\theta_{\rm W}$ distribution. Due purely to statistical fluctuations, a number of the subsamples will have $\cos\theta_{\rm W}$ distributions that are steeper than the Standard Model distribution. The fits of the CP-violating couplings to these subsamples will immediately be biased towards zero and the fits using just the $\cos\theta_{\rm W}$ distribution will all give a coupling value of zero. This obvious bias only manifests in the $\tilde{\kappa}_z$ fit and not those of the other two CP-violating couplings. This is because the W production angle is much less sensitive to $\tilde{\lambda}_z$ and g_4^z than $\tilde{\kappa}_z$, so for these the SDM element fits completely dominate in the combined fit results.

Figure 6.11 shows the distributions of the fit of the CP-violating couplings to just the $\cos\theta_{\rm W}$ distribution. It can be seen that in all coupling fits there

is a large spike at zero demonstrating the effect discussed.

The pull distributions for the combined fit of $\tilde{\kappa}_z$, shown in figure 6.10, has a width much less than unity, as would be expected. This then means that the width of the distribution of fitted values cannot be taken as the expected error. For all the CP-violating couplings the expected error has been taken as the mean value of the statistical error from all the fits to the subsamples.

Table 6.9 shows the expected value of the statistical error that should be calculated in the fits to the OPAL data.

Coupling	SDM elements	$\cos\theta_{\mathrm{W}}$ distribution	Combined
$\Delta\kappa_\gamma{}^{(BG)}$	0.321	0.335	0.257
$\lambda^{(BG)}$	0.184	0.100	0.096
$\Delta g_1^{z(BG)}$	0.205	0.111	0.079
$\Delta\kappa_\gamma{}^{(WVC)}$	0.336	0.401	0.266
$\lambda^{(WVC)}$	0.192	0.106	0.091
$\Delta g_1^{z(WVC)}$	0.186	0.096	0.091
$\tilde{\kappa}_z$	0.090	0.174	0.084
$\tilde{\lambda}_z$	0.122	0.259	0.110
g_4^z	0.184	0.700	0.180

Table 6.9: *The expected statistical error of the fit to the TGC parameters. These were calculated from the fits to many Monte Carlo subsamples. For the CP-conserving TGCs, the first three are using the BILGOU reweighting scheme and the next three are using the WVCXME scheme.*

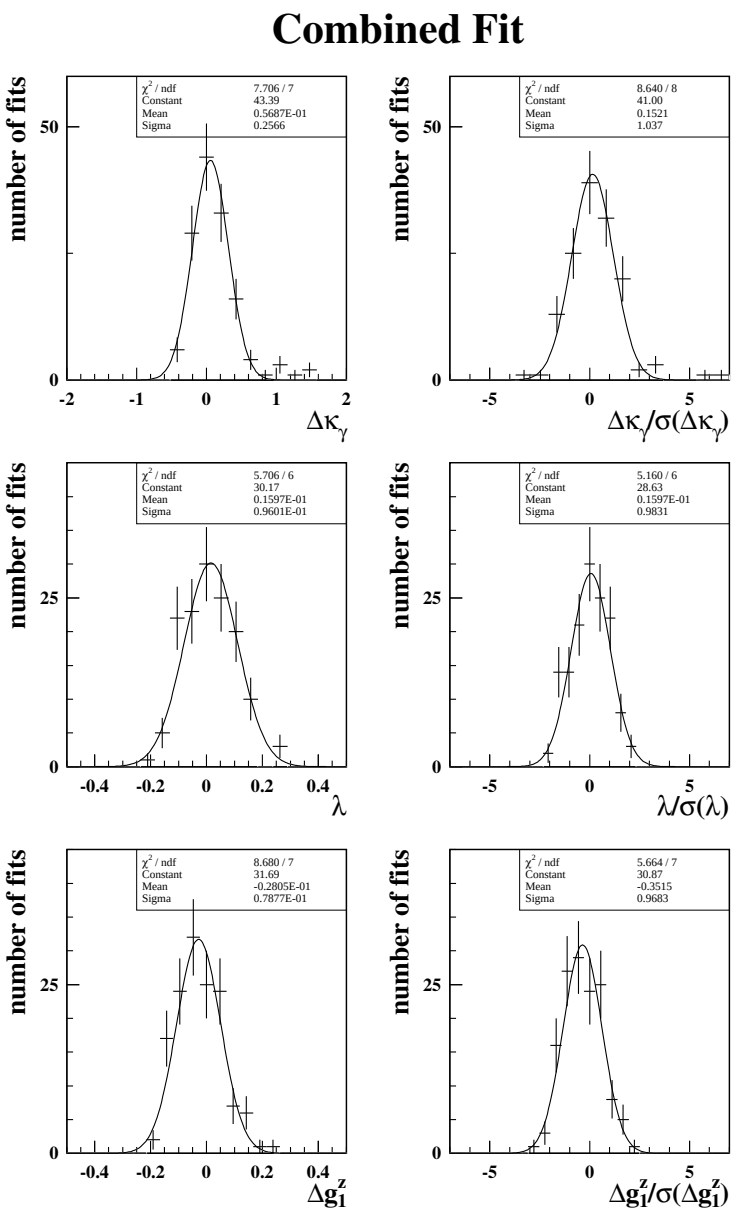

Figure 6.7: *Combined fit results to 139 subsamples of Standard Model EXCALIBUR Monte Carlo. The BILGOU reweighting scheme was used in the fits. The widths of the distributions of the plots on the left side represent the expected error for the analysis for the corresponding coupling parameters. The width of the pull distributions, the plots on the right side, should be compatible with unity if the statistical error is reliable.*

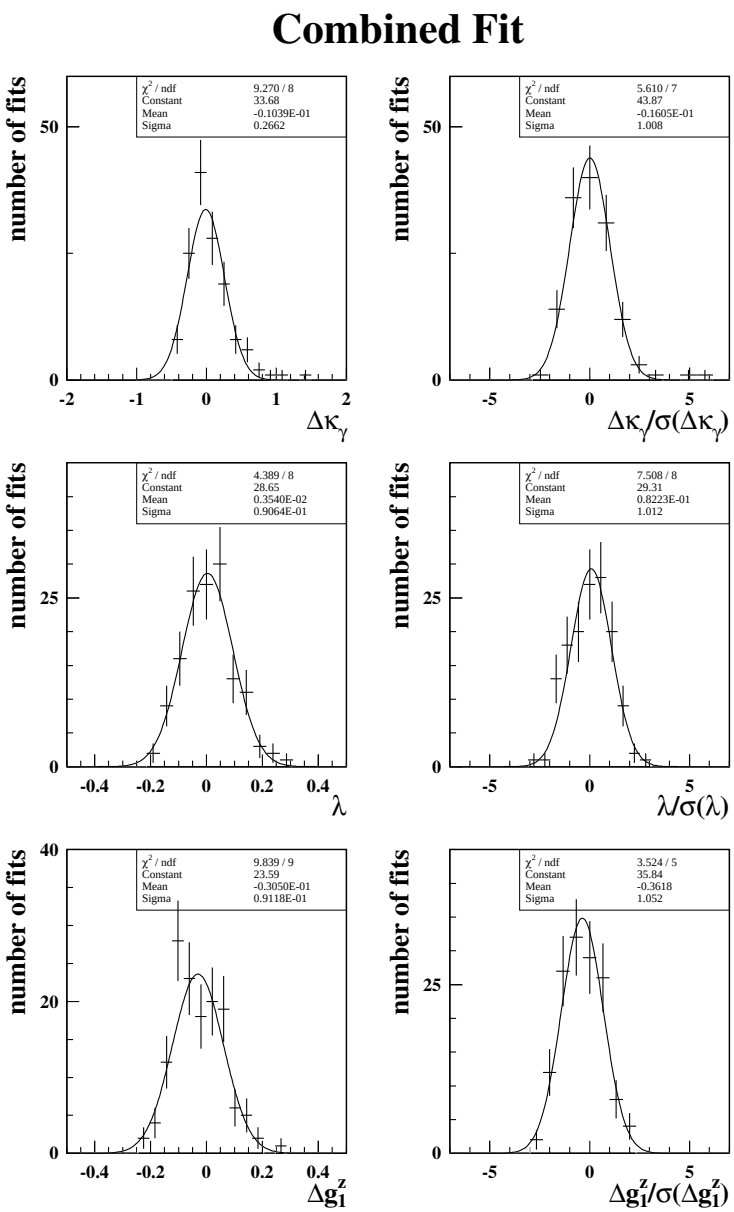

Figure 6.8: *Combined fit results to 139 subsamples of Standard Model EXCALIBUR Monte Carlo. The WVCXME reweighting scheme was used in the fits. The widths of the distributions of the plots on the left side represent the expected error for the analysis for the corresponding coupling parameters. The width of the pull distributions, the plots on the right side, should be compatible with unity if the statistical error is reliable.*

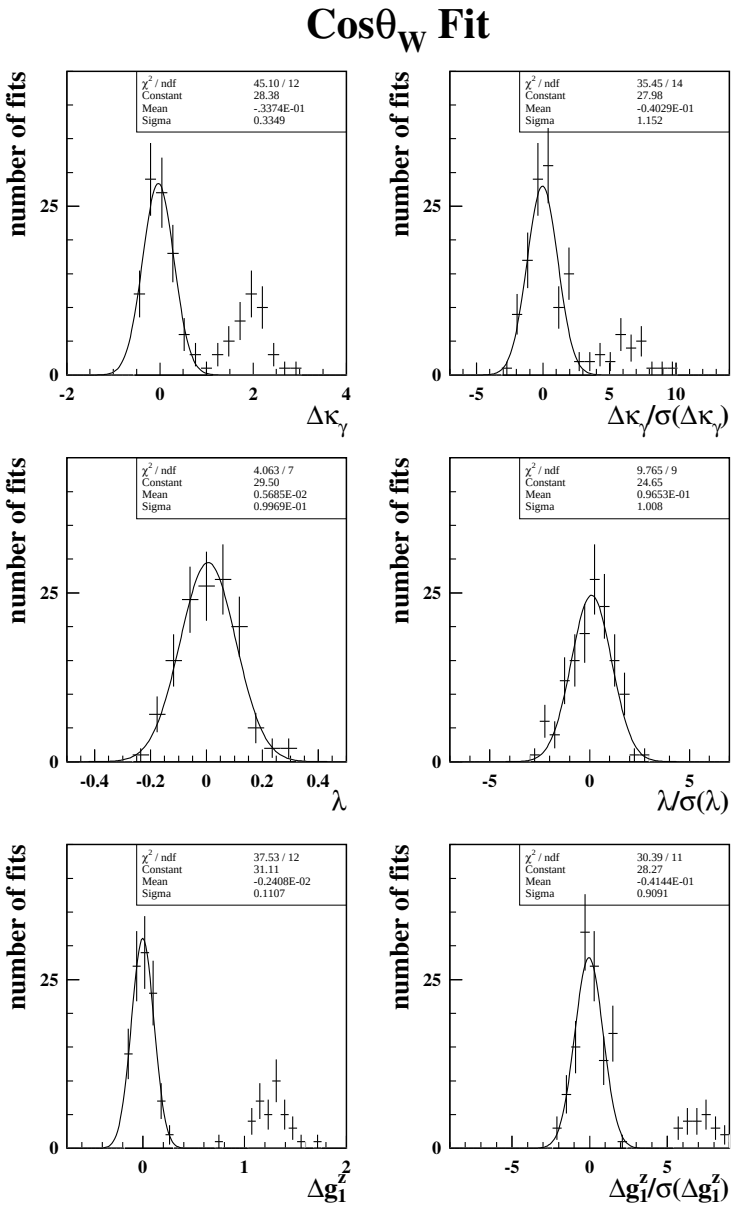

Figure 6.9: $\cos\theta_W$ *fit results of 139 subsamples to Standard Model EXCALIBUR Monte Carlo. The BILGOU reweighting scheme was used for these fits The widths of the distributions of the plots on the left side represent the expected error for the analysis for the corresponding coupling parameters. The width of the pull distributions, the plots on the right side, should be compatible with unity if the statistical error is reliable.*

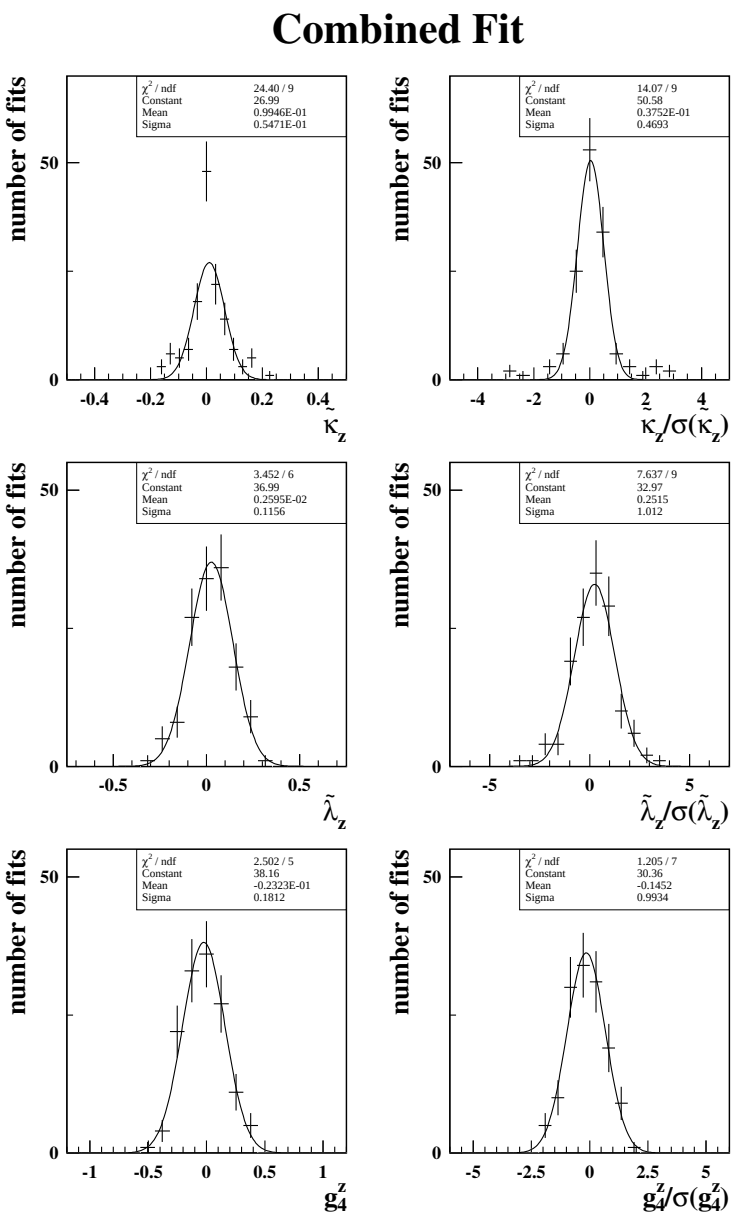

Figure 6.10: *Combined fit results for the CP-violating couplings to 139 subsamples of Standard Model EXCALIBUR Monte Carlo. The plots on the left are the distributions of fitted values and the plots on the right are the pull distributions.*

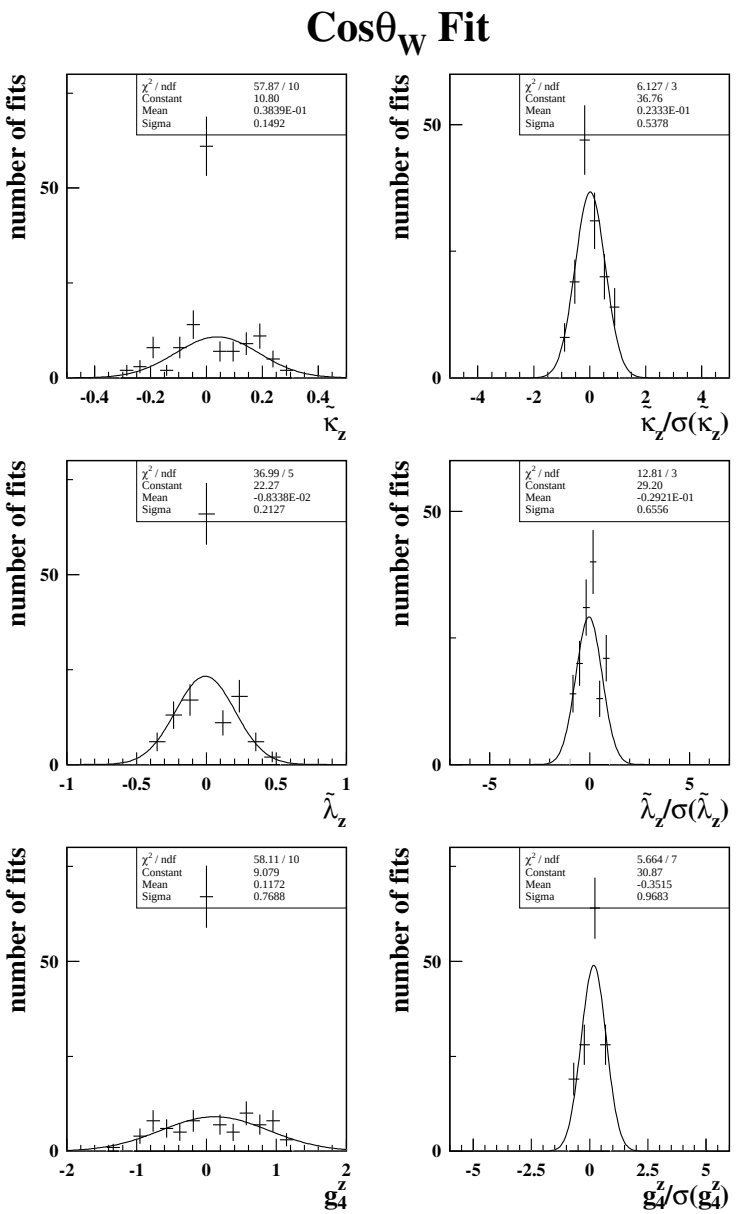

Figure 6.11: $\cos\theta_{\mathrm{W}}$ *fit results for the CP-violating couplings to 139 subsamples of Standard Model EXCALIBUR Monte Carlo. The plots on the left are the distributions of fitted values and the plots on the right are the pull distributions.*

Chapter 7

TGCs from 189 GeV Data

In this chapter the results of the TGC fits to the data set described in chapter 5 will be presented. Measurements of the $SU(2)_L \times U(1)_Y$ gauge invariant set of CP-conserving couplings $\Delta\kappa_\gamma$, Δg_1^z and λ, were made along with the $SU(2)_L \times U(1)_Y$ gauge invariant set of CP-violating couplings $\tilde{\kappa}_z$, $\tilde{\lambda}_z$ and g_4^z. In all cases the constraints given in chapter 3, equation 3.16 were implemented.

Fits were performed to both the single W SDM elements extracted from the $W \to \ell\bar{\nu}_\ell$ decay angles and the W boson production angle as described in chapter 6. These two fits were combined to give an overall value for each TGC.

7.1 Fit to Single W SDM Elements

The nine single W SDM elements extracted from the 189 GeV data are shown in figure 7.1. These elements were extracted from the leptonically decaying W bosons in the W-pair only, and CPT-invariance was assumed in all cases so that the results from the leptons and anti-leptons could be

combined, as described in chapter 4 by equation 4.6. The errors shown on the plots are purely statistical. A χ^2 fit was performed to these elements. Overlaid on these plots are the predicted SDM elements extracted from fully simulated Monte Carlo.

The correlations between all the first bins of the nine observables are given in table 7.1. For the calculation of the CP-conserving couplings a fit was made only to the six real single W SDM elements, as these are the only ones sensitive to the CP-conserving couplings.

	ρ_{++}	ρ_{--}	ρ_{00}	$\mathrm{Re}(\rho_{+-})$	$\mathrm{Re}(\rho_{+0})$	$\mathrm{Re}(\rho_{-0})$	$\mathrm{Im}(\rho_{+-})$	$\mathrm{Im}(\rho_{+0})$	$\mathrm{Im}(\rho_{-0})$
ρ_{++}	1.00	0.28	-0.82	-0.09	-0.26	0.02	0.11	-0.18	-0.13
ρ_{--}	0.28	1.00	-0.78	-0.15	-0.10	0.14	-0.02	-0.09	-0.20
ρ_{00}	-0.82	-0.78	1.00	0.15	0.23	-0.10	-0.06	0.17	0.21
$\mathrm{Re}(\rho_{+-})$	-0.09	-0.15	0.15	1.00	-0.26	0.34	0.13	0.16	0.05
$\mathrm{Re}(\rho_{+0})$	-0.26	-0.10	0.23	-0.26	1.00	-0.62	-0.01	0.04	0.01
$\mathrm{Re}(\rho_{-0})$	0.02	0.14	-0.10	0.34	-0.62	1.00	0.13	0.02	0.08
$\mathrm{Im}(\rho_{+-})$	0.11	-0.02	-0.06	0.13	-0.01	0.13	1.00	-0.06	-0.18
$\mathrm{Im}(\rho_{+0})$	-0.18	-0.09	0.17	0.16	0.04	0.02	-0.06	1.00	0.68
$\mathrm{Im}(\rho_{-0})$	-0.13	-0.20	0.21	0.05	0.01	0.08	-0.18	0.68	1.00

Table 7.1: *The correlations between the* $-1 < \cos\theta_{\mathrm{W}} < -0.875$ *bin of all the single W SDM observables extracted from the 189 GeV data.*

The fitted values using the WVCXME reweighting scheme are:

$$\begin{aligned} \Delta\kappa_\gamma &= -0.170^{+0.461}_{-0.305} \\ \Delta g_1^Z &= +0.047^{+0.117}_{-0.144} \\ \lambda &= +0.007^{+0.208}_{-0.226} \end{aligned}$$

The χ^2 plots for these fits can be seen in figure 7.3, where the dashed line represents the fit to the SDM elements. A similar fit of the couplings was made using the BILGOU reweighting scheme. The fitted values are:

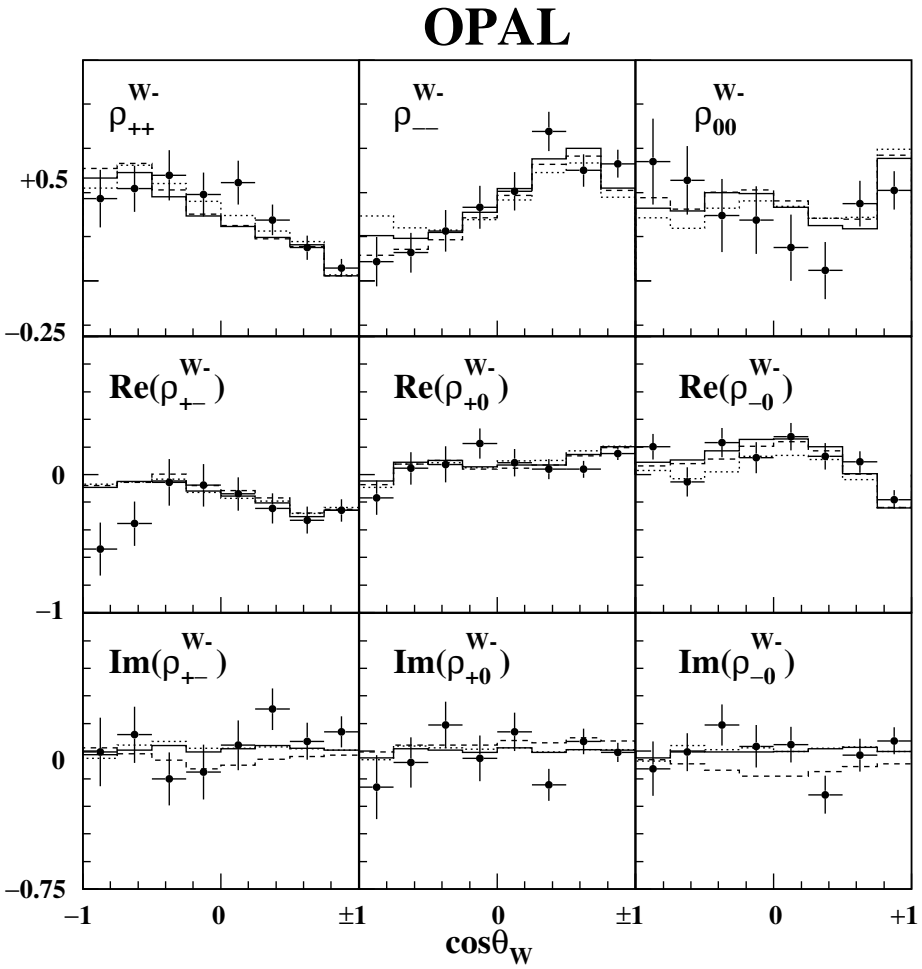

Figure 7.1: *Single W SDM elements extracted from the 189 GeV data (points). The solid line is the Standard Model prediction the dotted is the predictions for* $\Delta g_1^z = +0.5$ *and the dashed line is the prediction for* $g_4^z = +1.5$.

$$\begin{aligned} \Delta\kappa_\gamma &= -0.229^{+0.496}_{-0.425} \\ \Delta g_1^Z &= +0.040^{+0.116}_{-0.158} \\ \lambda &= +0.051^{+0.168}_{-0.177} \end{aligned}$$

The χ^2 plots for these fits can be seen in figure 7.4, where the dashed line represents the fit the the SDM elements. The results for Δg_1^z and λ agree well with those calculated using the WVCXME reweighting scheme. The difference in the fitted values for $\Delta\kappa_\gamma$ is slightly greater, but still much less than the statistical error. It will be seen later that this difference has little effect on the overall combined result once information about the W production angle is included in the fit.

The CP-violating couplings were calculated by performing fits to all nine single W SDM elements. The BILGOU reweighting scheme was used for these fits. The fitted values are:

$$\begin{aligned} \tilde{\kappa}_Z &= -0.191^{+0.078}_{-0.066} \\ \tilde{\lambda}_Z &= -0.089^{+0.159}_{-0.152} \\ g_4^Z &= +0.029^{+0.211}_{-0.215} \end{aligned}$$

The χ^2 plots for these fits can be seen in figure 7.5. The plot for the fit of $\tilde{\kappa}_z$ to the SDM elements displays a second minimum. This is because the real SDM elements are sensitive only to the magnitude of the coupling and not the sign, and the relative contribution from the real SDM elements in the fit is similar to that from the imaginary parts. A second minimum is not shown for the other CP-violating couplings because the relative contribution from the real parts of the SDM is much less than that of the imaginary for these couplings.

7.2 Fit to the Normalised $\cos\theta_W$ Distribution

Figure 7.2 shows the normalised $\cos\theta_W$ distribution extracted from the 189 GeV data.

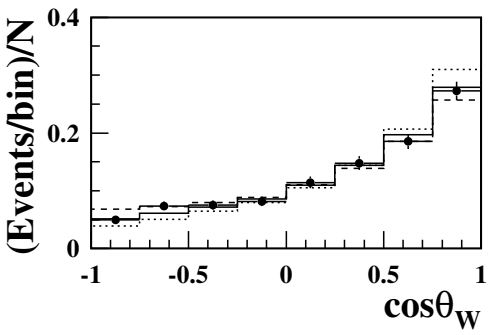

Figure 7.2: *Normalised* $\cos\theta_W$ *disribution extracted from the 189 GeV data (points). The solid line is the Standard Model prediction, the dotted is the predictions for* $\Delta g_1^z = +0.5$ *and the dashed line is the prediction for* $g_4^z = +1.5$.

The fitted values using the WVCXME reweighting scheme are:

$$\begin{aligned} \Delta\kappa_\gamma &= -0.267^{+0.297}_{-0.245} \\ \Delta g_1^Z &= -0.075^{+0.085}_{-0.081} \\ \lambda &= -0.090^{+0.091}_{-0.088} \end{aligned}$$

And for the BILGOU reweighting scheme the fitted values are:

$$\begin{aligned} \Delta\kappa_\gamma &= -0.265^{+0.285}_{-0.244} \\ \Delta g_1^Z &= -0.070^{+0.089}_{-0.081} \\ \lambda &= -0.090^{+0.093}_{-0.085} \end{aligned}$$

The agreement between the two methods is once again very good, with agreement between each measured coupling using the two methods being better than 5% of the statistical error.

The χ^2 plots for the WVCXME and BILGOU fits are represented by the dotted lines shown in figures 7.3 and 7.4 respectively.

The fitted values for the CP-violating couplings are:

$$\begin{aligned} \tilde{\kappa}_Z &= -0.189^{+0.444}_{-0.085} \\ \tilde{\lambda}_Z &= -0.289^{+0.669}_{-0.122} \\ g_4^Z &= +0.672^{+0.371}_{-1.710} \end{aligned}$$

The χ^2 plots are the dotted lines shown in figure 7.5. All plots show a double minimum for the fit of CP-violating couplings. The sign of the coupling has no effect on the $\cos\theta_{\mathrm{W}}$ distribution, only the magnitude, so this double minimum is expected.

7.3 The Combined Fit

The fits to the SDM elements and $\cos\theta_{\mathrm{W}}$ distributions are completely uncorrelated and are combined to form a final fit result.

Using the WVCXME reweighting scheme the final fitted values for the CP-conserving couplings are:

$$\begin{aligned} \Delta\kappa_\gamma &= -0.235^{+0.232}_{-0.200} \\ \Delta g_1^Z &= -0.049^{+0.081}_{-0.080} \\ \lambda &= -0.075^{+0.090}_{-0.081} \end{aligned}$$

Using the BILGOU reweighting scheme the final fitted values for the CP-conserving couplings are:

$$\begin{aligned} \Delta\kappa_\gamma &= -0.248^{+0.222}_{-0.197} \\ \Delta g_1^Z &= -0.050^{+0.080}_{-0.078} \\ \lambda &= -0.070^{+0.089}_{-0.078} \end{aligned}$$

Using the BILGOU reweighting scheme the final fitted values for the CP-violating couplings are:

$$\begin{aligned} \tilde{\kappa}_Z &= -0.191^{+0.062}_{-0.054} \\ \tilde{\lambda}_Z &= -0.191^{+0.182}_{-0.126} \\ g_4^Z &= +0.009^{+0.224}_{-0.223} \end{aligned}$$

The χ^2 plots for all these fits can be seen in figures 7.3, 7.4 and 7.5.

As mentioned earlier, the $\cos\theta_{\mathrm{W}}$ is much more sensitive to the CP-conserving couplings than the SDM elements are. This means that the fit to $\cos\theta_{\mathrm{W}}$ dominates the overall result. However, for the CP-violating couplings the converse is true, the $\cos\theta_{\mathrm{W}}$ distribution is much less sensitive to these couplings and therefore the fit to the SDM elements dominates the overall results.

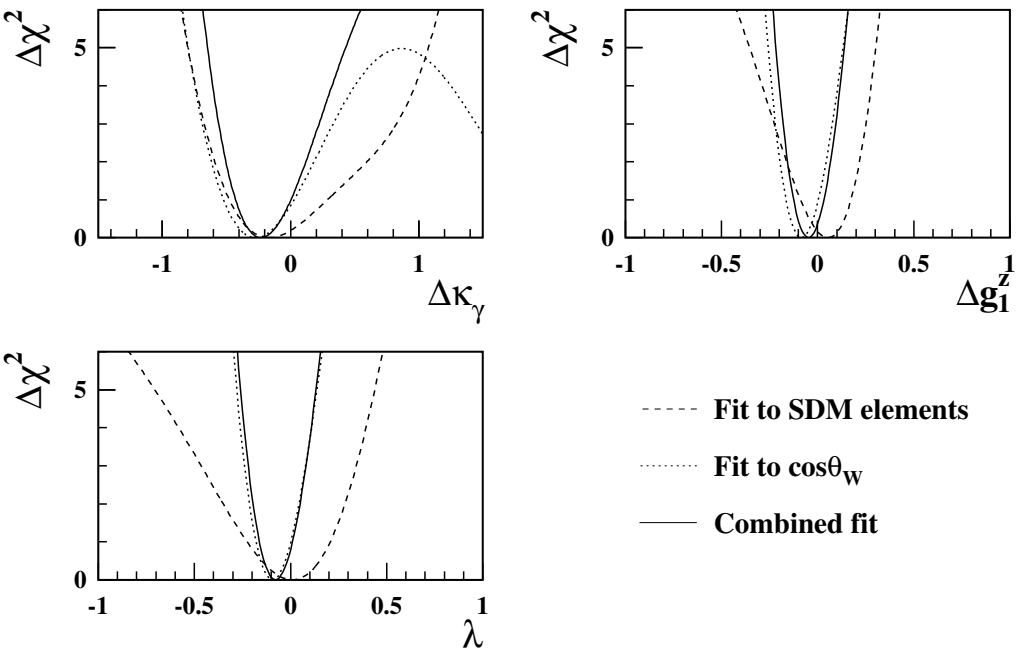

Figure 7.3: χ^2 *plots of the fit of the CP-conserving couplings using the WVCXME reweighting scheme. The dashed line is the fit to single W SDM elements. the dotted line is the fit to the* $\cos\theta_{\mathrm{W}}$ *distribution, and the solid line is the combined fit.*

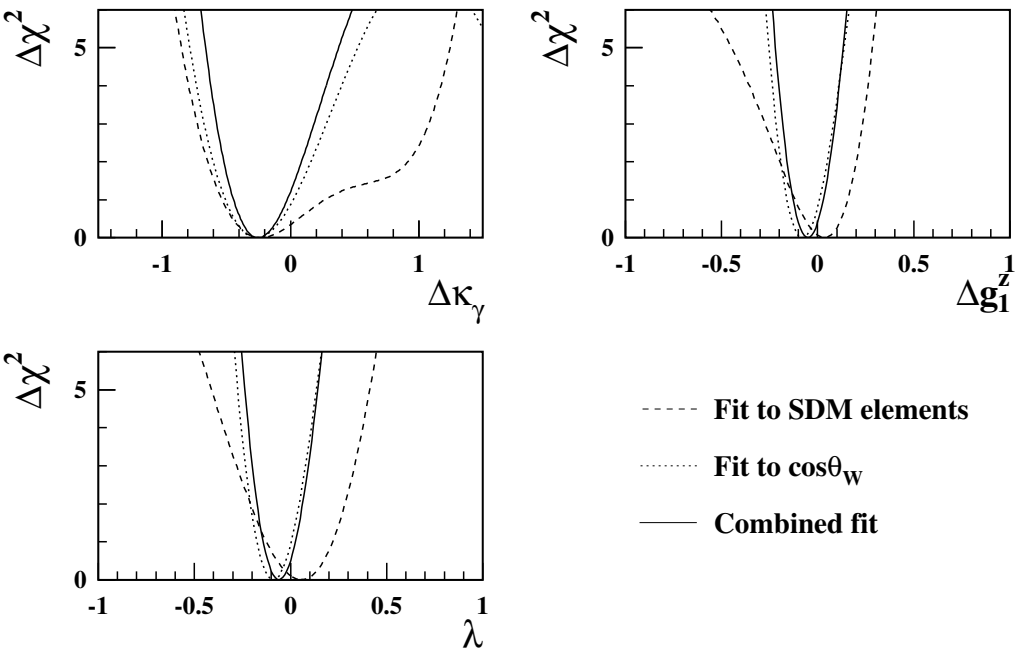

Figure 7.4: χ^2 *plots of the fit of the CP-conserving couplings using the BILGOU reweighting scheme. The dashed line is the fit to single W SDM elements, the dotted line is the fit to the* $\cos\theta_{\mathrm{W}}$ *distribution, and the solid line is the combined fit.*

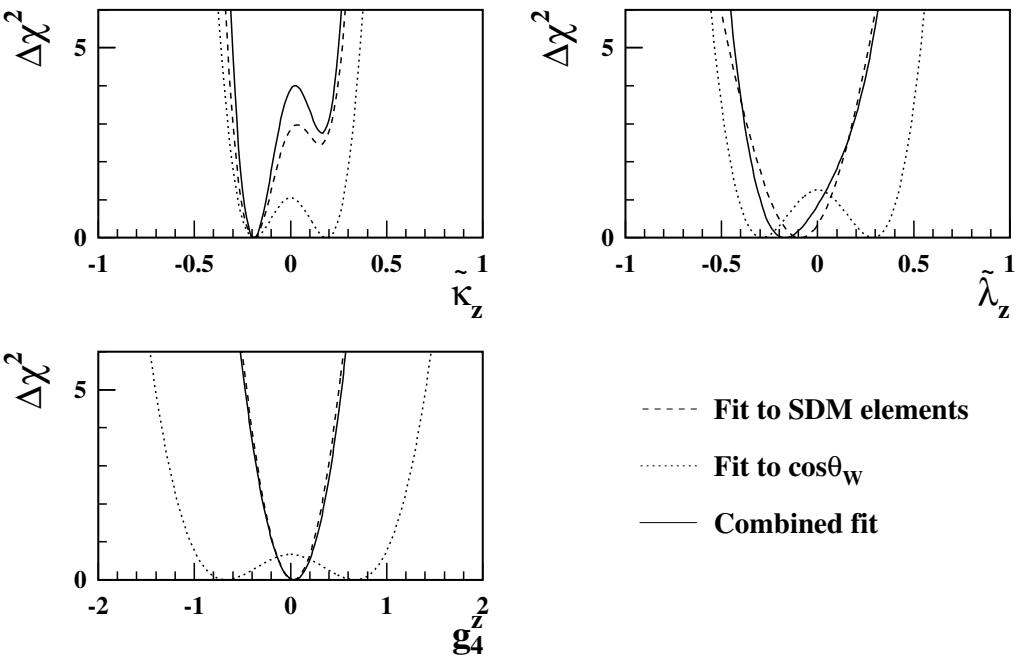

Figure 7.5: χ^2 *plots of the fit of the CP-violating couplings using the BILGOU reweighting scheme. The dashed line is the fit to single W SDM elements, the dotted line is the fit to the* $\cos\theta_{\mathrm{W}}$ *distribution, and the solid line is the combined fit.*

The goodness of the fit is given by the absolute value of the χ^2. The calculated values of the χ^2 for the combined fit for each coupling is given in table 7.2. For a good fit there should be a χ^2 of one per degree of freedom. The values calculated with the WVCXME give a lower χ^2 than BILGOU thus suggesting a slightly better fit.

Coupling	WVCXME	BILGOU
$\Delta\kappa_\gamma$	53.6	57.8
Δg_1^z	54.2	58.6
λ	53.8	58.6
$\tilde{\kappa}_z$	-	74.7
$\tilde{\lambda}_z$	-	77.9
g_4^z	-	78.7

Table 7.2: *Absolute values of the χ^2 minimum for each measured coupling using the combined fit.*

7.4 Including Systematics

The areas of systematic uncertainties investigated and their individual contributions are described in Chapter 10. The inclusion of these systematic uncertainties occurs before the fit is performed. In this way, not only changes in the overall error, but also a shift in the minimum value due to this uncertainty can be calculated.

A systematic error is calculated on each observable that is measured. This means that all eight bins of each of the nine SDM elements and the eight bins of the $\cos\theta_W$ distribution will be assigned an error.

These systematics are then included in the χ^2 fit given by equation 6.6 by including them directly in the covariance matrix as follows:

$$V_{ij}(k) = \omega_{ij}(k)\left(\sigma_i^{\rm stat}(k)\sigma_j^{\rm stat}(k) + \sigma_i^{\rm sys}(k)\sigma_j^{\rm sys}(k)\right) \tag{7.1}$$

Where $\sigma_i^{\rm stat}(k)$ is the statistical error and $\sigma_i^{\rm sys}(k)$ is the systematic error. The correlation matrix $\omega_{ij}(k)$ is only for statistical correlations, it does not include any extra correlations which may be introduced by the systematic uncertainty. This may not be an exact treatment of the correlations, but will give a reasonable estimate. Calculation of exact correlations for each systematic error would be an extremely difficult and involved task.

All the final fit results for both the CP-conserving and CP-violating couplings, using the BILGOU reweighting scheme, including the systematic uncertainties can be seen in table 7.3. The results for the combined fit are listed below.

Using the WVCXME reweighting scheme the final fitted values for the CP-conserving couplings including systematic uncertainties are:

$$\begin{aligned} \Delta\kappa_\gamma &= -0.235^{+0.282}_{-0.232} \\ \Delta g_1^Z &= -0.038^{+0.095}_{-0.089} \\ \lambda &= -0.082^{+0.102}_{-0.095} \end{aligned}$$

Using the BILGOU reweighting scheme the final fitted values for the CP-conserving couplings including systematic uncertainties are:

$$\begin{aligned} \Delta\kappa_\gamma &= -0.263^{+0.263}_{-0.218} \\ \Delta g_1^Z &= -0.029^{+0.092}_{-0.089} \\ \lambda &= -0.045^{+0.099}_{-0.093} \end{aligned}$$

Using the BILGOU reweighting scheme the final fitted values for the CP-violating couplings including systematic uncertainties are:

$$\begin{aligned} \tilde{\kappa}_Z &= -0.184^{+0.091}_{-0.065} \\ \tilde{\lambda}_Z &= -0.136^{+0.161}_{-0.194} \\ g_4^Z &= +0.070^{+0.263}_{-0.255} \end{aligned}$$

The χ^2 plots for the fits of the CP-conserving couplings using the WVCXME and BILGOU reweighting schemes can be seen in figures 7.6 and 7.7 respectively. The χ^2 plots for the fits of the CP-violating couplings are shown in figure 7.8.

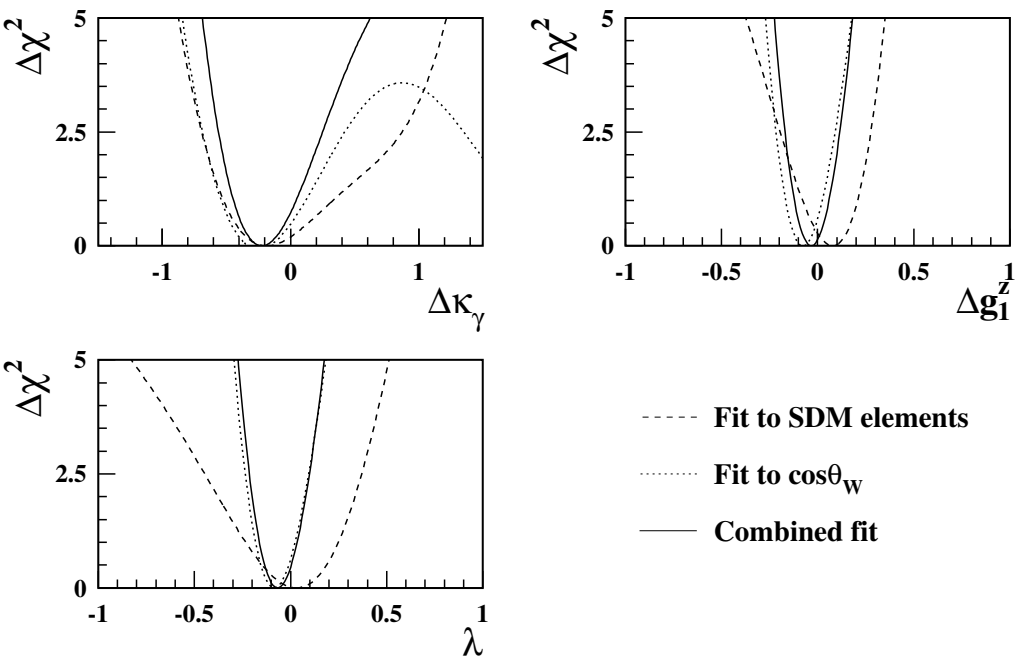

Figure 7.6: χ^2 *plots of the fit of the CP-conserving couplings, including systematic uncertainties, using the WVCXME reweighting scheme. The dashed line is the fit to single W SDM elements, the dotted line is the fit to the* $\cos\theta_{\mathrm{W}}$ *distribution, and the solid line is the combined fit.*

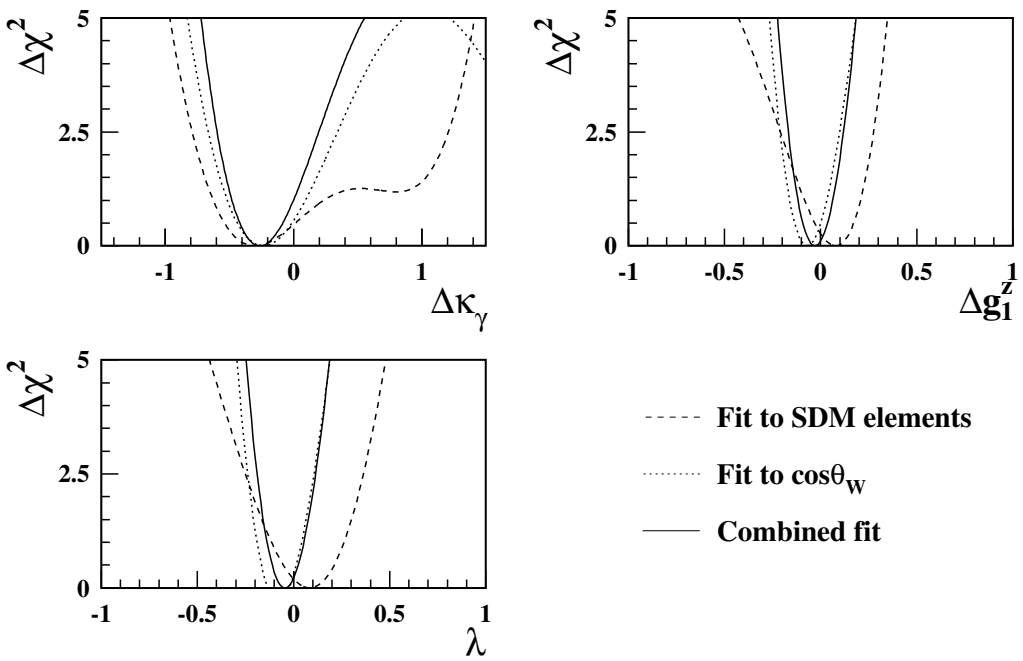

Figure 7.7: χ^2 *plots of the fit of the CP-conserving couplings, including systematic uncertainties, using the BILGOU reweighting scheme. The dashed line is the fit to single W SDM elements, the dotted line is the fit to the* $\cos\theta_{\mathrm{W}}$ *distribution, and the solid line is the combined fit.*

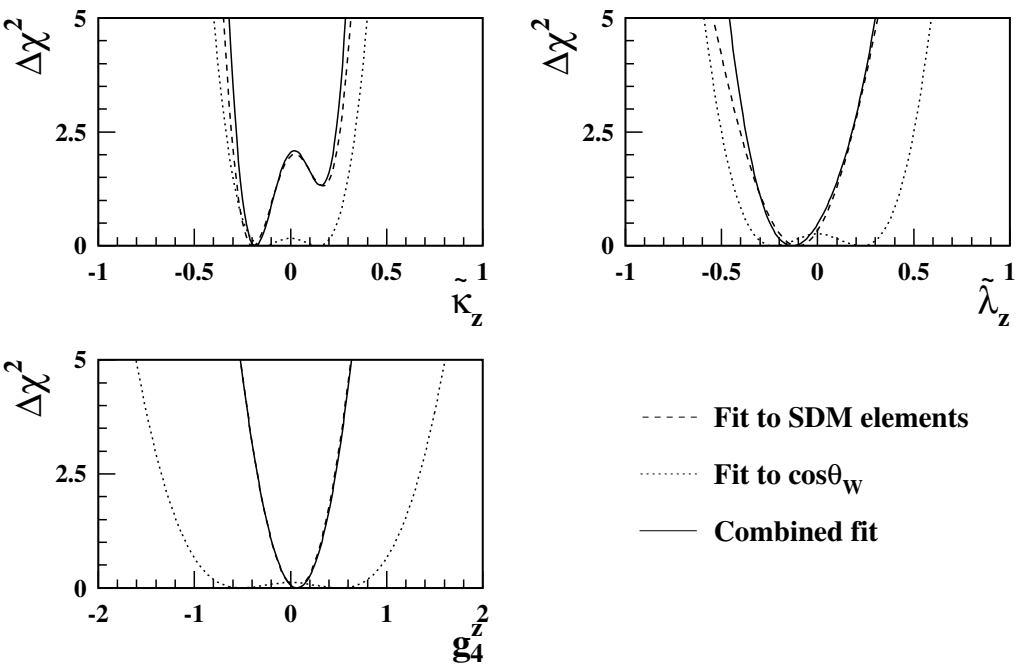

Figure 7.8: χ^2 *plots of the fit of the CP-violating couplings, including systematic uncertainties, using the BILGOU reweighting scheme. The dashed line is the fit to single W SDM elements, the dotted line is the fit to the* $\cos\theta_{\mathrm{W}}$ *distribution, and the solid line is the combined fit.*

	$\Delta\kappa_\gamma$	Δg_1^z	λ	$\tilde{\kappa}_z$	$\tilde{\lambda}_z$	g_4^z
SDM Elements						
Fit	$-0.23^{+0.50}_{-0.30}$	$0.04^{+0.12}_{-0.16}$	$0.05^{+0.17}_{-0.18}$	$-0.19^{+0.08}_{-0.07}$	$-0.09^{+0.16}_{-0.15}$	$0.03^{+0.21}_{-0.22}$
Expected Stat. Error	± 0.32	± 0.21	± 0.18	± 0.09	± 0.12	± 0.18
Fit Including Systematic Uncertainties	$-0.30^{+0.54}_{-0.33}$	$0.08^{+0.13}_{-0.16}$	$0.08^{+0.19}_{-0.20}$	$-0.20^{+0.10}_{-0.07}$	$-0.10^{+0.18}_{-0.19}$	$0.06^{+0.25}_{-0.26}$
$\cos\theta_W$						
Fit	$-0.27^{+0.29}_{-0.24}$	$-0.08^{+0.09}_{-0.08}$	$-0.09^{+0.09}_{-0.08}$	$-0.19^{+0.44}_{-0.09}$	$-0.29^{+0.67}_{-0.12}$	$0.67^{+0.37}_{-1.60}$
Expected Stat. Error	± 0.34	± 0.11	± 0.10	± 0.17	± 0.26	± 0.70
Fit Including Systematic Uncertainties	$-0.24^{+0.33}_{-0.28}$	$-0.07^{+0.10}_{-0.09}$	$-0.08^{+0.11}_{-0.10}$	$-0.14^{+0.41}_{-0.13}$	$-0.23^{+0.61}_{-0.19}$	$0.63^{+0.52}_{-1.71}$
Combined						
Fit	$-0.25^{+0.22}_{-0.20}$	$-0.05^{+0.08}_{-0.08}$	$-0.06^{+0.09}_{-0.08}$	$-0.19^{+0.06}_{-0.05}$	$-0.17^{+0.19}_{-0.13}$	$0.04^{+0.22}_{-0.23}$
Expected Stat. Error	± 0.26	± 0.08	± 0.10	± 0.08	± 0.11	± 0.18
Fit Including Systematic Uncertainties	$-0.26^{+0.26}_{-0.22}$	$-0.03^{+0.09}_{-0.09}$	$-0.05^{+0.10}_{-0.09}$	$-0.18^{+0.09}_{-0.07}$	$-0.14^{+0.16}_{-0.19}$	$0.07^{+0.26}_{-0.26}$

Table 7.3: *Measured values of all the TGC parameters using the BILGOU reweighting scheme*

Chapter 8

Method to Measure Polarised Cross-sections

The spin density matrix gives full information about the helicities of the W bosons and as seen in equations 3.33 and 3.38, certain elements can be used to calculate the polarised cross-section.

It has already been shown in chapter 6 that the SDM elements extracted directly from the data do not represent the true SDM elements, figure 6.1. This did not pose a problem when calculating the TGC values from the data because the data could be compared directly to fully simulated Monte Carlo. However, this does cause a problem when trying to calculate the polarised cross-sections. For these, the SDM elements corrected for detector, acceptance and background effects are required.

8.1 Correcting for Detector Effects

The correction of angular resolution, finite selection efficiency and detector acceptance effects can be made by introducing a correction factor into the

calculation of the SDM elements. This correction factor is calculated from the ratio of the number of fully detector simulated, selected Monte Carlo events, to the number of generated Monte Carlo events.

This is done in a bin-wise manner, so a correction factor is calculated for a certain volume of phase space as the ratio of the number of events in that phase space, before simulation and selection, to the number of events after full simulation and selection.

The relevant SDM elements for calculating the W-pair polarised cross-sections and the individual W polarised cross-sections are only functions of the W production angle $\cos\theta_{\mathrm{W}}$, and the polar angle of the W decay product, $\cos\theta^*$, so the correction factor only has to be calculated as a function of these variables.

The correction factor will then be calculated as:

$$f = \left(\frac{\mathrm{d}\sigma}{\mathrm{d}\cos\theta_{\mathrm{W}}\mathrm{d}\cos\theta^*_\ell,\mathrm{d}\cos\theta^*_{\mathrm{j}}}\right)^{\mathrm{rec}} \Bigg/ \left(\frac{\mathrm{d}\sigma}{\mathrm{d}\cos\theta_{\mathrm{W}}\mathrm{d}\cos\theta^*_\ell,\mathrm{d}\cos\theta^*_{\mathrm{j}}}\right)^{\mathrm{true}} \tag{8.1}$$

Where rec denotes the selected, reconstructed cross-section and true denotes the generated cross-section. θ^*_{j} is the folded polar angle of the decay hadron. The hadronic jet with $\theta^*_{\mathrm{j}} > 0$ is the angle used. θ^*_ℓ is the polar angle of the decay lepton. If the $\cos\theta_{\mathrm{W}}$ distribution is separated into k bins, then there will be a set of correction factors for each bin of $\cos\theta_{\mathrm{W}}$, each of which will only be a function of the polar angles of the W decay products. This correction factor can be applied to the calculation of the appropriate SDM element as follows:

$$\rho^k_{\tau\tau\tau'\tau'} = \frac{1}{N^{\mathrm{cor}}_k}\sum_{i=1}^{N_k}\frac{1}{\{f^k(\theta^*_\ell,\theta^*_{\mathrm{j}})_i\}}\Lambda_{\tau\tau}(\cos\theta^*_\ell)_i\Lambda_{\tau'\tau'}(\cos\theta^*_{\mathrm{j}})_i \tag{8.2}$$

where N_k^{cor} is the corrected number of events in bin k given by equation (8.3).

$$N_k^{\rm cor} = \sum_{i=1}^{N_k} \frac{1}{\{f^k(\theta_\ell^*, \theta_{\rm j}^*)_i\}} \tag{8.3}$$

The single W SDM elements are only a function of the polar decay angle of one of the W bosons. For these the correction factor is only calculated as a function of the one relevant angle. The value of N_k^{cor} therefore also changes. The full set of equations needed to calculate SDM element combinations for all the W-pair and individual W cross-sections, including the correction factor would then be:

$$\begin{aligned}
{\rm TT} &\equiv \rho_{++++} + \rho_{++--} + \rho_{--++} + \rho_{----} && (8.4)\\
&= \frac{1}{N_k^{\rm cor}} \sum_{i=1}^{N_k} \frac{1}{\{f^k(\theta_\ell^*, \theta_{\rm j}^*)_i\}} (5\cos^2\theta_\ell^* - 1)_i (5\cos^2\theta_{\rm j}^* - 1)_i \\
{\rm LL} &\equiv \rho_{0000} && (8.5)\\
&= \frac{1}{N_k^{\rm cor}} \sum_{i=1}^{N_k} \frac{1}{\{f^k(\theta_\ell^*, \theta_{\rm j}^*)_i\}} (2 - 5\cos^2\theta_\ell^*)_i (2 - 5\cos^2\theta_{\rm j}^*)_i \\
{\rm TL} &\equiv \rho_{++00} + \rho_{--00} + \rho_{00++} + \rho_{00--} && (8.6)\\
&= \frac{1}{N_k^{\rm cor}} \sum_{i=1}^{N_k} \frac{1}{\{f^k(\theta_\ell^*, \theta_{\rm j}^*)_i\}} (5\cos^2\theta_\ell^* - 1)_i (2 - 5\cos^2\theta_{\rm j}^*)_i \\
&+ \frac{1}{N_k^{\rm cor}} \sum_{i=1}^{N_k} \frac{1}{\{f^k(\theta_\ell^*, \theta_{\rm j}^*)_i\}} (2 - 5\cos^2\theta_\ell^*)_i (5\cos^2\theta_{\rm j}^* - 1)_i \\
{\rm T} &\equiv \rho_{++} + \rho_{--} && (8.7)\\
&= \frac{1}{N_k^{\rm cor}} \sum_{i=1}^{N_k} \frac{1}{\{f^k(\theta_i^*)\}} (5\cos^2\theta_i^* - 1) \\
{\rm L} &\equiv \rho_{00} && (8.8)\\
&= \frac{1}{N_k^{\rm cor}} \sum_{i=1}^{N_k} \frac{1}{\{f^k(\theta_i^*)\}} (2 - 5\cos^2\theta_i^*)
\end{aligned}$$

The correction factors are calculated from Monte Carlo data. The width of the bins used has to be small enough to give reasonable results, but its

width is limited by the resolution of the angular variables. Although the correction is designed to account for events migrating between bins, if the bin width is much less than the resolution, then the correction will be less reliable due to the very large numbers of events migrating between bins. The angular resolutions of the W production and polar decay angles are shown in figure 8.1.

The resolution of $\cos\theta_{\mathrm{W}}$ is 0.04, the resolution of $\cos\theta_l^*$ is 0.06 and the resolution of of $\cos\theta_{\mathrm{j}}^*$ is 0.08, so the bin widths have to be larger than these. If the $\cos\theta_{\mathrm{W}}$ distribution is once again divided into 8 equal bins, the width of each will be 0.25, which is much larger than the resolution. For the polar angles it is important to have more bins as it is these that are most sensitive to the W polarisation. For the lepton the bin width is chosen as 0.1, which means that the $\cos\theta_\ell^*$ distribution is split into 20 equal bins in the range $[-1,+1]$. For $\cos\theta_{\mathrm{j}}^*$ a bin width of 0.1 is used in the folded range of $[0,+1]$, thus it is divided into 10 equal bins when calculating the correction factor. Examples of some of the correction factor distributions are shown in figures 8.2 and 8.3. For the $\cos\theta_{\mathrm{W}}$ range $[-0.25,0.0]$ it is obvious that the correction is limited by Monte Carlo statistics.

The correction can be tested by applying it to fully simulated Monte Carlo samples. It will obviously correct the EXCALIBUR sample used to calculate the correction factors to extremely good accuracy, but as figure 8.4 demonstrates, it also gives a good approximation of the true SDM elements when applied to a sample of fully simulated PYTHIA Monte Carlo. Figure 8.4 shows the combinations of SDM elements needed to calculate the polarised cross-sections.

Using these corrected SDM elements to calculate the individual W and W-pair polarised differential cross-sections for the PYTHIA sample, as described

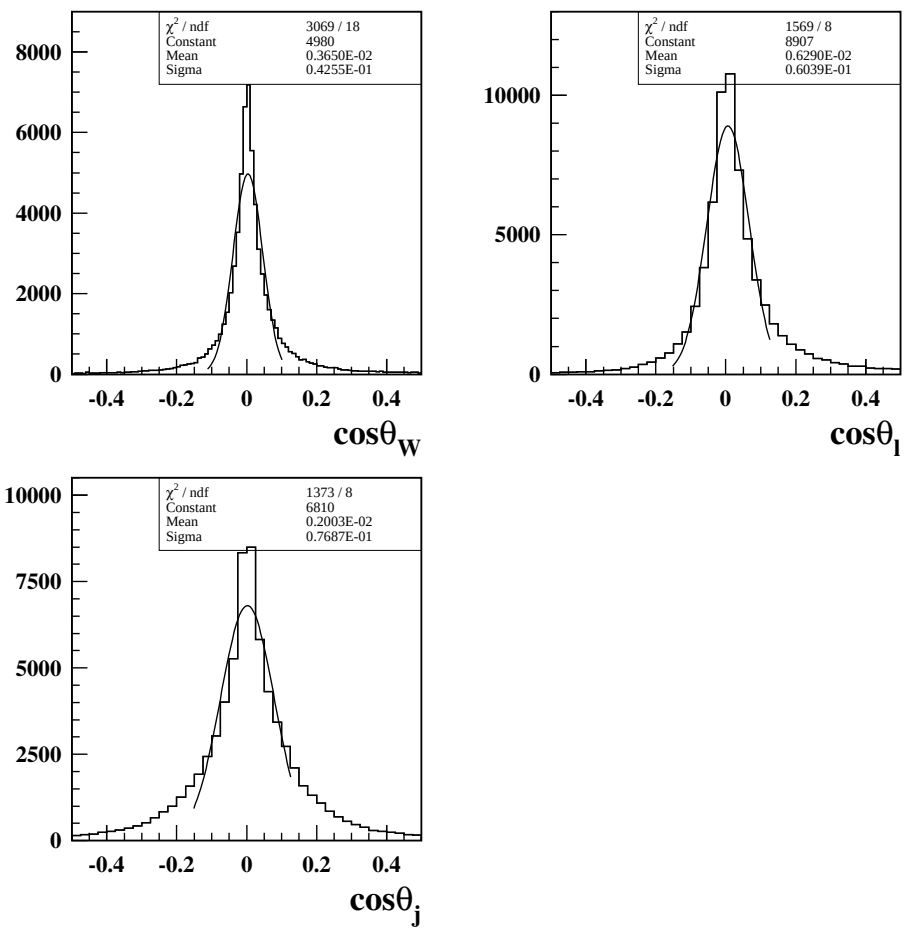

Figure 8.1: *The resolution of the angular variables* $\cos\theta_{\mathrm{W}}$, $\cos\theta^*_\ell$ *and* $\cos\theta^*_{\mathrm{j}}$ *used in calculating the polarised cross-sections. These were calculated from Monte Carlo data as* $x_{\mathrm{measured}} - x_{\mathrm{true}}$.

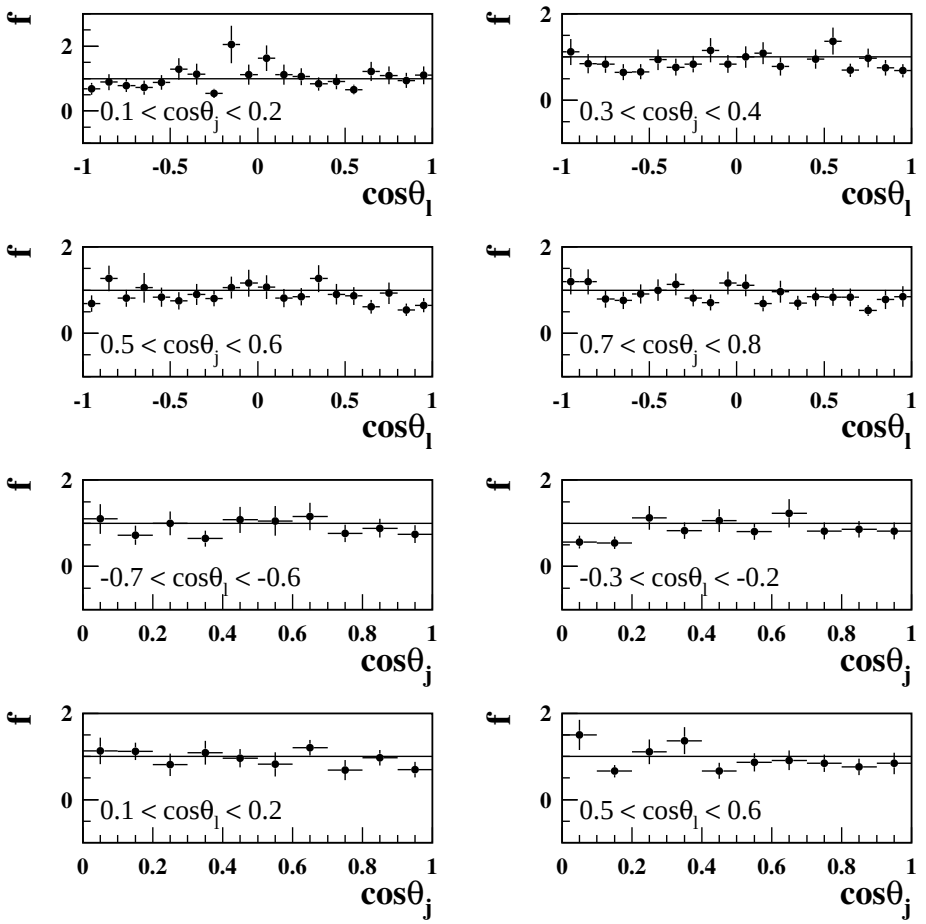

Figure 8.2: *Distributions of the correction factors calculated from EXCALIBUR Monte Carlo. The first four are a function of* $\cos\theta_\ell$ *for one bin of* $\cos\theta_{\rm j}$ *and the last four are a function of* $\cos\theta_{\rm j}$ *for one bin of* $\cos\theta_\ell$*. All eight are for* $-0.25 <\cos\theta_{\rm W}< 0.0$.

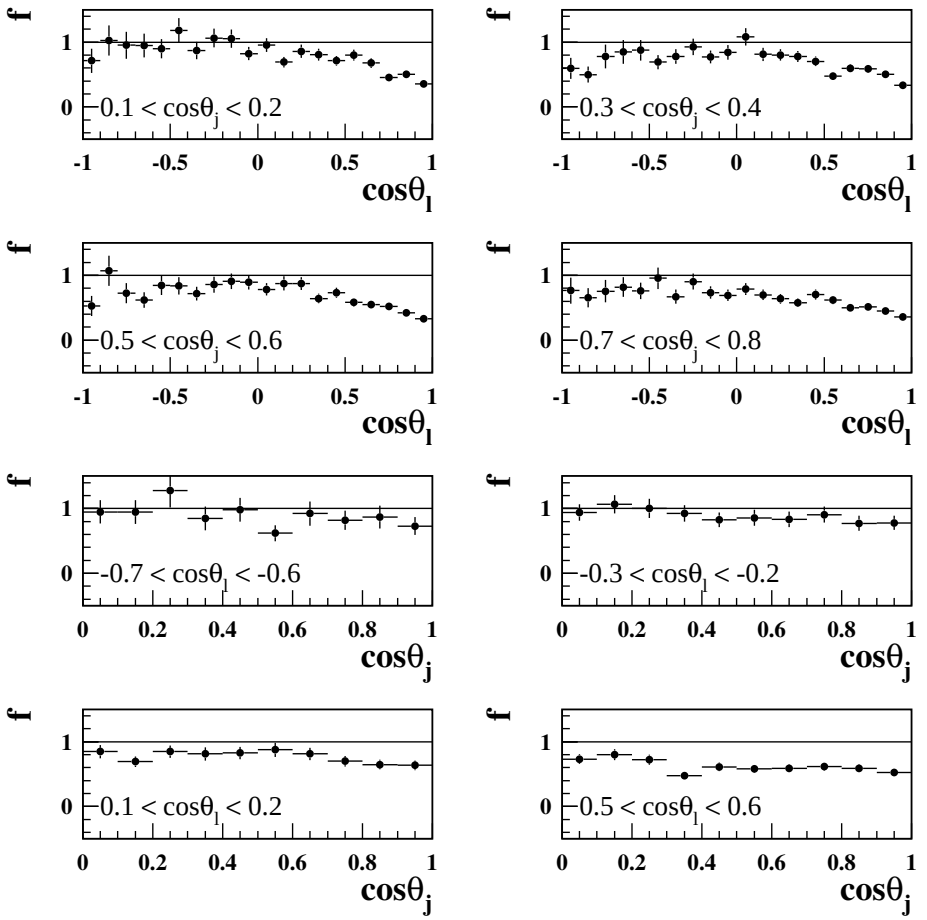

Figure 8.3: *Distributions of the correction factors calculated from EXCALIBUR Monte Carlo. The first four are a function of* $\cos\theta_\ell$ *for one bin of* $\cos\theta_{\rm j}$ *and the last four are a function of* $\cos\theta_{\rm j}$ *for one bin of* $\cos\theta_\ell$*. All eight are for* $0.75 < \cos\theta_{\rm W} < 1.0$.

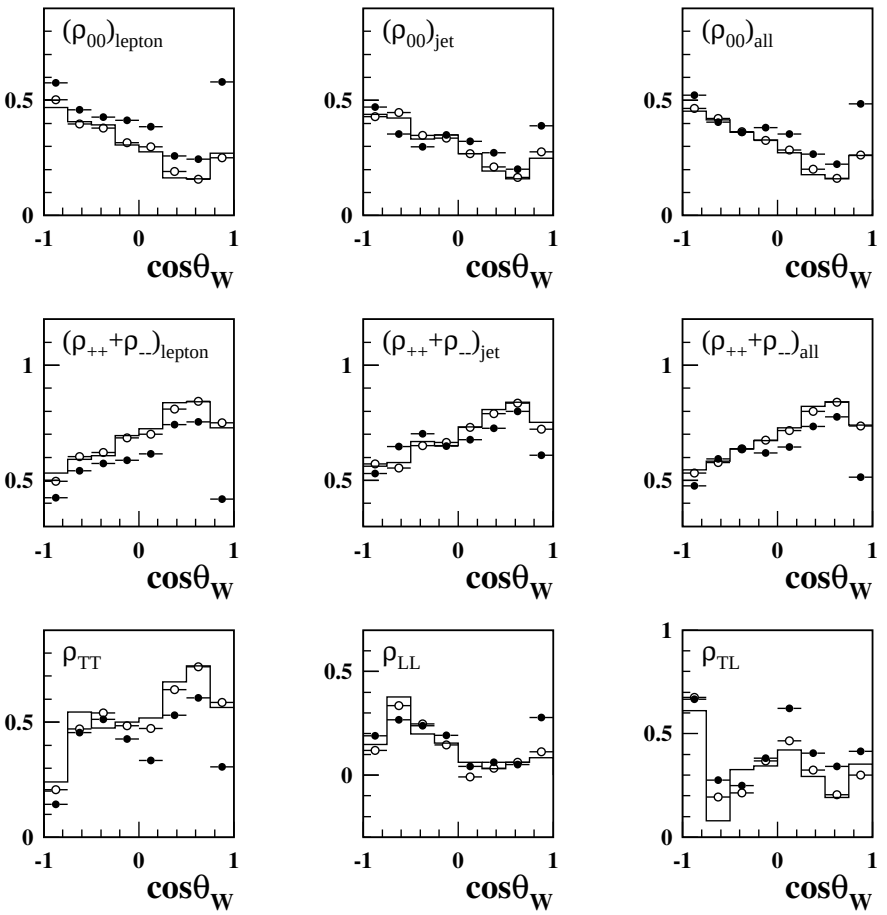

Figure 8.4: *Comparison of the SDM elements extracted from a fully detector simulated sample of Standard Model PYTHIA Monte Carlo. The solid circles are the measured and the open circles are the corrected. The histogram shows the true SDM elements extracted from the generator level Monte Carlo. Shown, are only the combinations of SDM elements needed to calculate the polarised cross-sections.* ρ_{TT} *indicates that it is the combination needed to calculated* σ_{TT}*, i.e.* $\rho_{++++}+\rho_{++--}+\rho_{--++}+\rho_{----}$*. The same applies for* ρ_{LL} *and* ρ_{TL}*.*

by equations 3.38 and 3.33, the plots in figure 8.5 are obtained. Once again, the correction produces a good approximation of the true cross-sections.

Integrating over $\cos\theta_W$ on the polarised differential cross-sections gives the total polarised cross-section. The total polarised cross-section divided by the total cross-section gives the fraction of each polarisation state. Calculating these numbers from generator level Monte Carlo and from the corrected polarised cross-sections will give a quantitative check of the detector correction. Figure 8.6 shows the calculated fractions from generator level Monte Carlo and also fully simulated Monte Carlo, both before and after the detector correction. Shown, are the results for a number of Standard Model Monte Carlo samples and also some non-Standard Model samples. It is obvious that the detector simulation has a large effect on the measured polarised fraction. In all cases, for both Standard and non-Standard Model Monte Carlo the detector correction gives results that are within one standard deviation of the true polarised fractions. It is interesting to note that for all Monte Carlo samples the detector simulation has a similar effect. The fraction of TT pairs is decreased and thus the fraction of other polarised W-pairs is enhanced. This is due to the detector simulation having the largest effect in the high $\cos\theta_W$ region and this is where most of the TT W-pairs are found, as can be seen for example in figure 8.5.

The correction has also been tested on the polarised cross-sections extracted from Monte Carlo subsamples with the same statistics to the data sample. Figure 8.7 shows an example of one of these tests. The correction appears to give a good approximation of the true cross-sections.

The fractional polarised cross-sections have also been extracted from the subsamples. They were calculated for both the generator level Monte Carlo and the fully simulated Monte Carlo. Figure 8.8 shows the difference between

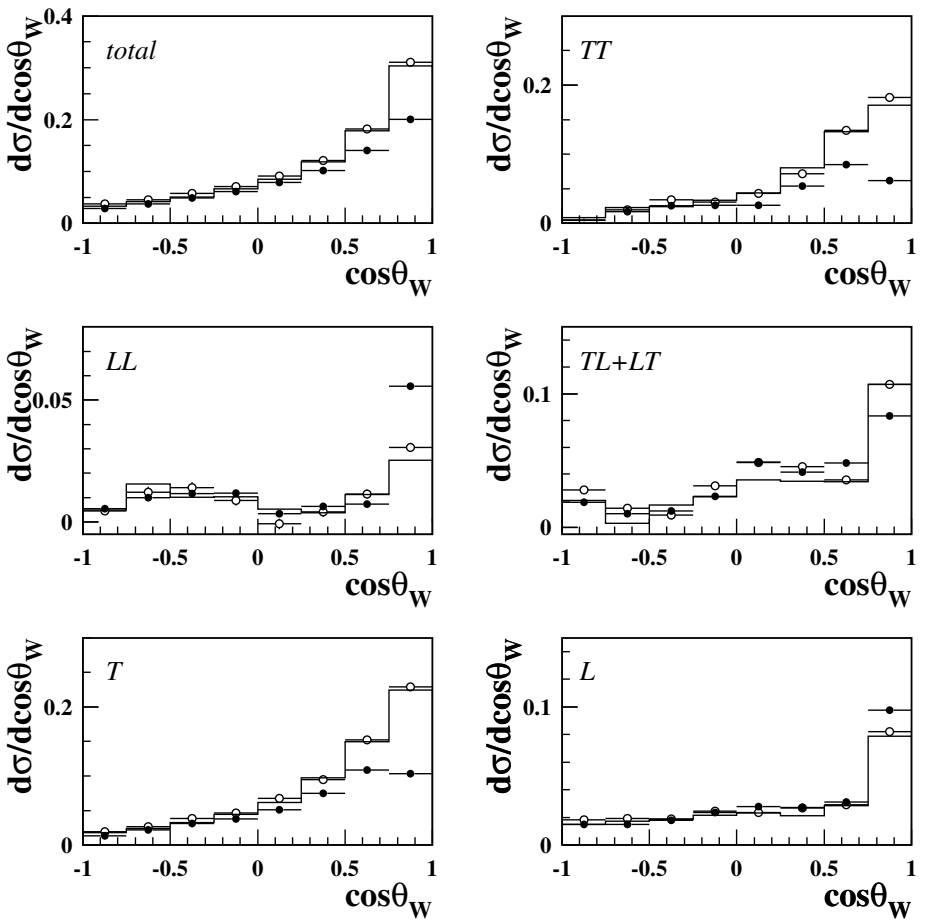

Figure 8.5: *Comparison of the differential cross-sections extracted from a fully detector simulated sample of Standard Model PYTHIA Monte Carlo. The solid circles are the measured and the open circles are the corrected. The histogram shows the true differential cross-sections extracted from the generator level Monte Carlo.*

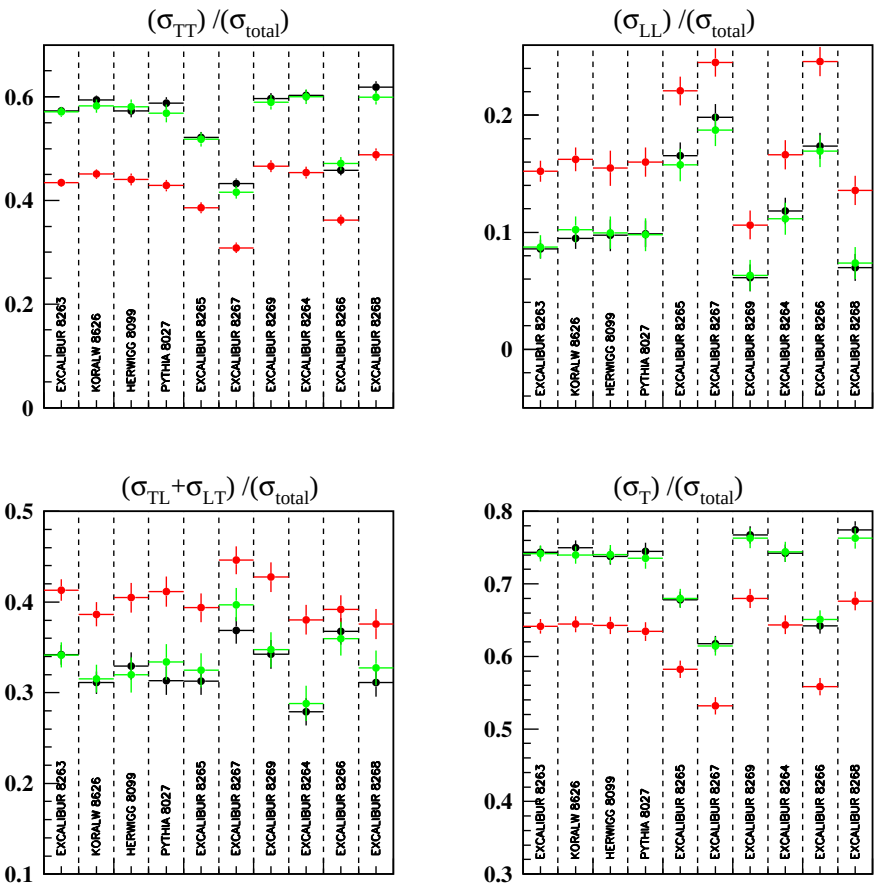

Figure 8.6: *The fraction of each polarisation state calculated from different Monte Carlo samples. The black circle is for generator level Monte Carlo, the red for fully detector simulated and the green is the result after the fully simulated has been corrected for detector effects. Descriptions of each Monte Carlo sample can be found in table 5.1.*

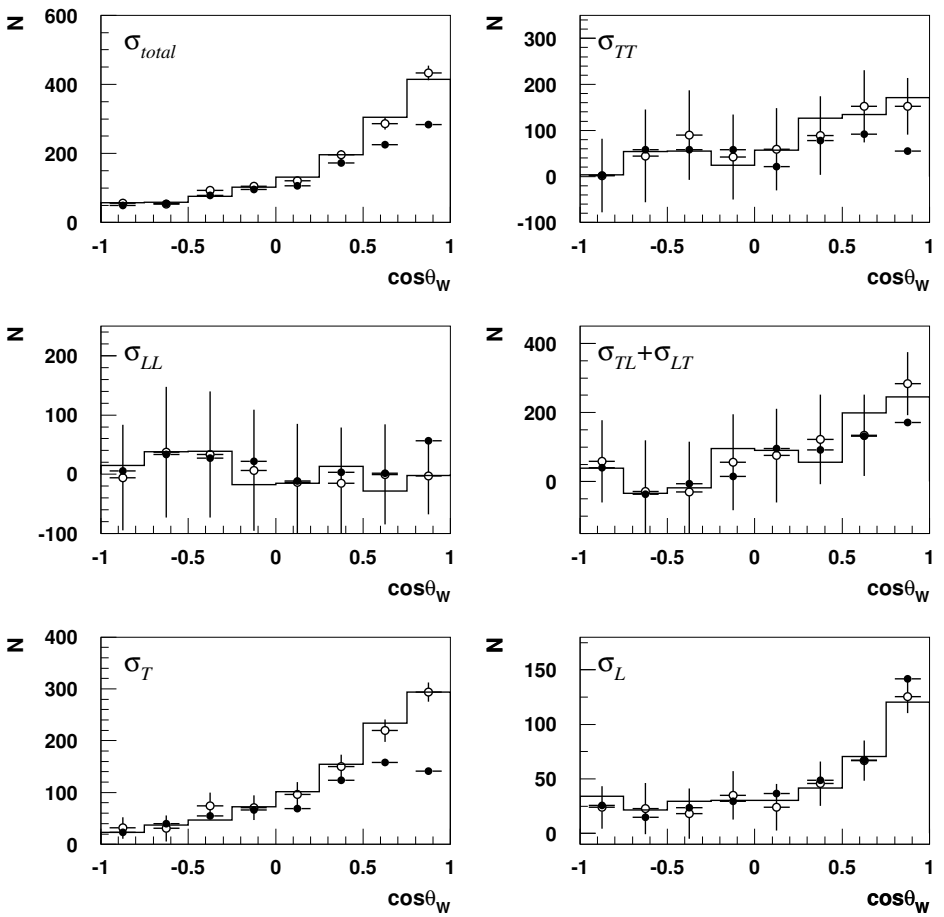

Figure 8.7: *The polarised differential cross-sections extracted from a small Standard Model Monte Carlo sample. The histogram represents the true cross-sections extracted from the generator level Monte Carlo. The solid circles are those extracted from the fully detector simulated Monte Carlo and the open circles are as for the solid circles except the detector correction has been implemented. The errors represented are purely statistical and only for the corrected results.*

the true (generator level) and measured (fully simulated, corrected) values of the fraction of W bosons with longitudinal polarisation. Results for both the leptonically and hadronically decaying W boson as well as the combined result are shown. Good agreement is seen between the measured and true values. Also shown on figure 8.8 are the pull distributions for these results. The widths are all close to unity, although the width for the hadronically decaying W boson is slightly low, suggesting that the statistical error may be slightly overestimated.

Similar plots for the W-pair polarised cross-sections can be seen in figure 8.9. Good agreement between the true and measured values is once again seen. The pull distributions all have widths close to unity except that for σ_{TT}, which is slightly low, again suggesting a slight overestimation in the statistical error.

The distributions of the measured values of both the fraction of longitudinal W bosons and the W-pair polarised cross-section fractions can be seen in figure 8.10. The width of these distributions can be taken as the expected statistical error on the measured values.

8.2 Correction for Background

The expected contribution from background events needs to be subtracted from the data sample before the polarised cross-sections are measured, so that the true fraction of each polarisation state can be calculated. The expected accepted cross-section of each background type was given in chapter 5.

Figure 8.11 shows the contribution of background events to the polarised differential cross-sections. The background can have both a positive and negative contribution. This is indicated clearly in figure 8.12, which shows

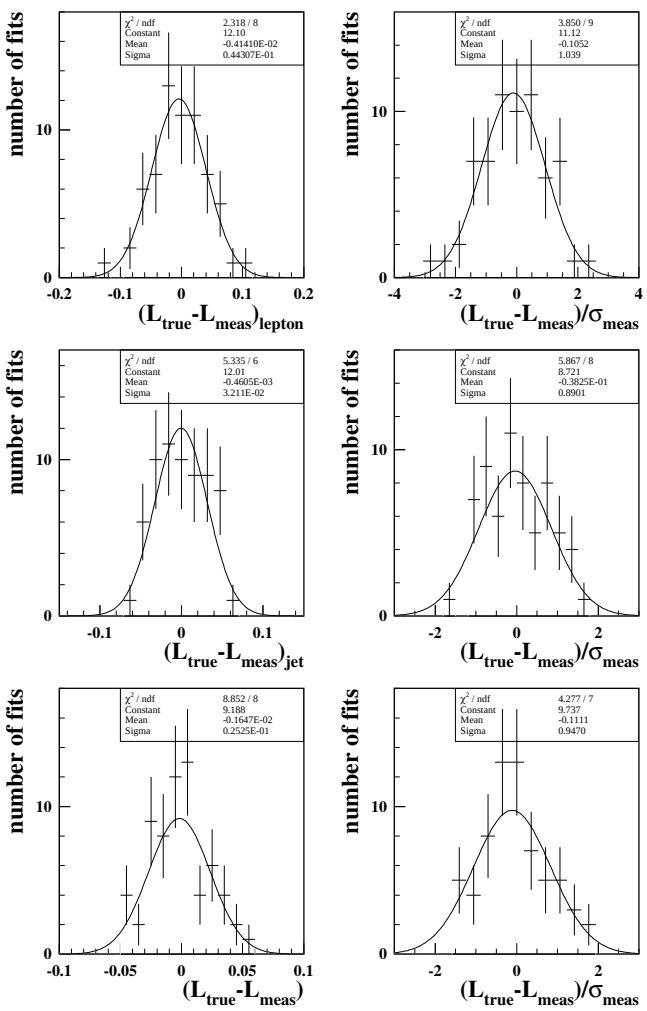

Figure 8.8: *Distribution of the comparison of the true to the measured fractions of longitudinal W bosons calculated from Monte Carlo subsamples. The true values were calculated from generator level Monte Carlo. The measured values were calculated from fully detector simulated Monte Carlo and have been corrected for detector effects. The first two plots are for leptonically decaying W bosons. The next two plots are for the hadronically decaying W boson. The last two plots are the combined results. The three plots on the left show the difference between the measured and true results. The three plots on the right are the pull distributions.*

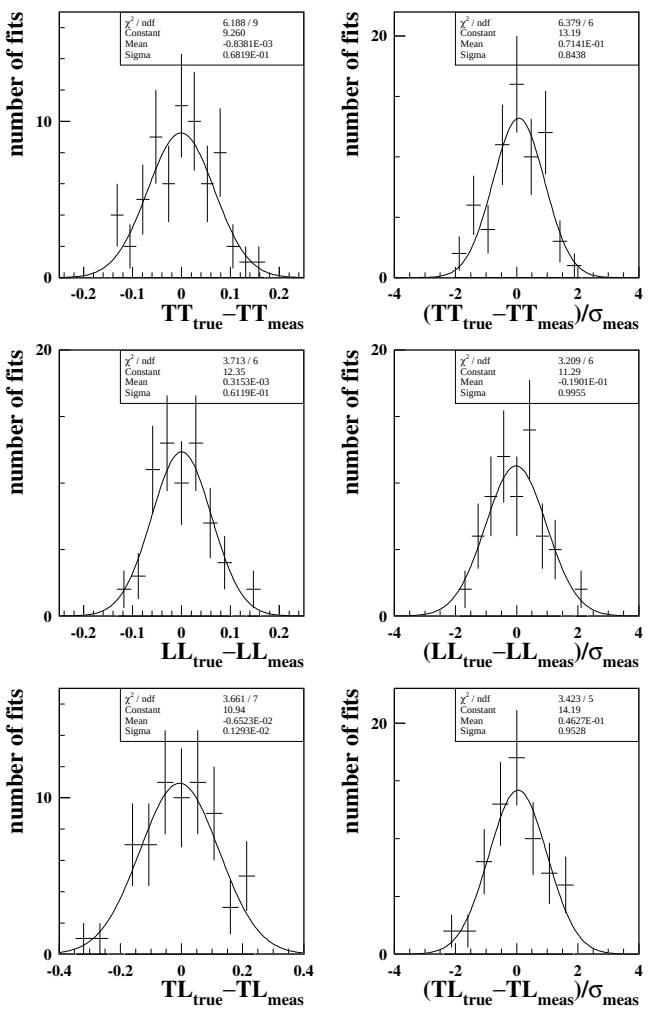

Figure 8.9: *Distribution of the comparison of the true to the measured fractions of each polarisation state calculated from Monte Carlo subsamples. The true values were calculated from generator level Monte Carlo. The measured values were calculated from fully detector simulated Monte Carlo and have been corrected for detector effects. The three plots on the left show the difference between the measured and true results. The three plots on the right are the pull distributions.*

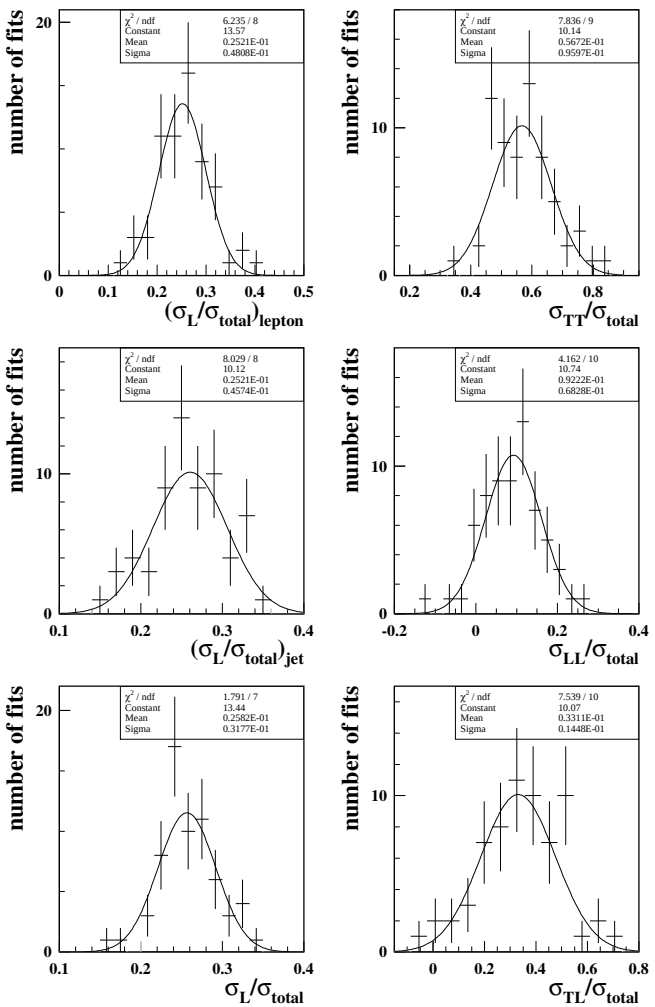

Figure 8.10: *Distribution of the measured values of the fraction of each polarisation state from fully simulated Monte Carlo. All measured values have been corrected for detector effects. The three plots on the left are the fraction of longitudinally polarised W bosons from the leptonically, hadronically decaying W bosons and all W bosons respectively. The three plots on the right are for the W-pair polarised cross-sections.*

the normalised polarised differential cross-sections calculated from Monte Carlo with and without the expected background events.

Table 8.1 shows the values for the helicity fractions calculated from a large CC03 Monte Carlo sample and also a Monte Carlo sample containing the expected background events as well as the signal events. From this, it is clear that, although not as large a contributer as the detector effects, the background is an important consideration and must be corrected for.

The correction is achieved by adding the expected selected background Monte Carlo events to the data sample before the SDM analysis is undertaken. These Monte Carlo events are assigned a negative weight so that their contribution is effectively subtracted from the data sample.

	Without Background	With Background
$\sigma_{\mathrm{TT}}/\sigma_{\mathrm{total}}$	57.24 ± 0.98	60.07 ± 0.99
$\sigma_{\mathrm{LL}}/\sigma_{\mathrm{total}}$	8.57 ± 0.81	5.97 ± 0.81
$\sigma_{\mathrm{TL}}/\sigma_{\mathrm{total}}$	34.18 ± 1.62	33.96 ± 1.64
$\sigma_{\mathrm{L}}^{\ell\nu}/\sigma_{\mathrm{total}}$	25.43 ± 0.51	20.42 ± 0.51
$\sigma_{\mathrm{L}}^{\mathrm{q\bar{q}}}/\sigma_{\mathrm{total}}$	25.91 ± 0.51	25.45 ± 0.50
$\sigma_{\mathrm{L}}/\sigma_{\mathrm{total}}$	25.67 ± 0.36	22.07 ± 0.36

Table 8.1: *The fractional polarised cross-sections calculated from just signal Monte Carlo and from signal Monte Carlo plus the expected accepted background.*

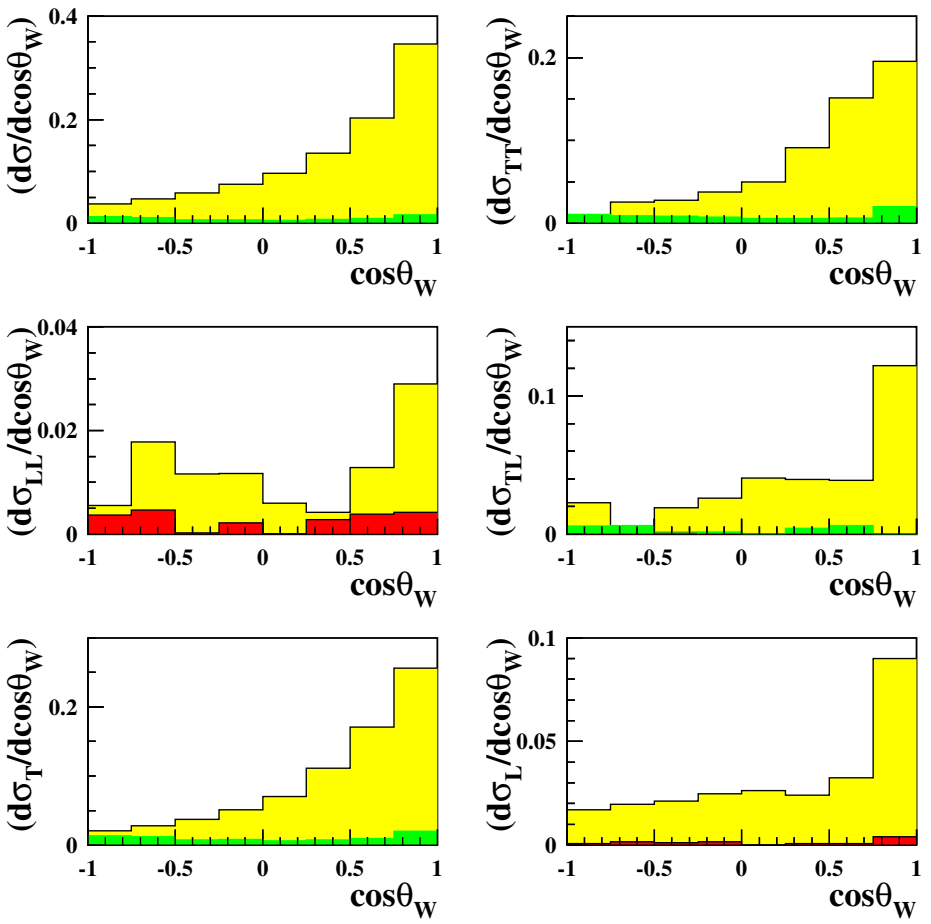

Figure 8.11: *The contributions to the polarised cross-sections from background events. The yellow histogram shows the signal events, the green histogram indicates an overall positive contribution from background events and the red histogram indicates an overall negative contribution from background events.*

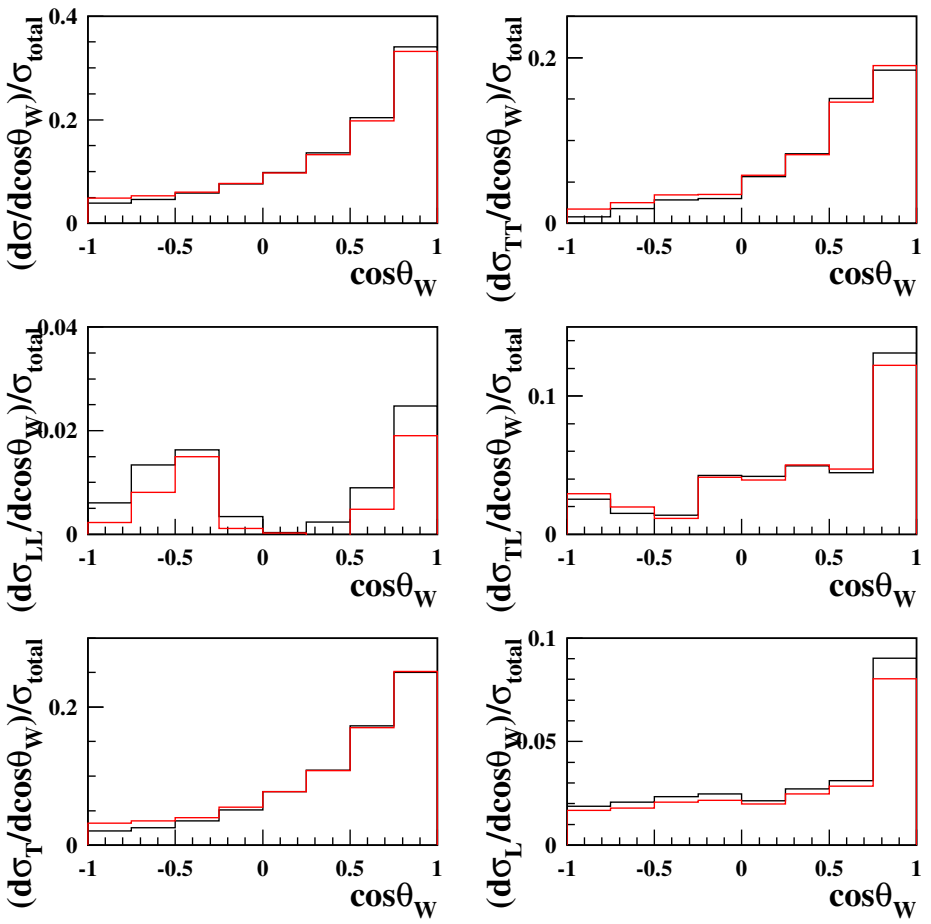

Figure 8.12: *The normalised polarised differential cross-sections with and without background contributions. The black histogram is CC03 signal events only. The red histogram is for CC03 events plus the expected background contribution.*

Chapter 9

Measurements of Polarised Cross-sections from Data

9.1 Individual W Polarised Cross-Sections

Figure 9.1 shows the differential cross-sections for the production of transversely and longitudinally polarised W bosons obtained from the 189 GeV data by the procedure described in the previous chapter. Represented are the differential cross-sections for leptonically decaying W bosons and hadronically decaying W bosons, along with the sum of all W bosons.

Integrating over $\cos\theta_{\mathrm{W}}$ and dividing by the total cross-section gives the fraction of each polarisation. Table 9.1 gives the results for the 189 GeV data along with the predicted fractions calculated from generator level EXCALIBUR Monte Carlo. The results from the data have both a statistical error and a systematic error. The sources of possible systematic uncertainty investigated to calculate the second of these errors are described in detail in chapter 10.

The polarisation of the leptonically and hadronically decaying W bosons

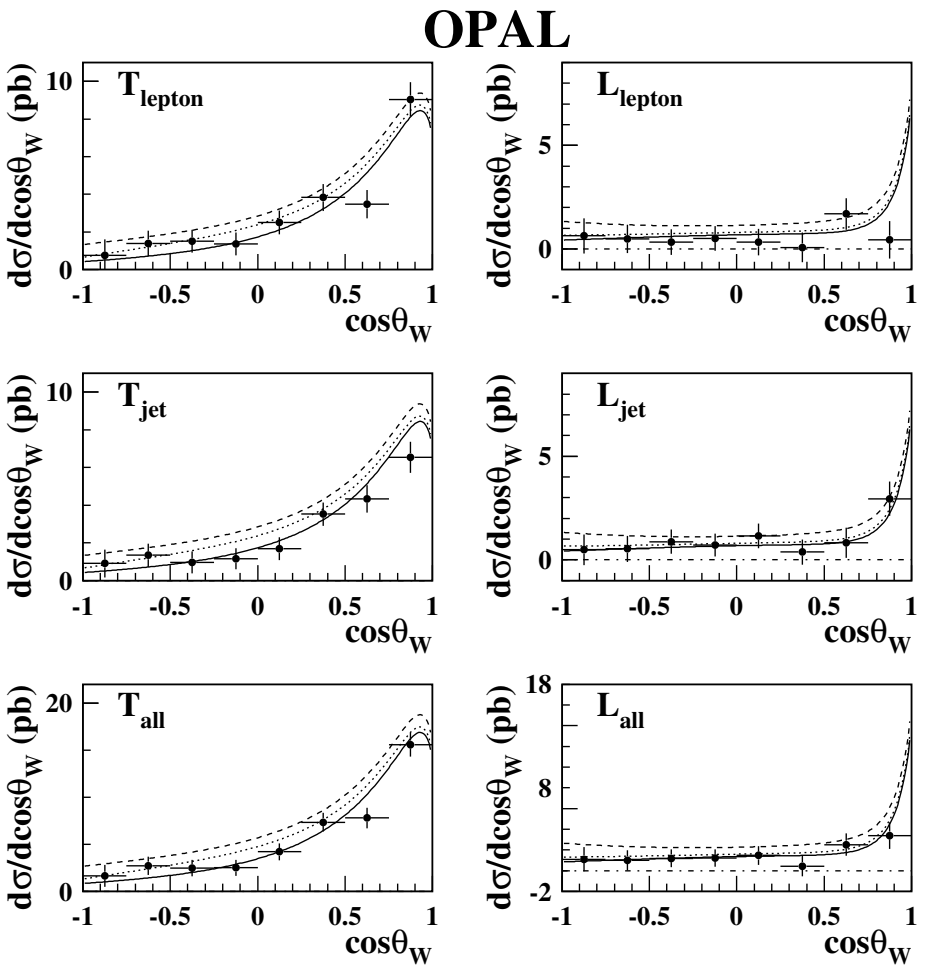

Figure 9.1: *The differential cross-sections for producing transversely (T) and longitudinally (L) polarised W bosons calculated from the 189 GeV data (points). The first two plots are for the leptonically decaying W boson in the pair. The next two are for the hadronically decaying W boson in the pair. The last two are for all W bosons. Overlaid are the predictions for the Standard Model (solid line),* $\tilde{\kappa}_z$*= +1.0 (dotted line) and* $\tilde{\lambda}_z$*= -1.0 (dashed line). The dotted-dashed line shows the zero.*

in a W-pair were obtained independently of each other. However these are not independent measurements, the correlation between them was found to be[1] 0.071 ± 0.030. The total fraction of longitudinal W bosons was calculated by taking the average of the leptonic and hadronic fractions. The correlation was included when calculating the statistical error on this value.

	$\sigma_{\mathrm{L}}/\sigma_{\mathrm{total}}$	σ_{L} (pb)
Data		
W$\rightarrow \ell\nu$	$0.158 \pm 0.046 \pm 0.023$	$1.11 \pm 0.32 \pm 0.16$
W$\rightarrow$ qq	$0.279 \pm 0.045 \pm 0.025$	$1.96 \pm 0.32 \pm 0.18$
All	$0.219 \pm 0.034 \pm 0.016$	$3.08 \pm 0.50 \pm 0.23$
Standard Model Expectation		
W$\rightarrow \ell\nu$	0.254 ± 0.005	1.86 ± 0.04
W$\rightarrow$ qq	0.259 ± 0.005	1.90 ± 0.04
All	0.257 ± 0.004	3.76 ± 0.06

Table 9.1: *The fractions longitudinally polarised W bosons. The expected values are from generator level EXCALIBUR Monte Carlo. The first error on the measured values is statistical and the second is the systematic uncertainty. Also shown is the total cross-section these fractions relate to at 189 GeV.*

Taking the total integrated luminosity as $183.05 \pm 0.16(\mathrm{stat.}) \pm 0.37(\mathrm{syst.})$ pb^{-1} [101], the total cross-section for the process $\mathrm{W^+W^-} \rightarrow \mathrm{q\bar{q}}\ell\bar{\nu}_\ell$ was measured at 189 GeV in [66] as $7.04 \pm 0.22(\mathrm{sys.}) \pm 0.10(\mathrm{stat.})$ pb. This means the total cross-section for production of longitudinal W bosons in

[1] The correlations were calculated from the data on an event by event basis using a statistical analysis.

$W^+W^- \to q\bar{q}\ell\bar{\nu}_\ell$ events is $\sigma_L = 3.08 \pm 0.50(\text{stat.}) \pm 0.23(\text{syst.})$ pb. The expected cross-section at 189 GeV is 3.76 pb.

9.2 W-Pair Polarised Cross-Sections

Figure 9.2 shows the total differential cross-section for the production of W-pairs and the differential cross-section for the production of two transversely polarised W bosons, two longitudinally polarised W bosons and the production of W bosons of opposite polarisation. All these were obtained from the 189 GeV data by the procedure described in the previous chapter.

Integrating over $\cos\theta_W$ and dividing by the total cross-section will once again give the fraction of each helicity state. The results for this are shown in table 9.2. The areas of systematic uncertainty are described in chapter 10 and the overall systematic uncertainty is added in quadrature with the statistical error. The fractions are highly correlated and the correlations are obtained directly from the data by a statistical analysis on an event by event basis. The following correlations are obtained for the 189 GeV data:

$$\begin{aligned} TT : LL &= +0.648 \pm 0.018 \\ TT : TL &= -0.890 \pm 0.006 \\ LL : TL &= -0.867 \pm 0.008 \end{aligned}$$

Using the results in table 9.2 and taking into consideration the above correlations, the χ^2 value of the three measurements compared to the Standard Model expectations, including systematic uncertainties, is 4.7. This corresponds to a χ^2 probability of 10%. Also shown in table 9.2 are the total cross-sections for the production of the different W-pair polarisation states.

These were calculated using the total cross-section for W-pair production at 189 GeV measured at OPAL.

	Fraction	Cross-section (pb)
Data		
TT	$0.768 \pm 0.090 \pm 0.032$	$5.41 \pm 0.65 \pm 0.24$
LL	$0.206 \pm 0.072 \pm 0.018$	$1.45 \pm 0.35 \pm 0.09$
TL	$0.026 \pm 0.147 \pm 0.038$	$0.18 \pm 1.02 \pm 0.26$
Standard Model Expectation		
TT	0.570 ± 0.010	4.17 ± 0.07
LL	0.090 ± 0.008	0.66 ± 0.06
TL	0.340 ± 0.016	2.49 ± 0.12

Table 9.2: *The fraction of two transversely polarised W bosons (TT), two longitudinal W bosons (LL) and one of each polarisation (TL) calculated from the 189 GeV data. The first error is statistical and the second error is systematic. Also shown are the total cross-sections for the production of each polarisation state. In all cases the Standard Model expectations are calculated from EXCALIBUR Monte Carlo.*

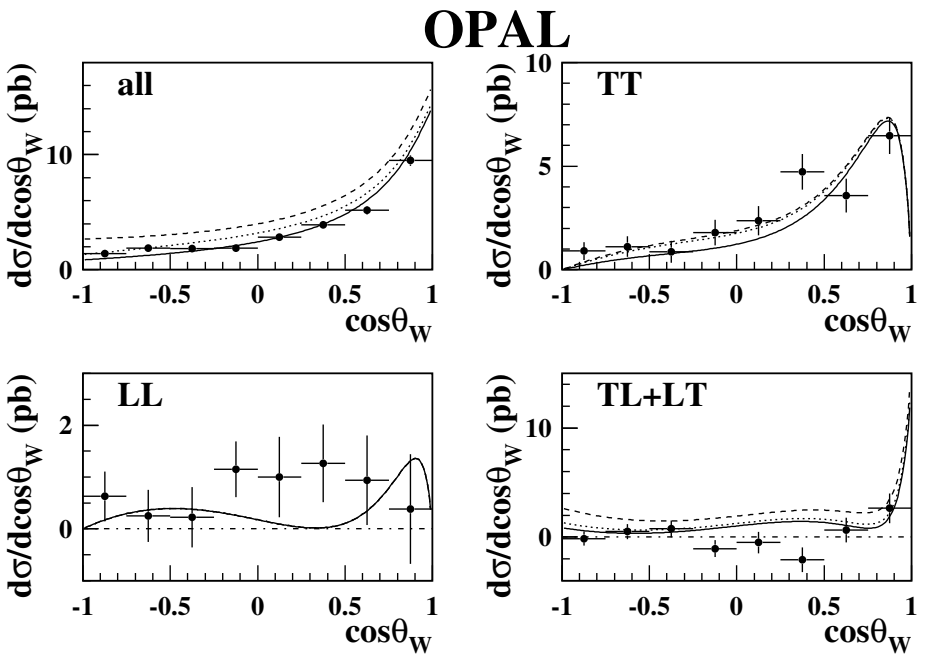

Figure 9.2: *The differential cross-sections for producing W-pairs (all), transversely polarised W-pairs (TT), longitudinally polarised W-pairs (LL) and pairs of W bosons with opposite polarisation (TL+LT) calculated from the 189 GeV data (points). Overlaid are the prediction for the Standard Model (solid line),* $\tilde{\kappa}_z = +1.0$ *(dotted line) and* $\tilde{\lambda}_z = -1.0$ *(dashed line). The dotted-dashed line shows the zero.*

Chapter 10

Evaluation of Systematic Uncertainties

In this chapter all areas of possible systematic uncertainty are investigated. In each case the uncertainty is quantified so that it can be included in the final results. For the TGC fit a systematic error is calculated for each bin of the SDM elements and $\cos\theta_{\mathrm{W}}$ distribution, and these are then included in the χ^2 fit as detailed in chapter 7. These uncertainties are calculated by comparing the SDM elements and $\cos\theta_{\mathrm{W}}$ observables. For each area of systematic uncertainty detailed in this chapter the absolute difference between the observables is taken as the systematic error.

An error on the polarised cross-section fractions is calculated for each area of uncertainty. These are combined with the statistical error in quadrature to give the overall uncertainty on each of the measured values from the 189 GeV data.

10.1 Uncertainties in Electroweak Modelling

All Monte Carlo generators do not model the events in exactly the same manner. There may be some uncertainty introduced by the way that the generators model the fundamental interactions occurring. Samples of fully detector simulated four-fermion Monte Carlo generated by EXCALIBUR are compared to samples generated by grc4f and ERATO.

Figure 10.1 shows the comparison of the SDM elements extracted from a large EXCALIBUR sample to those extracted from a large grc4f sample. Table 10.1 quantifies the systematic uncertainties as a fraction of the statistical uncertainties measured on the data sample.

The systematic uncertainties due to the generator modelling of the events on the helicity fractions were calculated by comparing the measured helicity fractions from the EXCALIBUR to the those from the grc4f and ERATO. The overall difference was taken as the uncertainty. These are shown in table 10.9.

10.2 Jet Fragmentation

The modelling of the quark fragmentation into jets is another possible source of uncertainty. This process is not well understood, so it is an important area to investigate. The fragmentation simulation program most commonly used is JETSET. This program was used as the fragmentation scheme in the EXCALIBUR Monte Carlo employed for both the TGC fit and the helicity studies. To evaluate the uncertainty, large samples of grc4f Monte Carlo which use different fragmentation schemes are compared. Both samples have identical initial four-vectors, but one has then used the JETSET

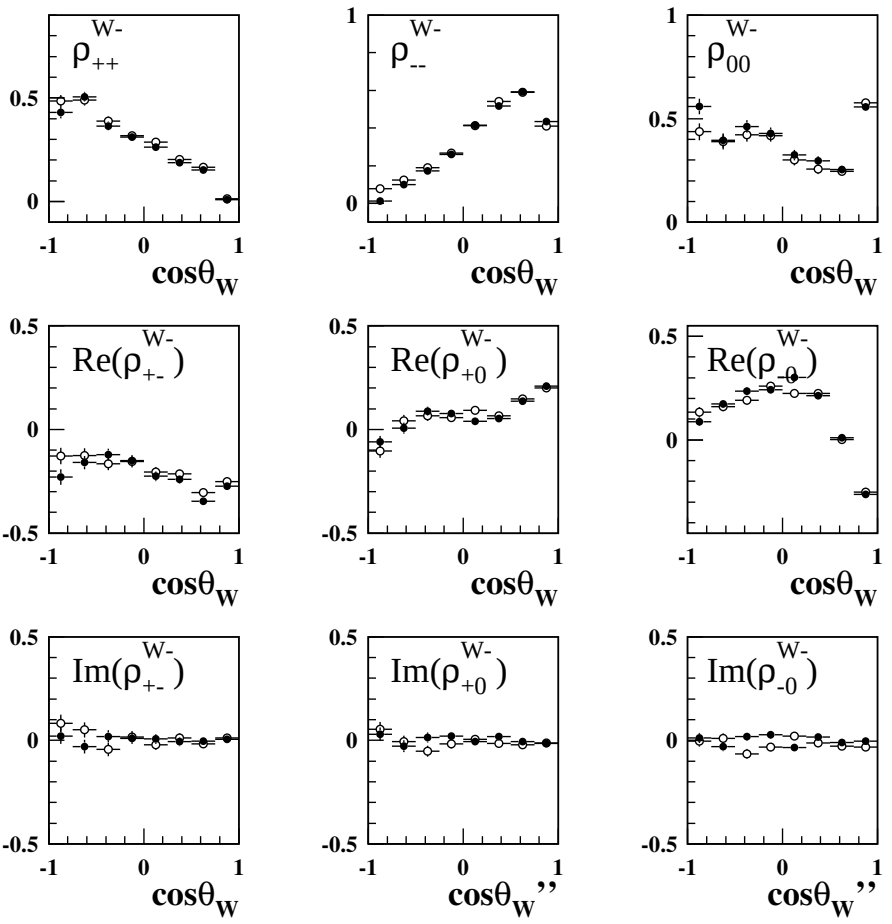

Figure 10.1: *Single W SDM elements extracted from fully detector simulated four-fermion EXCALIBUR Monte Carlo (closed circles) and grc4f Monte Carlo (open circles).*

	1	2	3	4	5	6	7	8
$\cos\theta_{\mathrm{W}}$	0.07	0.45	0.31	0.07	0.27	0.01	0.12	0.17
ρ_{++}	0.43	0.16	0.20	0.05	0.24	0.20	0.24	0.15
ρ_{--}	0.55	0.26	0.17	0.07	0.02	0.28	0.04	0.39
ρ_{00}	0.61	0.04	0.24	0.08	0.15	0.30	0.10	0.21
$\mathrm{Re}(\rho_{+-})$	0.52	0.21	0.25	0.36	0.17	0.23	0.42	0.28
$\mathrm{Re}(\rho_{+0})$	0.35	0.31	0.17	0.18	0.53	0.17	0.17	0.10
$\mathrm{Re}(\rho_{-0})$	0.47	0.12	0.39	0.16	0.76	0.10	0.09	0.14
$\mathrm{Im}(\rho_{+-})$	0.33	0.53	0.43	0.04	0.19	0.16	0.14	0.05
$\mathrm{Im}(\rho_{+0})$	0.13	0.15	0.50	0.30	0.10	0.37	0.20	0.04
$\mathrm{Im}(\rho_{-0})$	0.10	0.40	0.71	0.52	0.53	0.27	0.20	0.39

Table 10.1: *The systematic uncertainty due to generator modelling. The numbers represent the size of the error as a fraction of the statistical error from the data sample on each bin of each variable used in the TGC fits.*

fragmentation scheme, and the other utilises the HERWIG fragmentation scheme. As before, the extracted SDM elements and $\cos\theta_{\mathrm{W}}$ are compared and the difference in each bin is assigned as the uncertainty on that bin. The plots of the single W SDM elements can be seen in figure 10.2. The magnitude of the systematic uncertainty on each bin is given in table 10.2.

The helicity fractions are calculated for both these samples and the differences are taken as the systematic uncertainty. These are shown in table 10.9.

10.3 Jet Reconstruction

Extensive studies of back-to-back jets at LEP Z^0 energies have been carried out. By comparing the data with the Monte Carlo events, the accuracy

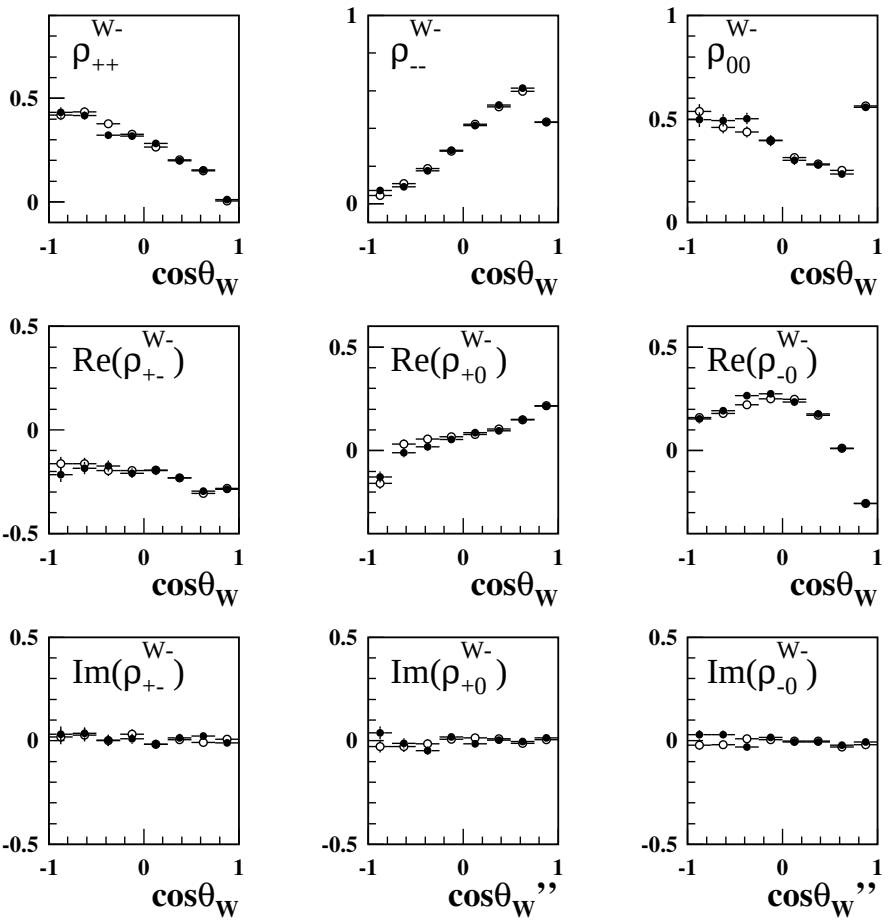

Figure 10.2: *Single W SDM elements extracted from two samples of fully detector simulated grc4f Monte Carlo. Both samples were initially the same, however, for jet fragmentation, one uses the JETSET fragmentation scheme (closed circles) and the other the HERWIG fragmentation scheme (open circles).*

	1	2	3	4	5	6	7	8
$\cos\theta_{\mathrm{W}}$	0.01	0.38	0.25	0.14	0.04	0.27	0.29	0.17
ρ_{++}	0.10	0.14	0.47	0.06	0.18	0.07	0.05	0.18
ρ_{--}	0.23	0.19	0.11	0.04	0.06	0.11	0.21	0.02
ρ_{00}	0.20	0.21	0.39	0.01	0.08	0.04	0.18	0.06
$\mathrm{Re}(\rho_{+-})$	0.28	0.12	0.12	0.08	0.02	0.01	0.11	0.04
$\mathrm{Re}(\rho_{+0})$	0.25	0.35	0.27	0.13	0.08	0.10	0.01	0.07
$\mathrm{Re}(\rho_{-0})$	0.08	0.12	0.40	0.22	0.14	0.06	0.04	0.01
$\mathrm{Im}(\rho_{+-})$	0.07	0.04	0.01	0.15	0.08	0.07	0.29	0.21
$\mathrm{Im}(\rho_{+0})$	0.34	0.46	0.13	0.01	0.29	0.05	0.51	0.28
$\mathrm{Im}(\rho_{-0})$	0.32	0.48	0.35	0.09	0.04	0.05	0.08	0.19

Table 10.2: *The systematic uncertainty due to jet hadronisation modelling. The numbers represent the size of the error as a fraction of the statistical error from the data sample on each bin of each variable used in the TGC fits.*

of the jet reconstruction can be measured. It was found that the uncertainties in the resolutions of the three parameters, energy, $\cos\theta_{\mathrm{W}}$ and ϕ_W, were about 10%. A possible systematic shift of 0.5% was found in the absolute jet energy. For calculating the systematic uncertainty in the SDM elements due to the uncertainty in jet reconstruction a large sample of EXCALIBUR Monte Carlo was generated and then modified to form new samples by smearing the resolution of the jet parameters by 10% and shifting the jet energy by 0.5%. This was done to both the hadronic and the τ jets, although studies into the τ jet uncertainties have not been carried out, so it is only an assumption that the uncertainty will be the same.

The SDM elements and $\cos\theta_{\mathrm{W}}$ distribution were calculated for each sample and compared to the original Monte Carlo sample. The differences were

taken as the systematic uncertainty. The systematics for each bin were added in quadrature to give an overall systematic due to jet reconstruction, these can be seen in table 10.3.

	1	2	3	4	5	6	7	8
$\cos\theta_W$	0.25	0.10	0.11	0.27	0.34	0.31	0.17	0.59
ρ_{++}	0.10	0.19	0.17	0.14	0.09	0.85	1.42	1.09
ρ_{--}	0.07	0.18	0.11	0.05	0.08	0.13	0.15	0.13
ρ_{00}	0.09	0.19	0.16	0.11	0.08	0.12	0.11	0.14
$\mathrm{Re}(\rho_{+-})$	0.09	0.16	0.11	0.47	0.11	0.12	0.09	0.12
$\mathrm{Re}(\rho_{+0})$	0.12	0.11	0.09	0.06	0.10	0.12	0.06	0.06
$\mathrm{Re}(\rho_{-0})$	0.09	0.17	0.07	0.08	0.09	0.15	0.09	0.13
$\mathrm{Im}(\rho_{+-})$	0.11	0.13	0.14	0.09	0.14	0.16	0.05	0.05
$\mathrm{Im}(\rho_{+0})$	0.08	0.07	0.06	0.06	0.16	0.15	0.07	0.06
$\mathrm{Im}(\rho_{-0})$	0.06	0.13	0.81	0.18	0.21	0.15	0.08	0.06

Table 10.3: *The systematic uncertainty due to jet reconstruction. The numbers represent the size of the error as a fraction of the statistical error from the data sample on each bin of each variable used in the TGC fits.*

For the helicity studies, the helicity fractions were calculated for each sample and compared to the original sample. The differences were added in quadrature and the total result was taken as the systematic uncertainty shown in table 10.9.

Further studies in estimating the possible systematic shift in the reconstructed direction of the boson have been carried out by looking at radiative $Z^0/\gamma \to q\bar{q}$ events. The possible shift in $|\cos\theta_W|$ was found to be less than 0.01 [102].

10.4 Background

Determining the contribution of background events within the data sample is important throughout the analysis. For fitting the TGCs, the expected contribution is added to the Monte Carlo sample that is compared to data, and for the helicity studies the expected contribution is removed from the data sample.

Calculating any possible systematic uncertainties in this area is then vital. The shape of the $Z^0/\gamma \to q\bar{q}$ background is varied by using a sample of HERWIG Monte Carlo instead of the PYTHIA to simulate these events. The SDM elements and $\cos\theta_W$ distribution extracted from the standard fit sample of Monte Carlo are compared to those calculated for the same sample, except the $Z^0/\gamma \to q\bar{q}$ background contribution is replaced with a HERWIG sample.

The modelling of the two-photon background is much less understood. To calculate any possible systematic shift due to this, the two-photon background is removed from the standard fit sample and then the SDM elements and $\cos\theta_W$ distribution are compared to those from the standard fit sample. This procedure is repeated, except this time the two-photon background is doubled. The total uncertainty due to background contributions formed by adding the uncertainties from each source in quadrature can be seen in table 10.4.

For the helicity studies, the background contribution subtracted from the data sample is varied in a similar way as described above, and then the differences in the calculated helicity proportions are taken as the systematic uncertainty. The total systematic uncertainties due to background studies are shown in table 10.9.

	1	2	3	4	5	6	7	8
$\cos\theta_{\mathrm{W}}$	0.06	0.02	0.02	0.02	0.01	0.01	0.02	0.03
ρ_{++}	0.01	0.01	0.01	0.01	0.01	0.01	0.01	0.01
ρ_{--}	0.01	0.03	0.04	0.05	0.01	0.03	0.01	0.01
ρ_{00}	0.01	0.01	0.01	0.01	0.01	0.02	0.01	0.01
$\mathrm{Re}(\rho_{+-})$	0.18	0.06	0.04	0.06	0.02	0.03	0.01	0.01
$\mathrm{Re}(\rho_{+0})$	0.17	0.01	0.02	0.04	0.01	0.03	0.01	0.01
$\mathrm{Re}(\rho_{-0})$	0.06	0.05	0.06	0.08	0.02	0.04	0.01	0.01
$\mathrm{Im}(\rho_{+-})$	0.01	0.01	0.01	0.01	0.01	0.01	0.01	0.01
$\mathrm{Im}(\rho_{+0})$	0.02	0.01	0.01	0.01	0.01	0.01	0.01	0.01
$\mathrm{Im}(\rho_{-0})$	0.02	0.01	0.01	0.01	0.01	0.01	0.01	0.01

Table 10.4: *The systematic uncertainty due to background modelling. The numbers represent the size of the error as a fraction of the statistical error from the data sample on each bin of each variable used in the TGC fits.*

10.5 Detector Simulation and Lepton Response

The way that GOPAL [90] simulates the detector so that the Monte Carlo can be compared directly to the data is an integral part of the analysis. It is very difficult to measure this as any differences between the data and Monte Carlo could be due to physical effects, such as anomalous TGCs, rather than poor modelling of the detector.

The most important part of detecting a $\mathrm{q\bar{q}}\ell\bar{\nu}_\ell$ event is identification of the lepton. Parameters of the lepton which are less sensitive to the TGC value must be compared. For the lepton, the polar angle in the lab frame, $\cos\theta_\ell$, and the lepton energy are chosen. A comparison using these two variables between the data and fully simulated Monte Carlo are made, and then lines are fitted to the distributions. These lines are used to weight the Monte Carlo.

Then a comparison between the SDM elements and $\cos\theta_{\rm W}$ distributions, for the TGC fit, and the helicity proportions for the helicity studies, before and after the weighting is made. As this test is limited by statistics and also TGC dependent, no correction is made to the overall result. However, a systematic uncertainty is assigned due to each of the tests. For the SDM elements and $\cos\theta_{\rm W}$ these can be seen in tables 10.5 and 10.6.

	1	2	3	4	5	6	7	8
$\cos\theta_{\rm W}$	0.01	0.05	0.15	0.06	0.06	0.05	0.15	0.03
ρ_{++}	0.01	0.01	0.01	0.09	0.10	0.05	0.01	0.13
ρ_{--}	0.02	0.01	0.10	0.11	0.03	0.01	0.02	0.02
ρ_{00}	0.01	0.01	0.05	0.13	0.09	0.02	0.01	0.07
$\mathrm{Re}(\rho_{+-})$	0.01	0.05	0.05	0.07	0.01	0.01	0.08	0.01
$\mathrm{Re}(\rho_{+0})$	0.13	0.33	0.02	0.01	0.01	0.04	0.19	0.13
$\mathrm{Re}(\rho_{-0})$	0.01	0.29	0.01	0.02	0.03	0.01	0.20	0.20
$\mathrm{Im}(\rho_{+-})$	0.06	0.11	0.06	0.11	0.04	0.14	0.06	0.11
$\mathrm{Im}(\rho_{+0})$	0.16	0.15	0.04	0.06	0.05	0.01	0.09	0.02
$\mathrm{Im}(\rho_{-0})$	0.21	0.07	0.02	0.09	0.01	0.01	0.01	0.08

Table 10.5: *The systematic uncertainty due to lepton identification as a function of the lepton polar angle in the lab frame. The numbers represent the size of the error as a fraction of the statistical error from the data sample on each bin of each variable used in the TGC fits.*

The overall uncertainty due to the lepton identification on the helicity proportions is shown in table 10.9. However, for the calculation of the helicity fractions, a further systematic uncertainty is assigned due to the detector simulation. In correcting for detector effects Standard Model Monte Carlo

	1	2	3	4	5	6	7	8
$\cos\theta_{\mathrm{W}}$	0.13	0.15	0.11	0.09	0.02	0.04	0.11	0.13
ρ_{++}	0.19	0.25	0.21	0.23	0.19	0.21	0.20	0.17
ρ_{--}	0.05	0.10	0.16	0.21	0.28	0.32	0.44	0.44
ρ_{00}	0.09	0.11	0.05	0.02	0.03	0.10	0.20	0.24
$\mathrm{Re}(\rho_{+-})$	0.01	0.02	0.02	0.01	0.02	0.03	0.01	0.01
$\mathrm{Re}(\rho_{+0})$	0.01	0.02	0.05	0.07	0.09	0.14	0.13	0.02
$\mathrm{Re}(\rho_{-0})$	0.02	0.08	0.11	0.10	0.11	0.11	0.05	0.10
$\mathrm{Im}(\rho_{+-})$	0.01	0.01	0.01	0.01	0.01	0.01	0.01	0.01
$\mathrm{Im}(\rho_{+0})$	0.00	0.01	0.01	0.01	0.01	0.01	0.01	0.02
$\mathrm{Im}(\rho_{-0})$	0.01	0.01	0.01	0.01	0.01	0.01	0.01	0.01

Table 10.6: *The systematic uncertainty due to lepton identification as a function of the lepton energy. The numbers represent the size of the error as a fraction of the statistical error from the data sample on each bin of each variable used in the TGC fits.*

is used, however this could cause a bias towards the Standard Model. This is tested by comparing the calculated helicity fractions for non-Standard Model samples of Monte Carlo at generator level, to those from the same sample after full detector simulation and detector correction. Samples with anomalous couplings, $\Delta\kappa_\gamma$, Δg_1^z, and λ set at ± 1 are used. The largest variation from the six tests is taken as the systematic uncertainty. These are shown in table 10.9.

Uncertainties on the measured lepton energy are estimated to be less than 0.3%. Any effects this would have are tested by shifting the lepton energy by this amount. In all cases this is found to have a negligible effect.

Differences in the charge misassignment between the Monte Carlo and

data could have a significant effect on all the results, especially as the wrong value of $\cos\theta_{\mathrm{W}}$ is assigned when the charge is incorrectly identified. Misidentification most commonly occurs in the higher momentum leptons where there is little bending of the lepton track in the magnetic field. A test of the effect was performed by randomly doubling the amount of expected misassigned charges in a large Monte Carlo sample from 0.8% to 1.5%. The effect this had was found to be small.

Any charge misassignment can also cause a problem in the measured lepton momentum. This was accounted for by varying the resolution in Q/p_t by 10% in the Monte Carlo. Where Q is the lepton charge and p_t is the transverse momentum of the lepton. Differences before and after the change are taken as the systematic uncertainty. The uncertainties for the TGC fit can be seen in table 10.7 and the uncertainties on the measured helicity fractions are shown in table 10.9.

10.6 Overall Systematic Uncertainty

For the TGC fit the overall systematic uncertainty on each observable is calculated by adding in quadrature all the calculated uncertainties discussed above. These are then included into the fit as described by equation 7.1 in chapter 7. The overall systematic uncertainty on each data observable as a fraction of the statistical error on the data can be seen in table 10.8.

The overall systematic uncertainty on the helicity fractions are calculated by adding in quadrature all the uncertainties calculated from each area described above. These are shown in table 10.9. The overall systematic uncertainties are added in quadrature with the statistical error to give the overall uncertainty on each polarised cross-section measured from the data.

	1	2	3	4	5	6	7	8
$\cos\theta_{\mathrm{W}}$	0.05	0.11	0.01	0.00	0.02	0.03	0.07	0.23
ρ_{++}	0.07	0.11	0.09	0.08	0.05	0.10	0.09	0.16
ρ_{--}	0.08	0.12	0.08	0.06	0.01	0.01	0.00	0.02
ρ_{00}	0.09	0.15	0.11	0.09	0.04	0.06	0.05	0.08
$\mathrm{Re}(\rho_{+-})$	0.16	0.16	0.09	0.08	0.09	0.08	0.08	0.15
$\mathrm{Re}(\rho_{+0})$	0.00	0.03	0.06	0.04	0.02	0.02	0.03	0.04
$\mathrm{Re}(\rho_{-0})$	0.08	0.01	0.06	0.04	0.01	0.00	0.02	0.03
$\mathrm{Im}(\rho_{+-})$	0.02	0.05	0.00	0.03	0.01	0.02	0.01	0.02
$\mathrm{Im}(\rho_{+0})$	0.03	0.01	0.02	0.01	0.02	0.02	0.05	0.04
$\mathrm{Im}(\rho_{-0})$	0.03	0.03	0.01	0.00	0.01	0.02	0.01	0.02

Table 10.7: *The systematic uncertainty due to lepton charge/momentum uncertainty. The numbers represent the size of the error as a fraction of the statistical error from the data sample on each bin of each variable used in the TGC fits.*

	1	2	3	4	5	6	7	8
$\cos\theta_{\mathrm{W}}$	0.31	0.63	0.47	0.34	0.45	0.42	0.41	0.66
ρ_{++}	0.50	0.41	0.60	0.31	0.40	0.91	1.47	1.15
ρ_{--}	0.61	0.41	0.32	0.28	0.31	0.47	0.52	0.61
ρ_{00}	0.67	0.34	0.51	0.22	0.22	0.36	0.32	0.38
$\mathrm{Re}(\rho_{+-})$	0.65	0.35	0.32	0.62	0.23	0.28	0.47	0.34
$\mathrm{Re}(\rho_{+0})$	0.51	0.59	0.35	0.26	0.56	0.29	0.30	0.20
$\mathrm{Re}(\rho_{-0})$	0.50	0.40	0.59	0.32	0.79	0.23	0.25	0.30
$\mathrm{Im}(\rho_{+-})$	0.37	0.56	0.47	0.22	0.25	0.29	0.34	0.26
$\mathrm{Im}(\rho_{+0})$	0.42	0.52	0.53	0.31	0.36	0.41	0.57	0.30
$\mathrm{Im}(\rho_{-0})$	0.42	0.65	1.14	0.58	0.58	0.32	0.24	0.45

Table 10.8: *The total systematic uncertainty on the SDM observables and* $\cos\theta_{\mathrm{W}}$ *distribution. These were calculated by adding in quadrature the values of the all systematic uncertainties discussed in this chapter. The numbers represent the size of the error as a fraction of the statistical error from the data sample on each bin of each variable used in the TGC fits.*

Systematic		TT	LL	TL	T,L
MC Generator	WW→ qq$\ell\nu$	0.015	0.013	0.028	0.001
	W→ $\ell\nu$	-	-	-	0.004
	W→ qq	-	-	-	0.006
Jet Reconstruction	WW→ qq$\ell\nu$	0.013	0.004	0.008	0.007
	W→ $\ell\nu$	-	-	-	0.005
	W→ qq	-	-	-	0.011
Hadronisatation	WW→ qq$\ell\nu$	0.016	0.002	0.014	0.009
	W→ $\ell\nu$	-	-	-	0.003
	W→ qq	-	-	-	0.021
Background	WW→ qq$\ell\nu$	0.004	0.001	0.004	0.002
	W→ $\ell\nu$	-	-	-	0.003
	W→ qq	-	-	-	0.004
Lepton id	WW→ qq$\ell\nu$	0.017	0.005	0.014	0.010
	W→ $\ell\nu$	-	-	-	0.017
	W→ qq	-	-	-	0.003
Detector Effect Correction	WW→ qq$\ell\nu$	0.004	0.008	0.012	0.002
	W→ $\ell\nu$	-	-	-	0.009
	W→ qq	-	-	-	0.005
Lepton Charge/Momentum	WW→ qq$\ell\nu$	0.007	0.001	0.008	0.005
	W→ $\ell\nu$	-	-	-	0.011
	W→ qq	-	-	-	0.001
Total	WW→ qq$\ell\nu$	0.032	0.017	0.038	0.016
	W→ $\ell\nu$	-	-	-	0.023
	W→ qq	-	-	-	0.025

Table 10.9: *The contribution to the systematic uncertainty on the polarised cross-section fractions from the sources discussed in this chapter. The total uncertainty is calculated by adding each of the uncertainties in quadrature.*

Chapter 11

Conclusions

In this thesis the CP-violating triple gauge coupling parameters have been measured from the LEP2 data with the $SU(2)_L \times U(1)_Y$ gauge invariance constraints in place. Along with these couplings, the CP-conserving couplings $\Delta\kappa_\gamma$, Δg_1^z, and λ have been measured. All couplings were measured using a spin density matrix analysis.

The W-pair polarised cross-sections have been measured for the first time ever. These results along with the individual W polarised cross-sections and the measured values of the CP-violating TGCs have been published by the OPAL collaboration in [103].

In this chapter the evidence (or lack there of) for CP-violation is discussed. Then the measured values of all the TGCs are reviewed and a comparison to other measured values from both OPAL and other experiments is given. Finally conclusions on the measured W polarised fractions are drawn.

11.1 Tests of CP-Invariance

Measurement of the CP-violating TGCs was performed by combing information from the SDM elements and from the W production angle. Constraining the interaction to $\mathrm{SU}(2)_L \times \mathrm{U}(1)_Y$ gauge invariance, the values obtained are as follows:

$$\begin{aligned} \tilde{\kappa}_Z &= -0.184^{+0.091}_{-0.065} \\ \tilde{\lambda}_Z &= -0.136^{+0.161}_{-0.194} \\ g_4^Z &= +0.070^{+0.263}_{-0.255} \end{aligned}$$

The errors on these results are due to both statistical and systematic uncertainties.

Within the Standard Model at tree level there is no CP-violation at the WWZ^0 and $\mathrm{WW}\gamma$ vertex, therefore the CP-violating TGCs are zero. The measured values of the couplings are all consistent with the Standard Model expectations.

A further test of CP-invariance in the W-pair production process is given by the imaginary parts of the single W SDM elements. At tree level CP-invariance requires the following:

$$Im\left(\rho^{W^-}_{\tau\tau'}(s, \cos\theta_W)\right) - Im\left(\rho^{W^+}_{-\tau'-\tau}(s, \cos\theta_W)\right) = 0 \qquad (11.1)$$

This equation gives a completely Model independent test of CP-violation in the W-pair production process. Plots of the combinations of imaginary SDM observables needed to test CP-invariance calculated from the 189 GeV data can be seen in figure 11.1. No obvious deviations from zero are observed. Calculating the χ^2 for each plot, the following are obtained:

$$\begin{aligned}
\chi^2 : Im\left(\rho_{+-}^{W^-}(s,k)\right) - Im\left(\rho_{-+}^{W^+}(s,k)\right) &= 6.48 \\
\chi^2 : Im\left(\rho_{+0}^{W^-}(s,k)\right) - Im\left(\rho_{-0}^{W^+}(s,k)\right) &= 8.90 \\
\chi^2 : Im\left(\rho_{-0}^{W^-}(s,k)\right) - Im\left(\rho_{+0}^{W^+}(s,k)\right) &= 6.77
\end{aligned}$$

The χ^2 includes both statistical and systematic uncertaintes. As each histogram contains eight degrees of freedom, these results are consistent with Standard Model expectations.

Also included in figure 11.1 are the plots that test for effects beyond tree level, as discussed in chapter 3, equation 3.48. Any deviations in these plots could only be due to effects beyond tree level or CPT-violation. No obvious deviations from zero are seen. Calculating the χ^2 for each plot, the following results are obtained:

$$\begin{aligned}
\chi^2 : Im\left(\rho_{+-}^{W^-}(s,k)\right) + Im\left(\rho_{-+}^{W^+}(s,k)\right) &= 4.12 \\
\chi^2 : Im\left(\rho_{+0}^{W^-}(s,k)\right) + Im\left(\rho_{-0}^{W^+}(s,k)\right) &= 5.63 \\
\chi^2 : Im\left(\rho_{-0}^{W^-}(s,k)\right) + Im\left(\rho_{+0}^{W^+}(s,k)\right) &= 7.56
\end{aligned}$$

These results do not give an indication of effects beyond tree level.

11.2 Measurement of TGCs

The CP-conserving couplings were measured using a SDM analysis with the inclusion of information about the W production angle.

Measurements of the CP-conserving TGCs were undertaken using two different Monte Carlo reweighting methods, the WVCXME and BILGOU programs. The results using the two methods were found to be consistent.

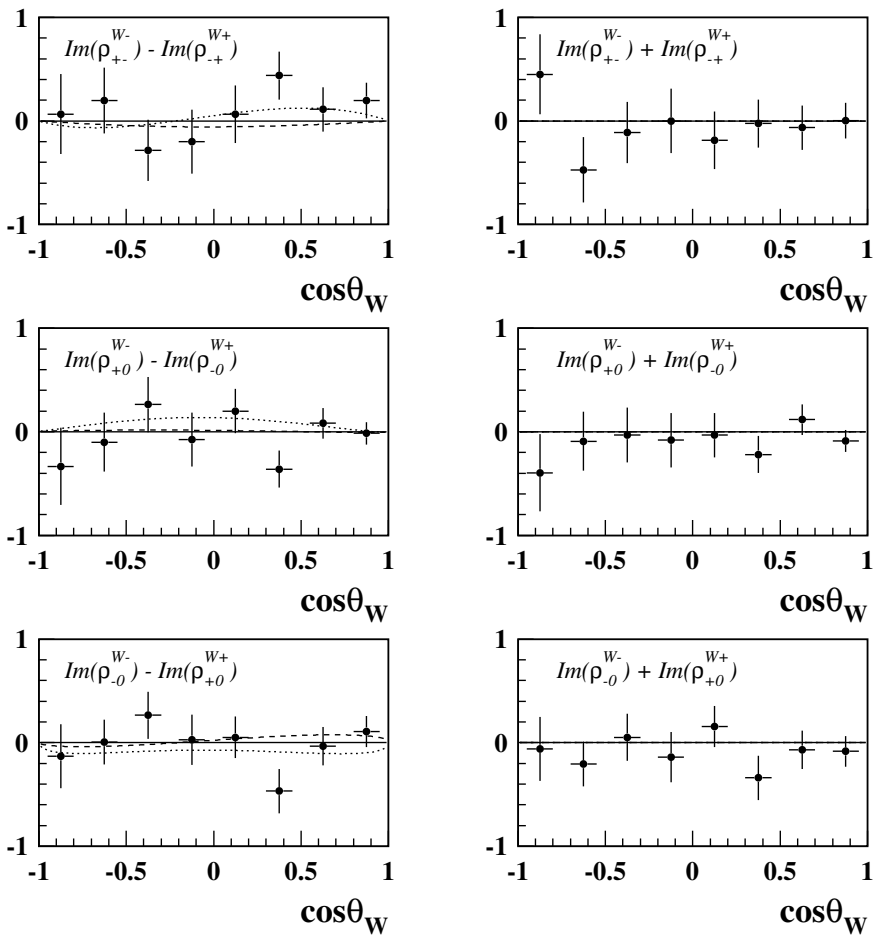

Figure 11.1: *The three plots on the left give a test of CP-violation at tree level. Any deviation from zero could only be caused by CP-violation. Overlaid on these plots are the analytical predictions for CP-violating couplings* $\tilde{\lambda}_z = -0.5$ *(dotted line) and* $\tilde{\kappa}_z = +0.5$ *(dashed line). The three plots on the right give a test of CPT-invariance and effects beyond tree level. Any deviation from zero could only be caused by effects beyond tree level or CPT-violation.*

Measurement of the CP-violating couplings could only be done using the BILGOU program. For consistency, the final quoted results for the CP-conserving couplings will be those measured using the BILGOU program.

The measured values of the CP-conserving TGCs, with the $SU(2)_L \times U(1)_Y$ gauge invariance constraints, including systematic uncertainties were found to be,

$$\begin{aligned} \Delta\kappa_\gamma &= -0.263^{+0.263}_{-0.218} \\ \Delta g_1^Z &= -0.029^{+0.092}_{-0.089} \\ \lambda &= -0.045^{+0.099}_{-0.093} \end{aligned}$$

These results are consistent with the Standard Model expectations and the published OPAL results for the 189 GeV data, where an optimal observable method was used to measure them [104].

The CP-violating couplings have been measured for the first time at OPAL. Measurements of the WWγ CP-violating couplings have been made at ALEPH [59, 60], the DELPHI collaboration [63] and at the Tevatron [61, 62]. ALEPH also measured the CP-violating WWZ^0 coupling. All these couplings were measured without the $SU(2)_L \times U(1)_Y$ gauge invariant constraints, so all other couplings were set to zero. All results are consistent with Standard Model expectations.

Figure 11.2 shows the χ^2 plots for all the TGCs measured in this thesis. It was seen that the CP-conserving couplings have a greater effect on the shape of the $\cos\theta_W$ distribution than on the SDM elements and the converse was true for the CP-violating couplings.

11.3 Measurement of W Polarisation

The polarisation of the W bosons in W-pair production was measured through the spin density matrix. It was found that $(21.9 \pm 3.44 \pm 1.6)\%$ of the W bosons were longitudinally polarised. This result is consistent with the Standard Model expectation and also the result measured by L3 at the same centre-of-mass energy [105], with the results presented in this thesis being more precise.

The polarisation state of the W-pairs has been measured for the first time. Of the three possible polarisation states, transverse-transverse (TT), longitudinal-longitudinal (LL), and transverse-longitudinal (TL), it was found that all were present and the fraction of each in the sample was:

$$\begin{aligned} \mathrm{TT} &= 0.768 \pm 0.090 \pm 0.032 \\ \mathrm{LL} &= 0.206 \pm 0.072 \pm 0.018 \\ \mathrm{TL} &= 0.026 \pm 0.147 \pm 0.038 \end{aligned}$$

These measured values are highly correlated, the correlations were found to be:

$$\begin{aligned} \mathrm{TT:LL} &= +0.648 \pm 0.018 \\ \mathrm{TT:TL} &= -0.890 \pm 0.006 \\ \mathrm{LL:TL} &= -0.867 \pm 0.008 \end{aligned}$$

These χ^2 probablity of these results compared to the Standard Model expectations is 10%. Thus all results are consistent with the Standard Model expectations.

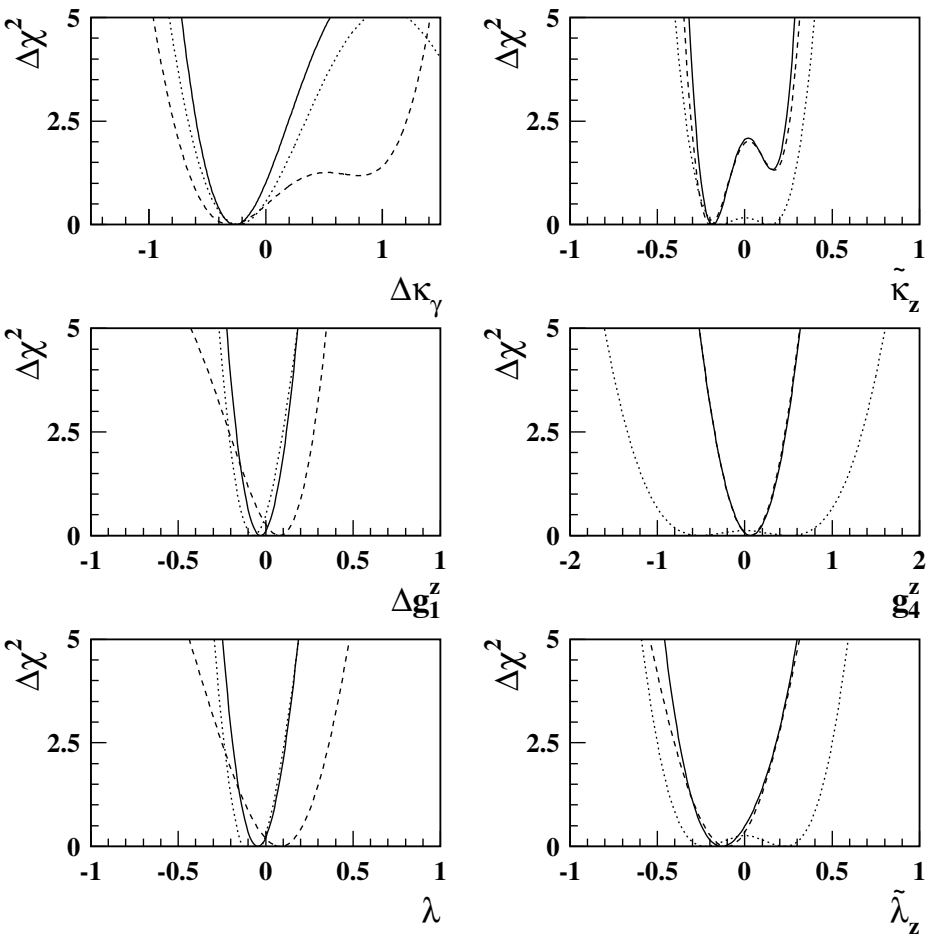

Figure 11.2: *The χ^2 plots for the fits to the CP-conserving and CP-violating anomalous couplings. For the CP-conserving couplings the dashed line is the fit to just the six real SDM elements, for the CP-violating couplings it is the fit to all nine SDM elements. The dotted line is the fit to just the $\cos\theta_{\mathrm{W}}$ distribution. The solid line is the combined fit. All fits include systematic uncertainties.*

Appendix A

Summations to Calculate SDM Elements

A.1 Summation to Calculate Single W SDM Elements

In this appendix the summations of operators needed to calculate the elements of the single W Spin Density Matrix are listed. In each equation θ_{f_1} is the polar angle and ϕ_{f_1} is the azimuthal angle of the decay fermion from the W^- in the W^- rest frame. The elements are extracted in bins of $\cos\theta_W$, the W^- production angle. k is the bin of $\cos\theta_W$ and N_k is the number of events in that bin.

$$\rho_{++}^{W^-}(k) = \frac{1}{N_k}\sum_{i=1}^{N_k}\frac{1}{2}(5\cos^2\theta_{f_1} - 2\cos\theta_{f_1} - 1)$$

$$\rho_{--}^{W^-}(k) = \frac{1}{N_k}\sum_{i=1}^{N_k}\frac{1}{2}(5\cos^2\theta_{f_1} + 2\cos\theta_{f_1} - 1)$$

$$
\begin{aligned}
\rho_{00}^{W^-}(k) &= \frac{1}{N_k}\sum_{i=1}^{N_k} 2 - 5\cos^2\theta_{f_1} \\
Re\left(\rho_{+-}^{W^-}(k)\right) &= \frac{1}{N_k}\sum_{i=1}^{N_k} 2\cos 2\phi_{f_1} \\
Im\left(\rho_{+-}^{W^-}(k)\right) &= \frac{1}{N_k}\sum_{i=1}^{N_k} -2\sin 2\phi_{f_1} \\
Re\left(\rho_{+0}^{W^-}(k)\right) &= \frac{1}{N_k}\sum_{i=1}^{N_k} \frac{-8}{3\pi\sqrt{2}}(1 - 4\cos\theta_{f_1})\cos\phi_{f_1} \\
Im\left(\rho_{+0}^{W^-}(k)\right) &= \frac{1}{N_k}\sum_{i=1}^{N_k} \frac{8}{3\pi\sqrt{2}}(1 - 4\cos\theta_{f_1})\sin\phi_{f_1} \\
Re\left(\rho_{-0}^{W^-}(k)\right) &= \frac{1}{N_k}\sum_{i=1}^{N_k} \frac{-8}{3\pi\sqrt{2}}(1 + 4\cos\theta_{f_1})\cos\phi_{f_1} \\
Im\left(\rho_{-0}^{W^-}(k)\right) &= \frac{1}{N_k}\sum_{i=1}^{N_k} \frac{-8}{3\pi\sqrt{2}}(1 + 4\cos\theta_{f_1})\sin\phi_{f_1}
\end{aligned}
$$

A.2 Summation to Calculate Two-Particle Joint W SDM Elements

In this appendix the summations of operators needed to calculate all 81 elements of the two-particle joint Spin Density Matrix are listed. In each equation θ_{f_1} is the polar angle and ϕ_{f_1} is the azimuthal angle of the decay fermion from the W^- in the W^- rest frame. $\theta_{\bar{f}_4}$ is the polar angle and $\phi_{\bar{f}_1}$ is the azimuthal angle of the decay anti-fermion from the W^+ in the W^+ rest frame. The elements are extracted in bins of $\cos\theta_W$, the W^- production angle. k is the bin of $\cos\theta_W$ and N_k is the number of events in that bin.

$$
\begin{aligned}
Re\left(\rho_{++++}(k)\right) &= \frac{1}{N_k}\sum_{i=1}^{N_k}\frac{1}{4}(5\cos^2\theta_{f_1}-2\cos\theta_{f_1}-1)(5\cos^2\theta_{\bar{f}_4}+2\cos\theta_{\bar{f}_4}-1)\\
Im\left(\rho_{++++}(k)\right) &= 0\\
Re\left(\rho_{+++0}(k)\right) &= \frac{1}{N_k}\sum_{i=1}^{N_k}\frac{-4}{3\pi\sqrt{2}}(5\cos^2\theta_{f_1}-2\cos\theta_{f_1}-1)(1+4\cos\theta_{\bar{f}_4})\cos\phi_{\bar{f}_4}\\
Im\left(\rho_{+++0}(k)\right) &= -\frac{1}{N_k}\sum_{i=1}^{N_k}\frac{4}{3\pi\sqrt{2}}(5\cos^2\theta_{f_1}-2\cos\theta_{f_1}-1)(1+4\cos\theta_{\bar{f}_4})\sin\phi_{\bar{f}_4}\\
Re\left(\rho_{+++-}(k)\right) &= \frac{1}{N_k}\sum_{i=1}^{N_k}(5\cos^2\theta_{f_1}-2\cos\theta_{f_1}-1)\cos 2\phi_{\bar{f}_4}\\
Im\left(\rho_{+++-}(k)\right) &= \frac{1}{N_k}\sum_{i=1}^{N_k}-(5\cos^2\theta_{f_1}-2\cos\theta_{f_1}-1)\sin 2\phi_{\bar{f}_4}\\
Re\left(\rho_{++0+}(k)\right) &= \frac{1}{N_k}\sum_{i=1}^{N_k}\frac{4}{3\pi\sqrt{2}}(5\cos^2\theta_{f_1}-2\cos\theta_{f_1}-1)(1+4\cos\theta_{\bar{f}_4})\cos\phi_{\bar{f}_4}\\
Im\left(\rho_{++0+}(k)\right) &= \frac{1}{N_k}\sum_{i=1}^{N_k}\frac{4}{3\pi\sqrt{2}}(5\cos^2\theta_{f_1}-2\cos\theta_{f_1}-1)(1+4\cos\theta_{\bar{f}_4})\sin\phi_{\bar{f}_4}\\
Re\left(\rho_{++00}(k)\right) &= \frac{1}{N_k}\sum_{i=1}^{N_k}\frac{1}{2}(5\cos^2\theta_{f_1}-2\cos\theta_{f_1}-1)(2-5\cos^2\theta_{\bar{f}_4})\\
Im\left(\rho_{++00}(k)\right) &= 0\\
Re\left(\rho_{++0-}(k)\right) &= \frac{1}{N_k}\sum_{i=1}^{N_k}\frac{4}{3\pi\sqrt{2}}(5\cos^2\theta_{f_1}-2\cos\theta_{f_1}-1)(1-4\cos\theta_{\bar{f}_4})\cos\phi_{\bar{f}_4}\\
Im\left(\rho_{++0-}(k)\right) &= \frac{1}{N_k}\sum_{i=1}^{N_k}\frac{-4}{3\pi\sqrt{2}}(5\cos^2\theta_{f_1}-2\cos\theta_{f_1}-1)(1-4\cos\theta_{\bar{f}_4})\sin\phi_{\bar{f}_4}\\
Re\left(\rho_{++-+}(k)\right) &= \frac{1}{N_k}\sum_{i=1}^{N_k}(5\cos^2\theta_{f_1}-2\cos\theta_{f_1}-1)\cos 2\phi_{\bar{f}_4}\\
Im\left(\rho_{++-+}(k)\right) &= \frac{1}{N_k}\sum_{i=1}^{N_k}(5\cos^2\theta_{f_1}-2\cos\theta_{f_1}-1)\sin 2\phi_{\bar{f}_4}\\
Re\left(\rho_{++-0}(k)\right) &= \frac{1}{N_k}\sum_{i=1}^{N_k}\frac{4}{3\pi\sqrt{2}}(5\cos^2\theta_{f_1}-2\cos\theta_{f_1}-1)(1-4\cos\theta_{\bar{f}_4})\cos\phi_{\bar{f}_4}\\
Im\left(\rho_{++-0}(k)\right) &= \frac{1}{N_k}\sum_{i=1}^{N_k}\frac{4}{3\pi\sqrt{2}}(5\cos^2\theta_{f_1}-2\cos\theta_{f_1}-1)(1-4\cos\theta_{\bar{f}_4})\sin\phi_{\bar{f}_4}
\end{aligned}
$$

$$
\begin{aligned}
Re\left(\rho_{++--}(k)\right) &= \frac{1}{N_k}\sum_{i=1}^{N_k}\frac{1}{4}(5\cos^2\theta_{f_1}-2\cos\theta_{f_1}-1)(5\cos^2\theta_{\bar{f}_4}-2\cos\theta_{\bar{f}_4}-1)\\
Im\left(\rho_{++--}(k)\right) &= 0\\
Re\left(\rho_{+0++}(k)\right) &= \frac{1}{N_k}\sum_{i=1}^{N_k}\frac{-4}{3\pi\sqrt{2}}(1-4\cos\theta_{f_1})\cos\phi_{f_1}(5\cos^2\theta_{\bar{f}_4}+2\cos\theta_{\bar{f}_4}-1)\\
Im\left(\rho_{+0++}(k)\right) &= \frac{1}{N_k}\sum_{i=1}^{N_k}\frac{4}{3\pi\sqrt{2}}(1-4\cos\theta_{f_1})\sin\phi_{f_1}(5\cos^2\theta_{\bar{f}_4}+2\cos\theta_{\bar{f}_4}-1)\\
Re\left(\rho_{+0+0}(k)\right) &= \frac{1}{N_k}\sum_{i=1}^{N_k}\frac{-32}{9\pi^2}((1-4\cos\theta_{f_1})\cos\phi_{f_1}(1+4\cos\theta_{\bar{f}_4})\cos\phi_{\bar{f}_4}\\
&- (1-4\cos\theta_{f_1})\sin\phi_{f_1}(1+4\cos\theta_{\bar{f}_4})\sin\phi_{\bar{f}_4})\\
Im\left(\rho_{+0+0}(k)\right) &= \frac{1}{N_k}\sum_{i=1}^{N_k}\frac{32}{9\pi^2}((1-4\cos\theta_{f_1})\cos\phi_{f_1}(1+4\cos\theta_{\bar{f}_4})\sin\phi_{\bar{f}_4}\\
&+ (1-4\cos\theta_{f_1})\sin\phi_{f_1}(1+4\cos\theta_{\bar{f}_4})\cos\phi_{\bar{f}_4})\\
Re\left(\rho_{+0+-}(k)\right) &= \frac{1}{N_k}\sum_{i=1}^{N_k}\frac{-8\sqrt{2}}{3\pi}((1-4\cos\theta_{f_1})\cos\phi_{f_1}\cos 2\phi_{\bar{f}_4}\\
&- (1-4\cos\theta_{f_1})\sin\phi_{f_1}\sin 2\phi_{\bar{f}_4})\\
Im\left(\rho_{+0+-}(k)\right) &= \frac{1}{N_k}\sum_{i=1}^{N_k}\frac{8\sqrt{2}}{3\pi}((1-4\cos\theta_{f_1})\cos\phi_{f_1}\sin 2\phi_{\bar{f}_4}\\
&+ (1-4\cos\theta_{f_1})\sin\phi_{f_1}\cos 2\phi_{\bar{f}_4})\\
Re\left(\rho_{+00+}(k)\right) &= \frac{1}{N_k}\sum_{i=1}^{N_k}\frac{-32}{9\pi^2}((1-4\cos\theta_{f_1})\cos\phi_{f_1}(1+4\cos\theta_{\bar{f}_4})\cos\phi_{\bar{f}_4}\\
&+ (1-4\cos\theta_{f_1})\sin\phi_{f_1}(1+4\cos\theta_{\bar{f}_4})\sin\phi_{\bar{f}_4})\\
Im\left(\rho_{+00+}(k)\right) &= \frac{1}{N_k}\sum_{i=1}^{N_k}\frac{-32}{9\pi^2}((1-4\cos\theta_{f_1})\cos\phi_{f_1}(1+4\cos\theta_{\bar{f}_4})\sin\phi_{\bar{f}_4}\\
&- (1-4\cos\theta_{f_1})\sin\phi_{f_1}(1+4\cos\theta_{\bar{f}_4})\cos\phi_{\bar{f}_4})\\
Re\left(\rho_{+000}(k)\right) &= \frac{1}{N_k}\sum_{i=1}^{N_k}\frac{-8}{3\pi\sqrt{2}}(1-4\cos\theta_{f_1})\cos\phi_{f_1}(2-5\cos^2\theta_{\bar{f}_4})\\
Im\left(\rho_{+000}(k)\right) &= \frac{1}{N_k}\sum_{i=1}^{N_k}\frac{8}{3\pi\sqrt{2}}(1-4\cos\theta_{f_1})\sin\phi_{f_1}(2-5\cos^2\theta_{\bar{f}_4})
\end{aligned}
$$

$$
\begin{aligned}
Re\left(\rho_{+00-}(k)\right) &= \frac{1}{N_k}\sum_{i=1}^{N_k}\frac{-32}{9\pi^2}((1-4\cos\theta_{f_1})\cos\phi_{f_1}(1-4\cos\theta_{\bar{f}_4})\cos\phi_{\bar{f}_4} \\
&- (1-4\cos\theta_{f_1})\sin\phi_{f_1}(1-4\cos\theta_{\bar{f}_4})\sin\phi_{\bar{f}_4}) \\
Im\left(\rho_{+00-}(k)\right) &= \frac{1}{N_k}\sum_{i=1}^{N_k}\frac{32}{9\pi^2}((1-4\cos\theta_{f_1})\cos\phi_{f_1}(1-4\cos\theta_{\bar{f}_4})\sin\phi_{\bar{f}_4} \\
&+ (1-4\cos\theta_{f_1})\sin\phi_{f_1}(1-4\cos\theta_{\bar{f}_4})\cos\phi_{\bar{f}_4}) \\
Re\left(\rho_{+0-+}(k)\right) &= \frac{1}{N_k}\sum_{i=1}^{N_k}\frac{-8\sqrt{2}}{3\pi}((1-4\cos\theta_{f_1})\cos\phi_{f_1}\cos 2\phi_{\bar{f}_4} \\
&+ (1-4\cos\theta_{f_1})\sin\phi_{f_1}\sin 2\phi_{\bar{f}_4}) \\
Im\left(\rho_{+0-+}(k)\right) &= \frac{1}{N_k}\sum_{i=1}^{N_k}\frac{-8\sqrt{2}}{3\pi}((1-4\cos\theta_{f_1})\cos\phi_{f_1}\sin 2\phi_{\bar{f}_4} \\
&- (1-4\cos\theta_{f_1})\sin\phi_{f_1}\cos 2\phi_{\bar{f}_4}) \\
Re\left(\rho_{+0-0}(k)\right) &= \frac{1}{N_k}\sum_{i=1}^{N_k}\frac{-32}{9\pi^2}((1-4\cos\theta_{f_1})\cos\phi_{f_1}(1-4\cos\theta_{\bar{f}_4})\cos\phi_{\bar{f}_4} \\
&+ (1-4\cos\theta_{f_1})\sin\phi_{f_1}(1-4\cos\theta_{\bar{f}_4})\sin\phi_{\bar{f}_4}) \\
Im\left(\rho_{+0-0}(k)\right) &= \frac{1}{N_k}\sum_{i=1}^{N_k}\frac{-32}{9\pi^2}((1-4\cos\theta_{f_1})\cos\phi_{f_1}(1-4\cos\theta_{\bar{f}_4})\sin\phi_{\bar{f}_4} \\
&- (1-4\cos\theta_{f_1})\sin\phi_{f_1}(1-4\cos\theta_{\bar{f}_4})\cos\phi_{\bar{f}_4}) \\
Re\left(\rho_{+0--}(k)\right) &= \frac{1}{N_k}\sum_{i=1}^{N_k}\frac{-4}{3\pi\sqrt{2}}(1-4\cos\theta_{f_1})\cos\phi_{f_1}(5\cos^2\theta_{\bar{f}_4}-2\cos\theta_{\bar{f}_4}-1) \\
Im\left(\rho_{+0--}(k)\right) &= \frac{1}{N_k}\sum_{i=1}^{N_k}\frac{4}{3\pi\sqrt{2}}(1-4\cos\theta_{f_1})\sin\phi_{f_1}(5\cos^2\theta_{\bar{f}_4}-2\cos\theta_{\bar{f}_4}-1) \\
Re\left(\rho_{+-++}(k)\right) &= \frac{1}{N_k}\sum_{i=1}^{N_k}\cos 2\phi_{f_1}(5\cos^2\theta_{\bar{f}_4}+2\cos\theta_{\bar{f}_4}-1) \\
Im\left(\rho_{+-++}(k)\right) &= \frac{1}{N_k}\sum_{i=1}^{N_k}-\sin 2\phi_{f_1}(5\cos^2\theta_{\bar{f}_4}+2\cos\theta_{\bar{f}_4}-1)
\end{aligned}
$$

$$
\begin{aligned}
Re\left(\rho_{+-+0}(k)\right) &= \frac{1}{N_k}\sum_{i=1}^{N_k}\frac{8\sqrt{2}}{3\pi}(\cos 2\phi_{f_1}(1+4\cos\theta_{\bar{f}_4})\cos\phi_{\bar{f}_4} \\
&- \sin 2\phi_{f_1}(1+4\cos\theta_{\bar{f}_4})\sin\phi_{\bar{f}_4}) \\
Im\left(\rho_{+-+0}(k)\right) &= \frac{1}{N_k}\sum_{i=1}^{N_k}\frac{-8\sqrt{2}}{3\pi}(\cos 2\phi_{f_1}(1+4\cos\theta_{\bar{f}_4})\sin\phi_{\bar{f}_4} \\
&+ \sin 2\phi_{f_1}(1+4\cos\theta_{\bar{f}_4})\cos\phi_{\bar{f}_4}) \\
Re\left(\rho_{+-+-}(k)\right) &= \frac{1}{N_k}\sum_{i=1}^{N_k}4(\cos 2\phi_{f_1}\cos 2\phi_{\bar{f}_4} - \sin 2\phi_{f_1}\sin 2\phi_{\bar{f}_4}) \\
Im\left(\rho_{+-+-}(k)\right) &= \frac{1}{N_k}\sum_{i=1}^{N_k}-4(\cos 2\phi_{f_1}\sin 2\phi_{\bar{f}_4} + \sin 2\phi_{f_1}\cos 2\phi_{\bar{f}_4}) \\
Re\left(\rho_{+-0+}(k)\right) &= \frac{1}{N_k}\sum_{i=1}^{N_k}\frac{8\sqrt{2}}{3\pi}(\cos 2\phi_{f_1}(1+4\cos\theta_{\bar{f}_4})\cos\phi_{\bar{f}_4} \\
&+ \sin 2\phi_{f_1}(1+4\cos\theta_{\bar{f}_4})\sin\phi_{\bar{f}_4}) \\
Im\left(\rho_{+-0+}(k)\right) &= \frac{1}{N_k}\sum_{i=1}^{N_k}\frac{8\sqrt{2}}{3\pi}(\cos 2\phi_{f_1}(1+4\cos\theta_{\bar{f}_4})\sin\phi_{\bar{f}_4} \\
&- \sin 2\phi_{f_1}(1+4\cos\theta_{\bar{f}_4})\cos\phi_{\bar{f}_4}) \\
Re\left(\rho_{+-00}(k)\right) &= \frac{1}{N_k}\sum_{i=1}^{N_k}2\cos 2\phi_{f_1}(2-5\cos^2\theta_{\bar{f}_4}) \\
Im\left(\rho_{+-00}(k)\right) &= \frac{1}{N_k}\sum_{i=1}^{N_k}-2\sin 2\phi_{f_1}(2-5\cos^2\theta_{\bar{f}_4}) \\
Re\left(\rho_{+-0-}(k)\right) &= \frac{1}{N_k}\sum_{i=1}^{N_k}\frac{8\sqrt{2}}{3\pi}(\cos 2\phi_{f_1}(1-4\cos\theta_{\bar{f}_4})\cos\phi_{\bar{f}_4} \\
&- \sin 2\phi_{f_1}(1-4\cos\theta_{\bar{f}_4})\sin\phi_{\bar{f}_4}) \\
Im\left(\rho_{+-0-}(k)\right) &= \frac{1}{N_k}\sum_{i=1}^{N_k}\frac{-8\sqrt{2}}{3\pi}(\cos 2\phi_{f_1}(1-4\cos\theta_{\bar{f}_4})\sin\phi_{\bar{f}_4} \\
&+ \sin 2\phi_{f_1}(1-4\cos\theta_{\bar{f}_4})\cos\phi_{\bar{f}_4}) \\
Re\left(\rho_{+--+}(k)\right) &= \frac{1}{N_k}\sum_{i=1}^{N_k}4(\cos 2\phi_{f_1}\cos 2\phi_{\bar{f}_4} + \sin 2\phi_{f_1}\sin 2\phi_{\bar{f}_4}) \\
Im\left(\rho_{+--+}(k)\right) &= \frac{1}{N_k}\sum_{i=1}^{N_k}4(\cos 2\phi_{f_1}\sin 2\phi_{\bar{f}_4} - \sin 2\phi_{f_1}\cos 2\phi_{\bar{f}_4})
\end{aligned}
$$

$$
\begin{aligned}
Re\left(\rho_{+--0}(k)\right) &= \frac{1}{N_k}\sum_{i=1}^{N_k}\frac{8\sqrt{2}}{3\pi}(\cos 2\phi_{f_1}(1-4\cos\theta_{\bar{f}_4})\cos\phi_{\bar{f}_4} \\
&+ \sin 2\phi_{f_1}(1-4\cos\theta_{\bar{f}_4})\sin\phi_{\bar{f}_4}) \\
Im\left(\rho_{+--0}(k)\right) &= \frac{1}{N_k}\sum_{i=1}^{N_k}\frac{8\sqrt{2}}{3\pi}(\cos 2\phi_{f_1}(1-4\cos\theta_{\bar{f}_4})\sin\phi_{\bar{f}_4} \\
&- \sin 2\phi_{f_1}(1-4\cos\theta_{\bar{f}_4})\cos\phi_{\bar{f}_4}) \\
Re\left(\rho_{+---}(k)\right) &= \frac{1}{N_k}\sum_{i=1}^{N_k}\cos 2\phi_{f_1}(5\cos^2\theta_{\bar{f}_4}-2\cos\theta_{\bar{f}_4}-1) \\
Im\left(\rho_{+---}(k)\right) &= \frac{1}{N_k}\sum_{i=1}^{N_k}-\sin 2\phi_{f_1}(5\cos^2\theta_{\bar{f}_4}-2\cos\theta_{\bar{f}_4}-1) \\
Re\left(\rho_{0+++}(k)\right) &= \frac{1}{N_k}\sum_{i=1}^{N_k}\frac{-4}{3\pi\sqrt{2}}(1-4\cos\theta_{f_1})\cos\phi_{f_1}(5\cos^2\theta_{\bar{f}_4}+2\cos\theta_{\bar{f}_4}-1) \\
Im\left(\rho_{0+++}(k)\right) &= \frac{1}{N_k}\sum_{i=1}^{N_k}\frac{-4}{3\pi\sqrt{2}}(1-4\cos\theta_{f_1})\sin\phi_{f_1}(5\cos^2\theta_{\bar{f}_4}+2\cos\theta_{\bar{f}_4}-1) \\
Re\left(\rho_{0++0}(k)\right) &= \frac{1}{N_k}\sum_{i=1}^{N_k}\frac{-32}{9\pi^2}((1-4\cos\theta_{f_1})\cos\phi_{f_1}(1+4\cos\theta_{\bar{f}_4})\cos\phi_{\bar{f}_4} \\
&+ (1-4\cos\theta_{f_1})\sin\phi_{f_1}(1+4\cos\theta_{\bar{f}_4})\sin\phi_{\bar{f}_4}) \\
Im\left(\rho_{0++0}(k)\right) &= \frac{1}{N_k}\sum_{i=1}^{N_k}\frac{32}{9\pi^2}((1-4\cos\theta_{f_1})\cos\phi_{f_1}(1+4\cos\theta_{\bar{f}_4})\sin\phi_{\bar{f}_4} \\
&- (1-4\cos\theta_{f_1})\sin\phi_{f_1}(1+4\cos\theta_{\bar{f}_4})\cos\phi_{\bar{f}_4}) \\
Re\left(\rho_{0++-}(k)\right) &= \frac{1}{N_k}\sum_{i=1}^{N_k}\frac{-8\sqrt{2}}{3\pi}((1-4\cos\theta_{f_1})\cos\phi_{f_1}\cos 2\phi_{\bar{f}_4} \\
&+ (1-4\cos\theta_{f_1})\sin\phi_{f_1}\sin 2\phi_{\bar{f}_4}) \\
Im\left(\rho_{0++-}(k)\right) &= \frac{1}{N_k}\sum_{i=1}^{N_k}\frac{8\sqrt{2}}{3\pi}((1-4\cos\theta_{f_1})\cos\phi_{f_1}\sin 2\phi_{\bar{f}_4} \\
&- (1-4\cos\theta_{f_1})\sin\phi_{f_1}\cos 2\phi_{\bar{f}_4})
\end{aligned}
$$

$$
\begin{aligned}
Re\left(\rho_{0+0+}(k)\right) &= \frac{1}{N_k}\sum_{i=1}^{N_k}\frac{-32}{9\pi^2}((1-4\cos\theta_{f_1})\cos\phi_{f_1}(1+4\cos\theta_{\bar{f}_4})\cos\phi_{\bar{f}_4} \\
&- (1-4\cos\theta_{f_1})\sin\phi_{f_1}(1+4\cos\theta_{\bar{f}_4})\sin\phi_{\bar{f}_4}) \\
Im\left(\rho_{0+0+}(k)\right) &= \frac{1}{N_k}\sum_{i=1}^{N_k}\frac{-32}{9\pi^2}((1-4\cos\theta_{f_1})\cos\phi_{f_1}(1+4\cos\theta_{\bar{f}_4})\sin\phi_{\bar{f}_4} \\
&+ (1-4\cos\theta_{f_1})\sin\phi_{f_1}(1+4\cos\theta_{\bar{f}_4})\cos\phi_{\bar{f}_4}) \\
Re\left(\rho_{0+00}(k)\right) &= \frac{1}{N_k}\sum_{i=1}^{N_k}\frac{-8}{3\pi\sqrt{2}}(1-4\cos\theta_{f_1})\cos\phi_{f_1}(2-5\cos^2\theta_{\bar{f}_4}) \\
Im\left(\rho_{0+00}(k)\right) &= \frac{1}{N_k}\sum_{i=1}^{N_k}\frac{-8}{3\pi\sqrt{2}}(1-4\cos\theta_{f_1})\sin\phi_{f_1}(2-5\cos^2\theta_{\bar{f}_4}) \\
Re\left(\rho_{0+0-}(k)\right) &= \frac{1}{N_k}\sum_{i=1}^{N_k}\frac{-32}{9\pi^2}((1-4\cos\theta_{f_1})\cos\phi_{f_1}(1-4\cos\theta_{\bar{f}_4})\cos\phi_{\bar{f}_4} \\
&+ (1-4\cos\theta_{f_1})\sin\phi_{f_1}(1-4\cos\theta_{\bar{f}_4})\sin\phi_{\bar{f}_4}) \\
Im\left(\rho_{0+0-}(k)\right) &= \frac{1}{N_k}\sum_{i=1}^{N_k}\frac{32}{9\pi^2}((1-4\cos\theta_{f_1})\cos\phi_{f_1}(1-4\cos\theta_{\bar{f}_4})\sin\phi_{\bar{f}_4} \\
&- (1-4\cos\theta_{f_1})\sin\phi_{f_1}(1-4\cos\theta_{\bar{f}_4})\cos\phi_{\bar{f}_4}) \\
Re\left(\rho_{0+-+}(k)\right) &= \frac{1}{N_k}\sum_{i=1}^{N_k}\frac{-8\sqrt{2}}{3\pi}((1-4\cos\theta_{f_1})\cos\phi_{f_1}\cos 2\phi_{\bar{f}_4} \\
&- (1-4\cos\theta_{f_1})\sin\phi_{f_1}\sin 2\phi_{\bar{f}_4}) \\
Im\left(\rho_{0+-+}(k)\right) &= \frac{1}{N_k}\sum_{i=1}^{N_k}\frac{-8\sqrt{2}}{3\pi}((1-4\cos\theta_{f_1})\cos\phi_{f_1}\sin 2\phi_{\bar{f}_4} \\
&+ (1-4\cos\theta_{f_1})\sin\phi_{f_1}\cos 2\phi_{\bar{f}_4}) \\
Re\left(\rho_{0+-0}(k)\right) &= \frac{1}{N_k}\sum_{i=1}^{N_k}\frac{-32}{9\pi^2}((1-4\cos\theta_{f_1})\cos\phi_{f_1}(1-4\cos\theta_{\bar{f}_4})\cos\phi_{\bar{f}_4} \\
&- (1-4\cos\theta_{f_1})\sin\phi_{f_1}(1-4\cos\theta_{\bar{f}_4})\sin\phi_{\bar{f}_4}) \\
Im\left(\rho_{0+-0}(k)\right) &= \frac{1}{N_k}\sum_{i=1}^{N_k}\frac{-32}{9\pi^2}((1-4\cos\theta_{f_1})\cos\phi_{f_1}(1-4\cos\theta_{\bar{f}_4})\sin\phi_{\bar{f}_4} \\
&+ (1-4\cos\theta_{f_1})\sin\phi_{f_1}(1-4\cos\theta_{\bar{f}_4})\cos\phi_{\bar{f}_4})
\end{aligned}
$$

$$
\begin{aligned}
Re\left(\rho_{0+--}(k)\right) &= \frac{1}{N_k}\sum_{i=1}^{N_k}\frac{-4}{3\pi\sqrt{2}}(1-4\cos\theta_{f_1})\cos\phi_{f_1}(5\cos^2\theta_{\bar{f}_4}-2\cos\theta_{\bar{f}_4}-1)\\
Im\left(\rho_{0+--}(k)\right) &= \frac{1}{N_k}\sum_{i=1}^{N_k}\frac{-4}{3\pi\sqrt{2}}(1-4\cos\theta_{f_1})\sin\phi_{f_1}(5\cos^2\theta_{\bar{f}_4}-2\cos\theta_{\bar{f}_4}-1)\\
Re\left(\rho_{00++}(k)\right) &= \frac{1}{N_k}\sum_{i=1}^{N_k}\frac{1}{2}(2-5\cos^2\theta_{f_1})(5\cos^2\theta_{\bar{f}_4}+2\cos\theta_{\bar{f}_4}-1)\\
Im\left(\rho_{00++}(k)\right) &= 0\\
Re\left(\rho_{00+0}(k)\right) &= \frac{1}{N_k}\sum_{i=1}^{N_k}\frac{8}{3\pi\sqrt{2}}(2-5\cos^2\theta_{f_1})(1+4\cos\theta_{\bar{f}_4})\cos\phi_{\bar{f}_4}\\
Im\left(\rho_{00+0}(k)\right) &= \frac{1}{N_k}\sum_{i=1}^{N_k}\frac{-8}{3\pi\sqrt{2}}(2-5\cos^2\theta_{f_1})(1+4\cos\theta_{\bar{f}_4})\sin\phi_{\bar{f}_4}\\
Re\left(\rho_{00+-}(k)\right) &= \frac{1}{N_k}\sum_{i=1}^{N_k}2(2-5\cos^2\theta_{f_1})\cos 2\phi_{\bar{f}_4}\\
Im\left(\rho_{00+-}(k)\right) &= \frac{1}{N_k}\sum_{i=1}^{N_k}-2(2-5\cos^2\theta_{f_1})\sin 2\phi_{\bar{f}_4}\\
Re\left(\rho_{000+}(k)\right) &= \frac{1}{N_k}\sum_{i=1}^{N_k}\frac{8}{3\pi\sqrt{2}}(2-5\cos^2\theta_{f_1})(1+4\cos\theta_{\bar{f}_4})\cos\phi_{\bar{f}_4}\\
Im\left(\rho_{000+}(k)\right) &= \frac{1}{N_k}\sum_{i=1}^{N_k}\frac{8}{3\pi\sqrt{2}}(2-5\cos^2\theta_{f_1})(1+4\cos\theta_{\bar{f}_4})\sin\phi_{\bar{f}_4}\\
Re\left(\rho_{0000}(k)\right) &= \frac{1}{N_k}\sum_{i=1}^{N_k}(2-5\cos^2\theta_{f_1})(2-5\cos^2\theta_{\bar{f}_4})\\
Im\left(\rho_{0000}(k)\right) &= 0\\
Re\left(\rho_{000-}(k)\right) &= \frac{1}{N_k}\sum_{i=1}^{N_k}\frac{8}{3\pi\sqrt{2}}(2-5\cos^2\theta_{f_1})(1-4\cos\theta_{\bar{f}_4})\cos\phi_{\bar{f}_4}\\
Im\left(\rho_{000-}(k)\right) &= \frac{1}{N_k}\sum_{i=1}^{N_k}\frac{-8}{3\pi\sqrt{2}}(2-5\cos^2\theta_{f_1})(1-4\cos\theta_{\bar{f}_4})\sin\phi_{\bar{f}_4}
\end{aligned}
$$

$$
\begin{aligned}
Re\left(\rho_{00-+}(k)\right) &= \frac{1}{N_k}\sum_{i=1}^{N_k} 2(2-5\cos^2\theta_{f_1})\cos 2\phi_{\bar{f}_4} \\
Im\left(\rho_{00-+}(k)\right) &= \frac{1}{N_k}\sum_{i=1}^{N_k} 2(2-5\cos^2\theta_{f_1})\sin 2\phi_{\bar{f}_4} \\
Re\left(\rho_{00-0}(k)\right) &= \frac{1}{N_k}\sum_{i=1}^{N_k} \frac{8}{3\pi\sqrt{2}}(2-5\cos^2\theta_{f_1})(1-4\cos\theta_{\bar{f}_4})\cos\phi_{\bar{f}_4} \\
Im\left(\rho_{00-0}(k)\right) &= \frac{1}{N_k}\sum_{i=1}^{N_k} \frac{8}{3\pi\sqrt{2}}(2-5\cos^2\theta_{f_1})(1-4\cos\theta_{\bar{f}_4})\sin\phi_{\bar{f}_4} \\
Re\left(\rho_{00--}(k)\right) &= \frac{1}{N_k}\sum_{i=1}^{N_k} \frac{1}{2}(2-5\cos^2\theta_{f_1})(5\cos^2\theta_{\bar{f}_4}-2\cos\theta_{\bar{f}_4}-1) \\
Im\left(\rho_{00--}(k)\right) &= 0 \\
Re\left(\rho_{0-++}(k)\right) &= \frac{1}{N_k}\sum_{i=1}^{N_k} \frac{-4}{3\pi\sqrt{2}}(1+4\cos\theta_{f_1})\cos\phi_{f_1}(5\cos^2\theta_{\bar{f}_4}+2\cos\theta_{\bar{f}_4}-1) \\
Im\left(\rho_{0-++}(k)\right) &= \frac{1}{N_k}\sum_{i=1}^{N_k} \frac{4}{3\pi\sqrt{2}}(1+4\cos\theta_{f_1})\sin\phi_{f_1}(5\cos^2\theta_{\bar{f}_4}+2\cos\theta_{\bar{f}_4}-1) \\
Re\left(\rho_{0-+0}(k)\right) &= \frac{1}{N_k}\sum_{i=1}^{N_k} \frac{-32}{9\pi^2}((1+4\cos\theta_{f_1})\cos\phi_{f_1}(1+4\cos\theta_{\bar{f}_4})\cos\phi_{\bar{f}_4} \\
&- (1+4\cos\theta_{f_1})\sin\phi_{f_1}(1+4\cos\theta_{\bar{f}_4})\sin\phi_{\bar{f}_4}) \\
Im\left(\rho_{0-+0}(k)\right) &= \frac{1}{N_k}\sum_{i=1}^{N_k} \frac{32}{9\pi^2}((1+4\cos\theta_{f_1})\cos\phi_{f_1}(1+4\cos\theta_{\bar{f}_4})\sin\phi_{\bar{f}_4} \\
&+ (1+4\cos\theta_{f_1})\sin\phi_{f_1}(1+4\cos\theta_{\bar{f}_4})\cos\phi_{\bar{f}_4}) \\
Re\left(\rho_{0-+-}(k)\right) &= \frac{1}{N_k}\sum_{i=1}^{N_k} \frac{-8\sqrt{2}}{3\pi}((1+4\cos\theta_{f_1})\cos\phi_{f_1}\cos 2\phi_{\bar{f}_4} \\
&- (1+4\cos\theta_{f_1})\sin\phi_{f_1}\sin 2\phi_{\bar{f}_4}) \\
Im\left(\rho_{0-+-}(k)\right) &= \frac{1}{N_k}\sum_{i=1}^{N_k} \frac{8\sqrt{2}}{3\pi}((1+4\cos\theta_{f_1})\cos\phi_{f_1}\sin 2\phi_{\bar{f}_4} \\
&+ (1+4\cos\theta_{f_1})\sin\phi_{f_1}\cos 2\phi_{\bar{f}_4})
\end{aligned}
$$

$$
\begin{aligned}
Re\left(\rho_{0-0+}(k)\right) &= \frac{1}{N_k}\sum_{i=1}^{N_k}\frac{-32}{9\pi^2}((1+4\cos\theta_{f_1})\cos\phi_{f_1}(1+4\cos\theta_{\bar{f}_4})\cos\phi_{\bar{f}_4} \\
&+ (1+4\cos\theta_{f_1})\sin\phi_{f_1}(1+4\cos\theta_{\bar{f}_4})\sin\phi_{\bar{f}_4}) \\
Im\left(\rho_{0-0+}(k)\right) &= \frac{1}{N_k}\sum_{i=1}^{N_k}\frac{-32}{9\pi^2}((1+4\cos\theta_{f_1})\cos\phi_{f_1}(1+4\cos\theta_{\bar{f}_4})\sin\phi_{\bar{f}_4} \\
&- (1+4\cos\theta_{f_1})\sin\phi_{f_1}(1+4\cos\theta_{\bar{f}_4})\cos\phi_{\bar{f}_4}) \\
Re\left(\rho_{0-00}(k)\right) &= \frac{1}{N_k}\sum_{i=1}^{N_k}\frac{-8}{3\pi\sqrt{2}}(1+4\cos\theta_{f_1})\cos\phi_{f_1}(2-5\cos^2\theta_{\bar{f}_4}) \\
Im\left(\rho_{0-00}(k)\right) &= \frac{1}{N_k}\sum_{i=1}^{N_k}\frac{8}{3\pi\sqrt{2}}(1+4\cos\theta_{f_1})\sin\phi_{f_1}(2-5\cos^2\theta_{\bar{f}_4}) \\
Re\left(\rho_{0-0-}(k)\right) &= \frac{1}{N_k}\sum_{i=1}^{N_k}\frac{-32}{9\pi^2}((1+4\cos\theta_{f_1})\cos\phi_{f_1}(1-4\cos\theta_{\bar{f}_4})\cos\phi_{\bar{f}_4} \\
&- (1+4\cos\theta_{f_1})\sin\phi_{f_1}(1-4\cos\theta_{\bar{f}_4})\sin\phi_{\bar{f}_4}) \\
Im\left(\rho_{0-0-}(k)\right) &= \frac{1}{N_k}\sum_{i=1}^{N_k}\frac{32}{9\pi^2}((1+4\cos\theta_{f_1})\cos\phi_{f_1}(1-4\cos\theta_{\bar{f}_4})\sin\phi_{\bar{f}_4} \\
&+ (1+4\cos\theta_{f_1})\sin\phi_{f_1}(1-4\cos\theta_{\bar{f}_4})\cos\phi_{\bar{f}_4}) \\
Re\left(\rho_{0--+}(k)\right) &= \frac{1}{N_k}\sum_{i=1}^{N_k}\frac{-8\sqrt{2}}{3\pi}((1+4\cos\theta_{f_1})\cos\phi_{f_1}\cos 2\phi_{\bar{f}_4} \\
&+ (1+4\cos\theta_{f_1})\sin\phi_{f_1}\sin 2\phi_{\bar{f}_4}) \\
Im\left(\rho_{0--+}(k)\right) &= \frac{1}{N_k}\sum_{i=1}^{N_k}\frac{-8\sqrt{2}}{3\pi}((1+4\cos\theta_{f_1})\cos\phi_{f_1}\sin 2\phi_{\bar{f}_4} \\
&- (1+4\cos\theta_{f_1})\sin\phi_{f_1}\cos 2\phi_{\bar{f}_4}) \\
Re\left(\rho_{0--0}(k)\right) &= \frac{1}{N_k}\sum_{i=1}^{N_k}\frac{-32}{9\pi^2}((1+4\cos\theta_{f_1})\cos\phi_{f_1}(1-4\cos\theta_{\bar{f}_4})\cos\phi_{\bar{f}_4} \\
&+ (1+4\cos\theta_{f_1})\sin\phi_{f_1}(1-4\cos\theta_{\bar{f}_4})\sin\phi_{\bar{f}_4}) \\
Im\left(\rho_{0--0}(k)\right) &= \frac{1}{N_k}\sum_{i=1}^{N_k}\frac{-32}{9\pi^2}((1+4\cos\theta_{f_1})\cos\phi_{f_1}(1-4\cos\theta_{\bar{f}_4})\sin\phi_{\bar{f}_4} \\
&- (1+4\cos\theta_{f_1})\sin\phi_{f_1}(1-4\cos\theta_{\bar{f}_4})\cos\phi_{\bar{f}_4})
\end{aligned}
$$

$$
\begin{aligned}
Re\left(\rho_{0---}(k)\right) &= \frac{1}{N_k}\sum_{i=1}^{N_k}\frac{-4}{3\pi\sqrt{2}}(1+4\cos\theta_{f_1})\cos\phi_{f_1}(5\cos^2\theta_{\bar{f}_4}-2\cos\theta_{\bar{f}_4}-1)\\
Im\left(\rho_{0---}(k)\right) &= \frac{1}{N_k}\sum_{i=1}^{N_k}\frac{4}{3\pi\sqrt{2}}(1+4\cos\theta_{f_1})\sin\phi_{f_1}(5\cos^2\theta_{\bar{f}_4}-2\cos\theta_{\bar{f}_4}-1)\\
Re\left(\rho_{-+++}(k)\right) &= \frac{1}{N_k}\sum_{i=1}^{N_k}\cos 2\phi_{f_1}(5\cos^2\theta_{\bar{f}_4}+2\cos\theta_{\bar{f}_4}-1)\\
Im\left(\rho_{-+++}(k)\right) &= \frac{1}{N_k}\sum_{i=1}^{N_k}\sin 2\phi_{f_1}(5\cos^2\theta_{\bar{f}_4}+2\cos\theta_{\bar{f}_4}-1)\\
Re\left(\rho_{-++0}(k)\right) &= \frac{1}{N_k}\sum_{i=1}^{N_k}\frac{8\sqrt{2}}{3\pi}(\cos 2\phi_{f_1}(1+4\cos\theta_{\bar{f}_4})\cos\phi_{\bar{f}_4}\\
&+ \sin 2\phi_{f_1}(1+4\cos\theta_{\bar{f}_4})\sin\phi_{\bar{f}_4})\\
Im\left(\rho_{-++0}(k)\right) &= \frac{1}{N_k}\sum_{i=1}^{N_k}\frac{-8\sqrt{2}}{3\pi}(\cos 2\phi_{f_1}(1+4\cos\theta_{\bar{f}_4})\sin\phi_{\bar{f}_4}\\
&- \sin 2\phi_{f_1}(1+4\cos\theta_{\bar{f}_4})\cos\phi_{\bar{f}_4})\\
Re\left(\rho_{-++-}(k)\right) &= \frac{1}{N_k}\sum_{i=1}^{N_k}4(\cos 2\phi_{f_1}\cos 2\phi_{\bar{f}_4}+\sin 2\phi_{f_1}\sin 2\phi_{\bar{f}_4})\\
Im\left(\rho_{-++-}(k)\right) &= \frac{1}{N_k}\sum_{i=1}^{N_k}-4(\cos 2\phi_{f_1}\sin 2\phi_{\bar{f}_4}-\sin 2\phi_{f_1}\cos 2\phi_{\bar{f}_4})\\
Re\left(\rho_{-+0+}(k)\right) &= \frac{1}{N_k}\sum_{i=1}^{N_k}\frac{8\sqrt{2}}{3\pi}(\cos 2\phi_{f_1}(1+4\cos\theta_{\bar{f}_4})\cos\phi_{\bar{f}_4}\\
&- \sin 2\phi_{f_1}(1+4\cos\theta_{\bar{f}_4})\sin\phi_{\bar{f}_4})\\
Im\left(\rho_{-+0+}(k)\right) &= \frac{1}{N_k}\sum_{i=1}^{N_k}\frac{8\sqrt{2}}{3\pi}(\cos 2\phi_{f_1}(1+4\cos\theta_{\bar{f}_4})\sin\phi_{\bar{f}_4}\\
&+ \sin 2\phi_{f_1}(1+4\cos\theta_{\bar{f}_4})\cos\phi_{\bar{f}_4})\\
Re\left(\rho_{-+00}(k)\right) &= \frac{1}{N_k}\sum_{i=1}^{N_k}2\cos 2\phi_{f_1}(2-5\cos^2\theta_{\bar{f}_4})\\
Im\left(\rho_{-+00}(k)\right) &= \frac{1}{N_k}\sum_{i=1}^{N_k}2\sin 2\phi_{f_1}(2-5\cos^2\theta_{\bar{f}_4})
\end{aligned}
$$

$$
\begin{aligned}
Re\left(\rho_{-+0-}(k)\right) &= \frac{1}{N_k}\sum_{i=1}^{N_k}\frac{8\sqrt{2}}{3\pi}(\cos 2\phi_{f_1}(1-4\cos\theta_{\bar{f}_4})\cos\phi_{\bar{f}_4} \\
&+ \sin 2\phi_{f_1}(1-4\cos\theta_{\bar{f}_4})\sin\phi_{\bar{f}_4}) \\
Im\left(\rho_{-+0-}(k)\right) &= \frac{1}{N_k}\sum_{i=1}^{N_k}\frac{-8\sqrt{2}}{3\pi}(\cos 2\phi_{f_1}(1-4\cos\theta_{\bar{f}_4})\sin\phi_{\bar{f}_4} \\
&- \sin 2\phi_{f_1}(1-4\cos\theta_{\bar{f}_4})\cos\phi_{\bar{f}_4}) \\
Re\left(\rho_{-+-+}(k)\right) &= \frac{1}{N_k}\sum_{i=1}^{N_k}4(\cos 2\phi_{f_1}\cos 2\phi_{\bar{f}_4} - \sin 2\phi_{f_1}\sin 2\phi_{\bar{f}_4}) \\
Im\left(\rho_{-+-+}(k)\right) &= \frac{1}{N_k}\sum_{i=1}^{N_k}4(\cos 2\phi_{f_1}\sin 2\phi_{\bar{f}_4} + \sin 2\phi_{f_1}\cos 2\phi_{\bar{f}_4}) \\
Re\left(\rho_{-+-0}(k)\right) &= \frac{1}{N_k}\sum_{i=1}^{N_k}\frac{8\sqrt{2}}{3\pi}(\cos 2\phi_{f_1}(1-4\cos\theta_{\bar{f}_4})\cos\phi_{\bar{f}_4} \\
&- \sin 2\phi_{f_1}(1-4\cos\theta_{\bar{f}_4})\sin\phi_{\bar{f}_4}) \\
Im\left(\rho_{-+-0}(k)\right) &= \frac{1}{N_k}\sum_{i=1}^{N_k}\frac{8\sqrt{2}}{3\pi}(\cos 2\phi_{f_1}(1-4\cos\theta_{\bar{f}_4})\sin\phi_{\bar{f}_4} \\
&+ \sin 2\phi_{f_1}(1-4\cos\theta_{\bar{f}_4})\cos\phi_{\bar{f}_4}) \\
Re\left(\rho_{-+--}(k)\right) &= \frac{1}{N_k}\sum_{i=1}^{N_k}\frac{1}{2}\cos 2\phi_{f_1}(5\cos^2\theta_{\bar{f}_4} - 2\cos\theta_{\bar{f}_4} - 1) \\
Im\left(\rho_{-+--}(k)\right) &= \frac{1}{N_k}\sum_{i=1}^{N_k}\frac{1}{2}\sin 2\phi_{f_1}(5\cos^2\theta_{\bar{f}_4} - 2\cos\theta_{\bar{f}_4} - 1) \\
Re\left(\rho_{-0++}(k)\right) &= \frac{1}{N_k}\sum_{i=1}^{N_k}\frac{-4}{3\pi\sqrt{2}}(1+4\cos\theta_{f_1})\cos\phi_{f_1}(5\cos^2\theta_{\bar{f}_4} + 2\cos\theta_{\bar{f}_4} - 1) \\
Im\left(\rho_{-0++}(k)\right) &= \frac{1}{N_k}\sum_{i=1}^{N_k}\frac{-4}{3\pi\sqrt{2}}(1+4\cos\theta_{f_1})\sin\phi_{f_1}(5\cos^2\theta_{\bar{f}_4} + 2\cos\theta_{\bar{f}_4} - 1)
\end{aligned}
$$

$$
\begin{aligned}
Re\left(\rho_{-0+0}(k)\right) &= \frac{1}{N_k}\sum_{i=1}^{N_k}\frac{-32}{9\pi^2}((1+4\cos\theta_{f_1})\cos\phi_{f_1}(1+4\cos\theta_{\bar{f}_4})\cos\phi_{\bar{f}_4} \\
&+ (1+4\cos\theta_{f_1})\sin\phi_{f_1}(1+4\cos\theta_{\bar{f}_4})\sin\phi_{\bar{f}_4}) \\
Im\left(\rho_{-0+0}(k)\right) &= \frac{1}{N_k}\sum_{i=1}^{N_k}\frac{32}{9\pi^2}((1+4\cos\theta_{f_1})\cos\phi_{f_1}(1+4\cos\theta_{\bar{f}_4})\sin\phi_{\bar{f}_4} \\
&- (1+4\cos\theta_{f_1})\sin\phi_{f_1}(1+4\cos\theta_{\bar{f}_4})\cos\phi_{\bar{f}_4}) \\
Re\left(\rho_{-0+-}(k)\right) &= \frac{1}{N_k}\sum_{i=1}^{N_k}\frac{-8\sqrt{2}}{3\pi}((1+4\cos\theta_{f_1})\cos\phi_{f_1}\cos 2\phi_{\bar{f}_4} \\
&+ (1+4\cos\theta_{f_1})\sin\phi_{f_1}\sin 2\phi_{\bar{f}_4}) \\
Im\left(\rho_{-0+-}(k)\right) &= \frac{1}{N_k}\sum_{i=1}^{N_k}\frac{8\sqrt{2}}{3\pi}((1+4\cos\theta_{f_1})\cos\phi_{f_1}\sin 2\phi_{\bar{f}_4} \\
&- (1+4\cos\theta_{f_1})\sin\phi_{f_1}\cos 2\phi_{\bar{f}_4}) \\
Re\left(\rho_{-00+}(k)\right) &= \frac{1}{N_k}\sum_{i=1}^{N_k}\frac{-32}{9\pi^2}((1+4\cos\theta_{f_1})\cos\phi_{f_1}(1+4\cos\theta_{\bar{f}_4})\cos\phi_{\bar{f}_4} \\
&- (1+4\cos\theta_{f_1})\sin\phi_{f_1}(1+4\cos\theta_{\bar{f}_4})\sin\phi_{\bar{f}_4}) \\
Im\left(\rho_{-00+}(k)\right) &= \frac{1}{N_k}\sum_{i=1}^{N_k}\frac{-32}{9\pi^2}((1+4\cos\theta_{f_1})\cos\phi_{f_1}(1+4\cos\theta_{\bar{f}_4})\sin\phi_{\bar{f}_4} \\
&+ (1+4\cos\theta_{f_1})\sin\phi_{f_1}(1+4\cos\theta_{\bar{f}_4})\cos\phi_{\bar{f}_4}) \\
Re\left(\rho_{-000}(k)\right) &= \frac{1}{N_k}\sum_{i=1}^{N_k}\frac{-8}{3\pi\sqrt{2}}(1+4\cos\theta_{f_1})\cos\phi_{f_1}(2-5\cos^2\theta_{\bar{f}_4}) \\
Im\left(\rho_{-000}(k)\right) &= \frac{1}{N_k}\sum_{i=1}^{N_k}\frac{-8}{3\pi\sqrt{2}}(1+4\cos\theta_{f_1})\sin\phi_{f_1}(2-5\cos^2\theta_{\bar{f}_4}) \\
Re\left(\rho_{-00-}(k)\right) &= \frac{1}{N_k}\sum_{i=1}^{N_k}\frac{-32}{9\pi^2}((1+4\cos\theta_{f_1})\cos\phi_{f_1}(1-4\cos\theta_{\bar{f}_4})\cos\phi_{\bar{f}_4} \\
&+ (1+4\cos\theta_{f_1})\sin\phi_{f_1}(1-4\cos\theta_{\bar{f}_4})\sin\phi_{\bar{f}_4}) \\
Im\left(\rho_{-00-}(k)\right) &= \frac{1}{N_k}\sum_{i=1}^{N_k}\frac{32}{9\pi^2}((1+4\cos\theta_{f_1})\cos\phi_{f_1}(1-4\cos\theta_{\bar{f}_4})\sin\phi_{\bar{f}_4} \\
&- (1+4\cos\theta_{f_1})\sin\phi_{f_1}(1-4\cos\theta_{\bar{f}_4})\cos\phi_{\bar{f}_4})
\end{aligned}
$$

$$
\begin{aligned}
Re\left(\rho_{-0-+}(k)\right) &= \frac{1}{N_k}\sum_{i=1}^{N_k}\frac{-8\sqrt{2}}{3\pi}((1+4\cos\theta_{f_1})\cos\phi_{f_1}\cos 2\phi_{\bar{f}_4} \\
&- (1+4\cos\theta_{f_1})\sin\phi_{f_1}\sin 2\phi_{\bar{f}_4}) \\
Im\left(\rho_{-0-+}(k)\right) &= \frac{1}{N_k}\sum_{i=1}^{N_k}\frac{-8\sqrt{2}}{3\pi}((1+4\cos\theta_{f_1})\cos\phi_{f_1}\sin 2\phi_{\bar{f}_4} \\
&+ (1+4\cos\theta_{f_1})\sin\phi_{f_1}\cos 2\phi_{\bar{f}_4}) \\
Re\left(\rho_{-0-0}(k)\right) &= \frac{1}{N_k}\sum_{i=1}^{N_k}\frac{-32}{9\pi^2}((1+4\cos\theta_{f_1})\cos\phi_{f_1}(1-4\cos\theta_{\bar{f}_4})\cos\phi_{\bar{f}_4} \\
&- (1+4\cos\theta_{f_1})\sin\phi_{f_1}(1-4\cos\theta_{\bar{f}_4})\sin\phi_{\bar{f}_4}) \\
Im\left(\rho_{-0-0}(k)\right) &= \frac{1}{N_k}\sum_{i=1}^{N_k}\frac{-32}{9\pi^2}((1+4\cos\theta_{f_1})\cos\phi_{f_1}(1-4\cos\theta_{\bar{f}_4})\sin\phi_{\bar{f}_4} \\
&+ (1+4\cos\theta_{f_1})\sin\phi_{f_1}(1-4\cos\theta_{\bar{f}_4})\cos\phi_{\bar{f}_4}) \\
Re\left(\rho_{-0--}(k)\right) &= \frac{1}{N_k}\sum_{i=1}^{N_k}\frac{-4}{3\pi\sqrt{2}}(1+4\cos\theta_{f_1})\cos\phi_{f_1}(5\cos^2\theta_{\bar{f}_4}-2\cos\theta_{\bar{f}_4}-1) \\
Im\left(\rho_{-0--}(k)\right) &= \frac{1}{N_k}\sum_{i=1}^{N_k}\frac{-4}{3\pi\sqrt{2}}(1+4\cos\theta_{f_1})\sin\phi_{f_1}(5\cos^2\theta_{\bar{f}_4}-2\cos\theta_{\bar{f}_4}-1) \\
Re\left(\rho_{--++}(k)\right) &= \frac{1}{N_k}\sum_{i=1}^{N_k}\frac{1}{4}(5\cos^2\theta_{f_1}+2\cos\theta_{f_1}-1)(5\cos^2\theta_{\bar{f}_4}+2\cos\theta_{\bar{f}_4}-1) \\
Im\left(\rho_{--++}(k)\right) &= 0 \\
Re\left(\rho_{--+0}(k)\right) &= \frac{1}{N_k}\sum_{i=1}^{N_k}\frac{4}{3\pi\sqrt{2}}(5\cos^2\theta_{f_1}+2\cos\theta_{f_1}-1)(1+4\cos\theta_{\bar{f}_4})\cos\phi_{\bar{f}_4} \\
Im\left(\rho_{--+0}(k)\right) &= \frac{1}{N_k}\sum_{i=1}^{N_k}\frac{-4}{3\pi\sqrt{2}}(5\cos^2\theta_{f_1}+2\cos\theta_{f_1}-1)(1+4\cos\theta_{\bar{f}_4})\sin\phi_{\bar{f}_4} \\
Re\left(\rho_{--+-}(k)\right) &= \frac{1}{N_k}\sum_{i=1}^{N_k}(5\cos^2\theta_{f_1}+2\cos\theta_{f_1}-1)\cos 2\phi_{\bar{f}_4} \\
Im\left(\rho_{--+-}(k)\right) &= \frac{1}{N_k}\sum_{i=1}^{N_k}-(5\cos^2\theta_{f_1}+2\cos\theta_{f_1}-1)\sin 2\phi_{\bar{f}_4}
\end{aligned}
$$

$$
\begin{aligned}
Re\left(\rho_{--0+}(k)\right) &= \frac{1}{N_k}\sum_{i=1}^{N_k}\frac{4}{3\pi\sqrt{2}}(5\cos^2\theta_{f_1}+2\cos\theta_{f_1}-1)(1+4\cos\theta_{\bar{f}_4})\cos\phi_{\bar{f}_4}\\
Im\left(\rho_{--0+}(k)\right) &= \frac{1}{N_k}\sum_{i=1}^{N_k}\frac{4}{3\pi\sqrt{2}}(5\cos^2\theta_{f_1}+2\cos\theta_{f_1}-1)(1+4\cos\theta_{\bar{f}_4})\sin\phi_{\bar{f}_4}\\
Re\left(\rho_{--00}(k)\right) &= \frac{1}{N_k}\sum_{i=1}^{N_k}\frac{1}{2}(5\cos^2\theta_{f_1}+2\cos\theta_{f_1}-1)(2-5\cos^2\theta_{\bar{f}_4})\\
Im\left(\rho_{--00}(k)\right) &= 0\\
Re\left(\rho_{--0-}(k)\right) &= \frac{1}{N_k}\sum_{i=1}^{N_k}\frac{4}{3\pi\sqrt{2}}(5\cos^2\theta_{f_1}+2\cos\theta_{f_1}-1)(1-4\cos\theta_{\bar{f}_4})\cos\phi_{\bar{f}_4}\\
Im\left(\rho_{--0-}(k)\right) &= \frac{1}{N_k}\sum_{i=1}^{N_k}\frac{-4}{3\pi\sqrt{2}}(5\cos^2\theta_{f_1}+2\cos\theta_{f_1}-1)(1-4\cos\theta_{\bar{f}_4})\sin\phi_{\bar{f}_4}\\
Re\left(\rho_{---+}(k)\right) &= \frac{1}{N_k}\sum_{i=1}^{N_k}(5\cos^2\theta_{f_1}+2\cos\theta_{f_1}-1)\cos 2\phi_{\bar{f}_4}\\
Im\left(\rho_{---+}(k)\right) &= \frac{1}{N_k}\sum_{i=1}^{N_k}(5\cos^2\theta_{f_1}+2\cos\theta_{f_1}-1)\sin 2\phi_{\bar{f}_4}\\
Re\left(\rho_{---0}(k)\right) &= \frac{1}{N_k}\sum_{i=1}^{N_k}\frac{4}{3\pi\sqrt{2}}(5\cos^2\theta_{f_1}+2\cos\theta_{f_1}-1)(1-4\cos\theta_{\bar{f}_4})\cos\phi_{\bar{f}_4}\\
Im\left(\rho_{---0}(k)\right) &= \frac{1}{N_k}\sum_{i=1}^{N_k}\frac{4}{3\pi\sqrt{2}}(5\cos^2\theta_{f_1}+2\cos\theta_{f_1}-1)(1-4\cos\theta_{\bar{f}_4})\sin\phi_{\bar{f}_4}\\
Re\left(\rho_{----}(k)\right) &= \frac{1}{N_k}\sum_{i=1}^{N_k}\frac{1}{4}(5\cos^2\theta_{f_1}+2\cos\theta_{f_1}-1)(5\cos^2\theta_{\bar{f}_4}-2\cos\theta_{\bar{f}_4}-1)\\
Im\left(\rho_{----}(k)\right) &= 0
\end{aligned}
$$

Appendix B

Stability of the χ^2 fit

In this appendix the stability of the χ^2 fit method is discussed and tested. When a χ^2 is formed containing a number of highly correlated observables it can become unstable. As the correlation tends to unity the χ^2 can fail and thus not give a meaningful result.

In chapter 6 the χ^2 fit used in the TGC calculations was tested extensively and found to be reliable. A further test can be performed where one of the diagonal SDM elements is omitted from the fit, this will then remove the problem of highly correlated elements. As the diagonal elements are highly correlated, this omission of one of them from the fit should produce little change in the fit results. In this appendix all fits are performed without the inclusion of ρ_{++}. This was an arbitary choice of SDM element to remove. It was found that the same result was yielded independent of which diagonal element was omitted from the fit.

All tests in this appendix were performed using only the BILGOU reweighting scheme, although similar tests were performed with the WVCXME reweighting scheme and the results were found to be compatible to those given here.

Figures B.1 and B.2 show the bias fits performed to Monte Carlo samples with various anomalous couplings and figures B.3 and B.4 show the fits to many Monte Carlo subsamples along with the pull distributions. All these results are consistent with those given in chapter 6

The expected statistical errors calculated using the fit method excluding ρ_{++}, are shown in table B.1. They are equivalent to the values calculated in chapter 6.

Finally the actual values of the TGCs calculated from the data are shown table B.1. These are consistent with those calculated in chapter 7. Once systematic uncertainties are included a number of the results differ very slightly from those quoted in chapter 7, this is expected due to the less than exact way the systematic uncertainties are included in the χ^2 fit. The differences are still much less than the statistical precision of the results. The χ^2 plots for these fits can be seen in figures B.5 and B.6.

This appendix thus verifies the correctness of the χ^2 fit method used in the thesis and indicates that the high correlations between the SDM elements does not introduce instabilities in the χ^2 at the precision achievable with the LEP2 data.

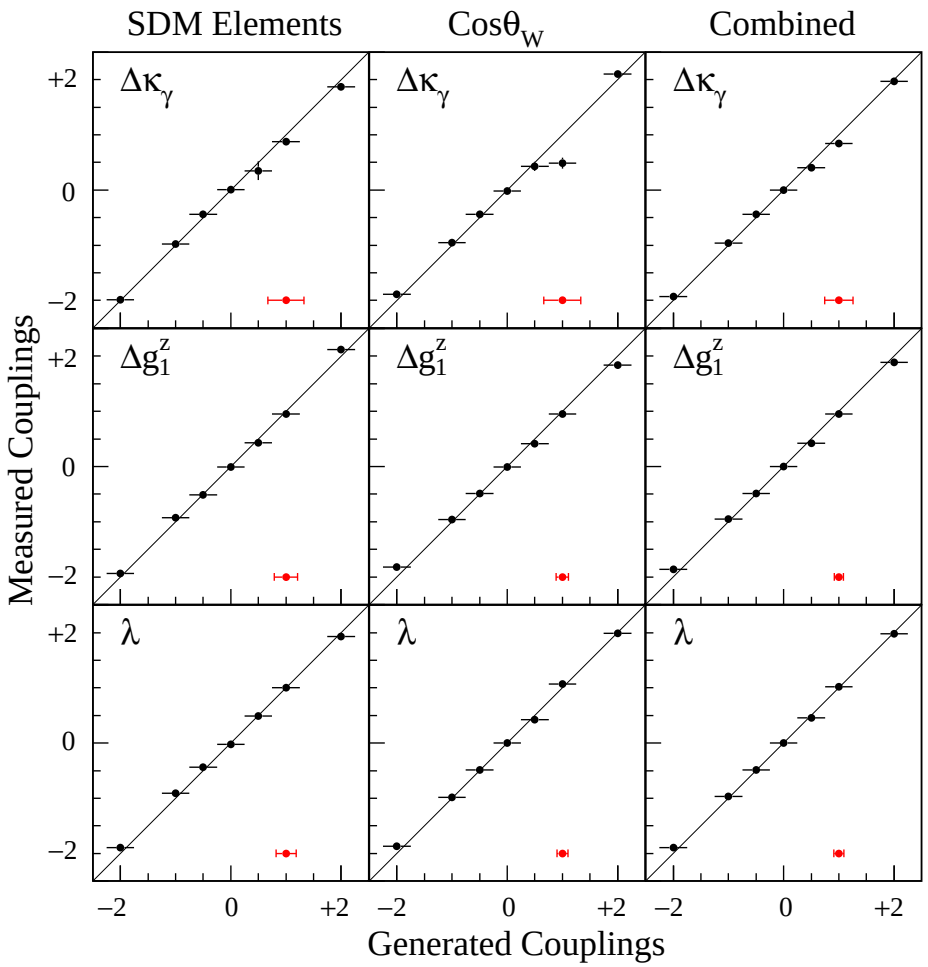

Figure B.1: *Bias plots of the CP-conserving TGC fits using the BILGOU reweighting scheme. The first column is the fit to the SDM elements excluding ρ_{++}, the second column is the fit to the W production angle, and the third column is the combined fit. The solid line represents the perfect fit. The red points represent the expected statistical error on the data.*

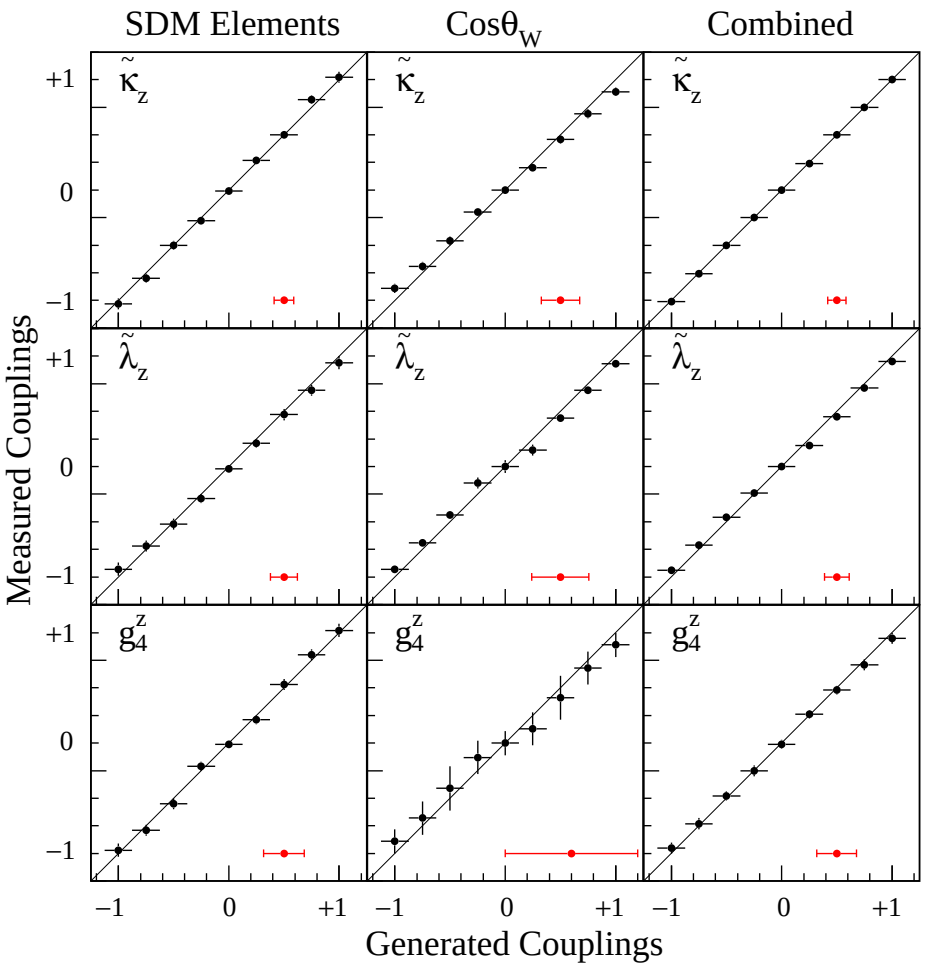

Figure B.2: *Bias plots of the CP-violating TGC fits using the BILGOU reweighting scheme. The first column is the fit to the SDM elements excluding ρ_{++}, the second column is the fit to the W production angle, and the third column is the combined fit. The solid line represents the perfect fit. The red points represent the expected statistical error on the data.*

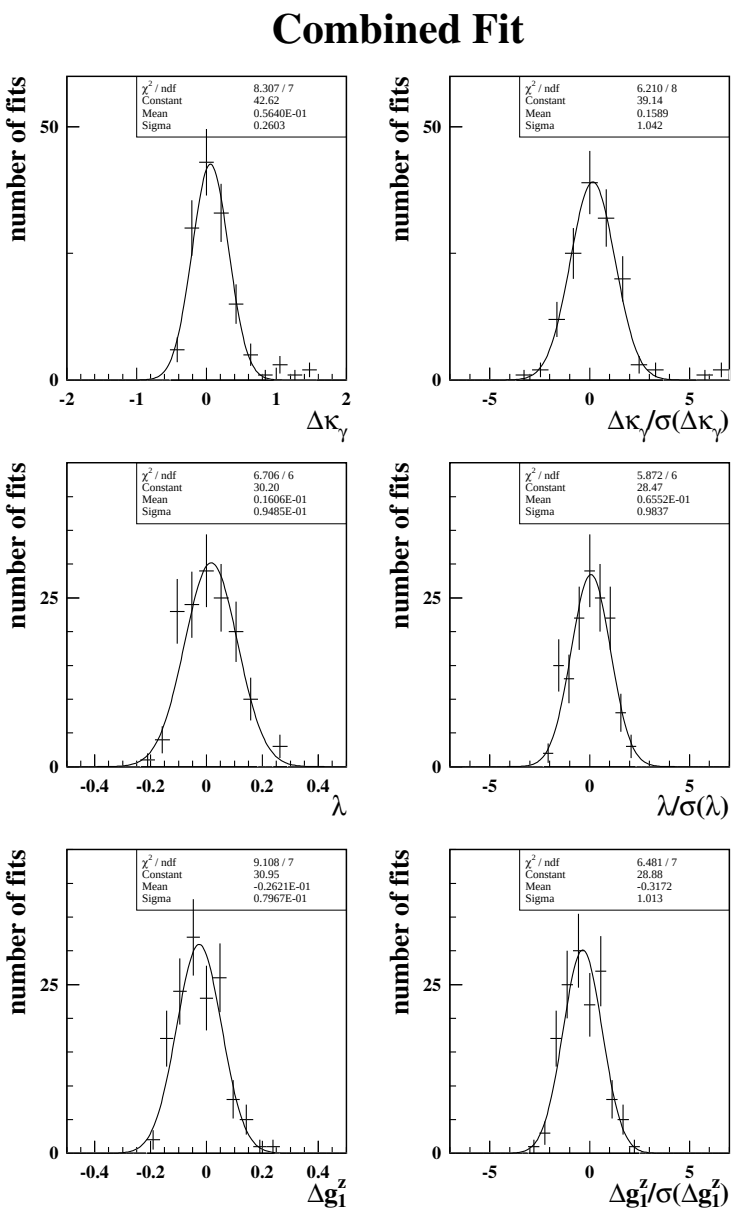

Figure B.3: *Combined fit results to 139 subsamples of Standard Model EXCALIBUR Monte Carlo. The BILGOU reweighting scheme was used in the fits. The widths of the distributions of the plots on the left side represent the expected error for the analysis for the corresponding coupling parameters. The width of the pull distributions, the plots on the right side, should be compatible with unity if the statistical error is reliable. All fits excluded* ρ_{++}

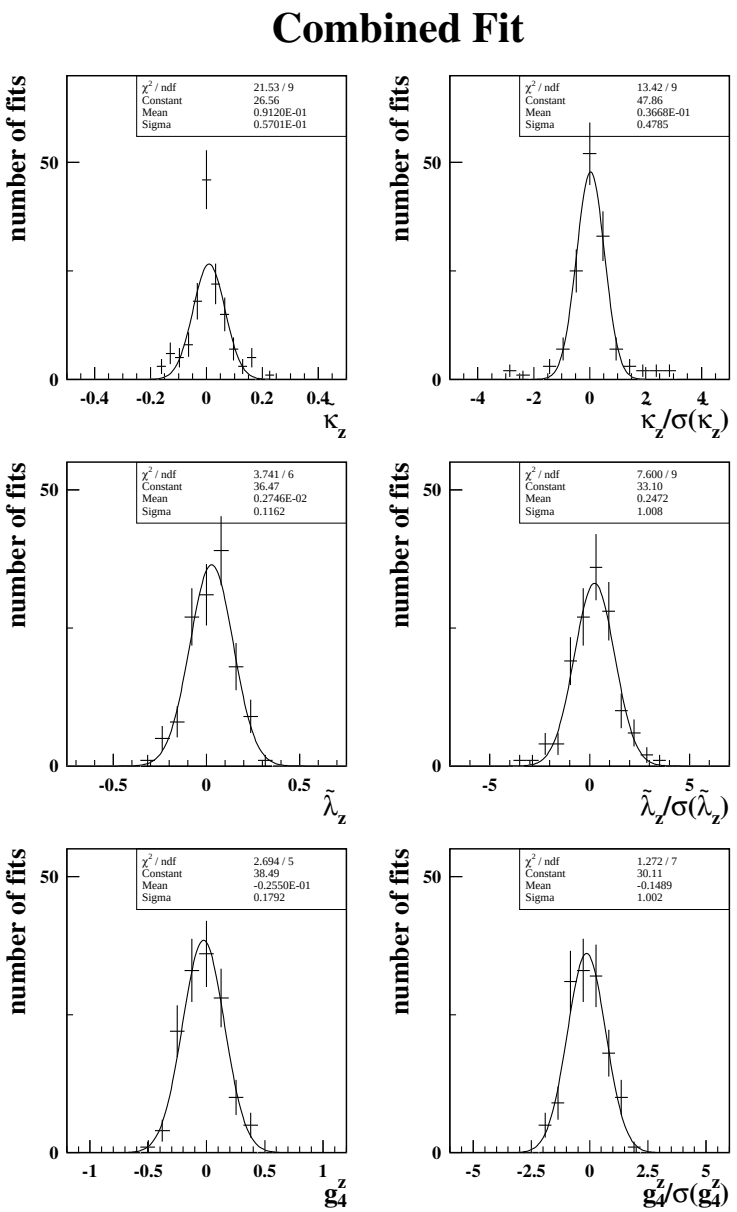

Figure B.4: *Combined fit results for the CP-violating couplings to 139 subsamples of Standard Model EXCALIBUR Monte Carlo. The plots on the left are the distributions of fitted values and the plots on the right are the pull distributions. All fits excluded* ρ_{++}.

	$\Delta\kappa_\gamma$	Δg_1^z	λ	$\tilde{\kappa}_z$	$\tilde{\lambda}_z$	g_4^z
<u>SDM Elements</u>						
Fit	$-0.23^{+0.50}_{-0.30}$	$0.04^{+0.12}_{-0.16}$	$0.05^{+0.17}_{-0.19}$	$-0.19^{+0.08}_{-0.07}$	$-0.09^{+0.16}_{-0.15}$	$0.03^{+0.21}_{-0.22}$
Expected Stat. Error	± 0.32	± 0.21	± 0.18	± 0.09	± 0.12	± 0.18
Fit Including Systematic Uncertainties	$-0.29^{+0.57}_{-0.34}$	$0.08^{+0.13}_{-0.16}$	$0.07^{+0.19}_{-0.20}$	$-0.20^{+0.10}_{-0.07}$	$-0.11^{+0.19}_{-0.21}$	$0.08^{+0.25}_{-0.25}$
<u>$\cos\theta_{\mathrm{W}}$</u>						
Fit	$-0.27^{+0.29}_{-0.24}$	$-0.08^{+0.09}_{-0.08}$	$-0.09^{+0.09}_{-0.08}$	$-0.19^{+0.44}_{-0.09}$	$-0.29^{+0.67}_{-0.12}$	$0.67^{+0.37}_{-1.60}$
Expected Stat. Error	± 0.34	± 0.11	± 0.10	± 0.17	± 0.26	± 0.70
Fit Including Systematic Uncertainties	$-0.24^{+0.33}_{-0.28}$	$-0.07^{+0.10}_{-0.09}$	$-0.08^{+0.11}_{-0.10}$	$-0.14^{+0.41}_{-0.13}$	$-0.23^{+0.61}_{-0.19}$	$0.63^{+0.52}_{-1.71}$
<u>Combined</u>						
Fit	$-0.25^{+0.22}_{-0.20}$	$-0.05^{+0.08}_{-0.08}$	$-0.06^{+0.09}_{-0.08}$	$-0.19^{+0.06}_{-0.05}$	$-0.17^{+0.19}_{-0.13}$	$0.04^{+0.22}_{-0.23}$
Expected Stat. Error	± 0.26	± 0.08	± 0.10	± 0.08	± 0.11	± 0.18
Fit Including Systematic Uncertainties	$-0.25^{+0.26}_{-0.22}$	$-0.03^{+0.09}_{-0.09}$	$-0.05^{+0.10}_{-0.09}$	$-0.18^{+0.09}_{-0.07}$	$-0.15^{+0.17}_{-0.18}$	$0.09^{+0.26}_{-0.25}$

Table B.1: *Measured values of all the TGC parameters using the BILGOU reweighting scheme. In the fits that include the SDM elements, ρ_{++} has been omitted*

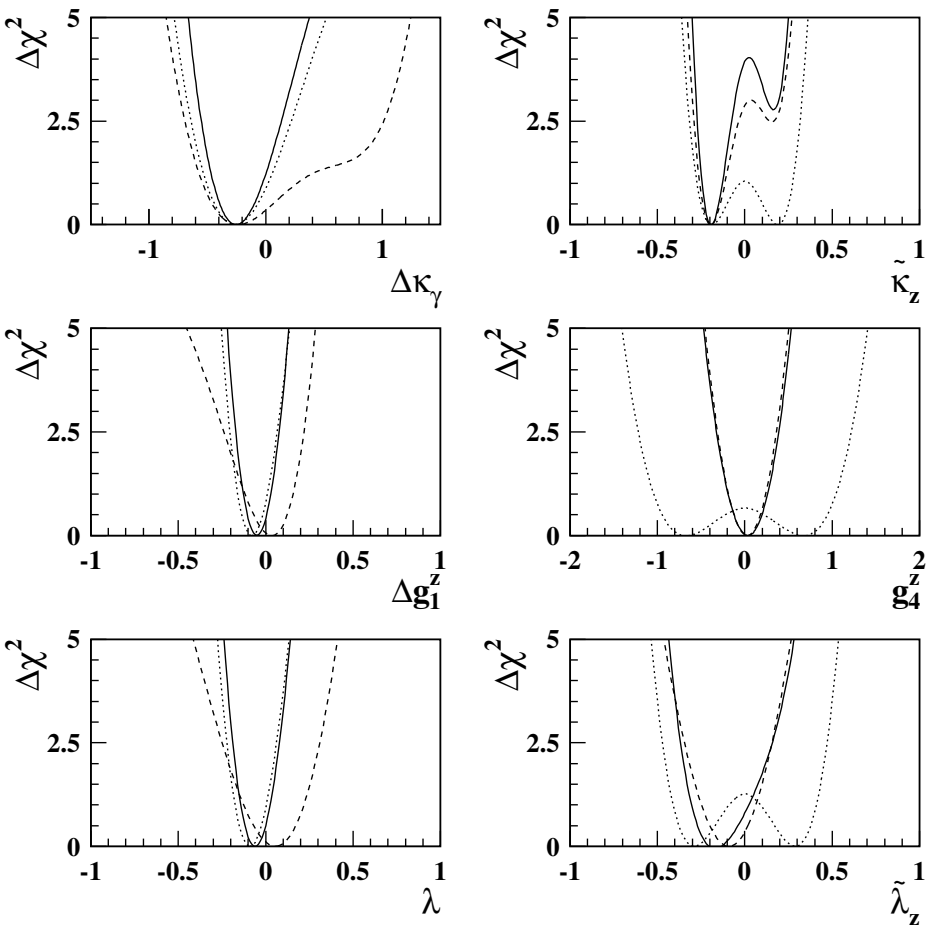

Figure B.5: *The χ^2 plots for the fits to the CP-conserving and CP-violating anomalous couplings. For the CP-conserving couplings the dashed line is the fit to just five real SDM elements, for the CP-violating couplings it is the fit to eight SDM elements. The ρ_{++} observable has been omitted. The dotted line is the fit to just the $\cos\theta_{\mathrm{W}}$ distribution. The solid line is the combined fit.*

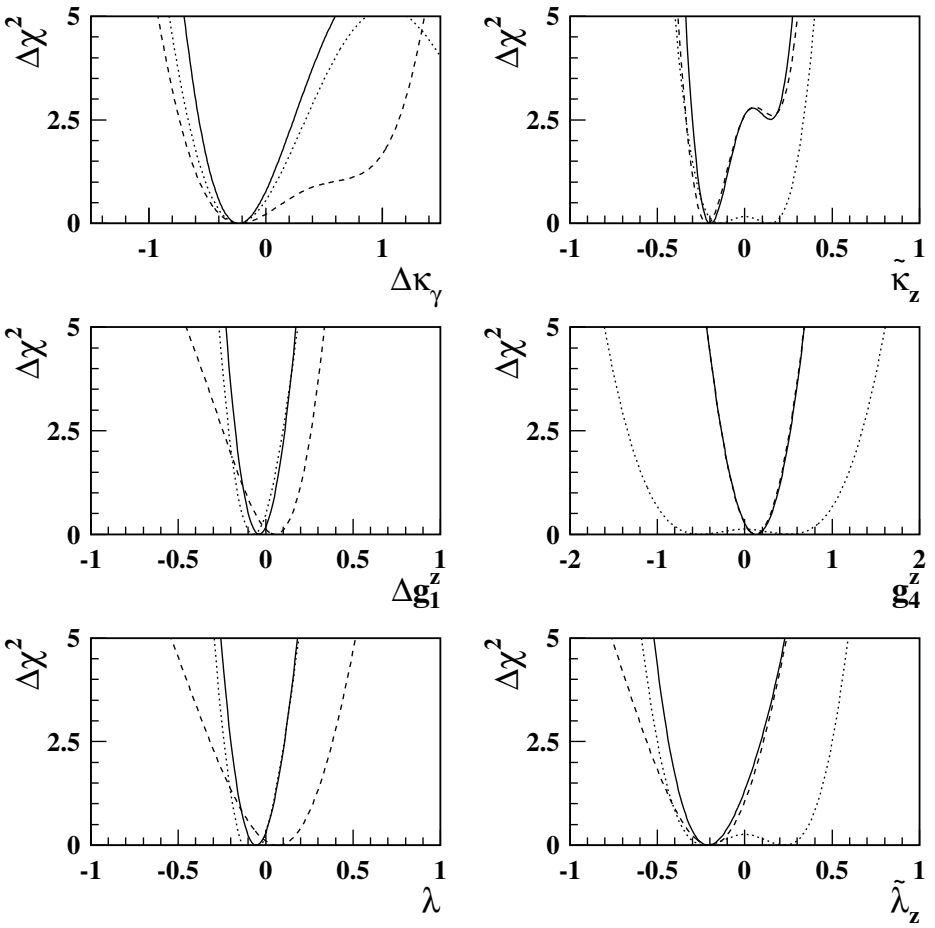

Figure B.6: *The χ^2 plots for the fits to the CP-conserving and CP-violating anomalous couplings. For the CP-conserving couplings the dashed line is the fit to just five real SDM elements, for the CP-violating couplings it is the fit to eight SDM elements. The ρ_{++} observable has been omitted. The dotted line is the fit to just the $\cos\theta_{\mathrm{W}}$ distribution. The solid line is the combined fit. All fits include systematic uncertainties.*

Bibliography

[1] G. T. Zatsepin, Nucl. Phys. Proc. Suppl. **33A** (1993) 136.

[2] Super-Kamiokande Collaboration, Y. Suzuki *et al.,* Nucl. Phys. Proc. Suppl. **77** (1999) 35.

[3] Super-Kamiokande Collaboration, Y. Fukuda *et al.,* Phys. Rev. Lett. **82** (1999) 1810.

[4] Super-Kamiokande Collaboration, "Solar neutrino measurements from Super-Kamiokande," *Prepared for 29th International Conference on High-Energy Physics (ICHEP 98), Vancouver, British Columbia, Canada, 23-29 Jul 1998.*

[5] C. Caso *et al.*, Eur. Phys. J. **C3** (1998) 1.

[6] A. R. Bohm and N. L. Harshman, Nucl. Phys. **B581** (2000) 91.

[7] T. Saeki, "W mass measurement at LEP," *to be published in the proceedings of 34th Rencontres de Moriond: QCD and Hadronic interactions, Les Arcs, France, 20-27 Mar 1999.*

[8] OPAL Collaboration, G. Abbiendi *et al.*, "Measurement of the Mass and Width of the W Boson in e+e- Collisions at 189 GeV " CERN-EP-2000-099, *Submitted to Phys. Lett. B.*

[9] F. Mandl & G. Shaw, Quantum Field Theory, John Wiley & Sons, 1996.

[10] S. Myers, "The LEP collider, from design to approval and commissioning, Nov 26, 1990," CERN-91-08 *Presented at CERN Accelerator School: The LEP Collider from Design to Approval and Commissioning, Geneva, Switzerland, Nov 26, 1990, CAS: CERN accelerator school, 6th John Adams Memorial lecture.*

[11] G. Altarelli, "Interim report on the physics motivations for an energy upgrade of LEP-2: Introduction," CERN-TH-95-151 (1995).

[12] Physics at LEP2, Edited by G. Altarelli, T. Sjöstrand, F. Zwirner, Report on the LEP2 Workshop 1995, CERN-96-01 (1996).

[13] R. Miquel, "Physics potential of LEP2," *published in Jaca 1994, The standard model and beyond.*

[14] OPAL Collaboration, K. Ahmet *et al.*, Nucl. Instrum. Meth. **A305** (1991) 275.

[15] P. P. Allport *et al.*, Nucl. Instrum. Meth. **A346** (1994) 476.

[16] J. R. Carter *et al.*, Nucl. Instrum. Meth. **A286** (1990) 99.

[17] M. Hauschild *et al.*, Nucl. Instrum. Meth. **A314** (1992) 74.

[18] H. M. Fischer *et al.*, Nucl. Instrum. Meth. **A283** (1989) 492.

[19] H. Mes *et al.*, Nucl. Instrum. Meth. **A265** (1988) 445.

[20] G. Aguillion *et al.*, Nucl. Instrum. Meth. **A417** (1998) 266.

[21] C. Beard *et al.*, Nucl. Instrum. Meth. **A286** (1990) 117.

[22] P. W. Jeffreys *et al.*, Nucl. Instrum. Meth. **A290** (1990) 76.

[23] G. Bella *et al.*, Nucl. Instrum. Meth. **A252** (1986) 503.

[24] OPAL Collaboration, S. Dado *et al.*, Nucl. Instrum. Meth. **A252** (1986) 511.

[25] G. Mikenberg, Nucl. Instrum. Meth. **A265** (1988) 223.

[26] R. J. Akers *et al.*, Nucl. Instrum. Meth. **A357** (1995) 253.

[27] G. T. Arnison *et al.*, Nucl. Instrum. Meth. **A294** (1990) 431.

[28] D. C. Imrie, S. J. Hall, D. J. Miller, P. Sherwood and N. C. Wood, Nucl. Instrum. Meth. **A283** (1989) 515.

[29] B. E. Anderson *et al.*, Nucl. Instrum. Meth. **A283** (1989) 650.

[30] B. E. Anderson *et al.*, IEEE Trans. Nucl. Sci. **41** (1994) 845.

[31] M. Arignon *et al.*, Nucl. Instrum. Meth. **A333** (1993) 330.

[32] M. Arignon *et al.*, Nucl. Instrum. Meth. **A313** (1992) 103.

[33] D. G. Charlton, F. Meijers, T. J. Smith and P. S. Wells, Nucl. Instrum. Meth. **A325** (1993) 129.

[34] C. Hawkes *et al.*, The ROPE Users Guide, ROPE410 (1996).

[35] K. Hagiwara, R. D. Peccei, D. Zeppenfeld and K. Hikasa, Nucl. Phys. **B282** (1987) 253.

[36] M. Bilenkii, J. L. Kneur, F. M. Renard and D. Schildknecht, Nucl. Phys. **B409** (1993) 22.

[37] G. Bálanger and F. Boudjema, Phys Lett. **B288** (1992) 201.

[38] G. Abu Leil and W. J. Stirling, J. Phys. **G21** (1995) 517

[39] W. J. Stirling and A. Werthenbach, Eur. Phys. J. **C14** (2000) 103.

[40] OPAL Collaboration G. Abbiendi *et al.,* , Phys. Lett. **B471** (1999) 293.

[41] G. Gounaris, J. Layssac, G. Moultaka and F. M. Renard, Int. J. Mod. Phys. **A8** (1993) 3285.

[42] G. J. Gounaris and C. G. Papadopoulos, Eur. Phys. J. **C2** (1998) 365.

[43] H. C. Corben and J. Schwinger, Phys. Rev. **58** (1940) 953.

[44] T. D. Lee and C. N. Yang, Phys. Rev. **128** (1962) 885.

[45] N. Cabibbo and R. Gatto, Phys. Rev. **124** (1961) 1577.

[46] K. J. Kim and Y. Tsai, Phys. Rev. **D7** (1973) 3710.

[47] J. Wudka, Int. J. Mod. Phys. **A9** (1994) 2301.

[48] L. Rolandi, "Precision tests of the electroweak interaction," *Talk given at 26th International Conference on High Energy Physics (ICHEP 92), Dallas, TX, 6-12 Aug 1992.* CERN-PPE-92-175.

[49] L. Rolandi, "LEP results," *Published in Trieste 1993, Proceedings, High Energy Physics and Cosmology (1-13).*

[50] M. Koratzinos, "Electroweak results from LEP," *Published in a Thuile 1994, Results and Perspectives in Particle Physics (319-332).*

[51] Y. Galaktionov, "The review of LEP results," *Published in Saariselkae 1994, Future Physics and Accelerators (91-137).*

[52] M. Kuroda, F. M. Renard and D. Schildknecht, Phys. Lett. **B183** (1987) 366.

[53] G. J. Gounaris, *private communication.*

[54] C. G. Papadopoulos, Comput. Phys. Commun. **101** (1997) 183.

[55] K. F. Smith *et al.*, Phys. Lett. **B234** (1990) 191.

[56] P. G. Harris *et al.*, Phys. Rev. Lett. **82** (1999) 904.

[57] W. J. Marciano and A. Queijeiro, Phys. Rev. **D33** (1986) 3449.

[58] F. Boudjema, C. P. Burgess, C. Hamzaoui and J. A. Robinson, Phys. Rev. **D43** (1991) 3683.

[59] ALEPH Collaboration, R. Barate *et al.,* "Measurement of Triple Gauge-Boson Couplings at LEP energies up to 189 GeV," ALEPH 2000-015 CONF (CONFerence) 2000-012, *Conference note.*

[60] ALEPH Collaboration, R. Barate *et al.,* "Measurement of Triple Gauge-Boson Couplings at 192-202 GeV," ALEPH 2000-016 CONF (CONFerence) 2000-013, *Conference note.*

[61] D0 Collaboration, S. Abachi *et al.,* Phys. Rev. Lett. **78** (1997) 3634.

[62] J Ellison and J Wudka, *Ann. Rev. Nucl. Part. Sci.* **48** (1998) 33.

[63] DELPHI Collaboration, P. Abreu *et al.*, Phys. Lett. **B423** (1998) 194.

[64] P. Mery, M. Perrottet and F. M. Renard, Z. Phys. **C38** (1988) 579.

[65] G. Bella, D. Charlton and P. Clarke OPAL Technical Note, **TN-492** (1997).

[66] OPAL Collaboration, G Abbiendi *et al.*, "W^+W^- Production Cross section and W Branching Fractions in e^+e^- collisions at 189 GeV," CERN-EP-2000-101, *submitted to Phys. Lett. B.*

[67] G. Gounaris, D. Schildknecht and F. M. Renard, Phys. Lett. **B263** (1991) 291.

[68] N. Brown and W. J. Stirling, Phys. Lett. **B252** (1990) 657.

[69] S. Catani, Y. L. Dokshitzer, M. Olsson, G. Turnock and B. R. Webber, Phys. Lett. **B269** (1991) 432.

[70] S. Bethke, Z. Kunszt, D. E. Soper and W. J. Stirling, Nucl. Phys. **B370** (1992) 310.

[71] N. Brown and W. Stirling, Z. Phys. **C53** (1992) 629.

[72] D. Karlen, Computers in Physics **12** (1998) 380.

[73] I. Trigger and S. von Dobschütz, OPAL Technical Note, **TN-476** (1997).

[74] F. A. Berends, R. Pittau and R. Kleiss, Nucl. Phys. **B424** (1994) 308.

[75] F. A. Berends, R. Pittau and R. Kleiss, Comput. Phys. Commun. **85** (1995) 437.

[76] F. A. Berends, R. Pittau and R. Kleiss, Nucl. Phys. **B426** (1994) 344.

[77] R. Pittau, Phys. Lett. **B335** (1994) 490.

[78] V. S. Fadin, V. A. Khoze, A. D. Martin and W. J. Stirling, Phys. Lett. **B363** (1995) 112.

[79] J. Fujimoto *et al.*, Comput. Phys. Commun. **100** (1997) 128.

[80] D. Bardin, J. Biebel, D. Lehner, A. Leike, A. Olchevski and T. Riemann, Comput. Phys. Commun. **104** (1997) 161.

[81] M. Skrzypek, S. Jadach, W. Placzek and Z. Was, Comput. Phys. Commun. **94** (1996) 216.

[82] S. Jadach, W. Placzek, M. Skrzypek, B. F. Ward and Z. Was, Comput. Phys. Commun. **119** (1999) 272.

[83] M. Skrzypek, S. Jadach, M. Martinez, W. Placzek and Z. Was, Phys. Lett. **B372** (1996) 289.

[84] T. Sjostrand, "PYTHIA 5.7 and JETSET 7.4: Physics and Manual," CERN-TH-7112-93-REV, Aug 1995. 321pp. Long version of publication in Comput.Phys.Commun.

[85] G. Marchesini, B. R. Webber, G. Abbiendi, I. G. Knowles, M. H. Seymour and L. Stanco, Comput. Phys. Commun. **67** (1992) 465.

[86] R. Engel, Z. Phys. **C66** (1995) 203.

[87] R. Engel and J. Ranft, Phys. Rev. **D54** (1996) 4244.

[88] R. J. Hemingway, OPAL Technical Note, **TN-279** (1995).

[89] C. Darling, OPAL Technical Note, **TN-322** (1995).

[90] D. R. Ward, "The OPAL Monte Carlo program: GOPAL," *Published in Amsterdam 1991, Proceedings, MC 91: Detector and event simulation in high energy physics (204-226). (see HIGH ENERGY PHYSICS INDEX 30 (1992) No. 3237).*

[91] R. Brun, F. Bruyant, M. Maire, A. C. McPherson and P. Zanarini, "Geant3," CERN-DD/EE/84-1.

[92] WW111 Manual, Coordinators: C.P.Ward, D.R.Ward & N.K.Watson, (1998).
http://opalinfo.cern.ch/opal/manuals/ww/pro/ww.html.

[93] Embryonic Users Manual for the WV package, the OPAL TGC Group, (1997).
http://opalinfo.cern.ch/opal/group/ww/TgcWorkPage/wv/wv110_manual.ps.

[94] OPAL Collaboration, K. Ackerstaff *et al.* Eur. Phys. J. **C1** (1998) 395.

[95] OPAL Collaboration, G. Abbiendi *et al.,* Eur. Phys. J. **C8** (1999) 191.

[96] OPAL Collaboration, M. Z. Akrawy *et al.* Phys. Lett. **B253** (1991) 511.

[97] D0 Collaboration, B. Abbott *et al.* Phys. Rev. Lett. **80** (1998) 3008.

[98] CDF Collaboration, F. Abe *et al.* Phys. Rev. Lett. **75** (1995) 11.

[99] R. J. BARLOW, Statistics, John Wiley & Sons,

[100] WVCXME Users Manual, D. Charlton & P. Clarke, (1998).
http://opalinfo.cern.ch/opal/group/ww/TgcWorkPage/wvc.html

[101] OPAL Collaboration, G. Abbiendi *et al.*, Eur. Phys. J. **C13** (2000) 553.

[102] OPAL Collaboration, K. Ackerstaff *et al.*, Eur. Phys. J. **C2** (1998) 597.

[103] OPAL Collaboration, G Abbiendi *et al.*, "Measurement of W Boson Polarisations and CP-violating Triple Gauge Couplings from W^+W^- Production at LEP " CERN-EP-2000-113, *Submitted to Phys. Lett. B.*

[104] OPAL Collaboration, G. Abbiendi *et al.,* "Measurement of Triple Gauge Boson Couplings from W^+W^- Production at LEP Energies up to 189 GeV," CERN-EP-2000-114, *Submitted to Eur. Phys. J. C.*

[105] L3 Collaboration, M. Acciarri *et al.*, 1997. Phys. Lett. **B474** (2000) 194.